Cardiff University
School of Engineering

The characterisation of a drive train test rig to engineer a Tidal Stream Turbine Condition-Based Maintenance strategy

A thesis submitted to Cardiff University for the

Degree of Doctor of Philosophy

By

Edith Rojo-Zazueta

2022

Acknowledgements

This research was financed with the Consejo Nacional de Ciencia y Tecnología and el Fondo para el Desarrollo de Recursos Humanos in Mexico.

I would like to extend my deepest thanks to my supervisors, Mr. Paul Prickett and Dr. Roger Grosvenor. Thank you for your guidance through the last years and encouragement to exceed my personal boundaries in order to believe in myself. A special thanks to Dr. Matthew Allmark, whose advices, full support and good friendship were key in order to be able to complete this thesis. I would also like to thank all the support provided by Prof. Tim O' Doherty and Dr. Allan Mason Jones. Because of you, I was able to join the CMERG Group. Special thanks to Prof. Agustin Valera-Medina, for encouraging me to do this PhD.

I would also like to thank Dr. Rodolfo Silva-Casarin and Dr. Ismael Mariño-Tapia for inviting me to become part of the 1st oceanographic CEMIE-Oceano campaign in 2019, and providing financial support to be able to attend the AWTEC Conference in 2018 in Taiwan. Thank you to Dr. Hector Bastida for his assistance in using MatLAB software. Special thanks to Dr. Tattiana Hernandez-Madrigal for encouraging me to join the CMERG group, and also for being my psychologist and best friend through the last years.

I wouldn't be able to finish this PhD without the support of my friends and family. First, I would like to thank Mr. Francisco Varela-Solis for all his support through the last two years of this process. To Rafael, no amount of thanks would be enough for all the love and support you've given me. To my Cardiff friends, Andrea, Nati, Tony, Shaun for always being for me in the UK and in Mexico. To my Mexican friends, Belia, Pamela and

Fernando, thanks for never letting me down during this process. To my grandparents Praxedis, Rita, and Julia, thanks for all your love and guidance. To my grandpa Roberto: I wish you could still be here with us to celebrate this personal milestone.

Finally, this thesis is dedicated to my mother, my sister and my father: Lupita, Karen and Mario. Soy todo lo que soy gracias a ustedes.

Abstract

This research examines the development and validation of a condition monitoring technique using a $1/20^{th}$ turbine scaling drive train test rig. The capability of the test rig was assessed operating under steady and unsteady state simulations. The steady state turbine operation was developed by considering the theoretical mean values of previously validated Computer Fluid Dynamics of Horizontal Axis Tidal Turbine (HATT) models. The unsteady state turbine operation was obtained from a experimental test campaign conducted in a flume tank. A range of fluid time series were built in order to incorporate further complex tidal profile conditions. The work undertaken to demonstrate the test rig capability to emulate both steady state and unsteady state turbine operations was successful. The test rig was able to replicate the torque and rotational speed in both the rotor and the generator. The work then progressed in order to determine the test rig reliability to assess the CM algorithm effectiveness.

The condition monitoring technique engineered in this research is a frequency signal processing tool. This is implemented in a range of tidal operating conditions and differing recorded time lengths. It was able to detect different scales of HATT rotor imbalance faults that occur. It was found that the presence of high turbulent flows and large length scales have a great impact on detecting rotor imbalance faults. A comparison of the detection of the rotor imbalance fault in both the rotor and the generator was considered, and it was shown that the generator side of the test rig can effectively detect different fault scales when a torque-fault time series was implemented. This demonstrates the CM algorithm effectiveness to detect rotor imbalance faults in the generator. This provides confidence in the energy sector to establish further condition monitoring practices that could allow turbine developers to prevent major HATT malfunctions.

Contents

Acknowledgements **iii**

Abstract **v**

List of Figures **xiii**

List of Tables **xxiii**

List of Abbreviations **xxv**

1 Introduction **1**

1.1 The need for renewable energy 1

1.2 Ocean energy 3

1.2.1 Tidal Energy 5

1.3 The need for Condition Monitoring 9

1.4 Thesis aims and objectives 10

1.5 Thesis Outline 11

2 Literature Review **13**

2.1 Tidal Stream Energy. 14

2.2 Tidal Stream devices 14

2.2.1 Vertical-axis tidal turbine 14

2.2.2 Venturi Open Centre 16

2.2.3 Oscillating hydrofoil 17

2.2.4 Archimedes screw 17

2.2.5 Tidal kite 18

2.3 Horizontal-axis tidal turbine 18

2.4 HATT Challenges 20

2.5 Numerical and Experimental modelling techniques 21

2.6 HATT large scaled devices. 23

2.7 Tidal Energy Resource. 24

2.7.1 Resource in the UK. 26

2.7.2 Resource in Mexico 26

2.7.3 Low velocities feasibility 29

2.8 Condition Monitoring 31

2.8.1 Vibration analysis 33

2.8.2 Acoustic Emission 34

2.8.3 Strain measurement 34

2.8.4 Electrical signal monitoring 35

2.8.5 Other novel techniques 36

2.9 Condition Monitoring research in TST 36

2.10 The use of test rigs in the energy industry 39

2.11 Summary 43

3 Methodology **45**

3.1 Turbine Scaling Model 46

3.1.1 HATT Operating Principle 46

3.1.2 HATT Topology 48

3.1.3 Turbine Control 51

3.1.4 CMERG lab-scaled Turbines 53

3.2 Drive Train Test Rig 54

3.2.1 Hardware 54

3.2.2 Instrumentation, Control and Software Implementation. 59

3.2.3 Steady State Simulations 61

3.2.4 Unsteady State Simulations 64

3.3 Techniques Utilised 67

3.3.1 Frequency Analysis 67

3.3.2 Statistical Analysis 68

3.4 Resource characterisation. 69

3.4.1 Turbulence Intensity 72

3.4.2 Integral length scale 73

3.4.3 Energy Spectra 74

3.5 Simulation Methodology matrix 76

4 Drive Train Test Rig Development **81**

4.1 First stage drive train test rig 82

4.2 Simulation Methodology 87

4.3 Steady State Power Curves Results 93

4.4 Statistical Validation 97

5 Rotor Imbalance Fault Condition **109**

5.1 Flow Tank Testing 110

5.2 Signal Monitoring 115

5.3 CM algorithm building process 120

5.4 Torque and Thrust frequency content. 124

5.5 Feature extraction and Control Charts 129

5.6 Unsteady State Methodology Matrix 136

6 Drive Train Simulation Results of Unsteady Experimental Data 141

6.1 Flume tank testing 142

6.1.1 Data recording and Instrumentation 143

6.1.2 Overview of the obtained results 145

6.2 DTTR torque data characterisation 149

6.2.1 Software Implementation 150

6.3 DTTR Unsteady Experimental Data Results 151

7 Drive Train Simulation Results of Unsteady Synthetic Data 171

7.1 Resource Simulation 172

7.2 Integral Length Scale and Resource validation 175

7.3 DTTR data characterisation and Software Implementation 179

7.4 DTTR Unsteady Synthetic Data Results 180

7.5 Impact of tidal conditions on CM algorithm 197

8 Conclusions and Contributions to Research 203

8.1 Steady State HATT Characterisation in a DTTR 203

8.2 Rotor Imbalance Fault Parameterisation 204

8.3 CM algorithm effectiveness in experimental data 204

8.4 CM algorithm effectiveness in synthetic data 205

8.5 Recommendations for further work 206

8.6 Contributions to research 207

References **209**

List of Figures

1.1 Global net anthropogenic GHG emissions 1990-2019. [IPCC, 2022] 2

1.2 Share of electricity production by source worldwide. [Ritchie et al., 2020] . 3

1.3 Total ocean energy deployment in MW by 2020. [IRENA, 2020] 5

1.4 Tidal energy potential worlwide. [Offshore Energy, 2015] 6

2.1 Tidal Stream Technology Devices. [Aqua-RET Project, 2012] 15

2.2 Schematic of a tidal stream tube and actuator disk. Adapted from [Jamieson and Hassan, 2011]. 19

2.3 Commercial Tidal Stream Projects. 25

2.4 UK tidal stream resource estimation. [Ebdon, 2019]. 27

2.5 Mexico Energy Potential. 30

2.6 Test Rigs that have successfully determine WT operating conditions and possible faults with a simpler and cost-effective experimental technique. . 42

3.1 Typical HATT breakdown [Tian et al., 2018]. 49

3.2 General control scheme of a HATT based on PMSMs with full-rated VSC. Adapted from [Cheah-Mane et al., 2014]. 51

3.3 The previous version of the drive train test rig used to perform the first set of simulations. Both PMSMs are emulating a 0.5 m diameter rotor and generator sides respectively, and are coupled via a 1:10 ratio gearbox. . . . 55

3.4 The final version of the drive train test rig used to perform the simulations. PMSM on the rotor side is emulating a 0.9 m rotor diameter, whilst the PMSM on the generator side is emulating a 0.5 m generator diameter, and are coupled via a 1:10 ratio gearbox. 56

3.5 Bosch Rexroth rotor/generator MSK 050Cs speed/torque characteristic. . 57

3.6 Drive train test rig set up that comprises the communication between components. 59

3.7 Overall structure of the position, velocity and current control loops utilised in the test rig setup utilising VOC and PMSMs encoder feedback values. . . 62

3.8 Drive train test rig diagram of the steady state simulations setup and the distribution of functionalities and parameters settings across the hardware and software platforms. 63

3.9 IndraWorks Easy StartUp mode window interface to set the $\overline{\tau}_{rotor}$ and the $\overline{\omega}_{gen}$ on each host PC simultaneously. 65

3.10 Drive train test rig diagram of the unsteady state simulations setup and the distribution of functionalities and parameters settings across the hardware and software platforms. 66

3.11 IndraWorks Analog input window interface to set the scaled voltage range from 0 V to 10 v to the maximum available torque at the chosen PMSM. . . 67

3.12 Overview of the testing and simulation methodology followed throughout this research. 79

4.1 Possible power curves with varying diameter and flow velocity that could be tested on the previous test rig version. 84

4.2 Combined power output and velocities from rotor and generator compared to the theoretical model of the previous test rig version. 86

4.3 Power curve from rotor and generator compared to the theoretical model of a 0.5 m diameter turbine at 1 ms^{-1}. 87

4.4 Comparison of torque force feedback value and torque calculated utilising equation 3.5 for both turbine diameters of 0.7 m and 0.9 m, with a flow velocity of 1 ms^{-1} at $\lambda = 4$ on a period of 5 s. 91

4.5 Torque signals from IndraWorks system from Rotor and Generator for turbine diameters of 0.7 m and 0.9 m at $\lambda = 4$ for a period of 15 s. 92

4.6 Histograms of 0.7 m diameter rotor and generator normalised torque signals for λ = 2,4 and 6. 93

4.7 Histograms of 0.9 m diameter rotor and generator normalised torque signals for λ = 2,4 and 6. 94

4.8 Power Curve comparison of theoretical values from CFD validated data, rotor and generator signals from the test rig for diameter 0.7 m. 95

4.9 Power Curve comparison of theoretical values from CFD validated data, rotor and generator signals from the test rig for diameter 0.9 m. 96

4.10 C_θ curve of generator signal for diameter 0.7 m. 98

4.11 C_θ curve of generator signal for diameter 0.9 m. 99

4.12 Power Curve for a diameter of 0.9 m, generator data repeated three times. 100

4.13 C_θ curve for a diameter 0.9 m. generator data repeated three times. 101

4.14 Normal Probability Distribution of the Rotor C_p signal for $\lambda = 4$. 103

4.15 Normal Probability Distribution of the Generator C_p signal for $\lambda = 4$. . . . 104

4.16 ANOVA ran three different times for $\lambda = 2$ in C_p rotor and generator signals. 104

4.17 ANOVA ran three different times for $\lambda = 4$ in C_p rotor and generator signals. 105

4.18 ANOVA ran three different times for $\lambda = 6$ in C_p rotor and generator signals. 105

4.19 Multiple comparison test for Generator C_{p} signal for $\lambda = 4$. 106

4.20 Normal distribution data of C_{p} signal for $\lambda = 4$ overlapped two times. . . . 106

5.1 Tow tank at the KHL at Strathclyde University. 111

5.2 One of the CMERG HATTs being tested at KHL. 111

5.3 Characteristic power curves obtained from the KHL tests for each of the three turbines. The figures show both the power curves obtained considering rotor transducer measurements and motor power measurements. . . . 113

5.4 Characteristic torque curves obtained from the KHL tests for each of the three turbines. The figures show both the torque curves obtained considering rotor transducer measurements and motor power measurements. . 114

5.5 Characteristic thrust curves obtained from the KHL tests for each of the three turbines. The figures show both the thrust curves obtained considering rotor transducer measurements and motor power measurements. . . . 115

5.6 Rotor thrust data signals for T1, T2 and T3 at flow velocity of 0.8 ms^{-1} and 1.0 ms^{-1} windowed five times from the total time length and a mean value was calculated from all the iterations. 117

5.7 Rotor torque data signals for T1, T2 and T3 at flow velocity of 0.8 ms^{-1} and 1.0 ms^{-1} windowed five times from the total time length and a mean value was calculated from all the iterations. 118

5.8 Motor torque data signals for T1, T2 and T3 at flow velocity of 0.8 ms^{-1} and 1.0 ms^{-1} windowed five times from the total time length and a mean value was calculated from all the iterations. 119

5.9 PSD of the rotor and motor torque data signals for T1, T2 and T3 at flow velocity of 0.8 ms^{-1} for λ = 2.5, 4 and 6.5. 124

5.10 PSD of the rotor and motor torque data signals for T1, T2 and T3 at flow velocity of 1.0 ms^{-1} for λ = 2.5, 4 and 6.5. 125

5.11 PSD of the rotor thrust data signals for T1, T2 and T3 at flow velocity of 0.8 ms^{-1} and 1.0 ms^{-1} for λ = 2.5, 4 and 6.5. 126

5.12 Comparison of values f/f_0 = 1, f/f_0 = 2 and f/f_0 = 3 of the rotor torque data signals for turbines T1, T2 and T3, flow velocities of 0.8 ms^{-1}, 1.0 ms^{-1} and 1.2 ms^{-1} for λ values from 1 to 7. 127

5.13 Comparison of values f/f_0 = 1, f/f_0 = 2 and f/f_0 = 3 of the motor torque data signals for turbines T1, T2 and T3, flow velocities of 0.8 ms^{-1}, 1.0 ms^{-1} and 1.2 ms^{-1} for λ values from 1 to 7. 128

5.14 Comparison of spectrograms for turbines T1, T2 and T3 respectively for λ = 4 With a flow velocity of 0.8 ms^{-1} and 1.0 ms^{-1}. 132

5.15 Comparison of control charts for T1, T2 and T3 respectively for λ = 2.5 with a flow velocity of 0.8 ms^{-1} and 1.0 ms^{-1}. 132

5.16 Comparison of control charts for T1, T2 and T3 respectively for λ = 4 with a flow velocity of 0.8 ms^{-1} and 1.0 ms^{-1}. 133

5.17 Comparison of control charts for T1, T2 and T3 respectively for λ = 6.5 with a flow velocity of 0.8 ms^{-1} and 1.0 ms^{-1}. 133

5.18 Methodology matrix for unsteady state scenarios defined for this research. 136

6.1 IFREMER's Boulogne-sur-Mer flume tank description [Mycek et al., 2014]. 142

6.2 Series of test cases setups undertaken at IFREMER test campaign in 2018. (a) Case 1, (b) Case 2, (c) Case 3. Adapted from [Allmark et al., 2021a]. . . . 144

6.3 Dimensions of the turbulence grid utilised at the IFREMER testing campaign. Adapted from [Blackmore et al., 2016]. 146

6.4 An overview of the LabVIEW code implementation. 152

6.5 Normalised rotor torque data signals for TI = 2%, 8% and 15.8% at $\lambda = 4$ and for fault sizes of 0%, 1%, 5%, 10% and 15% windowed five times from the total time length and a mean value was calculated from all the iterations. . 153

6.6 Torque loading time series obtained from the rotor and generator on the DTTR, overlapped with the theoretical torque data signals for TI = 2%, 8% and 15.8% at $\lambda = 4$ and fault size of 0% 154

6.7 Boxplot of torque signals for the three TI cases undertaken and for the five fault sizes cases, including repeats. Left size column are rotor torque signals, right size column are the generator torque signals. 155

6.8 Results from all the signals recorded at the generator DTTR for the TI= 2% case, recorded time length ~ 90 s, fault size = 0%. 156

6.9 PSDs calculated for each of the fault size cases recorded on the DTTR from the Rotor for $\lambda = 4$, with a flow velocity of 1.0 ms^{-1} and for three different TI cases. Recorded time length ~ 30 s. 157

6.10 PSDs calculated for each of the fault size cases recorded on the DTTR from the Rotor for $\lambda = 4$, with a flow velocity of 1.0 ms^{-1} and for three different TI cases. Recorded time length ~ 90 s. 158

6.11 PSDs calculated for each of the fault size cases recorded on the DTTR from the Generator for $\lambda = 4$, with a flow velocity of 1.0 ms^{-1} and for three different TI cases. Recorded time length ~ 30 s. 161

6.12 PSDs calculated for each of the fault size cases recorded on the DTTR from the Generator for $\lambda = 4$, with a flow velocity of 1.0 ms^{-1} and for three different TI cases. Recorded time length ~ 90 s. 162

6.13 Amplitude of each of the fault size cases recorded on the DTTR from the Rotor and the Generator for $\lambda = 4$, with a flow velocity of 1.0 ms^{-1}, for f/f_0 = 1, f/f_0 = 3 and f/f_0 = 6 and for three different TI cases. Recorded time length ~ 30 s. Yellow = No Fault Size, Dark blue = 1% Fault Size, Green = 5% Fault Size, Navy blue = 10% Fault Size and Light Blue = 15% Fault Size. . . . 163

6.14 Amplitude of each of the fault size cases recorded on the DTTR from the Rotor and the Generator for $\lambda = 4$, with a flow velocity of 1.0 ms^{-1}, for f/f_0 = 1, f/f_0 = 3 and f/f_0 = 6 and for three different TI cases. Recorded time length ~ 90 s. Yellow = No Fault Size, Dark blue = 1% Fault Size, Green = 5% Fault Size, Navy blue = 10% Fault Size and Light Blue = 15% Fault Size. . . . 164

6.15 Control Charts for each of the fault size cases recorded on the DTTR from the Rotor for $\lambda = 4$, with a flow velocity of 1.0 ms^{-1} and for three different TI cases. Recorded time length ~ 30 s. 166

6.16 Control Charts for each of the fault size cases recorded on the DTTR from the Rotor for $\lambda = 4$, with a flow velocity of 1.0 ms^{-1} and for three different TI cases. Recorded time length ~ 90 s. 167

6.17 Control Charts for each of the fault size cases recorded on the DTTR from the Generator for $\lambda = 4$, with a flow velocity of 1.0 ms^{-1} and for three different TI cases. Recorded time length ~ 30 s. 168

6.18 Control Charts for each of the fault size cases recorded on the DTTR from the Generator for $\lambda = 4$, with a flow velocity of 1.0 ms^{-1} and for three different TI cases. Recorded time length ~ 90 s. 169

7.1 Effect of sample time on mean velocity, turbulence intensity and integral length scale with a U= 1 ms^{-1}, TI = 5%, and L_x= 1 m over a time period of 150 s. 176

7.2 Effect of sample time on mean velocity, turbulence intensity and integral length scale with a U= 1 ms^{-1}, TI = 5%, and L_x= 5 m over a time period of 150 s. 177

7.3 Effect of sample time on mean velocity, turbulence intensity and integral length scale with a U= 1 ms^{-1}, TI = 5%, and L_x= 10 m over a time period of 150 s. 178

7.4 Normalised rotor torque data signals for TI = 2%, 5% and 15% at $\overline{u}$ = 1 ms^{-1}, L_x = 1 m, and for fault sizes of 0%, 1%, 5%, 10% and 15% windowed five times from the total time length and a mean value was calculated from all the iterations. 181

7.5 Normalised rotor torque data signals for TI = 2%, 5% and 15% at $\overline{u}$ = 1 ms^{-1}, L_x = 5 m, and for fault sizes of 0%, 1%, 5%, 10% and 15% windowed five times from the total time length and a mean value was calculated from all the iterations. 182

7.6 Normalised rotor torque data signals for TI = 2%, 5% and 15% at $\overline{u}$ = 1 ms^{-1}, L_x = 10 m, and for fault sizes of 0%, 1%, 5%, 10% and 15% windowed five times from the total time length and a mean value was calculated from all the iterations. 183

7.7 Torque loading time series obtained from the rotor and generator on the DTTR, overlapped with the theoretical torque data signals for TI = 2%, 8% and 15.8% at $\overline{u}$ = 1 ms^{-1}, L_x = 1 m, L_x = 5 m, L_x = 10 m, and fault size of 0%. 184

7.8 Boxplot of torque signals for the three TI cases undertaken, $\overline{u}$ = 1 ms^{-1}, L_x = 5 m and for the five fault sizes cases, including repeats. Left size column are rotor torque signals, right size column are the generator torque signals. 185

7.9 PSDs calculated for each of the fault size cases recorded on the DTTR from the Rotor for the $\overline{u}$ = 1.0 ms^{-1}, all three L_x cases and for three different TI cases. Recorded time length ~ 30 s. 186

7.10 PSDs calculated for each of the fault size cases recorded on the DTTR from the Rotor for the $\overline{u}$ = 1.0 ms^{-1}, all three L_x cases and for three different TI cases. Recorded time length ~ 90 s. 187

7.11 PSDs calculated for each of the fault size cases recorded on the DTTR from the Generator for the $\overline{u}$ = 1.0 ms^{-1}, all three L_x cases and for three different TI cases. Recorded time length ~ 30 s. 188

7.12 PSDs calculated for each of the fault size cases recorded on the DTTR from the Generator for the $\overline{u}$ = 1.0 ms^{-1}, all three L_x cases and for three different TI cases. Recorded time length ~ 90 s. 189

7.13 Amplitude of each of the fault size cases recorded on the DTTR from the Rotor for flow velocities of 0.8 ms^{-1}, 1.0 ms^{-1} and 1.2 ms^{-1}, for f/f_0 = 1, f/f_0 = 3 and f/f_0 = 6 and for three different TI cases and L_x cases. Recorded time length ~ 90 s.Green = $\overline{u}$ = 0.8 ms^{-1}, Yellow = $\overline{u}$ = 1.0 ms^{-1} and Light Blue = $\overline{u}$ = 1.2 ms^{-1}. 191

7.14 Amplitude of each of the fault size cases recorded on the DTTR from the Generator for flow velocities of 0.8 ms^{-1}, 1.0 ms^{-1} and 1.2 ms^{-1}, for f/f_0 = 1, f/f_0 = 3 and f/f_0 = 6 and for three different TI cases and L_x cases. Recorded time length ~ 90 s.Green = $\overline{u}$ = 0.8 ms^{-1}, Yellow = $\overline{u}$ = 1.0 ms^{-1} and Light Blue = $\overline{u}$ = 1.2 ms^{-1}. 192

7.15 Control Charts for each of the fault size cases recorded on the DTTR from the Rotor, with a flow velocity of 1.0 ms^{-1} and for three different TI cases and L_x cases. Recorded time length ~ 90 s. 195

7.16 Control Charts for each of the fault size cases recorded on the DTTR from the Generator, with a flow velocity of 1.0 ms^{-1} and for three different TI cases and L_x cases. Recorded time length ~ 90 s. 196

7.17 Impact of Tidal Conditions in CM algorithm 200

List of Tables

3.1 CMERG 3.0 Ansys CFX Model Turbine specifications and experimental testing main data from the University of Liverpool and CMERG last generation of turbine Ansys CFX Model Turbine specifications and experimental testing main data from IFREMER and KHL [Frost et al., 2015, Allmark, 2016, Ordonez-Sanchez et al., 2019, Ellis, 2016, Allmark et al., 2020] 54

3.2 PMSMs Characteristics utilised on the drive train test rig. 58

4.1 Theoretical input values for the drive train test rig 90

5.1 Table providing an overview of peak non-dimensional quantities, power and motor torque and power losses across the 3 different turbines and velocities in analysis. 112

5.2 Table providing an overview of motor and rotor torque and thrust across the three different turbines and velocities in analysis at λ=4. 117

5.3 Table providing an overview of the points of the built time series above their respective upper control limits in the motor from control charts of figures 5.15 to 5.17. 135

6.1 LDV measurements obtained at the IFREMER testing campaign of the flow characteristics observed in the pre-turbine installation phase (PTI) vs during experiments (TDE). [Allmark et al., 2021a] 147

6.2 Theoretical input values to run the experimental set of data obtained from the IFREMER testing campaign. 148

6.3 Table providing an overview of the points of the built time series above their respective upper control limits from control charts of figures 6.15 to 6.18. 170

7.1 Table providing an overview of the points of the built time series above their respective upper control limits from control charts of figures 7.15 to 7.16. 194

List of Abbreviations

Symbols	Description	Units
A	Rotor Area	m^2
C_p	Power coefficient	-
C_T	Thrust coefficient	-
C_θ	Torque coefficient	-
$\varnothing$	Diameter	m
F	Thrust	N
f	frequency	Hz
f/f_0	frequency x rotational frequency of the turbine	$2\pi \cdot f/\omega$
FS	Fault Size	%
fs	sampling frequency	Hz
H_0	Null Hypothesis	-
H_1	Alternative Hypothesis	-
K_M	Torque/force constant	Nm/A
L_x	Integral Length Scale	m
MCL	Mean Control Limit	Nm
P_{value}	Statistical measurement for hypothesis	-
PSD	Power Spectral Density	Nm^2/Hz, N^2/Hz
r	rotor radius	m
Re	Reynolds number	-
SE	Standard error	Nm

Continued on next page

Table 1 – *continued from previous page*

Symbols	Description	Units
T	Time	s
$T1$	Turbine 1	-
$T2$	Turbine 2	-
$T3$	Turbine 3	-
U	Velocity Vector	ms^{-1}
$\overline{u}$	time-averaged velocity	ms^{-1}
UCL	Upper Control Limit	Nm
v	free stream velocity	ms^{-1}

Symbols	Description	Units
κ	number of waves per unit distance	m
λ	Tip speed ratio	-
ω	turbine rotational velocity	RPM
$\propto$	angle of attack	°
$\propto$	significance level	%
ρ	Fluid Density	$kg \cdot m^3$
$\rho(\tau)$	Autocorrelation Coefficient	-
σ	standard deviation	-
τ	Torque	Nm
ξ	turbulence kinetic energy dissipation rate	Js^{-1}
η	Efficiency	-

Symbols	Description
AC	Alternating Current
ADCP	Acoustic Doupler Current Profiler
ADV	Acoustic Doppler Velocimeter
AI	Artificial Intelligence
ANOVA	Analysis of Variance
BEMT	Blade Element Momentum Theory
CBM	Condition-Based Maintenance
CFD	Computational Fluid Dynamics
CM	Condition Monitoring
CMERG	Cardiff Marine Energy Research Group
DC	Direct Current
DECC	Department of Energy and Climate Change
DFIG	Double-fed Induction Generator
DMaC	Dynamic Marine Component
DTFT	Discrete-time Fourier Transform
DTTR	Drive train test rig
FFT	Fast Fourier Transform
FMECA	Failure Mode and Effect Analysis
GC	Gulf of California
GHG	Greenhouse gases
GSC	Generator Side Converter
HATT	Horizontal-axis Tidal Turbine
IFREMER	Institut Français de Recherche pour l'Exploitation de la Mer
IPCC	Intergovernmental Panel on Climate Change
IRENA	International Renewable Energy Agency
KHL	Kelvin Hydrodynamics Laboratory
LCoE	Levelised Cost of Energy
LDV	Laser Doppler Velocimetry

Continued on next page

Table 3 – ***continued from previous page***

Symbols	Description
LES	Large Eddy Simulations
NSC	Network Side Converter
ORE	Offshore Renewable Energy
OTEC	Ocean Thermal Energy Conversion
PI	Proportional Integral Controller
PLC	Programmable Logic Controller
PMSM	Permanent Magnet Synchronous Machine
PSD	Power Spectral Density
PWM	Pulse Width Modulated controller
PXI	PCI eXtensions for Instrumentation Serial Interface Module
RANS	Reynolds Averaged Navier-Stokes
SCADA	Supervisory Control and Data Acquisition
STFT	Short-time Fourier Transform
SWT	Synchrosqueezing Wavelet Transform
TMS	Transient Monitoring Surfaces
TRL	Technology Readiness Level
TSA	Time Synchronous Averaging
TST	Tidal Stream Turbine
VATT	Vertical-axis Tidal Turbine
VOC	Vector Oriented Control
VSC	Voltage Source Converter
WT	Wind Turbine

1

Introduction

The energy sector is currently dealing with big challenges worldwide: the depletion and scarcity of fossil fuels, a higher energy demand due to the increase in population, the commitment to protect the environment and to mitigate the effects of climate change. It was a few decades ago when humanity began to take seriously the possibility of fossil fuel 'run-out' and to account for the destabilisation of natural ecosystems and global climate. Since then, energy policies around the world are looking forward to exploiting new renewable resources for electricity and energy consumption. Developing sustainable energy generation technology is therefore a matter of urgency.

1.1. The need for renewable energy

Throughout history, climate on earth has been constantly changing. According to the Intergovernmental Panel on Climate Change (IPCC) report [IPCC, 2022], an-

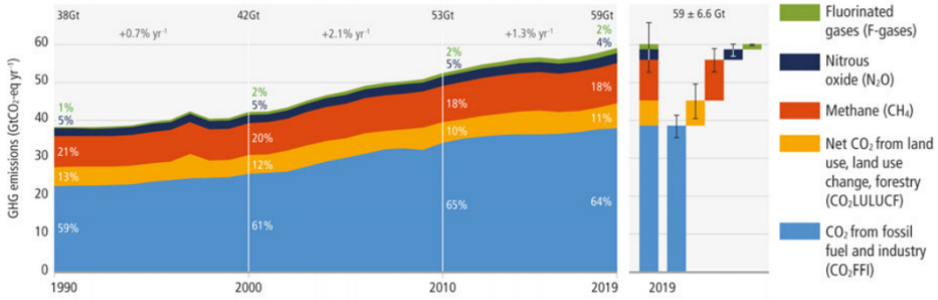

Figure 1.1: Global net anthropogenic GHG emissions 1990-2019. [IPCC, 2022]

thropogenic gas emissions (such as CO_2, CH_4 and NO_x) have increased since the pre-industrial era due to the high fossil fuel consumption in order to satisfy the economic and population growth. The annual average of global net anthropogenic GHG emissions during the decade 2010–2019 was 56±6.0 $GtCO_2$-eq, 9.1 $GtCO_2$-eq yr^{-1} higher than in 2000-2009. In 2021, a 6% increase from 2020 pushed emissions to 36.3 GT having a recovery in the energy demand after the pandemic, and therefore reaching their highest ever annual level [IEA, 2022]. Half of the anthropogenic CO_2 emissions have occurred in the last 40 years, leading to increases in average global temperature, changes in precipitation, melting of glaciers and reduced snow cover, and increases in ocean temperatures and acidity [Cherian, 2015]. Since 1993 the sea level has risen an average of 3.1 mm per year or a total 17 cm during the 20^{th} century since about 25% and 15% of the mountain glaciers and arctic ice sheets respectively has already melted [IPCC, 2022]. If no further action is taken in the upcoming years, global temperature could rise from 2 to 6°C, leading to the increase of storms, droughts and floods, the undermine food security and the change of landscapes and wildlife habitat. Figure 1.1 displays the global net GHG emissions from 1990 to 2019.

As an attempt to counter climate change, the Kyoto Protocol was drawn up in 1997 where 36 industrialised countries bound emission reduction targets to a 5% emission reduction period from 2008 to 2012 [UNFCCC, 2014]. The most recent international commitment against climate change was the Paris Agreement held on April 2016, where the central aim is to keep the temperature rise below to 2°C or even 1.5 if possible. In

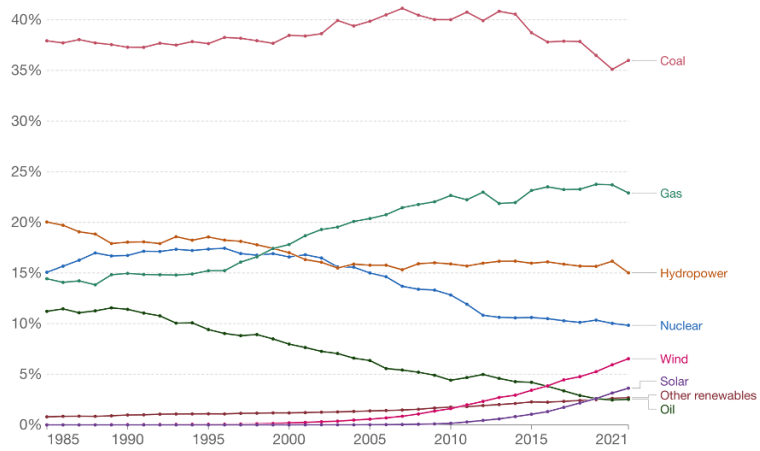

Figure 1.2: Share of electricity production by source worldwide. [Ritchie et al., 2020]

order to reach these goals, appropriate financial flows, technology framework and enhanced capacity building framework will have to be addressed. There are five key measures in order to meet a bridge scenario from current GHG emissions growth to reduce them, which are energy efficiency, reducing inefficient coal, methane reductions, fossil-fuel subsidy reform and renewables investment [IEA, 2016]. Renewable energies share in total final energy consumption by 2019 is of 17.7%, an increase of 1.6% compared to 2010. Hydropower remains by far the largest source of renewable electricity globally, followed by wind, then solar PV [IRENA, 2022]. Figure 1.2 shows the share of electricity production by source worldwide, demonstrating that coal and gas are the main energy sources to produce electricity, and appraising a need to find a faster solution into decarbonising the electricity sector in order to stop the global temperature to rise.

1.2. Ocean energy

Among all renewable resources, one that has attracted considerable attention is ocean energy. The potential for ocean energy technologies has been estimated at 7400 EJ yr^{-1}, exceeding current and future energy needs [Ellabban et al., 2014]. The International Renewable Energy Agency (IRENA) estimates that around 10 GW could be commercially

deployed by 2030, additional to the 534.7 MW already installed. By 2020, tidal stream and wave energy represents a total installed capacity of 12.91 MW being completely operational. Figure 1.3 shows the installed capacity of ocean energy technologies. It is noticeable that tidal barrage technologies dominate the ocean energy sector. Marine renewables can provide significant socio-economic opportunities to countries with coastal areas and island territories, and would contribute to the achievement of the United Nations Sustainable Development Goals in islands and coastal territories [IRENA, 2020]. Other significant advantages of marine energy are the high predictability, space availability and less competition in offshore resources compared to land-based renewables [Fraenkel, 2006].

Research has determined that hydrodynamic modelling of the marine devices and the interactions with the complex sea is improving. However it is not yet able to represent the non-linear conditions in the forces acting to produce power on the device. Therefore, researchers are currently seeking the method to predict simulated device response, performance and survival instead of forecasting the behaviour of the sea [Hardisty, 2009]. Ocean energy technologies have reached different Technology Readiness Levels (TRL). Among these, tidal range has been the only technology operating for more than 50 years and being classified as a full-scale commercial ocean energy power plant of farms, reaching a TRL of 9 [OES, 2020]. In order to facilitate the progression of these technologies to higher TRLs, increased innovation and research efforts should take place. This would spread the risk among stakeholders and the support to further development of test centres [Magagna and Uihlein, 2015].

In order to choose a renewable resource to be exploited in certain location, commercial, strategic and environmental considerations must be considered. The different energy extraction methods are: ocean thermal energy conversion (OTEC), salinity gradient, tidal range, wave energy and tidal stream. Of these options, this research is then focused with tidal energy.

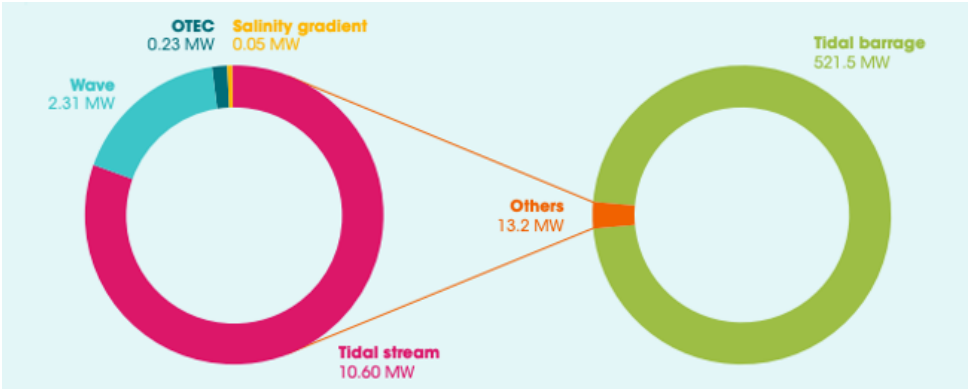

Figure 1.3: Total ocean energy deployment in MW by 2020. [IRENA, 2020]

1.2.1. Tidal Energy

Tidal energy can be described as the movement of water caused by the ebb and flow of tidal currents (tidal stream), or from the rise and fall in sea levels between high and low tides (tidal range) along with the gravitational effect of the Earth, Moon and Sun [McCrea, 2008]. Thus, the energy potential is proportional to the difference in the height of the water, which varies according to tide cycles and location.

There are two effects that explain how tides are formed: the centrifugal effect and the gravitational effect. A centrifugal force in the sea is large when the side of the Earth is furthest from the moon, and small when the face is closest to the rotation point between the Moon and the Earth's surface. On the other hand, the gravitational effects relate to the pull of the moon which attracts the Earth's surface nearest to the Moon into a bulge [Douglas, 2011]. Finally, there must be a balance within both effects into the sea, so when a small centrifugal force and an increased lunar pull acting on the seas facing the Moon occurs, the opposite effect will happen in the other side of the Earth. These will lead to two tides per day called semi-diurnal tides: two high tides and two low tides per day near the Equator [Boyle, 2012].

Even though there could be external factors that can alter tidal patterns (i.e. topography and weather), lunar cycles and their gravitational forces into the sea makes

1

tidal energy one of the most predictable alternative energies among others. Figure 1.4 displays the highest potential of tidal energy found per country, and the depth where the energy could be extracted from. Certainly the UK tidal potential represents the highest one worldwide, with 11,400 MW found in relatively shallow waters. Both types of tidal energy technologies are described next.

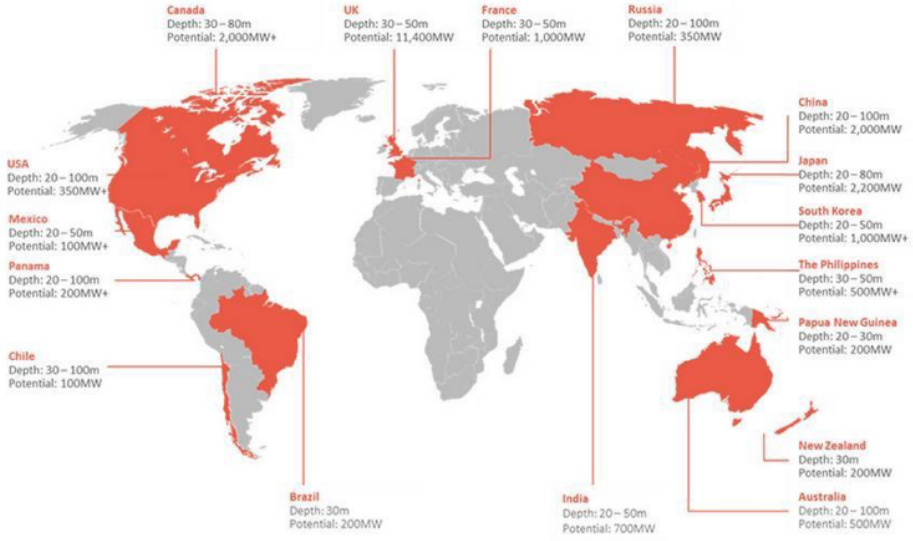

Figure 1.4: Tidal energy potential worlwide. [Offshore Energy, 2015]

Tidal Range

Tidal barrages is a technology that has been exploited for several decades. For example La Rance in France provides an annual output of 480 GWh. This method of power generation can create vast amounts of electricity and is able to integrate infrastructure such as road and rail crossings on top of the dam. However, further development of this technology has been hampered by significant environmental concerns and very high initial costs [Waters and Aggidis, 2016]. Instead, a less ambitious but equally effective alternative has been proposed as “bounded reservoir” or “tidal lagoon” systems. Even though they yield a smaller output compared to a barrage, this does produce a

larger output power per unit area enclosed [Boyle, 2012]. Tidal lagoons are coastal walls or dam structures with hydro turbines submerged that captures the head height of water levels [Charlier, 2007]. Lagoons would be in relatively shallow water and will be constructed like causeways with rock infill. An advantage compared with barrages is that it would not involve blocking off an estuary, thus the environmental impact would be less and it will avoid interfering with the passage of the ships [Boyle, 2012]. Power is generated as the sea outside the breakwater rises and is held back a difference in water levels is created. Once a sufficient head height is reached gates are opened, and water flows into the lagoon through turbines to generate electricity. This movement is reversed on the ebb tide, sea levels fall and a tidal head is created by holding water back within the lagoon [Tidal Lagoon Power, 2012]. Power can be produced using a two-way operation with the flow direction, which can generate electricity through all four tidal movements per day. It is a combination between the ebb and flood generation methods: the sluice gates are kept closed until there is sufficient head difference between the basin and sea. Once this happens, water passes through the now open sluice gates, flowing through the turbines creating energy. Subsequently when high tide is reached, the gates are closed until the tide recedes and the minimum head difference is reached. Finally, the gates are opened once more, allowing the water to flow back through the turbines again producing energy [Boyle, 2012].

Despite the benefits that could arise of developing further tidal barrages projects, it now faces various deployment challenges related to limited site availability, high capital investment and environmental impacts. Even though that in the last ten years, the UK has invested in developing high-scale projects in the Bristol Channel and the Swansea Bay, the UK Department of Energy and Climate Change (DECC) published a report in 2013 that stated that in 2-year cross government, Severn tidal power feasibility study could not see a strategic case for public investment in a Severn tidal scheme in the immediate term [IRENA, 2014].

1

Tidal Stream

Tidal currents can be predicted with harmonic tidal constituents to define the spring and neap cycles throughout the year. Tidal turbines use the flow power from the tidal currents, they convert these to rotary energy and they drive a generator to finally produce electricity [Hardisty, 2009]. According to Fraenkel [2002], the most eligible areas in estuaries for energy extraction are the ones where the flow is channelled by constraining land such as islands and straits, shallow waters between open seas or finally waters around the end of headlands, where the fluid velocity will accelerate thus the power density would be higher. As the resource is highly predictable albeit variable in intensity, its conversion to extracted energy offers an advantage over other renewable energy resources, such as wind or wave energy [Bahaj, 2011].

Some tidal stream technologies are also used to harvest ocean currents, that are derived from wind-driven and thermohaline ocean circulation [Hernandez, 2020]. Compared to tidal currents, ocean currents are unidirectional and generally slower but more continuous. Ocean current technologies are in an early developmental stage, and no full-scale prototype has been tested or demonstrated yet [IRENA, 2014]. It can be seen that tidal current extracting methods resembles the mature wind energy industry. It is likely that kinetic energy of the moving fluid can be similarly extracted and applied using a suitable type of turbine rotor. In order to enable the technology for energy production, further consideration should be given to analyse the physics and deployment of tidal stream power turbine. This includes understanding the present challenges to be met in its development over its lifetime if it is to be widely deployed as a contributor to future energy supply [Mueller and Wallace, 2008]. According to Murray et al. [2017],Hagerman et al. [2006], Frost et al. [2015], and Hardisty [2009], the following concepts are relevant to define a potential tidal stream energy extraction site: a free current speed greater than 2.5 ms^{-1}; a stable current that may have less fluctuations periods to avoid downtimes; a relatively uniform seabed in order to minimise both turbulence and the loss of velocity near the seabed; depth of water between 25 m to 50 m, enough to avoid ship traffic obstruction and tidal turbines maintenance availability; a wide enough area to permit the

installation of a large array; and to be sufficiently near to a shore-based grid connection to allow the energy produced to be delivered. Tidal energy technology has recently reach a TRL of 6-8 based on the selected turbine type, which means that the levelised cost of energy will not be incurred in a higher price [European Comission, 2016].

In order to underpin the tidal current technology challenges, increased attention needs to be paid to technical risks in design, construction, installation and operation. It is also clear that the levelised costs of energy (LCoE) needs to be reduced by 50%, in order to be competitive against offshore alternative energy sources, such as offshore wind. The initial installation, research and development costs as well as the manufacturing costs are also high due to the novelty and a lack of economies of scale. Moreover, risk assessments, environmental impact assessments and engineering standards need to be undertaken to overcome the market risks and demonstrate the tidal current technology availability to be deployed at larger scales [RenewableUK, 2013, IRENA, 2020, 2014].

1.3. The need for Condition Monitoring

Tidal stream turbine challenges in terms of operation, maintenance and survivability vary from faults already determined by wind turbines. Consideration to factors such as corrosion, varying operating speed and load and structural stresses induced by sea life must be made. Plus, sea-weather conditions and device and components' transportation from shore to the power plant location could represent more expensive associated costs compared to the wind onshore industry. A potential method to overcome these challenges in the future is to develop a condition based maintenance strategy. This may be defined as the continuous monitoring of system data to provide an accurate assessment of the health, status of a component or system and performing maintenance based on its observed health. A condition monitoring system may be able to perform a tidal stream turbine prognosis in order to estimate the remaining useful life of key components.

In order to underpin the long-term reliability of tidal current technologies, their

components' operating constraints, device maintenance and the operational costs are of particular concern. Condition-based maintenance (CBM) is an asset management technique that uses the regular assessment of the actual operating and health condition of a component or system to optimise its total operation [Davies, 1997]. CBM indicates when maintenance should be performed based on signs of decreasing performance or possible failure. Some advantages of introducing CBM to the tidal current industry would be to improve device reliability, reduce maintenance costs and improve the competitiveness of these technologies against other renewable energy technologies [Mérigaud and Ringwood, 2016, Butler, 2012]. However, implementing CBM requires the associated development of condition monitoring (CM) techniques to provide the information needed to underpin the approach. This consideration produces the need for an effective vehicle that can be used for testing CM approaches. Engineering CM elements that can be used to predict possible failures under real conditions would be very costly. One reason for this is the need to consider how the tidal stream turbine operation can be affected by specific faults. Often analysing this means that damaged components need to be installed to verify if the associated failure is being correctly detected. The need and associated cost of this has not been fully considered within the sector. In conclusion, it can be stated that CM is more important in tidal applications due to the hostile environment, accessibility, concerns and associated costs.

1.4. Thesis aims and objectives

The aims of this thesis are three fold. Firstly, to validate the capability of a drive train simulator test bed of $1/20^{th}$ scale to develop and test monitoring approaches under steady-state conditions. Secondly, a CM algorithm is to be engineered using data from previous experiments. Finally, the CM technique is to be tested under complex conditions. These include a range of different tidal current velocities, a range of turbulence intensities and integral length scales. The latter, in order to utilise the drive train test rig generator measurements to detect rotor damage under non-steady state turbine operation. This was achieved by executing the objectives:

- The further development of a previously utilised test rig in order to suit a variety of operating conditions for real time turbine operations
- A statistical validation of the test rig capability of creating representative tidal stream turbines simulations.
- The creation of a CBM technique by analysing the frequency content obtained from both the rotor and generator elements of the turbine.
- The implementation of the CBM technique in an experimental testing campaign dataset to be assessed at the test rig and evaluate the CBM technique reliability into detecting fault conditions
- The implementation of the CBM technique into a wider range of non-steady state operation variables in order to define the techniques' and test rig instrument suitability into detecting fault conditions

1.5. Thesis Outline

Chapter 1 provides the introduction of this research, the need to produce energy from renewable sources, the potential contribution of ocean energy to fulfill the energy demands, and the benefits and challenges for tidal energy. It also includes the thesis aims and outline.

Chapter 2 presents the literature review that describes the previous work performed in tidal turbines, the approach that has been undertaken to apply condition monitoring to both the tidal and wind energy industry, and the need to engineer a test bed in order to obtain more flexible turbine monitoring results. It also introduces the context of the tidal resource feasibility considered for two different locations.

Chapter 3 outlines the methodology being utilised in order to develop the drive train simulator test bed based on a turbine scaling model. It also presents the applicable theory of the statistical and frequency signal processing being applied throughout this research, and the main definitions of the non-steady state operation variables.

Chapter 4 describes the characterisation of the drive train simulator to replicate real time turbine operation and the process to perform steady state operations on it. It also presents a statistical validation to reproduce the expected turbine results.

Chapter 5 contains the results obtained from an experimental testing and considers how their results can build a condition monitoring approach to detect rotor imbalance faults.

Chapter 6 provides the results from driving the drive train simulator test bed with the datasets obtained at an experimental testing, and considers how to implement a fault condition to examine the built CBM technique reliability into detecting those faults.

Chapter 7 presents the CBM technique capability to detect fault conditions into more complex tidal conditions, such as a range of tidal current velocities, turbulence intensities and integral length scales values.

Chapter 8 provides the thesis conclusions, recommends further work for the future, and identifies research contributions of this work.

2

Literature Review

This chapter presents the work that it has been developed in tidal stream energy, and a brief description of the current device types that exist in the energy industry. Then, an emphasis in tidal energy resource in high fast tidal current velocities and low velocities is being presented, and consequently the outcomes found in the literature regarding the feasibility of tidal current turbines operating conditions in low velocity profiles. Also, this chapter contains the literature of the work that has been developed in the condition monitoring implemented in tidal stream turbines, and the similarities found in the wind industry. Finally, this chapter offers an examination of the up-to-date research in the rotor imbalance faults in both tidal and wind turbines, followed by the implementation of drive train test rigs in order to facilitate the fault detection process, that have led this research to take place.

2.1. Tidal Stream Energy

Tidal energy has the potential to deliver long-term carbon emissions reductions and appears to have low environmental impacts [RenewableUK, 2013]. Some of the benefits compared to other renewable alternate sources have been mentioned in chapter 1, being the high predictability and the high theoretical energy potential it contains the two most relevant ones. Thorpe [1999] reported that tidal energy alone may contribute approximately 10% of the level of world electricity supply in the UK. The harshness of the tidal stream energy environment results in designs that have to be able to survive the extremes of loading imposed by the sea and yet be cost-effective in extracting a low energy density resource. The challenge of maintaining operational devices for more than 20 years requires a clear understanding of their component material performance and associated environmental degradation [Wood et al., 2010].

2.2. Tidal Stream devices

Tidal stream devices converts the kinetic energy in the flow into electrical energy. Relying on IRENA [2020], there are currently six types of devices in the energy industry being researched: vertical-axis tidal turbines, Venturi Open Centre, Oscillating hydrofoil, Archimedes screw, Tidal kite, and Horizontal-axis tidal turbines (HATTs). All turbine examples are displayed in figure 2.1. HATTs were examined in further detail, in section 2.3, as it is the selected tidal stream device deployed for this research. Figure 2.1a displays a conventional HATT design.

2.2.1. Vertical-axis tidal turbine

Vertical-axis tidal turbines (VATTs) extract the energy from the tidal currents flow through a set of blades parallel to a rotating shaft. It has been less developed than HATTs, but it may have several advantages against the latter, such as the unidirectionality, the independence of operation and efficiency to the flow direction, their operability

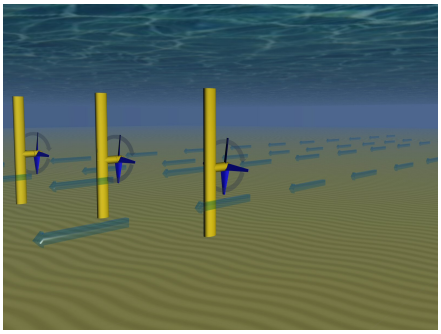

(a) Horizontal Axis Tidal Turbine.

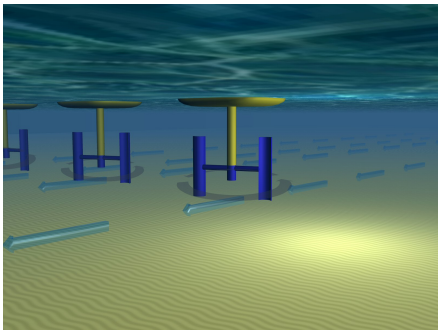

(b) Vertical Axis Tidal Turbine.

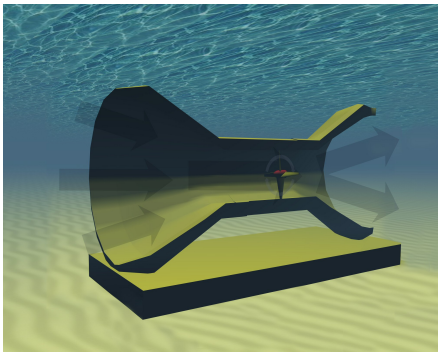

(c) Venturi Open Centre.

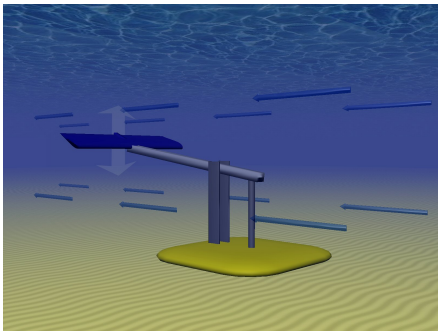

(d) Oscillating Hydrofoil.

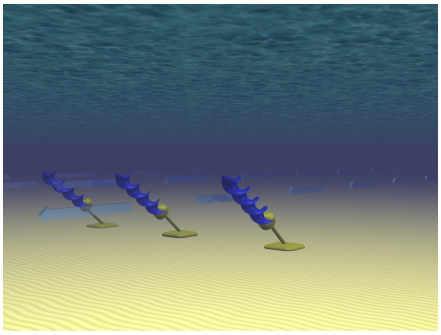

(e) Archimedes Screw.

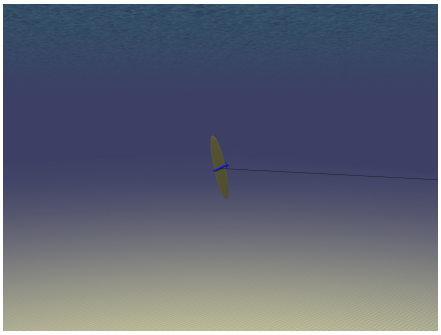

(f) Tidal Kite.

Figure 2.1: Tidal Stream Technology Devices. [Aqua-RET Project, 2012]

in lower tip-speed ratios (that is the ratio between the tidal stream flow speed and the turbine blade speed), which is believed to be more environmentally-friendly to reduce noise generation, and finally it is expected to work better in lower tidal current velocities [Ouro and Stoesser, 2017]. However, the main disadvantages associated with vertical axis

turbines are relative low self-starting capability, high torque fluctuations, and generally lower efficiency than horizontal axis turbine design [Benbouzid et al., 2017]. There are two main types of VATT being developed:the straight bladed Darrieus turbine and the helically shaped Gorlov turbine. Darrieus turbine is characterised by having the same azimuthal angle across all points on each blade at any time, leading into constant shaft torque and blade force changes. The Gorlov turbine is characterised by having a value of the azimuthal angle covering a section of the bladee at any point in time [Winchester and Quayle, 2009]. Image 2.1b represents a VATT design.

2.2.2. Venturi Open Centre

Venturi Effect devices increases the tidal current velocity by concentrating it into a duct. The duct houses the stator which is fixed to the rotor and enclosed within the direct drive generator, meaning no gearbox is required. Plus, the turbine open centre design allows marine wildlife to continue their migratory routes without disruptions [Hardisty, 2009]. A previous numerical study indicated that ducted turbines have a smaller power coefficient of the total device compared to other turbine sizes [Belloni, 2013]. On other work selected commercial ducted turbines have been compared to show that, with a rated flow speed between 2.5 ms^{-1} to 3 ms^{-1}, an overall device area of 20 m^2 and a rated power of 65 kW, the device can aim to a power coefficient of 0.23 [Roberts et al., 2016]. Considering that current power coefficient values are in the range between 0.40 to 0.45, it appears that ducted turbines have significantly low values in terms of power generation. Despite the previous findings, an OpenHydro 250 kW open centred turbine was installed in 2006, being the first tidal turbine to be grid connected and the first to successfully generate electricity to the national grid in the UK. Unfortunately, by 2018 the parent company of OpenHydro decided to stop further investments, leading to remove the turbine from the sea in 2022 [EMEC, 2022, Garanovic, 2021]. Image 2.1c represents a open centre turbine example.

2.2.3. Oscillating hydrofoil

An oscillating hydrofoil consists of a hydrofoil membrane attached to a lever arm, that is driven up and down as the dial flow lifts the hydrofoil wing, in order to power a generator and therefore, to produce electricity. Some of the advantages of this device over the rest of the tidal stream technologies is the simpler geometry being applied, meaning that they would not require twisting axial-flow turbine blades to extract the energy from the tide movement. This derives into a cheaper option compared to HATTs or VATTs. Plus, they are designed to be deployed at shallow and lower velocity waters (i.e. 2.0 ms^{-1}) where wave activity is limited, and they can be coupled with any number of foil groups to a single electricity generator. However, it has been also determined that oscillating hydrofoil efficiency can be poor due to the time required to reverse the direction of oscillation [Hardisty, 2009, Roberts et al., 2016]. The EEL Energy Company are developing pilot projects in France, for both fluvial and marine applications, where in the latter it is suggested to deploy machines generating up to 1MW, with 16x20 m membrane surface at 16 m depth [ENCORE Project, 2020]. Image 2.1d represents a oscillating hydrofoil turbine example.

2.2.4. Archimedes screw

The Archimedes Screw is a helical-shaped impeller that draws power from the tidal stream as the water moves up/through the spiral turning the turbines. It is considered one of the oldest devices for lifting water for irrigation and drainage purposes [Rorres, 2000]. Even though some research has been developed to define a strategy of implementing this types of turbines for hydro and tidal range [Waters, 2015, Rorres, 2000], little has been found in the literature into determining the tidal stream current technology capability. However, based in the application of these turbines in hydro energy, it is considered that they could be suitable for use in shallow water tidal applications [Roberts et al., 2016]. Image 2.1e represents a Archimedes screw turbine example.

2.2.5. Tidal kite

A tidal kite consists of a small turbine attached to a hydrofoil wing tethered to the sea bed. The mobile wing is about 12 m long and 3.3 m wide, with a 1.15 m diameter turbine, along with a 110 m to 140 m long cable of 11 tons. The motion of the tidal currents over the wing creates a lift force that pushes the kite forward through the water, and swoops in a figure of an eight-shape in order to increase the speed of the water flowing through the turbine. Among some of the benefits of this technology compared to HATTs, is the the ability to operate in low velocities (1.2 ms^{-1}), the capability to be installed in both shallow and deep waters, and the low maintenance costs associated to the detachable design technology concept [Minesto, 2021]. Plus, it has been claimed that that the device moves at a speed 10 times greater than the water current, leading into producing great amounts of power for the size of their rotors [Roberts et al., 2016]). Minesto is the market leader of tidal kite developers. In 2020, Minesto reached the milestone of delivering electricity to the Faroes Islands' power grid from the two commercial 0.1 MW units [IRENA, 2020]. Image 2.1f represents a tidal kite turbine example.

2.3. Horizontal-axis tidal turbine

HATTs use the tidal stream flow to transfer the energy from kinetic, to mechanical and finally electrical phases. HATT rotor design is mainly characterised from wind turbines (WTs), which is based on the physical principals of the open flow actuator disk theory. This is described as an energy extraction device that may be introduced into a uniform flow field of constant velocity [Jamieson and Hassan, 2011]. The mechanical energy that can be extracted from the free stream flow depends on the flow power difference between before (U_1) and after the converter (U_4)[Hernandez, 2020]. This is called the momentum theory, and it is used to examine how the amount of energy extracted by the turbine is related to the change in fluid velocity from upstream to downstream of the turbine. A diagram is displayed in figure 2.2, where the stream tube boundary represents the tidal stream flow field.

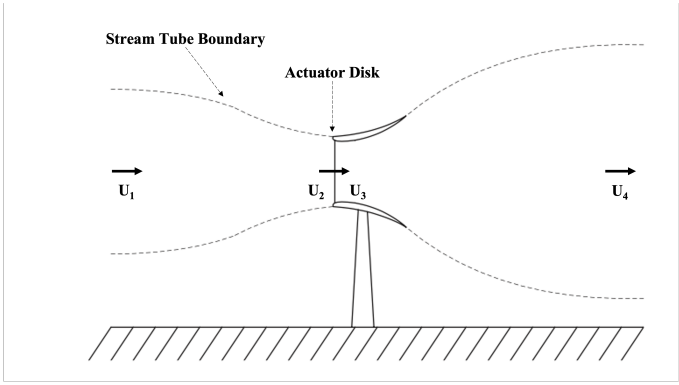

Figure 2.2: Schematic of a tidal stream tube and actuator disk. Adapted from [Jamieson and Hassan, 2011].

The maximum achievable value of extracting power from the actuator disk is called the 'Betz Limit', and it is based by the fact that full extraction of the actuator disk is physically unachievable, but rather is limited of a ratio of extracted energy to kinetic energy of the stream tube passing through the turbine disk of a ratio of 0.593 [Jamieson and Hassan, 2011]. This limitation is produced by the need for maintaining a balance between reducing a fluid velocity in order to extract the highest possible energy from an actuator disk, whilst not causing the flow to stagnate downstream the stream tube [Burton et al., 2021]. Thus, the operation of a HATT can be adjusted depending of both the existing flow conditions that the turbine is exposed, the Betz Limit physical limitation to the available power extraction and the turbine control type that is introduced to conduct the turbine performance to an idealised power output [Hachmann et al., 2018].

The HATT design has been conceptualised after the conventional WT design. The main difference into operating this design in tidal currents is that tidal turbine rotor diameters are at least 12 times smaller than WTs, since the water is about 800 times denser than air, producing exponentially more power.

2.4. HATT Challenges

Tidal stream energy sector is still in its infancy and it must overcome several technological barriers to prove the reliability and affordability of its devices. Magagna and Uihlein [2015] have found that, within the four main bottlenecks that have slowed down the development of tidal stream current extracting devices, the most important issue to address is the lack of long-term reliability due to the harsh environment turbines operate within. Consequently, this leads to financial issues which promote investor uncertainty. Carbon Trust [2012] indicates that the highest current costs, are related to installation (35%), the structure and prime mover (i.e. the rotor, 15%), the electrical connection (15%), and operation and maintenance (15%), with installation costs varying greatly according to the resource estimation locations. The rest of the costs are distributed by the power take-off technology (i.e. generator, 10%), and the foundations and moorings (10%). Estimates in 2020 of LCoE are in the range of € 0.20-0.45 kWh^{-1}, when it has been determined that the onshore wind reached a global LCoE average of \$0.039 kWh^{-1} [IRENA, 2020, IPCC, 2022].

Further work has been developed in order to examine the economic viability in the development of tidal energy projects, due to the high cost variability based on different approaches being taking in place, as well as different resource estimation locations. First, Denny [2009] presented a methodology for calculating the break-even costs of tidal generation and discussed the potential for tidal generation for a year utilising a technique called PLEXOS. The nature of the tidal generation, with four daily peaks and troughs in output, results in a low load factor for tidal generation. This led to relatively low emissions and fuel saving benefits for tidal generation. However, in order to produce positive net benefits, the capital costs of tidal generation would have to be less than €510,000 per MW installed which is currently an unrealistically low capital cost. Vazquez and Iglesias [2015] designed a tool to generate LCoE by numerical modelling, tidal farm projection and economic assessment, to be able to perform a LCoE calculation. This method delivered LCoE values below £0.125 kWh^{-1}, which refer to the most promising estimate for first commercial arrays, and that occurs in zones with a very good tidal re-

source. The latter competes with offshore wind costs, and in order to materialise this smallest cost, an annual production of 100 GWh would be needed. Finally, according to Magagna and Uihlein [2015] the learning investment necessary to bring tidal energy to cost-competitiveness would be of about €1.45 billion, requiring about 3.2 GW of installed capacity to achieve the LCoE target of €0.15 kWh^{-1}. Thus, it requires to design supporting policies aimed at the industrialisation of the sector to support materials to be more commercially available.

Since tidal energy projects are still in the demonstration stage, cost estimation are projected to decrease with deployment. Currently, tidal current extracting devices are said to be limited to a TRL of 6-8 [IRENA, 2023] and any advancement is constrained by the lack of funding and an associated high LCoE. This does not suggest that the sector is yet in position to move to a full commercial-scale stage. Much of the research reported has accomplished a TRL of 4, which means that design validation and intermediate testing at scale (i.e. flume test scale of 1:10) has been achieved. There are a small number of projects that have been able to advance to a TRL of 6-8. One example is Atlantis Resources being deployed in the Pentland Firth. Work has finished on the construction phase of what may be considered to be the world's largest tidal stream turbine (TST) array [Coles et al., 2018]. However, according to some assessments this may still be defined as a small scale project since it is under 20 MW generation [Magagna and Uihlein, 2015]. The nature of the challenges to be met suggest that there is still great potential in meeting them by identifying other possible solutions.

2.5. Numerical and Experimental modelling techniques

In order to achieve scaled testing, there are two approaches to be considered: numerical and experimental modelling techniques in order to reduce the financial risks involved in installing full-scale turbines at tidal sites. Firstly, numerical modelling is a common solution that compromises computer modelling. Throughout the options, the two most commonly utilised are Blade Element Momentum Theory (BEMT) and Com-

putational Fluid Dynamics (CFD). BEMT is a numerical method that combines blade element theory and momentum theory. By the creation of blade chord sections, a 2D computational method is used to calculate the hydrodynamic forces to subsequently calculate torque and thrust [Ebdon, 2019]. Time-wise, the use of BEMT could be a better option compared to CFD, but research has demonstrated that correction functions are needed to overcome under-prediction of turbine power output and to create unsteady flow simulations. On the other hand, CFD is widely used as it is a more complete computational model of a full-scale tidal turbine. It has the ability to predict the fluid behaviour by building a finite volume method of a grid or mesh, but considering physical model tests to validate final numerical results. Still, this tool is far more computationally intensive and time-consuming than the BEMT method, as CFD is restricted to a small time-step for a mesh construction in order to provide high accuracy to the model. Another option is to combine two methods, so the BEMT method is used to model the turbine, and CFD is employed to model the flow properties elsewhere in the domain, thus giving us a time-averaged estimate of the turbine wake while significantly reducing the computational cost compared to a geometry-resolved CFD model [Masters et al., 2015].

As for scaled HATT prototypes testing, some methodologies as re-circulating water flumes, flow tanks and field site testing with medium-scaled HATT prototypes have been utilised before [Jeffcoate et al., 2016]. Typically initial tests are conducted in small-scale towing tanks, even though they can only be utilised for a steady resource simulation as the flow will circulate into one direction only and will conserve its homogeneity throughout the cross-sectional area. On the other hand, if it is needed to simulate low levels of turbulence and a developed boundary layer, re-circulating water flumes may be considered a better solution. Larger scale experiments have been conducted, although not as intensively or thoroughly as small-scale tests; full-scale testing has been previously performed with a 4 m diameter rotor in still harbour waters [Starzmann et al., 2018]. Plus, testing scaled HATT prototypes has allowed researchers to test further complex situations, such as wake predictions, tidal turbulence, turbulence integral length scales and tidal flow directionality. Combining both numerical and experimental techniques for data acquisition has become crucial to provide better performance predic-

tions and more accurate results prior the large-scale turbine installation and evaluation.

2.6. HATT large scaled devices

Relying on IRENA [2020] and Magagna and Uihlein [2015], there are more than 34 companies involved in tidal energy worldwide, with 7.8 MW of the first phase of larger commercial tidal farms, 1.7 MW of smaller completed commercial projects, 1 MW of full-scale demonstration plants, and 0.1 MW of sub-scale test plants. Most of these projects are being deployed in the UK. Among the most representative companies that have developed large scaled projects are presented next.

First, Simec Atlantis Energy is considered the world leader in development of tidal energy devices [SIMEC Atlantis Energy Ltd, 2022]. The MeyGen first phase project is the largest tidal stream project and the only commercial multi-turbine array, that comprises four 1.5 MW turbines completely operational. It was grid connected in 2018, generating sufficient electricity to supply 2,600 homes. The AR1500 device (as shown in figure 2.3a) is a three-bladed 18 m diameter HATT that was designed to operate for 25 years, and that has been installed in the the north of the Stroma island, in Scotland, UK. It is integrated with a 2-stage gearbox and and a permanent magnet generator integrated in the gearbox itself. Plus, a supervisory control and data acquisition (SCADA) system provides remote internet access and collects operating data, by using a wide variety of sensors to warn a potential of maintenance needs.A second phase is under development to install an additional 80 MW, and a third one to deploy 252 MW. Plus, the company has agreed to develop up to 2 GW in Normandy, France, and installed and tested a turbine in Japan [Atlantis Resources Ltd, 2016].

Similarly, the HS1000 turbine designed by Andritz Hydro Hammerfest a 1 MW 21 m rotor diameter was first installed in 2011 and grid connected in 2012 in Orkney, UK, displayed in figure 2.3b. One of the cut-edge design particularities of this turbine is that blades can be pitched for two-direction current flows. Plus, the turbine incorporates a condition monitoring system to provide a predictive maintenance capability, in order to

avoid costly unplanned repair activities. As a second phase of this project, this technology is planed to be adopted in Sound of Islay, in Scotland, UK in a 10 MW commercial array [Andritz, 2022, Andritz Hydro Hammerfest, 2022].

Finally, the Verdant Power company has developed two phases project in the Long Island Sound connecting with the Atlantic Ocean in New York Harbor. First, the Gen4 Free Flow System represented the first operation of a grid-connected tidal turbine array, with 6 devices of 5 m diameter of 35 kW each in 2016, with their devices being fully bi-operational for ebb and flood tides. The Gen5 Free Flow System successfully installed a 105 kW of three 5 m turbine mounted at a TriFrame in 2020, as it is shown in figure 2.3c. The main advantage of this triangular frame mount is that multiple water turbines can be accessed through the same frame operation. Plus, the company has scheduled regularly on-water operations and maintenance work, leading into significant reductions to the cost of system installation, operation and maintenance [Verdant Power Inc., 2022].

2.7. Tidal Energy Resource

As previously seen in figure 1.4, tidal stream locations are geographically constrained in order to deploy large-scaled projects,as there are only a few areas with high enough average tidal current velocities needed for cost-effective energy recovery [Fraenkel, 2006]. Preliminary economic analysis being developed have suggested that ideally a stream velocity should be between 2 and 3.5 ms^{-1} with the resource located within 1 km from the shore and with a water depth between 25 to 50 m. Finally, these site specific requirements are mainly found in straits between islands and the mainland and shallows around headlands [Tavner, 2017, Sustainable Development Comission, 2007]. This research compares the literature in the resource estimation and energy potential for two countries, in order to increase resource availability.

(a) Simec Atlantic Energy AR1500 turbine.[SIMEC Atlantis Energy Ltd, 2022])

(b) Andritz Hydro HS1000 Turbine.[Andritz, 2022]

(c) Gen5 System Project of Verdant Power.[Verdant Power Inc., 2022])

Figure 2.3: Commercial Tidal Stream Projects.

2.7.1. Resource in the UK

Resource estimation has been found to be around 18 TWh yr^{-1} , and that is extractable within 1450 km^2 of UK waters by tidal-stream energy alone [Lewis et al., 2015]. Relying on Sustainable Development Comission [2007], approximately 20% of the UK resource is within sites of depth 30–40 m that have mean spring velocities between 2.5 and 4.5 ms^{-1}. Plus, approximately 50% of the UK resource is found in >40 m sites, that also comprises mean spring velocities >3.5 ms^{-1}; these are only suited to device designs that are capable of being installed and operated in water depths > 40m. Mainly, 10 sites around the UK coasts are considered extractable locations, that represents the 80% of the total resource, which only the Pentland Firth and the Channel Islands represents over 70% of this resource. Image 2.4 displays the UK tidal stream resource, by showing in brighest yellow velocities above 4.01 ms^{-1}, and dark purple for velocities around 0.1 ms^{-1}. Based in the analysis developed by Coles et al. [2021], these resource estimations are flexible to be re-estimated, as practical constraints were taken in place, such as high costs associated in remote locations, considering only the mean spring flow to calculate the energy yield, etc. Plus, it was mentioned that energy storage could be an option to meet the energy demand and increase the generated power, by charging the battery during spring tides and rely in backup power during neap tides. Therefore, it is expected that further resource estimation of the UK energy potential would be updated in the future to extend the possible locations where projects could be deployed.

2.7.2. Resource in Mexico

Mexico ranks second in the American continent with the largest ratio of continental coastlines per area [Burke et al., 2001]. The extension of their 11,122 km of coastlines is divided into two areas: the west (the Pacific Ocean and the Gulf of California) with 7,828 km, and the east (the Gulf of Mexico and the Caribbean Sea which are part of the Atlantic Ocean basin) with 3,294 km [CONABIO, 2015]. Research is being conducted in Mexico to define the tidal stream energy potential with lower velocities up to 2 ms^{-1}

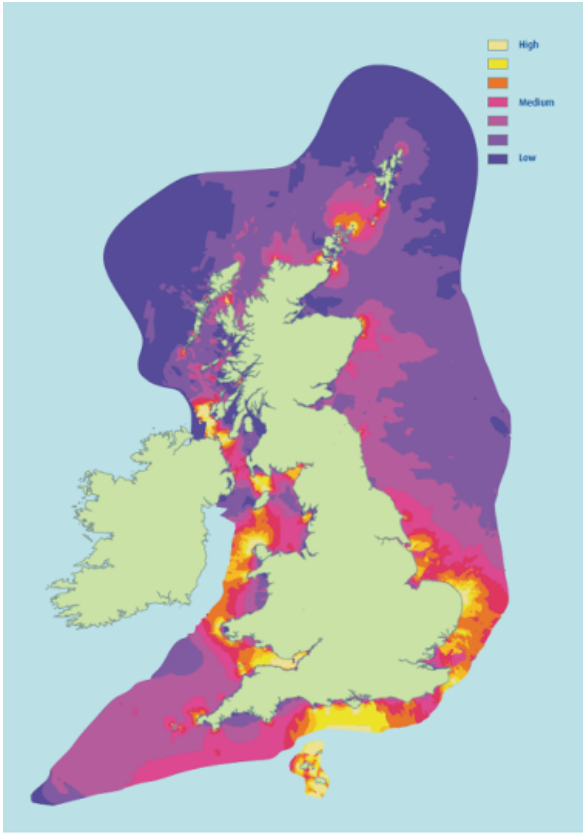

Figure 2.4: UK tidal stream resource estimation. [Ebdon, 2019].

in two main sites: The Gulf of California (GC) and the Yucatan Channel, at the northwest and southeast part of Mexico respectively, as shown in figure 2.5a.

Moreover, preliminary results suggest that in the GC there is an estimated power of 3.4 GW due to the large tidal range of a mean value of 7 m and a maximum current velocity of 1.5 ms^{-1} in places such as Canal del Infiernillo and de Ballenas, with an overall power output of 5 kW/m^2 [Magar, 2018]. A more recent study was developed by [Mejia-Olivares et al., 2020], finding that utilising different Acoustic Doppler Current Profiler (ADCP) measurement techniques, a 2.4 ms^{-1} peak current speed was found at San Lorenzo passage. The latter confirms that generally the tidal stream resource of the Gulf of California was higher when using higher resolution bathymetry products. Figure

2.5b displays the mean speed values found in the conducted research locations. However, research in the GC is constrained by natural reserved areas of endemic and endangered species and commercial fishing activities [Magar et al., 2017], and these relatively mild stream velocities are found at water depths around 400 to 600 m, making it technologically challenging to install turbines in such conditions.

Mexican research in tidal stream energy is focusing on the Cozumel Channel, due to its proximity to the shore and its shallow waters. The current work has been developed by two main research groups in Mexico: CANEK and CEMIE-O. According to a CEMIE-O report, the highest maximum values are found at the north of the Cozumel Channel, near Puerto Morelos with a mean value of 1.4 ms^{-1} and at the East of Cozumel island, with a mean value of 1.2 ms^{-1}. On the other hand, current maximum values are significantly higher at the surface (near 2 ms^{-1}) compared to 50 m depth which are pretty similar to the mean values found at the same locations (1.6 ms^{-1}). Similarly, the CANEK research group installed a long-range ADCP of 75 kHz anchorage at 400 m of depth on between latitudes 20.53° N and 20.57° N. During the sampling period the currents were unidirectional northwards with little variation. Mean, maximum and standard deviation values of stream velocities were found between 50 and 100 m. It was found that the maximum value of 2.3 ms^{-1} is at 81 m depth. The most feasible operational velocity option should be used at 49 m, where mean and maximum velocities of 0.97 and 1.84 ms^{-1} where found respectively. A more recent study of this testing campaign [Alcérreca-Huerta et al., 2019], determined that the most feasible area to deploy a potential tidal stream project would be found in those latitudes, between Punta Norte and San Miguel (as shown in figure 2.5c), since an average velocity of 0.93 ms^{-1} and peak flow velocities in the range of 1.8–1.9 ms^{-1} were detected at water depths between 20 and 35 m, which are suitable for the installation of floating devices. Plus, this area does not form part of a marine protected area, and it would not intervene with navigational channel and tourism activities. Additionally, it is thought that nearly 3.2 MW could be exploited in this region, that would supply 10% of the island energy consumption. Still, this corresponds less than 1% of the channel's width, therefore there may be more locations across the Channel to exploit the tidal resource, that should be contemplated for future

work. Finally, it is important to note that the flow characterisation demonstrated that the stream current at this location is continuous and single-directional, providing an advantage compared to other tidal stream locations worldwide.

2.7.3. Low velocities feasibility

In terms of maintenance and system availability, researchers affirm that a lower peak velocity between 1.2 ms^{-1} and 1.5 ms^{-1} becomes economically viable in locations with continuous or quasi-continuous flows [Belloni, 2013, Roberts et al., 2016, Candela et al., 2002]. Considering tidal-stream energy for peak tidal currents above 1.5 ms^{-1} for a resource assessment in a relatively shallow estuary will allow a much greater area to be developed and reduce the competition for sea space. On the other hand, maintenance costs could be positively affected as well, as a reduction in turbine speed of 10% would correspond to 10% increase of operating time for a given number of rotations, therefore operating at this 10% reduction in speed would reduce the number of maintenance event. Relying on Alcérreca-Huerta et al. [2019], the main advantage of tidal energy sites with low velocities such as the ones found in the Cozumel Channel, is the continuous and almost uniform energy generation due to the single-directional current flows, making it independent of the tidal cycle, providing a daily energy extraction rate possibly higher than other tidal sites in the world. However, site-specific tidal stream devices should be developed, since the velocity flow is around 1 ms^{-1}, and due to the low torque, higher rotational speeds are required. This results in the need to employ slenderer blades than those found in commercial large scale turbines, which could lead to rapid failure considering the shear and turbulent flows of the current. Therefore, the main justification for applying this technology in low velocities sites relates to the cost effectiveness that may potentially sacrifice efficiency in order to reduce costs or increase system availability [Candela et al., 2002].

Site-specific low stream velocity devices are currently being developed in several research groups. An economic feasibility approach was developed by Hernandez [2020] to propose a single rotor turbine and contra-rotating turbine in order to compare

(a) Potential sites in Mexico for tidal stream energy extraction.

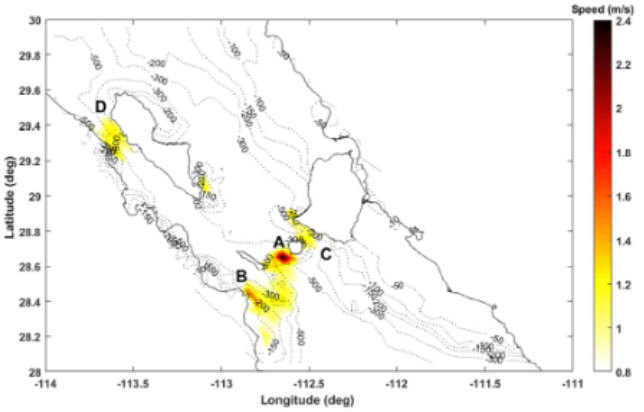

(b) Maximum current speeds found at the Gulf of California [Mejia-Olivares et al., 2020].

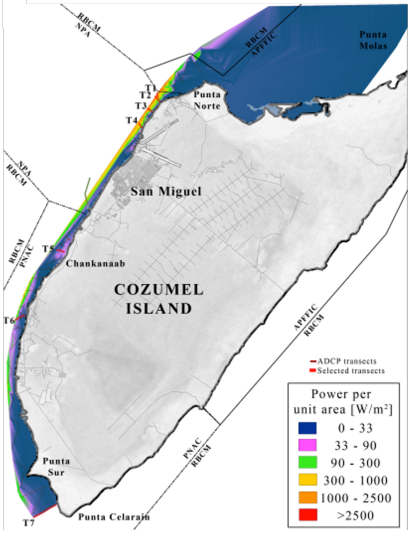

(c) ADCP measurements of power per unit area (kW/m^2) in the east coastal waters of Cozumel island [Alcérreca-Huerta et al., 2019].

Figure 2.5: Mexico Energy Potential.

the applicability of both devices in tidal stream velocities around 1.02 ms^{-1} that could be found in Costa Rica. The LCoE was calculated for a variety of rotor diameters, finding that the highest power to LCoE ratio was found to be a 14 m diameter turbine with five blades, with an expected power output of 71 kW and £164 MWh^{-1}. It was determined that this configuration was technically capable to operate in low velocity conditions and the cost will be within the expected LCoE range of commercial tidal stream plants. An initial techno-economic assessment was also developed for the Cozumel Channel, for \$342.8 MWh^{-1} utilising a 150 SeaGen and considering a 20 year-lifespan, that would produce 197 GWh/yr that represents near 5% of the electricity demand in the Cozumel Channel [Bárcenas Graniel et al., 2021]. However, a floating platform would need to be designed in order to access the 50 m water depths to extract the energy potential across the Cozumel Channel to deploy a tidal array, as the Channel depth is > 100 m. This notes the importance to develop further work in this topic, in order to design a site-specif device in low velocity regions.

2.8. Condition Monitoring

Condition Monitoring has been implemented on rotating electrical machines, such as generators and motors, for many years. Much of this work was aimed at high speed systems. The WT industry has adopted and standardised some CM technologies for a shorter period of time. CM should be understood as a measure to observe the development of faulty conditions in a turbine component and to provide information for the planning and organising of maintenance and repair activities [Burton et al., 2021]. Prognostics enables the prediction of failures in machines resulting in benefits to plant operators such as shorter downtimes, higher operation reliability, reduced operations and maintenance cost, and more effective maintenance and logistics planning [Kan et al., 2015]. Amongst most popular mechanical failures detected in electrical rotating machines, are: bearing failures, rotor mechanical integrity failure, and stator mechanical integrity failure. The main root causes are: overspeed, overload, excessive fatigue, excessive temperature, debris or corrosion [Tavner, 2008]. The reliability of an offshore WT

and the resources required to maintain it can make up around 30% of the overall cost of energy. Plus, as previously mentioned, maintenance and operation in tidal stream turbines (TSTs) represents 15% of the LCoE, meaning that different CM techniques could be implemented in order to tackle these associated costs.

Based in a statistical analysis performed by Carroll et al. [2016], it was determined that the average failure rate for an offshore WT levels out at approximately 10 failures per turbine per year by the 3rd operational year of the wind array, and with 80% of those repairs being minor repairs, 17.5% major repairs and 2.5% major replacements. The classification of minor repairs (<€1000),major repairs (between €1000 and €10,000), and major replacements (>€10,000) were calculated based on the material costs provided by a wind turbine manufacturer database. It is important to note that due to accessibility concerns, these turbines will often operate with existing minor faults. Such operations may be allowed, as CM could manage the fault and effectively prevent it to become a major one. It was also determined that the components that failed the most were the pitch/hydraulic system and the generator. The biggest failure modes in these groups were oil issues for pitch/hydraulic, door/hatch issues for other components and slip ring issues for generators. Plus, it was also determined that with higher wind speeds in offshore, there is a strong correlation to obtain higher failure rates. This attempt to determine the highest failure rates for each component allows the developers to determine repair times and costs associated to prevent a major fault to occur.

According to Kan et al. [2015], prognostic models can be categorised into three: model-based, data-driven based and combination models. Model-based methods contains physical models of the machine and characterises the system behaviour using physical laws. This would need a complete understanding of the specific possible fault to occur, which may be difficult to obtain due to the complicated dynamic interaction with all the machine components. On the other hand, data-driven based make use of condition monitoring data for analysing and predicting current and future health conditions. Mainly, this data is obtained from vibration, acoustic emission, electrical signals, etc. This approach generally requires the installation of additional sensors specifically for

CM purposes, which inevitably add costs to operation and maintenance. Plus, considering that operating circumstances in an electrical machine can occur randomly, it is very expensive to obtain sufficient representative data for all types of faults. Another solution commonly utilised in WTs is SCADA system, that does not contain detailed transient information, but rather collects practical WT data every 10 minutes, and utilises an anomaly detection approach in order to differentiate a WT normal behaviour against a component condition that significantly deviates from that estimation. This system can be practically applied to non-linear reliability prediction and require relatively higher computation effort than model-based methods, yet it is considered a cost-effective solution [Zhang et al., 2019].

Additional to the implementation of SCADA in WTs, the most common CM techniques implemented in the wind industry are: vibration analysis, acoustic emission, strain measurement, electrical signal monitoring, and some novel techniques that they have been recently adopted. These techniques are briefly summarised herein.

2.8.1. Vibration analysis

Vibration analysis continues to be the most popular technology employed in WTs. Current commercial CM systems are developed to supervise the drive train, and the vibration analysis is mainly utilised to examine the gearbox and bearings operation [Artigao et al., 2020]. Herein, sensors are positioned and set up in different frequencies: position transducers are used for the low-frequency range, velocity sensors in the middle frequency range, accelerometers in the high frequency range and spectral emitted energy sensors for very high frequencies [García Márquez et al., 2012]. Wang et al. [2004, 2012] applied a system to predict online rotating machine faults, by evaluation vibrations from a worn gear, a chipped gear tooth, and a cracked gear tooth, as well as data related to gear pitting damage and shaft misalignment. It was demonstrated that this system accurately predicted the machine health condition, as well as the bearing prognosis. Additionally, Tandon and Choudhury [1999] presented a review of utilising vibration analysis by measuring vibration in the time and frequency domains, sound measurements, the

shock pulse method and the acoustic emission technique, for CM of rolling bearings in electrical machines.

2.8.2. Acoustic Emission

Materials that are subjected to stress or strain release elastic waves that are generated when the structure of a metal is altered, and this can be analysed by acoustic emissions [Qiao and Lu, 2015, García Márquez et al., 2012]. Acoustic emissions have been used for bearing and gearboxes monitoring, but it has also been utilised for to detect damages in rotor blades for a real-time WT operation. Schulz and Sundaresan [2006] demonstrated the results of acoustic emissions obtained from sensors installed on WT blades, confirming that acoustic emissions events could be predicted time and location-wise, in order to predict the damage development in the future. Plus, it would accurately define possible further faults, such as fatigue, reduced stiffness, crack, and increased surface roughness. Despite its effectiveness, acoustic emissions sensors are considered highly costly, as large number of sensors should be installed in difficult areas of the WT structure. Plus, each sensor would need a dedicated data acquisition system for signal processing and transfer, that are complex and expensive systems [Qiao and Lu, 2015].

2.8.3. Strain measurement

Strain measurement by strain gauges is a common technique. Especially for wind turbines, strain measurement can be very useful for lifetime prediction and safe-guarding of the stress level, especially for the blades. The strain gauges are usually mounted in on the surface or embedded in the blade. The measured strain signals can be used to detect structural defects or damages in the blade, blade icing, mass unbalance, or lighting strikes. One of the main advantages of utilising this technique in comparison with other CM techniques, is that the strain-based CM techniques can be operated at lower sampling rates as they are looking to observe changes in the time domain. Plus, optical fibre sensors are being developed and are promising, as they are passive sensors

that do not require external power sources [Hameed et al., 2009, Qiao and Lu, 2015]. Hameed et al. [2009] examined the frequency spectral components of a WT, mainly at the 1st harmonic of the rotational velocity of the WT, in order to extract information regarding possible nacelle torsional loading faults. Strain gauge sensors were placed so the tower torsion torque could be measured directly. The 1st harmonic amplitude time history is generated using a digital band-pass algorithm. It was confirmed that during aerodynamic asymmetry conditions, the amplitude is significantly higher, leading to define a correlation between unsteady state conditions to a direct torsional loading in the WT nacelle.

2.8.4. Electrical signal monitoring

Voltage and current signals are widely monitored; equipment such as motors, generators and accumulators is typically performed using voltage and current analysis [García Márquez et al., 2012]. Discharge measurements are used for medium and high voltage grids. Electrical resistance varies with stiffness and abrupt changes can be used to detect cracks, delaminations, and fatigue. Plus, amplitudes of certain harmonics in electrical signals can be used to detect electrical faults at an early stage. As a mechanical fault in a WT component usually induces vibration of the component, the fault-induced vibration will modulate generator electrical signals. Consequently, the electrical signals will contain fault-related information, which are considered effective for diagnosis of the mechanical fault [Qiao and Lu, 2015]. Yang et al. [2009] have implemented a methodology to detect rotor electrical imbalance in an induction generator by using the voltage and current signals. Wenxian et al. [2010] successfully detected rotor mass imbalance of a synchronous generator as the generator electrical power signals carried the surface conditions of WT blades. The harmonics of the electrical signals revealed that there was an increment in the surface roughness of one blade or a yaw misalignment. Therefore, it is inferred that combining electrical signal monitoring with the power spectral density of the the WT electrical power could prevent major failures to occur [Jeffries et al., 1998].

2.8.5. Other novel techniques

When a process is too complex to be modeled analytically, qualitative process knowledge can be used to evaluate relations between measured signals and current operating conditions [Hameed et al., 2009]. Data-driven methods are mainly Artificial Intelligence (AI) techniques and neural networks. AI consists of processing elements called nodes and neurons which interact with each other through numerically weighted connections. A complex regression function can be established with a set of input, output and a network training procedure. Subsequently, training procedures can be categorised into supervised training and unsupervised training. Two major setbacks with this technique is the lack of transparency on how decisions are reached in a trained network and the optimisation of results . On the other hand, neural networks such as fuzzy logic could overcome the AI transparency problems, as a fuzzy logic system is a nonlinear mapping of an input data vector with a scalar output by utilising a continuum mathematics of fuzzy sets and thorough simulation. This technique has not been widely implemented in the wind industry, but has demonstrated effective results in a nuclear reactor providing thermal power. Other non-intrusive and cost-effective techniques that have been implemented are statistical methods, such as Bayesian inference, extended Karman filtering, Supported Vector Machines, Gaussian process regresion, to mention a few [Kan et al., 2015].

2.9. Condition Monitoring research in TST

Based upon the CM foundations developed in the wind industry, a small number of researchers have considered how to develop CM for application on HATT. This is a sensible approach, given the similarity between faults experienced on wind and tidal turbines. Even though CM techniques have been developed for HATT, their use to date has been very limited and needs further research focus. As stated before, primary attention has been placed to the rotor efficiency and blade design, but less to the operational process of the turbine under sea itself. Therefore, tidal energy has yet to be proven

in terms of long term operational availability and reliability. Additionally, further challenges should be considered such as fatigue loads (currents' speed variations, direction of water flow and turbulence), cavitation (blade erosion and unhealthy vibration) and marine mammals impact [Chen and Lam, 2015]. Thus, a key factor in any reliability strategy must be effective and cost-efficient control of maintenance, using the most appropriate condition monitoring and diagnostic techniques that are currently available since minimising uncertainty of the latter improves investor confidence and support to achieve economically viable power extraction [Davies, 1997].

A FMECA (Failure Mode and Effect Criticality Analysis) was conducted by Elasha et al. [2014a] to calculate the failure rate of each tidal turbine component and thus to define a CM strategy based on the highest failure rate value. It was founded that the gearbox is the most critical component in a tidal turbine due to the pitting and abrasive wear that the gearbox is enduring on a tidal cycle. Finally, they conclude that the gear life prediction showed that the transmission system exposed to tidal currents will experience a shorter life compared to that exposed to wind load conditions, with a 13-year life expectancy compared to the one stated for wind turbines of 20 years, also stating that the main problems are said to occur due to the pitting and abrasive wear it would have to endure during a tidal cycle. Moreover, the use of a numerical simulation based on measured field data has been applied to generate torque and speed data that was used to predict the load and fatigue experienced by a HATT gearbox throughout its life [Elasha et al., 2014b]. This approach allowed the development of a prognostics model. This was used to estimate that gearboxes in HATTs will experience a shorter life compared to the ones exposed to wind load conditions.

Some researchers have adapted different CM techniques to make further analysis of a particular drivetrain component. Blackmore et al. [2016] showed that, by using the power output signal of the turbine, they could accurately obtain estimates of blade loads. They were consequently able to monitor blades without the need for additional instrumentation. They have had successful results in terms of using TSR surfaces by CFD, real-time drivetrain simulation and the tow tank testing to provide more realistic

operational data. Similarly, Grosvenor et al. [2014] has developed a technique to rely on Fast Fourier Transform and Time Synchronous Averaging (FFT, TSA) principles to use a test rig for comprising electrical current as a failure detection in rotor imbalance. Allmark et al. [2017] has engineered a parametric model called Transient Monitoring Surfaces (TMS), to calculate developed turbine rotor torque in real-time and to recreate the results of realistic flow conditions on the TST rotor that subsequently was based on a Computational Fluid Dynamics (CFD) modelling. The parametric model used the mean rotor torque signal and an added fluctuating component, based on fluid velocity turbulence, to represent a non-stationary condition. This approach was utilised to detect rotor imbalance faults and it was found that a minimum amount of extracted data was required in order to accurately detect a fault in the system.

The equipment and instrumentation needed to validate CM algorithms and techniques using a drivetrain simulator test rig has been considered [Wenxian et al., 2010]. Here both the properties of realistic flow conditions and the turbine rotor mechanical behaviour were incorporated. This allowed researchers to verify if the proposed technique could efficiently provide a solution for CM systems. Once the algorithm has been validated, it could be implemented in a set-up intended for use in a flume tanks or to enable offshore simulations. Combining both accurate instrumentation and a spectral analysis tool, CM simulations can explore the benefits and downfalls of new ideas at a relatively low cost before developing the latter to a larger scale [Doman et al., 2015]. Finally, another attempt to define a CM strategy was performed by Rinaldi et al. [2016] with a reliability tool to improve decision-making processes of cost reduction and sensibility analysis by the estimate of failures, repairs and the availability of a marine energy array. The authors implemented a genetic algorithm and built an optimisation algorithm to identify objective and quantitative measure of the performance of the system (profit, time, potential energy or any quantity that can be represented by a single number). Basically, an optimisation algorithm will be formed for the minimum variables, the constraints, cost and maximum profit [De Oliveira and Fernandes, 2012].

As previously stated HATT operation and maintenance have become two of the

biggest challenges to be met in establishing device reliability. Research is needed to find CBM techniques that can be deployed to meet these challenges. As part of this work appropriate CM approaches must be identified. Its use can be based on the principle that it should be a cost-effective and fast solution for emerging failures.

2.10. The use of test rigs in the energy industry

There are significant constraints in developing CM experimental research for both tidal and wind turbines. First, despite the relevant literature that has been developed in the wind industry, one of the major restrictions in CM research is data acquisition, as the available data from major wind companies are limited given the high competition in the industry. Additionally, if the data would become available, data must be useful to determine possible faults that could be prevented. If a system is installed on a single turbine it is likely to record large amounts of data where no faults are present. Plus, it would be very impractical to perform experimental monitoring in the field, as the cost associated to design a fault or force a turbine to perform under the presence of a fault would be unfeasible [Crabtree, 2011]. As for the tidal energy industry, faulty conditions developed in large-scaled projects is limited and insubstantial, as there has been only a few tidal turbines faults detected in large-scaled projects. To mention a few, the biofouling accumulation in the OpenHydro and the AR1000 tidal turbines being installed, that could lead to an increase in drag and decreased performance [Rashid et al., 2023], and the problems that arose in the MeyGen array for not being able to control the turbines from an office location, leading to site visits from the personnel that would not necessarily have been required under normal circumstances [Black and Veatch, 2020].Therefore, the challenge is to accurately establish failure modes and associated reliability data for the components and subsystems of TSTs, in order to fit the TST design to operate in a hostile marine environment [Thies et al., 2011].

The use of test rigs is widely adopted in most industries, mainly in the automotive, aerospace and energy industries. The main advantage of utilising this test rig is

its ability to adapt to a variety of operating conditions for real time turbine simulations, and hence enable the testing and monitoring of turbine performance by using a more flexible, cost-effective and less time-consuming device. Although it is not considered a novel technique to develop further CM techniques as there are only a few test rigs operating in the wind and tidal industry at the present moment, the capability of a simpler and more flexible tool to adapt and examine fault-like conditions is very appealing. Still, the literature of both tidal and wind turbine conditions applied in test rigs are detailed herein.

An example of a test rig developed by Wenxian et al. [2010] of a WT condition monitoring technique that utilised the generator output power and rotational speed to derive a fault detection signal. An induction generator was fitted to a test rig, that was comprised of a 54-kW DC variable-speed motor and a two-stage gearbox, instrumented and controlled using LabVIEW. This research attempted to simulate a 2 MW WT with a variety of speed and turbulence. This research managed to deploy two fault conditions into the test rig, such as a mechanical unbalance in the generator, and the effect of a rotor winding fault. The author determined that their method not only reduced the calculation needed to extract features from lengthy online data, but that both faults were detected in WT drive trains of different types. Crabtree [2011] examined rotor electrical asymmetry, shaft mass unbalance and gear tooth failures in a test rig, comprised by a wound rotor induction generator, gearbox and DC driving motor. A test rig image utilised in this research is shown in figure 2.6a. Plus, several CM techniques were engineered in order to monitor the eventual faults in the electrical signals given by the test rig, such as the Short-Time Fourier Transform, the Wavelet-Based Frequency Tracking and a Localised Discrete Fourier Transform. Llano et al. [2014] utilised a permanent magnet synchronous machine and a Ginlong 1800 PM machine coupled together to reproduce the static and dynamic response of a real WT and in order to evaluate the performance of small wind turbine generators. Instead of utilising the emulator to prevent emerging faults, the author tested 4 different control strategies to be compared under different wind operating conditions. A test rig image utilised in this research is shown in figure 2.6b. Finally, a large test rig with a nominal power of 13.2 MW and a peak power capacity

of 16.8 MW was deployed by Helsen et al. [2011]. The aim was to simulate certain dynamic loads on all drive train components and helps to identify transient loading that may possibly affect the gearbox. Therefore, a back-to-back gearbox configuration was used, and it was found that the 13.2 MW test rig was able to accurately apply the needed dynamics on the tested gearboxes. A test rig image utilised in this research is shown in figure 2.6c.

Some test rigs have been utilised in the tidal energy research. Research in defining performance tests in turbine and pump operation for tidal range turbines by the use of a test rig was performed by Schechtl et al. [2017]. A closed loop test rig was equipped with an electronic drive system that would be driven by an axial flow pump, which is driven by a variable-speed asynchronous motor, in order to model flow rates of up to 0.7 ms^{-1} and a head of up to 8 m. The use of a drive train simulator test bed at $1/20^{\text{th}}$ scale has been developed to create representative HATT simulations. This has been utilised to engineer CM algorithms to develop and test monitoring approaches under steady-state and non-steady-state conditions [Allmark, 2016]. A dynamometer was deployed by Mjit et al. [2011] in order to acquire vibration data to evaluate the ability of the detection algorithms to detect the presence of incipient faults. Herein, approaches to diagnose ocean turbine faults were the Cepstrum or the Hilbert transform and transient detection techniques (Short Time Fourier Transform and kurtosis). Such methods have shown to be efficient, for detecting faults that affect the component health of machines, mainly in the rotor, gearbox and generator.

Finally, in order to implement dedicated component reliability in both wave and tidal technologies, two test rig facilities have been deployed: the Nautilus Powertrain test rig at athe Offshore Renewable Energy (ORE) Catapult, and the Dynamic Marine Component test rig (DMaC) at the University of Exeter. The Nautilus Powertrain test rig is mainly utilised to test drive train components, such as gearboxes, generators, mechanical couplings and bearings. It is comprised with a motor, a generator, a Force Application System and a test piece nacelle that can be accommodated in the test rig. Case studies such as studying the performance of the brake and conducting accelerating lifecycle

(a) Emulator test rig utilised in [Crabtree, 2011].

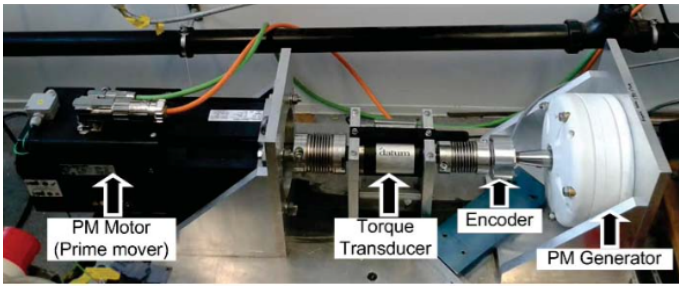

(b) Emulator test rig utilised in [Llano et al., 2014].

(c) Emulator test rig utilised in [Helsen et al., 2011].

Figure 2.6: Test Rigs that have successfully determine WT operating conditions and possible faults with a simpler and cost-effective experimental technique.

testing to provide valuable hours of the turbine in a Atlantis AR1000 was initially tested in this test facility under a controlled environment. On the other hand, the DMaC test rig is designed to replicate the dynamic movements of mooring assemblies and other components in order to assess the reliability of wave energy converters. Case studies such as performing stress-strain response at pre-tension levels, extreme storm condition testing and endurance tests were carried out to validate the working principle and the performance characteristics of a tether in a wave energy application [Thies et al., 2015].

It has been shown that the application of test rigs in the energy industry have successfully evaluated different operating and reliability turbine conditions to enable the key reliability aspects to be tested in a controlled environment prior to undergo to full scaled turbine prototypes.

2.11. Summary

It has been stated that amongst the TSTs being researched and in some cases, actually being large-scaled tested, HATTs design is the leading type of commercially scaled turbines and the one that has addressed a larger TRL level, therefore it was decided to be carried out as the device to focus this thesis. HATT technological barriers were also presented, stating that lack of long-term reliability due to the harsh environments that the turbines will be subjected to investors uncertainty, that subsequently derives into higher LCoE associated to deploy large scale projects. 15% of this costs are contained in the operation and maintenance of HATTs. Additionally, a comparison of possible outcomes of operating HATTs in high and low flow velocities in the UK and Mexico respectively are presented herein. It was stated that even though the UK resource is considered cost-effective due to the mean spring velocities to be found around 2.5 and 4.5 ms^{-1}, the Mexican tidal resource may have a high potential to be exploited, mainly for its single-directional and continous stream current found at the Cozumel Channel, that could potentially reduce maintenance costs.

On the other hand, an introduction to the implementation of CM in rotating

electrical machines, and mainly in the wind industry, has been explained. It was stated that the prediction of emerging failures in a turbine component may provide information to plan and organise maintenance and repair activities, cutting off the associated costs in LCoE early mentioned. Across the different CM techniques being employed, there are high-intrusive and non-intrusive techniques that could be implemented, and that the ones that are data-driven based or combination models would be more effective nowadays to be used. CM techniques such as electrical signal monitoring and statistical techniques were of major importance for this research development, that will be thoroughly discussed after. Then, work that have been developed in the literature regarding CM research in TSTs was also presented, demonstrating the lack of development compared to the WT research. Most of the work that has been previously performed is focused in monitoring particular turbine components, but little has been found in faults that have been detected in the tidal energy industry, emphasising the need to model possible turbine failures to then engineer a CM algorithm in order to detect and prevent those failures. Therefore, a presentation of test rigs that have been utilised in order to recreate a turbine operation in a cheaper, less time-consuming and simpler option was addressed. This research will focus in developing a drive train test rig and a condition-based maintenance algorithm into preventing emerging failures in TSTs.

3

Methodology

This chapter outlines the overview of the procedure engineered by the author throughout this research in order to test the drive train test rig reliability and the ability to perform fault conditions on the selected emulating instrument. The chapter has been separated into four different sections: section 3.1 is the synthesis of the turbine scaling model, section 3.2 provides an overview of the drive train test rig. Then, the featuring statistical and frequency techniques defined to be utilised through this research to later employ them onto the analysis stage of this research. Also, since this research's objective is to operate the chosen emulator test bed over a range of stochastic variables, a brief summary of the definition of turbulence and its calculation method is detailed in section 3.4. Finally, a methodology matrix is presented to define the three main simulations performed in this research at section 3.5.

3.1. Turbine Scaling Model

3.1.1. HATT Operating Principle

The performance characteristics of a tidal turbine rotor are typically described using several dimensionless parameters. Firstly, the tip speed ratio, or λ, that is the ratio between the tidal stream flow speed (U_0) and the turbine blade speed.

$$\lambda = \frac{\omega \cdot r}{U_0} \tag{3.1}$$

where ω and r are the rotational speed and the rotor radius respectively. Secondly, the rotor power coefficient (C_p), can be described as the ratio of the mechanical power developed by the rotor (P_{rotor}), to the power available in the tidal stream flow in an area A with the same HATT's radius r described in equation 3.1:

$$C_\mathrm{p} = \frac{P_\mathrm{rotor}}{\frac{1}{2} \cdot \rho \cdot \pi \cdot r^2 \cdot {U_0}^3} \tag{3.2}$$

where ρ is the water density and is typically assumed to be 1025 $kg \cdot m^3$. This means that seawater has a density approximately 840 times that of air allowing a HATT to operate at much lower rotational speeds but with higher axial thrust loading [Mason-Jones, 2009]. Similarly the turbine's thrust F and rotor torque τ are normalised to the upstream rotor area and flow velocity to calculate C_T and C_θ respectively as follows [Harrold and Ouro, 2019]:

$$C_\mathrm{T} = \frac{F}{\frac{1}{2} \cdot \rho \cdot \pi \cdot r^2 \cdot {U_0}^2} \tag{3.3}$$

$$C_\theta = \frac{\tau}{\frac{1}{2} \cdot \rho \cdot \pi \cdot r^2 \cdot {U_0}^2} \tag{3.4}$$

There is a functional relationship of C_p , C_T and C_θ to Reynolds Number (Re). Reynolds number gives an indication of the flow regime. Relying on Ebdon [2019], above

a particular Reynolds number, fluid flows become inherently unstable, and turbulence occurs. As the Reynolds number is dependent on fluid stream flow velocity and lengths of the fluid, larger HATT geometries with higher velocity fluids are more likely to experience a turbulent flow regime. It has been shown to be such that, above a particular threshold of Re, C_p , C_T and C_θ non-dimensional values are independent from Re for a particular geometry [Mason-Jones et al., 2012], and therefore effectively become dependent only on λ values. The latter assumption is crucial to determine the featured power extraction and directly compare a HATT-scaled experimental data to a full scale operating HATT.

The variation of generated power with tidal stream flow speed, is characterised by a power curve. Most HATTs are controlled to operate at the maximum power coefficient, or $C_{p_{max}}$, at $\lambda \approx 4$ [Harrold and Ouro, 2019]. After reaching this value, the rotor limits the power by overspeeding, therefore λ increases while C_p decreases. This is called the stall control, where the former control strategy operates on the principle that for high flow speeds the blades' angle of attack ($\propto$) increases such that flow separation occurs above the leading edge of the blade and results in a decrease of the mechanical torque (C_θ) and the generated power (C_p), but also an increase in the thrust (C_T) [Hachmann et al., 2018]. Then, a control strategy that changes the rotational speed depending on the flow velocity is needed in order to avoid the turbine stall for high flow speeds. On the contrary, when $\propto$ decreases then the blade pitch increases; this reduces the lift force on the blade, therefore the torque on the rotor is reduced and the power is regulated. This control strategy is called feathering control. Hence, it is determined that the variation of C_p and C_T along with λ depends on the control strategy of the turbine. Typically, a HATT turbine is represented by a range of λ values from 1 to 7, and $C_{p_{max}}$ typically yields at $\lambda \approx 4$. The evaluation of a range of tip-speed ratios for turbine diameters of 0.5 m and 0.9 m is undertaken in chapter 4.

3.1.2. HATT Topology

HATT is composed with a drive train, gearing, blades, a generator, power electronic converter tools and the related control system. This section outlines a generic description of major sub-systems and sub-assemblies of a basic HATT design, following the basic turbine breakdown from figure 3.1. First, a drivetrain consists of two subsystems: a rotor and a generator. All these subsystems are housed by a nacelle, along with the yawing system, sensors, instrumentation for performance monitoring and control systems [Hernandez, 2020].

A rotor can be described as the first mechanical component of a turbine to accumulate the energy of the tidal flow. It delivers torque through its shaft axis to a rotating generator. Plus, the hub connects blades to the rotor's shaft, and contains the hub bearings and in a few cases a pitch control mechanism. Research has been conducted to attain the effective amount of number of blades and blades geometry, [Hau, 2013, Burton et al., 2021, Sørensen and Sørensen, 2010] leading into findings as choosing a three blade-HATT design and tapered, twisted aerofoil shape design that has become prominent within the industry. Some of the other components of the transmission system prior to the conversion of electrical energy inside the driveshaft are the engine brake and the gearbox. The function of the gearbox is to step up the speed of rotor rotation to a value suitable for the generator [Hau, 2013]. The rotor first develops low-speed, high torque power, which a gearbox converts into high-speed, low-torque power needed for electrical generation. Depending in the gearbox ratio, it may facilitate the rotational conversion by utilising single or multiple stages between the turbine-shaft and generator. Despite that gearboxes are considered a vital component in the transport and process industries, and that the reliability of onshore wind turbine gearboxes has considerably improved, where only the 15% of the share of estimated failure rates are attributed to gearbox malfunctions, there are several different opinions whether a gearbox should be included in a HATT drivetrain or not [Polinder et al., 2006, Delorm, 2014, Sheng, 2016]. The research carried out by Touimi et al. [2018] analyses different direct-drive and indirect drive options comparing the academic and industry experiences both in tidal stream

and wind devices. It was found that direct- drive options, such as the permanent magnet generators could be an attractive choice to minimise maintenance issues. These can be more expensive due to the low speed and high torque generator needed for the turbine. Given that gearbox reliability is improving and that single-stage gearboxes are considered appropriate for HATTs the decision on drive train configuration is open. This is a statement of great significance on this research to develop a CM technique based on an indirect drivetrain for a HATT simulation on a test rig.

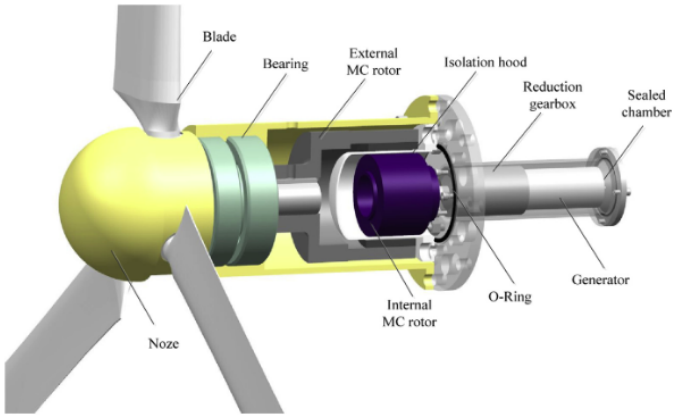

Figure 3.1: Typical HATT breakdown [Tian et al., 2018].

Finally, there are two basic approaches of the generator based on the rotational energy of the shaft [Hardisty, 2009]: the synchronous and asynchronous generator. A synchronous generator consists of a stator and a rotor, where a rotating electromagnetic field is produced by three-phase AC current flowing in the machine windings. Synchronous generators may be powered either by an external applied direct current or by permanent magnets. By utilising a large number of pole pairs, it yields a low synchronous speed matching the rotor's rotational speed, disregarding the use of a gearbox. Yet, a disadvantage of this generator configuration relies on the lack of ability and damping to directly connect to the AC grid, since the tidal stream power fluctuations will translate to heavy torque fluctuations and high peak loads in the drivetrain, mismatching the constant speed a synchronous generator will work with. Still, a gearbox could be installed in order to increase the rotational speed and then overcome the high peak

loads aforementioned [Touimi et al., 2020]. On the other hand, an asynchronous generator can operate at a varying speed different from the synchronous speed. If both motor and generator are asynchronous motors, then the direction of power flow in the connecting wires differs only whether torque is applied to or taken from the shaft or if the rotor speed is slightly above or below synchronous speed. Usually, a slip generator is installed on this type of configuration as this increases torsional compliance and damping in the turbine drive train and helps limit torsional oscillations in the drivetrain induced by the periodic rotor torque variations [Burton et al., 2021]. As stated in [Sørensen and Sørensen, 2010], for the same level of torque, the higher resistance of the rotor windings, the higher the slip is. A higher slip means more power consumed by the rotor ($\approx 2\%$), a consequent generation of heat and a lower generator efficiency. An alternative of this energy dissipation is to exchange the energy between the rotor and the electricity grid, by the use of a double-fed induction generator (DFIG). This controls the rotor active power flow and the rotor speed by adding resistance into the rotor circuit using an external resistor. The aforementioned option is more suitable to be utilised in the tidal energy industry compared to synchronous generators to directly connect the generator to the electrical grid.

Among the two generator options, the Permanent Magnet Synchronous Machines (PMSMs) are mostly utilised for experimental testing, since it enables higher efficiency to a smaller tidal energy generator diameter [Sai et al., 2015]. PMSMs do not require any external excitement current, as it uses a diode rectifier and a supply-side inverter to regulate the turbine speed with the DC-link voltage. The latter comprises a compensator for the reactive power demand and the reduction of harmonic distorsions in the system (voltage source converter [VSC]), and a driver that works as a control system to match the stator frequency changes along with change in DC-link voltage (pulse width modulated controller [PWM]). The reference electrical power is compared with the actual DC energy extracted and the result is used to determine the new operating DC voltage drop. The current control loop of this inverter receives the brand new operating DC voltage and outputs a great instantaneous driving indication for the PWM. This allows to reference the fixed voltage, so the voltage on the inverter may be fixed at a precise

optimum tidal stream velocity. Figure 3.2 shows the general control scheme of a HATT based on using PMSMs. It can be observed that there are three different control blocks: Optimum Tidal Power extraction, the Generator Control and the DC link Voltage Control. For very low tidal stream speed values, the rotor speed is kept almost constant and for high values there is a limit related to the nominal rotor speed and nominal power, that is being controlled by the generator. After reaching its rated output, the generator power in higher flow conditions is held constant through a reduction in generator torque (i.e. stall control) by the use of the PWMs [Harrold et al., 2020]. The aim is to provide the necessary power or torque reference based on the operational points of maximum efficiency (previously defined in section 3.1.1). In here, two back-to-back VSC are utilised to provide a variable speed operation for the PMSM: the Generator Side Converter (GSC) controls the power extracted from the turbine, whereas the Network Side Converter (NSC) is responsible for keeping constant the voltage of the DC link between the two VSC [Cheah-Mane et al., 2014, Anaya-Lara et al., 2009]. The GSC utilises a vector control that will be explained in section 3.2.2 and the NSC regulates the DC voltage through a proportional integral (PI) controller, furtherly explained in section 3.2.2.

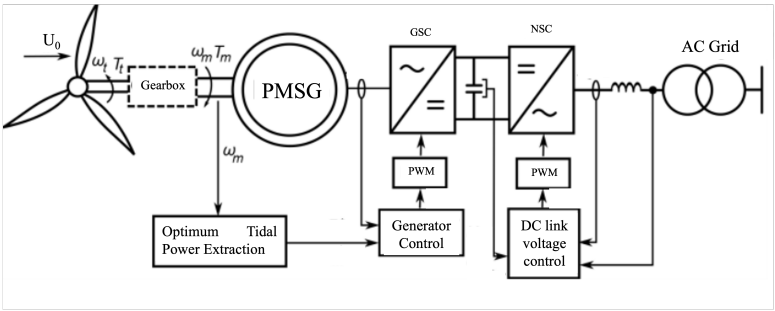

Figure 3.2: General control scheme of a HATT based on PMSMs with full-rated VSC. Adapted from [Cheah-Mane et al., 2014].

3.1.3. Turbine Control

Tidal turbine control strategies are similar to the validated wind control strategies, that inherently conserves the overall characteristic of maximising the power pro-

duction while preventing damage to the device from excessive mechanical loading. The author categorises these control turbines as follows: Fixed-speed fixed-pitch (FS-FP), Fixed-speed variable-pitch (FS-VP), Variable-speed fixed-pitch (VS-FP) and Variable-speed variable-pitch (VS-VP) [Harrold, 2016].

Both first fixed-speed scenarios are considered an attractive configuration since is directly connected to the grid, therefore no additional components are required to manipulate the output power. However, it has the disadvantage of no control over the rotational speed, therefore it cannot track the tidal stream velocity variation and hence the operational time when the turbine will achieve optimum power performance will be reduced. However, the use of fixed-speed turbines has been in decline due to the development of more complex and resourceful control system configurations. Still, fixed-speed turbine control was included on this research since the approach of the first stage of it is to validate the initial reproduction of a HATT operation under steady-state conditions, or no added turbulence intensity or flow variation. The fixed speed operation of the drive train test rig will be achieved by setting the generator rotational velocity to the value that corresponds to the desired λ value to be simulated given the desired mean fluid velocity over the entire simulation. This approach is taken in consideration in chapter 5.

On the other hand, for the VS-FP scenario the turbine operates in variable speed mode and the pitch angle is set to the optimal pitch to extract the maximum power available from the flow. Once rated torque is reached at the optimal power, the generator torque demand is held constant and the pitch angle of the blade is adjusted in order to regulate the rotor speed and keep the turbine operating on the constant power curve [Whitby, 2013]. Similarly, the same approach is utilised in the VS-VP control strategy only by adding a pitch system to achieve greater control flexibility, in which the rotor blades are pitched to change the inflow angle.The latter are held constant until the turbine reaches rated power, and it may decrease the angle of attack to stall the rotor and therefore keep the torque and speed constant [Harrold, 2016]. Additionally, it is possible to regulate the rated power or torque by controlling the flow speed, rotor speed and/or the pitch angle to reach the optimal value of the λ, which corresponds to the maximum

C_p value [Djebarri et al., 2015]. This is called the optimal λ control, where the measured operating point is compared with the optimal λ, known prior to operation to give maximum power output under continuous turbine operation. The latter is passed to a controller to regulate the generator load to achieve the torque required to minimise the λ error [Allmark, 2016]. This approach was also utilised in the unsteady state simulations at the drive train test rig in order to regulate the speed to maintain the $C_{p_{max}}$ and keep a variable torque on the test rig, further explained in chapter 6 and 7.

3.1.4. CMERG lab-scaled Turbines

The turbine geometry used in this research has been the subject of many previous numerical and experimental studies within the Cardiff Marine Energy Research Group (CMERG). Firstly, a 0.5 m diameter turbine of a HATT was modelled in CFD and experimentally validated by Mason-Jones et al. [2012]. Then, a second generation of HATTs were developed by Frost et al. [2015]. Herein, the authors decided to coupled the turbine rotor and braking motor directly via a short drive shaft. The motor was mounted inside the turbine housing, replicating the commercial set ups currently applied. Finally, a third generation turbine was created using a similar rotor setup to the previous model scale, only that the turbine was fitted with a thrust and twisting moment transducer for a single blade, an accelerometer was installed in the nose cone, and the rotor was measured via the PMSM [Allmark et al., 2020]. This turbine corresponds to the CMERG Turbine 3.0 model with a turbine geometry described in table 3.1. The non-dimensional performance characteristics were used as the basis of the steady-state simulations presented in chapter 4.

The last generation of turbines developed by CMERG to date were modelled in CFD and experimentally validated in [Allmark et al., 2020] and Allmark et al. [2021a] respectively. Herein, three 0.9 m diameter turbines were tested in different facilities to study them under the influence of a variety of conditions, such as wake, turbulence intensity and turbine controls. Mainly, data obtained in the testing campaign at the Institut Français de Recherche pour l'Exploitation de la Mer (IFREMER) and the Kelvin Hydrody-

Turbine Specification	Value	
Experimental Turbine Diameter	0.5 m	0.9 m
CFD Domain Dimensions	4 m X 1.4 m X 0.8 m	4 m X 2 m X 18 m (IFREMER)
Blade Profile	Wortmann FX 63-137	Wortmann FX 63-137
Blade twist (root to tip)	33°	35°
Stanchion diameter	0.09 m	0.071 m
Blockage ratio	17.5%	8% (IFREMER) and 6.9% (KHL)%

Table 3.1: CMERG 3.0 Ansys CFX Model Turbine specifications and experimental testing main data from the University of Liverpool and CMERG last generation of turbine Ansys CFX Model Turbine specifications and experimental testing main data from IFREMER and KHL [Frost et al., 2015, Allmark, 2016, Ordonez-Sanchez et al., 2019, Ellis, 2016, Allmark et al., 2020]

namics Laboratory (KHL), tests performed in 2018 and 2019 respectively were utilised for this research. The recorded data from the operation of the lab-scaled turbines at the KHL testing campaign was utilised to develop a new CM algorithm to replicate rotor imbalance fault conditions in both the rotor and the generator on a drive train test rig, whilst the recorded data from IFREMER was utilised to replicate the torque and speed signals recorded under a variety of turbulence intensity values on the test rig, and therefore validate the CM algorithm functionality under the influence of flume tank experimental recorded data. Both results are displayed in chapters 5 and 6 respectively. Details of the CFD and experimental main data are presented in section 3.1.

3.2. Drive Train Test Rig

3.2.1. Hardware

The set-up deployed by the author to represent different HATT simulations is based on a $1/20^{th}$ scale drive train test rig. The test bed motor can be controlled to replicate the turbine rotor input to the drive train. An initial setup was validated in [Allmark, 2016], where two PMSMs emulating a 0.5 m diameter rotor and generator respectively where coupled together. An early first setup was developed by the author as part of

the research reported in this thesis by embedding a gearbox between the two PMSMs. However, several correction functions were needed to be put in place. Therefore, a second setup was designed and commissioned by the author to increase the emulated rotor PMSM size from 0.5 m to 0.9 m. The detailed of the aforementioned situation is explained in chapter 4. A final version of the drive train test rig was engineered by the author to validate CFD and experimental scaled HATT prototype testing in order to replicate the turbine conditions onto a homogeneous tidal flow and a turbulent flow situation. Figures 3.3 and 3.4 represent the first and second setup of the drive train test rigs respectively. The final setup comprises a PMSM emulating a 0.9 m rotor side, a 1:10 ratio gearbox and a PMSM emulating a 0.5 m generator side.

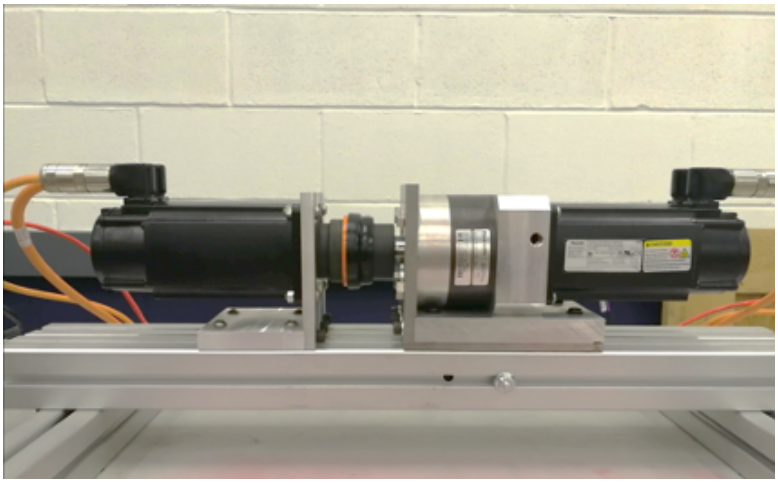

Figure 3.3: The previous version of the drive train test rig used to perform the first set of simulations. Both PMSMs are emulating a 0.5 m diameter rotor and generator sides respectively, and are coupled via a 1:10 ratio gearbox.

Permanent Magnet Synchronous Machines

The emulated rotor part of the test rig is a PMSM size 130 E from Bosch Rexroth and it is part of the IndraDyn T series. It consists of a stator and a rotor with a laminated core with multipolar winding. It represents a 0.9 m diameter and it has a rated torque of 42 Nm, a maximum torque of 65 Nm, a maximum speed of 350 RPM and a rated power of

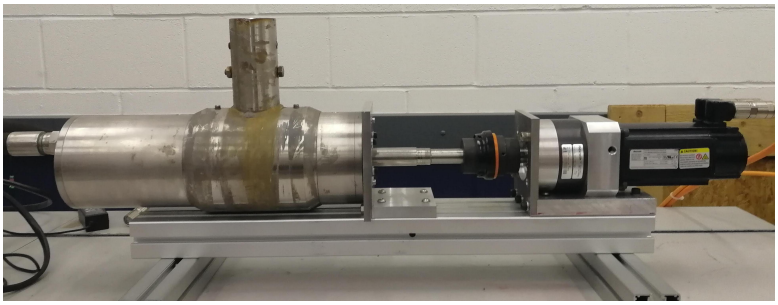

Figure 3.4: The final version of the drive train test rig used to perform the simulations. PMSM on the rotor side is emulating a 0.9 m rotor diameter, whilst the PMSM on the generator side is emulating a 0.5 m generator diameter, and are coupled via a 1:10 ratio gearbox.

0.6 kW. This characteristics were chosen since it was decided that, in order to be able to replicate tidal flow characteristics from experimental testing datasets, it was important to increase the emulated rotor size to obtain the expected results from the generator side. This argument is thoroughly explained in chapter 4. On the other hand, it is important to denote that ambient climatic conditions are critical for the correct operation of the rotor, since it has been observed that after long periods of operation time, temperature influences the rotor windings, and subsequently the peak current that affects the rotor torque output. Therefore, it was decided that, if the research simulations may exceed the rated torque rotor limit, the test rig will be run at ambient temperatures between 20° C and 33° C and a cooling time between simulations of 30 min-60 min to avoid further variation on the simulation results.

The emulated generator part of the test rig is a 0.5 m diameter PMSM Bosch Rexroth Indradyn MSK 050C, rated with a maximum velocity of 4700 RPM and a maximum torque of 15 Nm. An advantage of utilising the MSK series is that it includes a data memory in the motor encoder. Figure 3.5 shows a graph of the speed/torque capabilities of the MSK 050Cs used in the setup. Curve 1 to 4 show the characteristic voltage limit curves. When a speed at the safe commutation limit is reached, the voltage limit curve limits the available maximum torque. The maximum motor speed is determined by the DC link voltage used. For this research, the mains setup adopted was a three-phase 400 V controlled mains feed. On the other hand, the S1 curve represent the available contin-

uous current at standstill 60° Kelvin, that is the temperature rise from natural convection to motor windings for a 10- minute intermittent operation. The S3 curve the intermittent service characteristic curve at 25% operating rate of the motor and maximum cycle time of 10 minutes. As the simulations are expected to be short relative to the 10 minutes operation time specified in the S3 curve, curve 1 was used as the limiting characteristics of the first test rig setup outlined in chapter 4 to limit both the rotor and the generator sides of the test rig, and only limit the generator on the second test rig setup as aforementioned. These characteristics allowed to run the drivetrain setup with a higher torque and higher rotational speeds to maximise the set of simulations that could be performed on the test rig. The latter could be also possible by the installation of a gearbox, later explained.

Finally, in order to couple the rotor side to the gearbox and the generator, a Renold spiderflex coupling was utilised. This setup has a a maximum power of 33 kW and maximum torque of 3,150 Nm, which are limit characteristics far bigger than the ones allowed in both PMSMs. Table 3.2 summarises the PMSMs rotor and generator characteristics installed on the drive train test rig.

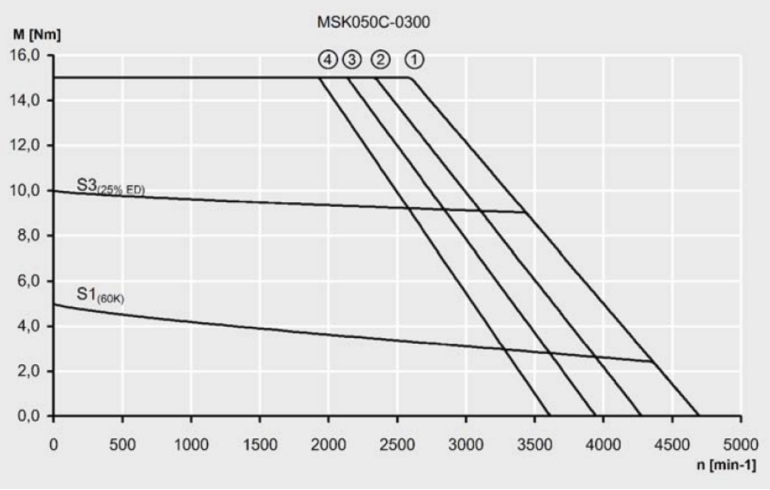

Figure 3.5: Bosch Rexroth rotor/generator MSK 050Cs speed/torque characteristic.

Characteristic	PMSM Rotor	PMSM Generator
Emulated Diameter (m)	0.9	0.5
Maximum Torque (Nm)	65	15
Maximum Speed (RPM)	350	4700
No. of Pole Pairs	10	4

Table 3.2: PMSMs Characteristics utilised on the drive train test rig.

Gearbox

The gearbox selected to be installed on this test rig setup is a Bosch Rexroth GTE 120 two-stage planetary device with a maximum input of 6500 RPM. The gear ratio was set to be of 1:10 on the user interface utilised to drive the motors, explained later. This GTE series offers a coaxial output shaft of the motor, that is connected to the sun gear with a torsionally-stiff compression coupling. The planetary gears are fixed to the planet carrier, that consequently drives the output shaft. The latter allows for a very compact with a high power density. It has a range of maximum input torque between 5.8 Nm- 21.7 Nm and a maximum output torque range of 230 Nm - 260 Nm. It also has a maximum efficiency η = 94%. This matches the nominal torque of the rotor characteristics and allows to run the generator to a larger torque value. Compared to the previous test rig setup in [Allmark, 2016], where the author decided to use a virtual gearbox to artificially scale the torque, for this research it was decided to install the gearbox on the driveshaft to have more realistic generator simulation results.

Drivers

PMSMs were managed by two drive controllers, one for each motor, which were located in cooled drive cabinets. The drives sections are made up of a mains choke, a mains filter, a rectifier and an inverter. First, a three- phase connection was created between the mains choke and the mains filter in order to maintain power quality in the supply to the rectifier. Then, the filtered three-phase connection feeds the rectifier to convert AC current to DC via a VSC. The inverter then creates a three-phase AC again that is connected to each motor. The power flow to and from the motor is managed by the

VSCs either side of a DC bus link that works as a connector between the rectifier and the inverter [Allmark et al., 2020]. These back-to-back VSCs allow to compensate the reactive power demand by controlling the power extracted from the motors and keeping the DC bus link voltage constant. Plus, these VSCs control the rotor torque and the generator rotational velocity via Vector Oriented Control (VOC) loops, later explained. The drives utilised for both the rotor and the generator are the Indradrives C HCS01 model. These drives work as master and slave to communicate through a Sercos III master and operate as an encoder interface to the PMSMs. This connection facilitates the passing of rotor and generator commands to the IndraDrives, whilst allowing data collection. Data was transferred from and to the motors via on board encoders. The particular model chosen to be utilised on the drive train system has a mains connection system of a three-phase AC with a control voltage supply of 24 V, and a maximum current of 28 A.

3.2.2. Instrumentation, Control and Software Implementation

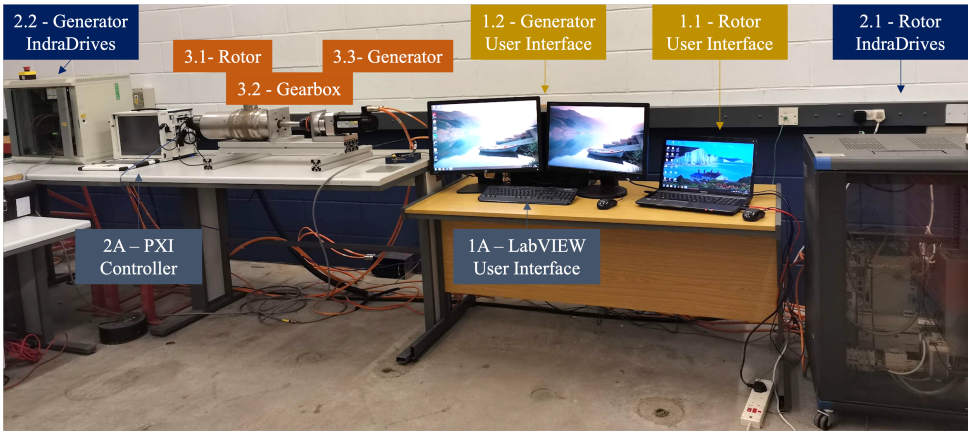

Figure 3.6: Drive train test rig set up that comprises the communication between components.

The different components of the drive train test rig is shown in figure 3.6. Each set of components are categorised into colours: yellow to highlight the two PCs utilised to set and receive the data from the simulations through software applications; orange to accentuate the drive train test rig hardware components, dark blue to show the In-

draDrives location, and light blue to introduce two alternative components on this setup, outlined in this section. First, it is necessary to decide which simulation scenarios will be run on the test rig. The author decided to run a fixed speed-fixed torque set up on the test rig, called steady state simulations, and two setups of fixed speed-variable torque called unsteady state simulations, described later on this section.

The main user interface utilised to drive the motors is the IndraWorks Engineering Bosch Rexroth tool, installed on two host PCs, one for each PMSM motor. This supports the automated programmable logic controller (PLC) and motion control programming with object-oriented language extensions. As explained in section 3.1.3, the main objective is to run the rotor with both fixed and variable torque scenarios, and to control the generator load with optimal λ control. This translates to the need of implementing VOC. One of the main advantages of utilising VOC is the ability of measuring the rotor input torque by considering the generator feedback torque neglecting the option of installing a rotor transducer, that could be considered more costly and less reliable than this option [Anaya-Lara et al., 2009]. It has a high dynamic performance including fast acceleration and deceleration. The use of VOC loops at the IndraWorks software is dependent of the following: the switching frequency of the PWM (max. 16 kHz) and the configuration of the axis controller, that subsequently is divided into three different loops: the current, velocity and position loops. These loops operate in a cascade structure and are interconnected within each other. Plus, these three loops are represented by a rotating $d-q$ reference frame, in which the d-axis is oriented along the rotor flux vector position and the q-axis leads the d-axis by 90°. There is a set of three inductance coils organised throughout these $d-q$ axis reference frame, that have induced voltages v_q and v_d, that if connected to a load will result into currents I_q and I_d [Liang and Whitby, 2011, Whitby, 2013].

The VOC implemented on the current loop consists in generating the transformed currents I_q and I_d in controlled form, which are described as torque-generating current and flux-generating current respectively. The main objective to utilise current control on the test rig is the torque/force control output, as the actual current value is

measured and not the force or the motor torque. Then, a torque force feedback value command can be obtained as follows:

$$\tau_{\text{rotor}} = K_{\text{M}} * I_{\text{q}} \tag{3.5}$$

where K_M is a torque/force constant determined by default on the IndraWorks software, where the torque constant given for the rotor is 6.60 Nm/A and 1.77 Nm/A for the generator.

K_M, however, is not a statistic value, as it can be changed by the amount of actual flowing current and the temperature change of the motor windings. This may cause deviations of the torque at the motor shaft compared with the value shown on the drive side.

The velocity loop derives from the current loop itself. It is characterised from the standardisation of the output value to obtain a command called velocity loop proportional gain, by the translation of the rotary motor in Nm (from equation 3.5) * rads^{-1}. Finally, the position loop presets a cyclic position command value for the drive in a specific cycle time. This command value interpolated in the drive and jerk-limited via filters, if necessary, before being transmitted to the position loop. The three described loops are closed-loops axis control and they use the mean values of the generator encoder feedback. Thereby, the available commands from the IndraWorks software to be recorded from the simulations are supported by VOC and the generator encoder feedback. Figure 3.7 represents the schematic of the control process implemented on the test rig via the three-cascaded control loops interconnected between each other.

3.2.3. Steady State Simulations

In order to implement the steady state simulation on the test rig, the author utilised the IndraWorks software to set the mean torque and rotational velocity input values to consequently load the rotor and generator. First, data from the selected power

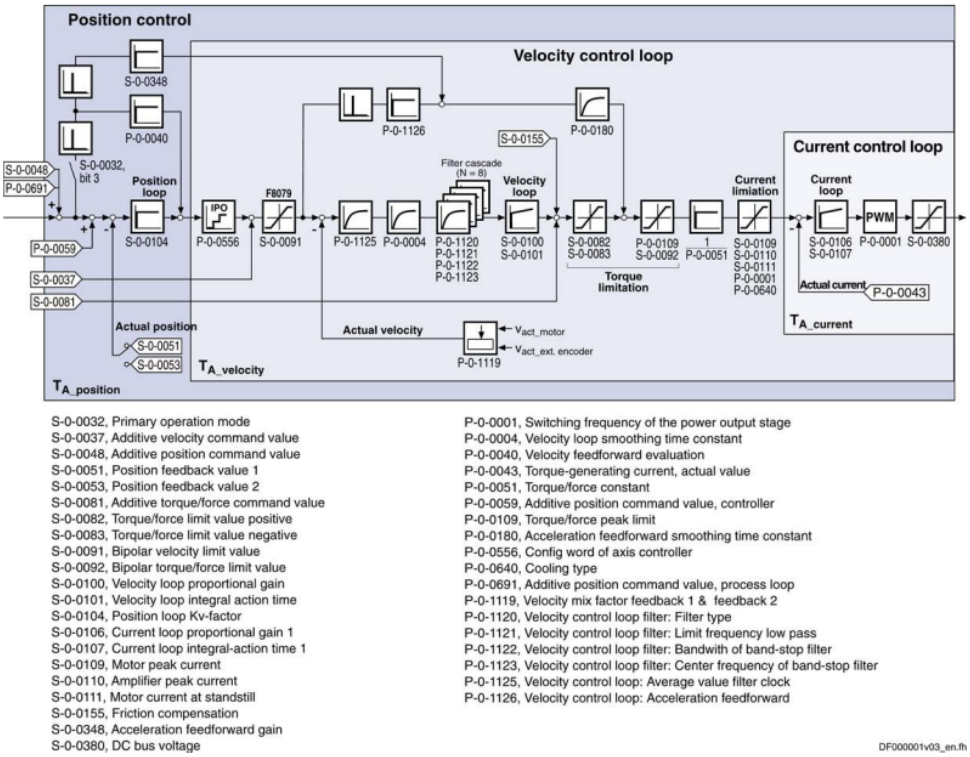

S-0-0032, Primary operation mode
S-0-0037, Additive velocity command value
S-0-0048, Additive position command value
S-0-0051, Position feedback value 1
S-0-0053, Position feedback value 2
S-0-0081, Additive torque/force command value
S-0-0082, Torque/force limit value positive
S-0-0083, Torque/force limit value negative
S-0-0091, Bipolar velocity limit value
S-0-0092, Bipolar torque/force limit value
S-0-0100, Velocity loop proportional gain
S-0-0101, Velocity loop integral action time
S-0-0104, Position loop Kv-factor
S-0-0106, Current loop proportional gain 1
S-0-0107, Current loop integral-action time 1
S-0-0109, Motor peak current
S-0-0110, Amplifier peak current
S-0-0111, Motor current at standstill
S-0-0155, Friction compensation
S-0-0348, Acceleration feedforward gain
S-0-0380, DC bus voltage

P-0-0001, Switching frequency of the power output stage
P-0-0004, Velocity loop smoothing time constant
P-0-0040, Velocity feedforward evaluation
P-0-0043, Torque-generating current, actual value
P-0-0051, Torque/force constant
P-0-0059, Additive position command value, controller
P-0-0109, Torque/force peak limit
P-0-0180, Acceleration feedforward smoothing time constant
P-0-0556, Config word of axis controller
P-0-0640, Cooling type
P-0-0691, Additive position command value, process loop
P-0-1119, Velocity mix factor feedback 1 & feedback 2
P-0-1120, Velocity control loop filter: Filter type
P-0-1121, Velocity control loop filter: Limit frequency low pass
P-0-1122, Velocity control loop filter: Bandwith of band-stop filter
P-0-1123, Velocity control loop filter: Center frequency of band-stop filter
P-0-1125, Velocity control loop: Average value filter clock
P-0-1126, Velocity control loop: Acceleration feedforward

DF000001v03_en.fh

Figure 3.7: Overall structure of the position, velocity and current control loops utilised in the test rig setup utilising VOC and PMSMs encoder feedback values.

curve of the desired turbine are taken into consideration, such as the λ values, the C_θ and a desired U_0 for modelling the required simulations. The set of parameters to be utilised on the test rig were selected by the author from the previously validated CFD results from CMERG, in order to provide continuity to the research from validating steady state simulations to real experimental data from a flume tank for the unsteady state simulations. The set of simulations required to validate the ability of the test rig to emulate HATTs are outlined in chapter 4. These values are utilised to obtain $\overline{\tau}_{rotor}$ and $\overline{\omega}_{rotor}$ by applying equations 3.1 and 3.4. Within the IndraWorks software, the option to set a torque and velocity input on the test rig is given by the easy startup mode operated via a Modbus TCP/IP to share these mean input values into the IndraDrives. These Modbus link sends the torque and rotational velocity commands to the master IndraDrive via the Sercos III

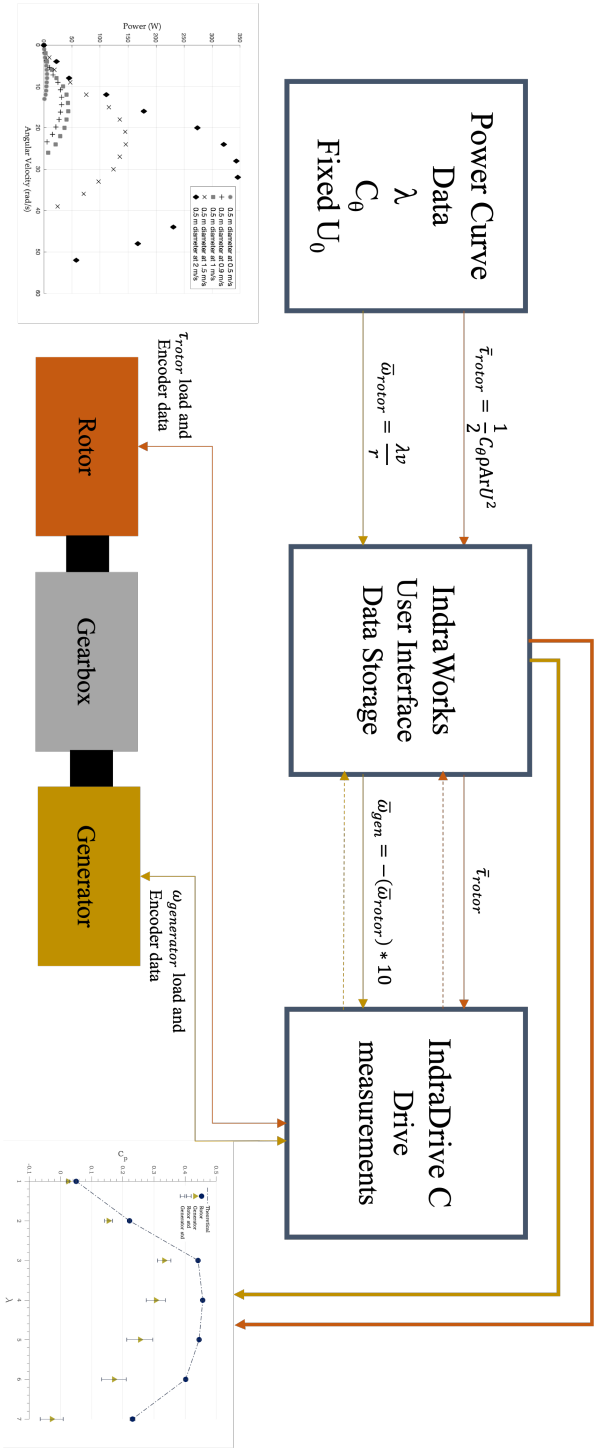

Figure 3.8: Drive train test rig diagram of the steady state simulations setup and the distribution of functionalities and parameters settings across the hardware and software platforms.

communication protocol and receives the required signals from the IndraDrives back at the IndraWorks software from the implementation of VOC, as previously explained. Both torque and velocity mean input values are set manually into each designated host PCs simultaneously. Note that the rotational velocity mean generator input value is set as follows:

$$\overline{\omega}_{\text{gen}} = -(\overline{\omega}_{\text{rotor}} \cdot 10) \tag{3.6}$$

as the gearbox gear ratio is fixed to be 1:10 in the IndraWorks system and the generator will run at the opposite side of the emulated rotor side. Prior to run the set of simulations, the oscilloscope option at the IndraWorks system is utilised in order to record the set of commands at a specific recording time length and desired frequency rate. These commands are automatically programmed by the software, and within both steady and unsteady state simulation scenarios, the selected commands to be recorded are the torque/force feedback value, the velocity feedback value, the torque-generating current, position feedback value, among others. By setting the $\overline{\tau}_{rotor}$ and $\overline{\omega}_{gen}$ and selecting the required commands, time length and frequency rate, the rotor and the generator are loaded to finally receive the required signal back at the IndraWorks software. Finally, the output signals are stored and implemented on MatLAB scripts built by the author to further analyse the signals for the respective set of simulations. Figure 3.8 shows the schematic of the interaction between the hardware and software elements and the data distribution across the drive train test rig setup. Figure 3.9 display the IndraWorks window interface to manually input the required mean torque and rotational velocity values to run the steady state simulations.

3.2.4. Unsteady State Simulations

For the second set of simulations, a similar approach was developed, except for implementing another software Interface and a PXI Controller. The details of the two sets of simulations are explained in 3.5. Figure 3.10 shows the diagram between the

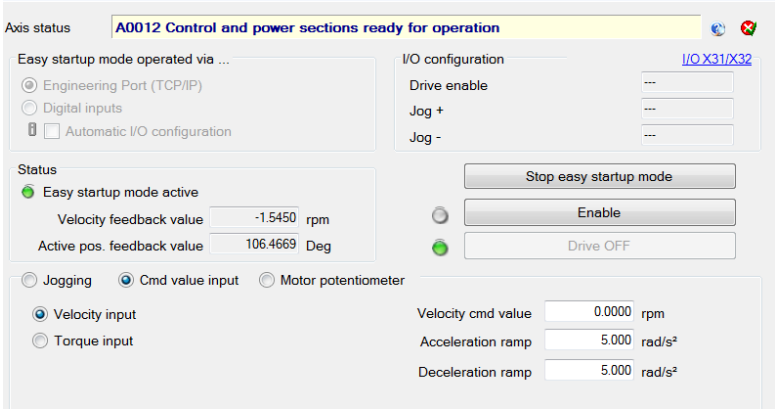

Figure 3.9: IndraWorks Easy StartUp mode window interface to set the $\overline{\tau}_{rotor}$ and the $\overline{\omega}_{gen}$ on each host PC simultaneously.

hardware and software platforms for the unsteady state simulations. A stochastic torque time series is used in both scenarios as an input to drive the rotor via a code built in LabVIEW. In addition, the CM algorithm to represent the rotor imbalance faults is also implemented in the LabVIEW code, explained in chapters 5, 6 and 7. The experimental and synthetic data torque time series are sent from the LabVIEW code to the National Instruments PXIe-8135 controller along with a monitor accessory NI PMA-1115 to implement the LabVIEW real-time operating system onto the IndraDrives. Subsequently, the built rotor torque time series signals are sent to a National Instruments NI SCB-68A connector block that converts the data into analog inputs to the IndraDrives and back to digital to measure the torsional loading on the torque time series via the IndraWorks software. The IndraWorks software converts the scaled voltage from the IndraDrives by using a time constant input filter of 0.5 ms on a range from 0 V to 10 V to the maximum rotor torque from the PMSM (as the maximum available torque for the chosen motor is 65 Nm, it was decided to round up the additive torque value to 70 Nm, bearing in mind not to run the test rig above the actual maximum available torque). Figure 3.11 displays the analog input window at the IndraWorks software to showcase how the voltage input is adjusted to the required torque output range. Finally, the same communication through components is repeated from the steady state simulation, as the $\overline{\omega}_{gen}$ is set at the IndraWorks system and the desired IndraWorks commands, the time length and

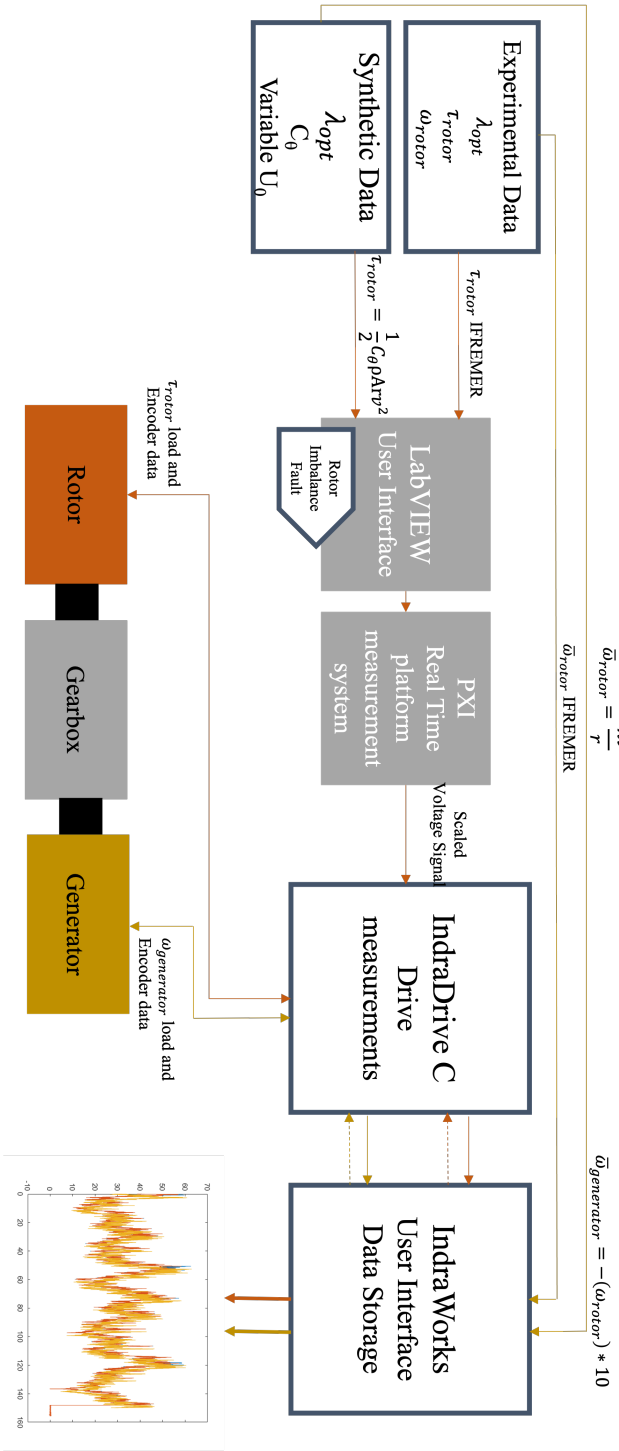

Figure 3.10: Drive train test rig diagram of the unsteady state simulations setup and the distribution of functionalities and parameters settings across the hardware and software platforms.

frequency rate are selected simultaneously onto the two hosts PCs to finally record the signal outputs from the test rig back at the IndraWorks software. Lastly, the signals are also stored and applied to the respective MatLAB codes designed for the signal analysis.

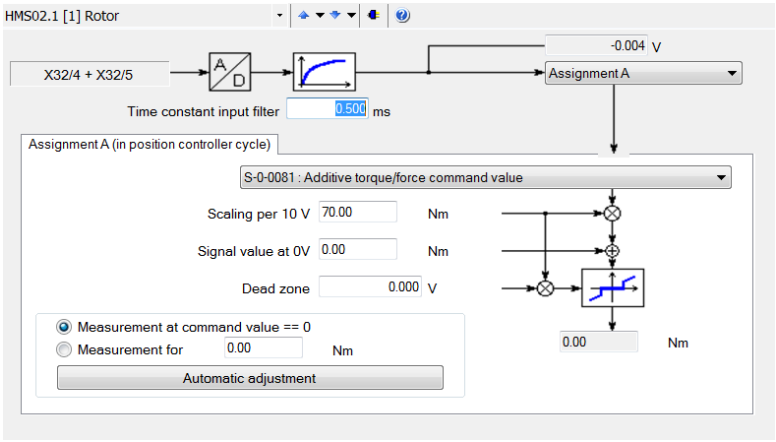

Figure 3.11: IndraWorks Analog input window interface to set the scaled voltage range from 0 V to 10 v to the maximum available torque at the chosen PMSM.

3.3. Techniques Utilised

3.3.1. Frequency Analysis

Frequency domain methods have been adopted in numerous power systems time series analysis. One of the most utilised approaches is the discrete-time fourier transform (DTFT), which entails a one-to-one scaling between the periodic sequence of the frequency and time domain. Sampling a continuous-time signal at equally spaced instants is commonly used to produce a discrete-time signal, that it is also an integer-valued independent variable [Ansari and Valbonesi, 2005]. In general, the DTFT of a signal is defined as:

$$X_{2\pi}(\omega) = \sum_{t=-\infty}^{\infty} x[n]e^{i\omega n} \tag{3.7}$$

The magnitude $X_{2\pi}(\omega)$ can be viewed as a measure of the strength of the signal content at different frequencies [Bloomfield, 2000]. Then, the fast fourier transform (FFT) is an algorithm for computing one cycle of the DTFT and is considered a faster and more efficient computation of the DTFT. Similarly, the short time fourier transform (STFT) reveals the Fourier spectrum to determine the sinusoidal frequency and phase content of a signal, frequently utilised in spectrograms. Both FFT and DTFT were computed throughout this research by MatLAB implementation. STFT was utilised to obtain the spectrograms needed to determine a thorough CM algorithm and the FFT was mainly utilised to analyse the frequency content of the output signals.

The squared magnitude of the STFT is called the spectrogram. By computing this function in MatLAB, the spectrogram returns the STFT vector into segments of the desired input vector by utilising a default Hamming window time series. This Hamming window overlaps the data by 50% between segments. The spectrogram is represented as follows:

$$S_s^{\omega}(t,f) = [\int_{-\infty}^{\infty} s(\tau)\omega(\tau - t)e^{-j2\pi f\tau} d\tau]^2 \tag{3.8}$$

where in the notation $S_s^{\omega}(t,f)$, subscript s stands for the signal and ω for the filtering window [Boashash, 2016]. The STFT output from the spectrogram function is utilised in assembling the CM algorithm to run control charts and be able to detect fault conditions based in frequency content. The rest of the representation of the frequency analysis deployed on this research is outlined in chapter 5.

3.3.2. Statistical Analysis

In order to rely on the CM algorithm, a set of different basic descriptive statistical approaches were produced by the author for throughout this research. The main tool endorsed to build up the approach on detecting rotor faults on HATTs was planned to be a simplistic yet precise tool that will adapt to the data acquired from the drive train test rig simulations. Control charts are used as a statistical process control to distinct

the presence of an assignable cause of variation in the process [Murakami and Matsuki, 2009]. It displays measurements of process samples over time and it is plotted with a center line showing the mean data across a time series, a upper and lower control limit. Usually, control charts convey outputs whether a process is predictable or unpredictable if the data points are outside of the displayed control limits. For this research, the author utilised control charts to display the built time series from the STFT signals obtained from the simulations and verify if the frequency data was contained within the upper control limits. These control charts deploys the CM algorithm effectiveness based on the chosen simulations, as shown in chapters 6 and 7.

3.4. Resource characterisation

Recently, researchers have given major importance into detailing the fluid velocities surrounding devices. During experimental test campaigns as for the operation of wind power generation, it is known that turbulent fluctuations reduce turbine performance and cause material fatigue, that subsequently shorten the turbine lifespan [Thomson et al., 2010]. Additionally, as studied in [Mycek et al., 2014], it deeply influences the wake shape, particularly affecting the power performance of turbine positioned downstream by the wake of upstream turbines in an array. Research developed for wind energy, has led to understand that energy is converted from the angular momentum of the rotor and not the tidal stream itself, therefore the power output and dynamic load responses are not linearly related to the fluid power fluctuations, but rather to the turbulent boundary layer that could be used to gain insight in the flow-turbine interaction [Tobin et al., 2015]. Relying on Blackmore et al. [2016], turbulence is correlated in both time and space, and since obtaining experimental high resolution spatial measurements may be highly costly, measurements are usually made at a single location over a time period. Therefore, researchers decompose velocity measurements into the mean, time-average velocity component and the fluctuating velocity component, as described in equation 3.9.

$$u_x(t) = \overline{U_x} + u'_x(t) \tag{3.9}$$

where $u_x(t)$ is the fluid velocity of time t decomposed into a stationary fluid velocity $\overline{U_x}$ and a fluctuating component $u'_x(t)$, that is time varying with the x direction perpendicular to the turbine rotor plane.

The latter is obtained from the Reynolds Averaged Navier-Stokes (RANS) Model, that are a series of momentum equations given in a Cartesian coordinate system to include the turbulence fluctuations in time by considering their variation with respect to a mean value, therefore modelling turbulence effects without the need of fluctuations resolution [Versteeg and Malalasekera, 2007]. The reason of this is that these small and rapid fluctuations in velocity are not important, compared with the mean velocity that is of relevance to tidal energy generation. Researchers have considered that the time average of the fluctuating velocity is zero. Therefore, if the Navier-Stokes equations were linear, the velocity would be replaced by the time averaged velocity. These variations to the original Navier-Stokes equations create additional unknown terms called 'turbulent' or 'Reynolds' stresses that represent the exchange of momentum between the mean and the fluctuating flow components, and must be modelled in order to close the Navier-Stokes equations and obtain a solution for $u_x(t)$.

There is a range of different techniques to fluid velocity data acquisition and numerical studies to model turbulent tidal current boundary layers. Among these, the most common instrumentation utilised are the Acoustic Doppler Current Profiler (ADCP) and the Acoustic Doppler Velocimeter (ADV) for tidal channels, and the Laser Doppler Velocimetry (LDV) for flume and flow tanks. The ADCP volume averaging data is normally obtained at different points through the water column and are measured co-currently. Then, the data obtained from this is tested against estimates from ground-truth ADV point measurement data collected a single height above the seabed, nominally within the rotor sweep of the planned turbine [Milne et al., 2013]. The use of ADCP and LDV has been widely utilised to understand the tidal current velocity and to measure the effects of a nonstationary mean velocity on the turbulent structure in several locations [Dom-

broski and Crimaldi, 2007, Veth, 1990, Milne et al., 2013]. On the other hand, the LDV is normally utilised by positioning the device from a certain distance upstream of the planned turbine and provides vectorised velocity data at single points measurements. The use of LDV compared to the ADV in flume and flow tanks depends primarily in the flow characterisation within the tank and whether the flume will recirculate or not. Even though that both instruments use seeding material to calculate the fluid velocity, ADVs been used in non-recirculating tanks need a redistribution of the seeding material in order to accomplish a high certainty in the measurement process [Gaurier et al., 2018b, Sutherland et al., 2017].

Similarly, other numerical models have been adapted to tidal energy to accurately predict turbine performance and durability by understanding the effects of the turbulence environment. A frequently used analysis is the large eddy simulations (LES), that was previously validated in the wind industry showing high-fidelity parameterisations of the key features of turbine behaviour and the effect of topological variables such the role of the boundary layer stability and surface roughness values in tidal turbine dynamics [Churchfield et al., 2013]. The results are used to quantify the vertical transport of momentum and kinetic energy across the boundary layer [Calaf et al., 2010]. As described in [Afgan et al., 2013], when comparing the RANS model over the LES model, the computational cost of the LES is far greater than RANS, yet it provides a greater insight into flow physics and unsteady loading, showing less variation of thrust and torque values when turbulence intensity is increased compared to RANS. Other approaches such as the one utilised in Lloyd et al. [2014], allowed the author to use a synthetic turbulence generator to predict unsteady blade loading and noise radiation to determine the acoustic impact on marine species from the tidal devices. Although the use of LES is not part of the approach of this research, it provides an insight into the different methods that exist in order to characterise turbulent flow to accurately correlate it to the tidal device behaviour.

3.4.1. Turbulence Intensity

As previously mentioned, a turbulent flow can be defined as one in which the fluid properties such as velocity, fluctuate around a mean value. Relying on Ebdon [2019], the fluctuations are characterised as eddies, that are swirling regions of fluid that display vortical motions in three dimensions. Since these eddies are irregular in shape and sizes and yet it has not been clarified in research how to reproduce individual fluctuations at a particular point in space and time, researchers still utilise Taylor's hypothesis, developed in 1938. Taylor reasoned that if the turbulence fluctuating component $u'_x(t)$ is small compared to the mean flow speed $\overline{U_x}$, the temporal response at a fixed point in space can be viewed as effectively constant as the eddies advect past the planned object in matter (i.e. HATT), therefore the change of the velocity within each eddy is negligible [Neill and Hashemi, 2018, Russell, 1996, Moin, 2009].

Accordingly, since turbulence fluctuating components in a fluid cannot be deterministically described due to its random nature, it has been historically expressed in statistical manners. Intrinsically, it has been referred as turbulence intensity (TI), that is a metric used to indicate the strength of the fluctuations when compared to the mean flow [Mycek et al., 2014]. Relying on Blackmore et al. [2016], turbulence intensity is the root-mean-squared of the velocity fluctuations normalised by the mean velocity and it is expressed as a percentage. For this research, equation 3.10 will be used determining TI as one-dimensional, and utilising the axial velocity with the x direction perpendicular to the turbine rotor plane.

$$I = \frac{\sqrt{u'^2}}{\overline{U}} \tag{3.10}$$

Different turbulence intensities have been defined by researchers, assuming 10 to 13.5% in mean flow velocities greater than 1.5 ms^{-1}. However, there are other estimations where there are 2 ms^{-1} flows with the order of 25 to 30% turbulence intensity. Still, this parameter does not provide turbulence spatial structure information, therefore it is possible to have two different flows with turbulence intensities of 10%, one with large

scale and low frequency turbulence structures, and the other one with small scale and high frequency structure. Hence, it is important to introduce integral length scale as a crucial parameter to understand the fluid properties and flow variations [Milne et al., 2013].

3.4.2. Integral length scale

Despite that it is unfeasible to characterise the size and shape of the eddies aforementioned, it is probable to obtain the estimate of them utilising integral length scale. This is an average quantity of the integration of an autocorrelation coefficient ($\rho(T)$) of the largest proportion of turbulent energy contained on the eddies. Equation 3.11 defines this process, that is the length of time when $u_x(t)$ is correlated with itself, and where T is the amount of time through which the original velocity has been lagged and the overline means the average of the function.

$$\rho(T) \equiv \frac{\overline{u(t)u(t+T)}}{\overline{u^2}} \tag{3.11}$$

As the time lag increases, the function becomes less correlated, the autocorrelation coefficient reduces until drops to zero, and the function is no longer correlated with itself. Therefore, the integration of $\rho(T)$ provides a measure of time when the velocity is correlated with itself, as described in equation 3.12:

$$L_x = \int_0^\infty \rho(T)dT \tag{3.12}$$

Still, there may be cases where $\rho(T)$ does not oscillate about zero, leading to a large time period and therefore a large length scale, possibly larger than the boundary conditions of the velocity of the matter. Thus, a threshold value corresponding to the maximum level of noise within the autocorrelation coefficient may be defined [Blackmore et al., 2016, Ebdon, 2019]. It is worth noting that research has been defined that L_x can be set approximately equal to 0.8 of the channel depth of the velocity of the matter,

as indicated in [Dey, 2014]. Integral length scale will be widely discussed in chapter 7, as it was one of the crucial components for the research developed on the chosen drive train test rig.

3.4.3. Energy Spectra

Stochastic properties of turbulence can be described by its energy spectral density, and it is useful to understand the distribution of turbulent energy over a range of frequencies. The energy spectral density is calculated by the following cosine transform:

$$S(\omega) = \frac{2}{\pi}\int_0^\infty R(s)cos(\omega s)ds \tag{3.13}$$

$S(\omega)$ can be defined as energy per unit frequency, but by applying the Taylor's hypothesis, it is possible to convert to wavenumber (number of waves per unit distance),or κ. This is defined as:

$$\kappa = \frac{f}{\overline{U}} \tag{3.14}$$

where f is the fluctuation frequency of $2\pi\omega$ and $\overline{U}$ is the mean velocity of the turbine. As previously mentioned, Taylor's hypothesis assumes that the energy density velocity is independent of both frequency and wavenumber and is simply equal to the local mean velocity of a given signal. The application of this hypothesis derives to assume that the temporal response at a fixed point in space can be viewed as the result of an unchanging spatial pattern reallocating uniformly beyond the point of velocity $\overline{U}$ [Taylor, 1935].

In terms of the power frequency content, there are three characteristic regions of the spectral domain with different behavioural responses to turbulence. The first region shows no effect to the turbine power output to flow scales smaller than the rotor diameter, whist in the third region, the turbine fluctuations appear to follow large scales

of the flow and are characterised by low wavenumbers. On the other hand, the second region show a non-linear interaction between the turbine power and the incoming flow, where it was found a phenomenological relation between the power and the velocity describing as a power law in the wavenumber κ, also known as the 'inertial sub-range' [Tobin et al., 2015]. Relying on Kolmogorov's theory, turbulence power spectra should become proportional to a straight line of gradient $f^{-5/3}$ as f increases [Russell, 1996]. This region is also known as the 'inertial sub-range'.

In order to represent turbulence in a spectral form, the von Karman spectrum is considered one of the most commonly used model [Sørensen and Sørensen, 2010]. This is based on the mean tidal stream velocity, the standard deviation and the integral length scale. If a von Karman spectrum is plotted in log-log axes, turbulence power spectra should become proportional to a straight line of gradient $f^{-5/3}$ as outlined above. Thus, the von Karman spectrum can be written in the non-dimensional form as follows:

$$\frac{fS(\omega)}{\sigma^2} = \frac{\frac{4fL_x}{\overline{U}}}{[1+70.78(\frac{fL_x}{\overline{U}})^2]^{\frac{5}{6}}} \tag{3.15}$$

where $S(\omega)$ is the spectral density function for the process, L_x is the integral length scale and σ is the standard deviation of the fluid velocity [Milne et al., 2010, Val et al., 2014].

Studying turbulence and its impact in tidal energy devices have gained attention recently. Appropriate strategies to obtain measurements of the turbulent flow at tidal energy sites have been developed to understand turbulence magnitude, but also the dominant scales and structures that are crucial for informing the rotor loading impacts [Milne et al., 2016]. To mention some of the work developed in this topic, Blackmore et al. [2016] defined that variations in turbulence intensity and length scales could possibly be the dominant driver of dynamic loading, affecting the turbine power and thrust coefficients by over 10%. Similarly, Mycek et al. [2014] revealed turbulence intensities did not affect the mean power and thrust coefficients substantially but it increased the standard deviations, which may lead to device fatigue. On a full-scale turbine at site-specific

studies, it has been proven that correlating the effect of the dissipation rate of the turbulence kinetic energy provide some of the first realistic conditions for estimating the fatigue loads and the performance of tidal turbines [Thomson et al., 2012, Guerra and Thomson, 2017]. Acknowledging the negligible effect of turbulence in the device operational lifespan motivated the author to conduct the research into defining a CM strategy of a common rotor failure that would effectively prevent a major fault to develop, even under the presence of high turbulent energy in the flow. Thus, considering the elements outlined at this chapter, a simulation matrix was defined in order to consider more realistic inputs to be tested in the test rig and later to be processed and analysed to parameterise possible failures that could be prevented. The simulation methodology matrix is presented in the next section.

3.5. Simulation Methodology matrix

An overview of the simulation methodology and testing is shown in figure 3.12. There are three different approaches to demonstrate the test rig's ability of emulating the HATT conditions and validating fault detection through a CM algorithm: by simulating a steady state HATT condition through the CFD based method, and by simulating the unsteady state HATT conditions through the experimental and synthetic based methods.

Each approach was developed and tested by the author. The CFD data represents the computational numerical outputs performed by CMERG to validate a diameter HATT of 10 m. At first, it was decided to perform the simulations with a wide set of flow velocities and turbine geometries. However, as thoroughly explained in chapter 4, due to the motor torque limitations at the drive train test rig, it was decided to narrow the expected set of simulations to run the test rig with the HATT non-dimensional values with diameters of 0.7 m and 0.9 m. The CFD data was utilised to develop initial rotor condition monitoring approaches, and to evaluate the test rig potential of replicating the turbine conditions in the rotor and the generator at a fixed tidal stream velocity. The latter was verified by utilising statistical techniques. This part of the research was the key

to move forward to the second stage of this research.

Prior to the assembling of the unsteady state simulation test scenarios, a CM algorithm was built by the analysis of the experimental testing performed at the KHL tow tank testing. A set of simulations were performed with three different turbines to individually characterise the non-dimensional values of each, as well as compare the operation and effects of turbine control on them. Data was also analysed to determine a rotor imbalance fault condition by utilising the frequency content of the data to finally parameterise a statistical tool to implement as an indication metric onto other simulation datasets on the test rig. The CM algorithm development is explained in chapter 5.

After the CM algorithm development phase, testing is needed into more realistic representation of HATT operation. Therefore, the unsteady state simulations are used two-fold. Firstly experimental data is used to explore the fault detection onto a more stochastic resource datasets, explained in chapter 6. Then, in order to compare more complex tidal conditions, such as integral length scales and a range of turbulence intensity %, the parameters displayed at this figure comprises the operating conditions chosen to develop on a MatLAB code to create these simulations datasets. Moreover, a set of different recorded time lengths were also examined, to compare the CM algorithm effectiveness under two different time datasets. Also, an impact analysis of a range of different fluid stream velocities and turbulence features to examine the CM algorithm reliability was developed in chapter 7. Finally, optimal λ control was chosen to be utilised on both scenarios and torque fault conditions sizes of 1%, 5%, 10% and 15% were added onto the input signals on the test rig.

Finally, this chapter has defined the three stages of this research, by firstly describing the HATT operating principles and control techniques to define the main characteristics to replicate in the chosen emulator test bed. Then, the DTTR components breakdown and the instrumentation and controls utilised in order to simulate a HATT was explained. A steady state simulation was outlined in order to analyse the reproducibility and reliability of the test rig over a range of selected tip-speed ratios, diam-

eters and fluid velocities. Two sets of unsteady sate simulations were built to test a CM algorithm effectiveness under the presence of more complex tidal conditions, such as integral length scales and turbulence intensity values. Finally, the drive train test rig steady state and unsteady state simulations were developed to finally assess the drive train test rig reliability of replicating the three sets of different datasets and the CM algorithm effectiveness.

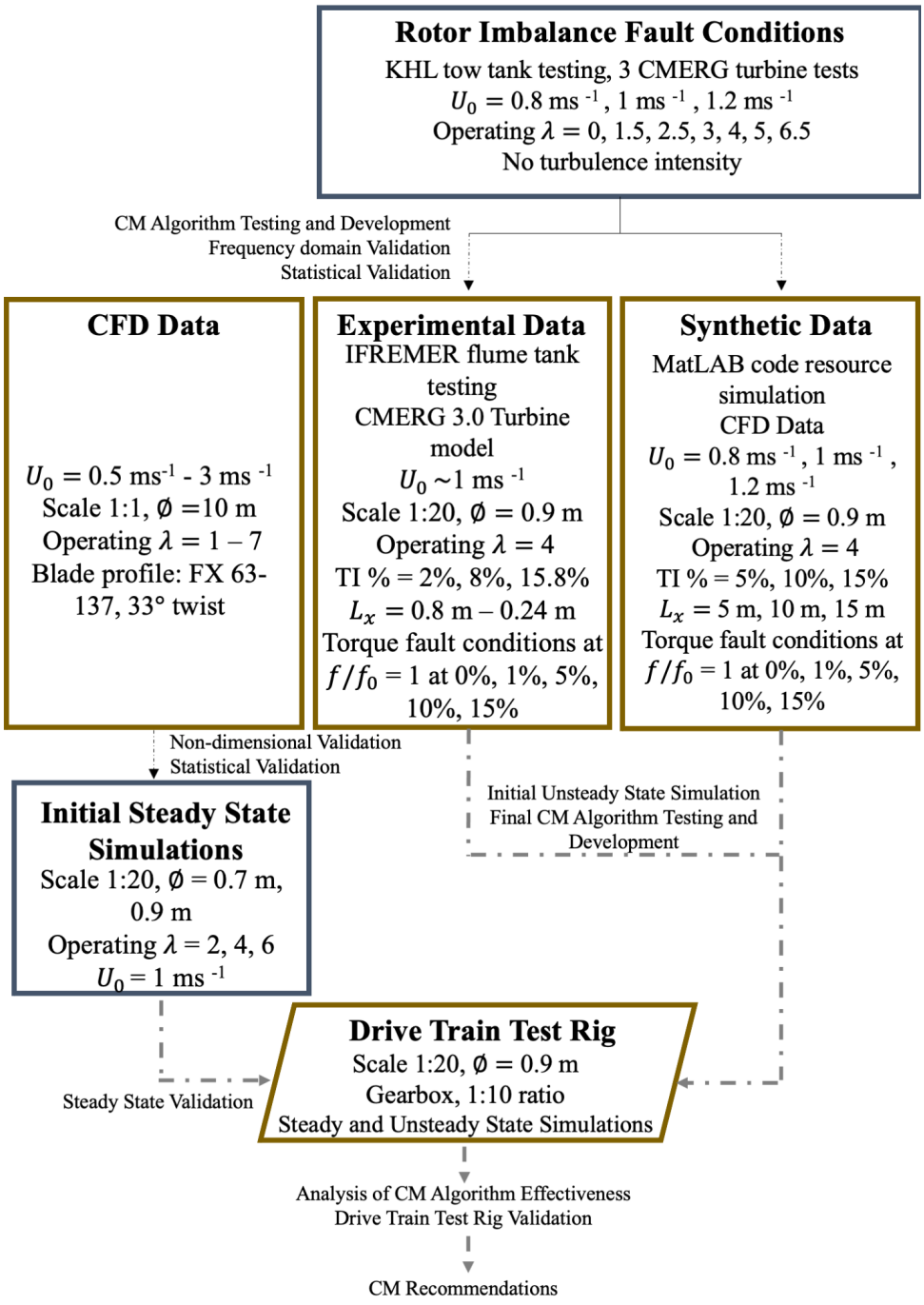

Figure 3.12: Overview of the testing and simulation methodology followed throughout this research.

4

Drive Train Test Rig Development

This chapter outlines the first approach that was made to replicate the tidal turbine conditions into a drive train test rig, of a $1/20^{th}$ scale. The primary objective is to develop a process that will enable to control the rotor of the drive train test rig to perform under steady state conditions of the selected turbine geometry. Therefore, once it has been determined that the test rig is able to emulate a tidal turbine operation, the aim will be to verify the availability to control the test rig onto more complex conditions. This chapter will explain the followed simulation methodology to determine the satisfactory steady state turbine configuration on the test rig, along with the simulation results. It will also detail the process the researcher experienced to characterise the test rig onto a steady state stage to later rely on adding variability on the system. A set of different test rig versions were performed until a satisfactory test rig version to determine the steady state condition of a HATT turbine was reached.

4.1. First stage drive train test rig

Firstly, a theoretical model of a HATT, previously modelled and validated by CMERG [Frost et al., 2015, Mason-Jones et al., 2012], was chosen to create the input parameters to apply to the test rig. This turbine corresponds to the CMERG Turbine 3.0 model with a turbine geometry described in chapter 3. Therefore, torque coefficient, power coefficient and tip speed ratio values from CFD results were taken to define the HATT used for the undertaken simulations.

Relying on Mason-Jones et al. [2012], non-dimensional characteristics when the turbine is exposed to a uniform inlet velocity profile are taken to be independent of Reynolds number for the particular geometry utilised the development of this research. Since the research undertaken will explore the non-steady state TST simulation as a first stage, it has been considered that non- dimensional values can be used. Then, given the turbine geometry, it is possible to define a theoretical model and hence obtain the input parameters needed to simulate the turbine on the test rig.

As previously mentioned in chapter 3, the drive train test rig development was being adapted given the methodology changes throughout this research. From utilising a drive train test rig previously validated in Allmark [2016], to adding a gearbox to replicate the most utilised turbine drive train configuration, it was needed to decide the Permanent Magnet Synchronous Machine sizes given the operation limits of the emulated rotor and generator on the driveshaft. The latter to define a range of simulations achievable on the test rig to explore a variety of turbine diameters, flow velocities and operating regions. Neglecting Reynolds effects in this first instance, it was decided to explore all the possible turbine geometries that could be emulated on the test rig. Therefore, diameters between 0.5 m to 20 m were considered, with a resolution of 0.5 m, thus giving a total of 40 diameters. Velocity values ranging from 0.5 ms^{-1} to 3 ms^{-1} with a resolution of 0.1 ms^{-1} were also considered, giving a total of 26 fluid velocities. Finally, λ values were extrapolated from the given values from 0 to 7 with a resolution of 0.5, giving a total amount of 15 tip speed ratios. Thus the sets of possible combinations of rotor

diameter, flow velocity and tip speed ratios were identified by combining these range of values.

The initial matrix of simulations with their respective calculations was reduced based on the maximum available torque from the rotor of 15 Nm, defined by the maximum torque achievable via the PMSMs. Limiting the configurations to allow the highest C_p with a λ of 3.5 based on the CMERG Turbine 3.0 model outputs, a refined set of 21 simulations were identified. Through this process a turbine of 0.5 m diameter rotor was selected with a rated fluid velocity of 1 ms^{-1}. Figure 4.1 shows some of the possible variations that could be simulated on the test rig that are below the 15 Nm limit. Two test scenarios were chosen to compare the experimental model with the theoretical model. The first scenario was a series of tests at varying fluid velocities for the highest torque setting for the HATT rotor - in this case for λ = 2.5. The second test scenario was planned to represent all the λ values with a turbine of 0.5 m diameter and a velocity of 1 ms^{-1}. This corresponds to a $Re_{\varnothing}$ of 5 x 10^6 which is above the Reynolds Independent threshold for the HATT [Mason-Jones et al., 2012]. Hence, the findings of these initial characterisation simulations were analysed and compared with the theoretical model used to create the simulation parameters. This was done to check that good agreement was found between the simulations and theoretical turbine given system losses and motor efficiencies.

The bearing lifetime is reduced by operation at impermissibly high temperatures (the bearing grease is decomposing). Switchoff caused by overtemperature despite operation on the basis of selected data, because the appropriate cooling is missing.

Initial simulations for both test scenarios aforementioned, led to excessive heating of the motor used to recreate the turbine rotor. Whilst this was within the default temperature warnings provided by Bosch Rexroth it was considered unsuitable for both safety reasons and the likely losses in efficiencies as the motor heated excessively. This is related to figure 3.5 previously explained in chapter 3, where the voltage limits the available maximum torque. Also, the overheating on the rotor may be caused by the motor losses generated from the motor windings and the current flowing; the larger the amount of current needed to achieve the torque values for the test scenarios, the larger the heat

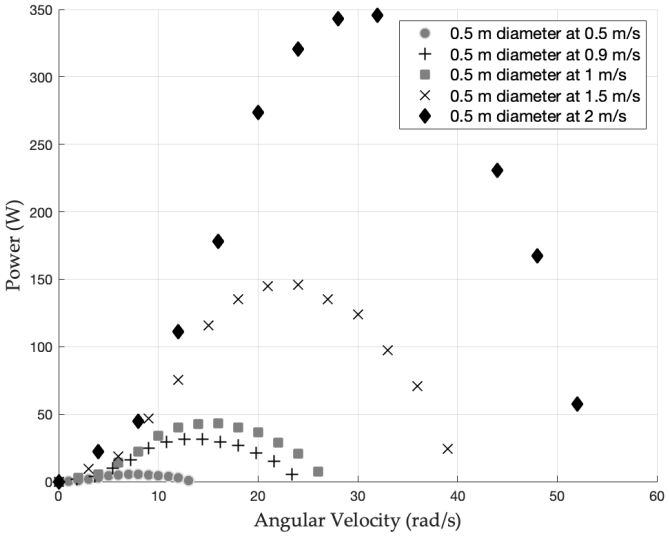

Figure 4.1: Possible power curves with varying diameter and flow velocity that could be tested on the previous test rig version.

generated by the motor losses. The implications of the motor overheating are the reduction of the bearing lifetime or the switch off of the test rig by neglecting the characteristic curves of the Bosch Rexroth rotor specifications shown in figure 3.5. Therefore, a more reserved limit was set at 11.5 Nm reducing the rate HATT speed from 2 ms^{-1} to 1.8 ms^{-1}. Plus, it was observed that when the signals were being recorded at the IndraWorks system, the generator τ signal was recording excessively high losses. The losses in the system in overcoming cogging torque from the two PMSM meant that for many simulations of lower torque settings both the rotor and generator were applying torque in the same direction. As this level of cogging torque was not expected within a HATT which would typically have only one PMSM or equivalent this effect was removed. This was done by observing the torque required to rotate the generator without the rotor applying any opposing torque. This torque value was measured for each of the rotational velocities tested and removed from the measured values by subtracting a specific τ value to correct the generator torque.

For the first test scenario detailed above, a series of test were performed at a λ = 2.5, considered the peak C_θ, for flow velocities of 0.5 ms^{-1} to 1.8 ms^{-1}. Taking the mean values of these variables from the 60 s of the tests at 33.33 Hz, a single signal for both the rotor and the generator was created. Figure 4.2 shows the results obtained for the varying fluid velocity test scenario and essentially shows the power developed via the simulated turbines for differing flow scenarios, given the aforementioned correction approach adopted. It can be seen that the rotor and the generator data collapses on a single exponential distribution, similar to the theoretical values. Clearly the generator data should always be less than the rotor data due to the drivetrain losses, gearbox interference and the heating losses. However, most of the generator data is either very similar to the rotor data or higher. This is likely to be due to over-correction of the losses in the system when adopting the loss correction approach described above. This notion add an inconvenience on the process of validating the steady state stage of this research with this test rig version, that led to apply further changes in order to achieve a more accurate test rig version.

Similarly, in order to represent all λ values with a turbine of 0.5 m diameter and a velocity of 1 ms^{-1}, C_p was calculated from the output power for both the generator and the rotor to compare the theoretical model power curve to the ones generated on the test rig. Figure 4.3 shows the results of the fixed flow velocity simulations undertaken. Figure 4.3 demonstrates how most of the points fall on a single curve with some losses through the points. There are some cases were the generator side still delivers more power compared to the rotor side, but as explained before, there is an over-correction of the actual power delivered by the test rig that causes these deficiencies in the test rig power curves. Despite this problem, the rotor and the generator develop the same curve characteristics as the ones expected base on the theoretical model. The highest C_p that could be reached by the test rig with a diameter of 0.5 m is 0.39 relying on the rotor and generator data, compared to a 0.43 by the theoretical model. There was only one point through the curve given by the generator at λ = 6 that decreased from the actual theoretical value by 19.14%. This finding was unexpected, yet the excessive losses in this case maybe down to motor heating which would lead to higher electrical losses in the

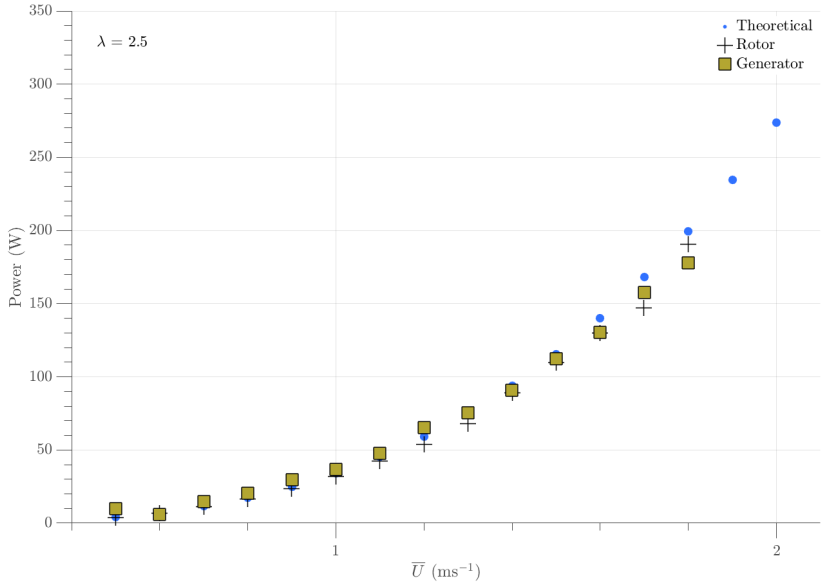

Figure 4.2: Combined power output and velocities from rotor and generator compared to the theoretical model of the previous test rig version.

system.

Overall, the first stage of this research was based on using a 0.5 m diameter rotor and generator on the test rig to replicate the CMERG Turbine 3.0 operation on this previous test rig version. However, it was observed that running the test rig at its maximum limit (11.5 Nm) led to excessive heating of the motor used to recreate the turbine rotor, that consequently meant more variability on the generator signal. These variations on the generator signals did not allow to replicate the expected power curves, nor to statistically repeat the generator signals, failing to comply with this research objectives. Since it was meant to run the test rig above the 15 Nm threshold to later implement further complex conditions to the simulations, plus it was mandatory to accurately reproduce and repeat both the rotor and the generator signals at this stage of the research, it was decided to utilise a bigger rotor diameter on the test rig as defined in chapter 3. Utilising a bigger PMSM rotor with a higher torque limitation and emulating a 0.9 m rotor diam-

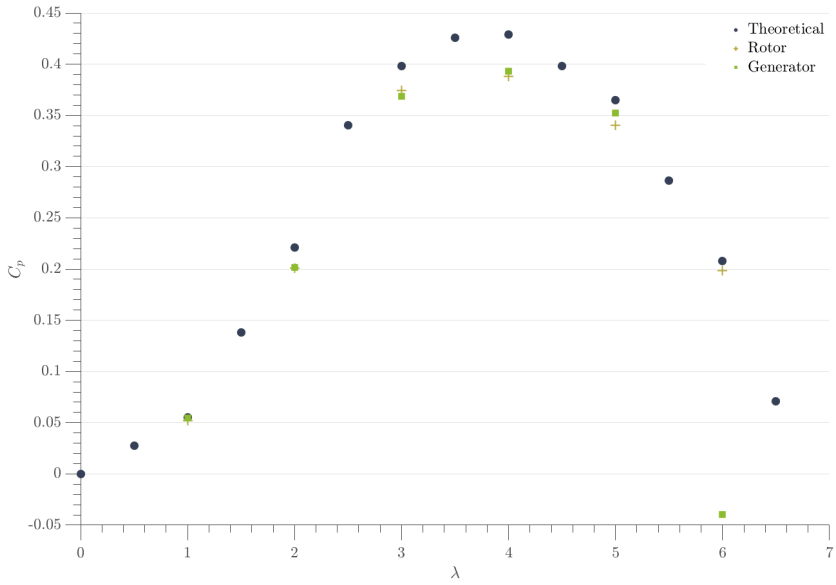

Figure 4.3: Power curve from rotor and generator compared to the theoretical model of a 0.5 m diameter turbine at 1 ms^{-1}.

eter, a 1:10 gearbox and the previous PMSM to replicate a 0.5 m diameter generator, will enable to adapt the proposed methodology matrix to the experimental results that were obtained from operating a scaled modelled HATT on flume tanks.

4.2. Simulation Methodology

Characterising the first version of the drive train test rig allowed to determine the current test rig configuration and the needed methodology matrix to conduct the steady state stage of this research. Installing a larger rotor on the drive train test rig allowed to maximise the torque limit to 65 Nm as explained in chapter 3. Consequently, this led to increase the simulations availability to further operating velocities and turbine diameters. Therefore, it was decided to run two bigger turbine diameters as in real-scaled turbine sizes to essentially compare the test rig outputs to experimental data

taken from HATT scaled-turbine sizes. Hence, the two chosen rotor diameters to be emulated in the current drive train test rig configuration were 0.7 m and 0.9 m respectively. Plus, velocity of 1 ms^{-1} was selected to be run again on this simulation datasets since it was the available fluid velocity from the theoretical data taken from Ansys CFX CMERG Turbine 3.0 model. Finally, after running the test rig with a range of λ value from 0 to 7 to compare the theoretical power curve with the test rig power output, it was determined that λ = 2, 4 and 6 will summarise the range of most important operating points of the power curve. A set of calculated test rig input values are summarised in table 4.1. C_p, power, rotor torque and generator speed values were taken from the theoretical values determined in [Frost et al., 2015] and neglecting Reynolds effects as previously determined in [Mason-Jones et al., 2012]. Notice that, due to a gear ratio of 1:10, generator torque and speed on the rotor will be:

$$\omega_{\text{rotor}} = \frac{abs(\omega_{\text{generator}})}{10} \tag{4.1}$$

$$\tau_{\text{gen}} = \frac{\tau_{\text{rotor}}}{10} \tag{4.2}$$

Generator speed is in negative values as it is running on the opposite direction from the rotor.

In order to compare the theoretical values obtained from the Ansys CFX simulations of turbine model CMERG 3.0 and compared them to the test rig output values, the following signals were recorded using the IndraWorks parameters:

- Torque force feedback value
- Velocity feedback value
- Torque-generating current

Hence, C_p and C_θ values could be calculated by utilising equations 3.2 and 3.4 using the torque force feedback value and the velocity feedback value both obtained

from the rotor and generator recorded signals respectively. Notice that all 3 signals were equally recorded for the rotor and generator output signals. The torque-generating current signal was also considered on this simulations in order to validate the obtained values at the recorded torque force feedback value. Usually, some experimental testing utilises a torque transducer installed on the rotor to validate the torque values given by the rotor itself and consequently build the power curves from these calculations. The use of a torque transducer was not explored on this research, yet the torque force feedback value was obtained from equation 3.5.

Following the steps defined previously in chapter 3, in order to obtain both the rotor torque and the generator rotational speed from the MSK 050Cs motors, the theoretical values mentioned in table 4.1 were implemented manually in both user IndraWorks interfaces for the rotor and the generator. For the first set of simulations, λ values from 0 to 7 were considered to obtain the complete power curve, however it was decided that for the repeatibility analysis, only λ= 2, 4 and 6 were utilised, in order to effectively represent the peak C_θ, peak C_p and peak C_T, respectively. For all the aforementioned cases, a sample rate of 50 Hz and a total length time of 50 s to be recorded for the future analysis were considered. The latter to replicate the power curves for both 0.7 m and 0.9 m diameter turbines and verify the test rig availability to reproduce HATT-scaled steady state conditions on this drivetrain configuration.

After running the first set of simulations on the test rig, it was noticed that the generator rotational speed being delivered on the test rig was the exact value that was manually implemented on the user IndraWorks interface, with small standard deviation ranges from 1.4-2.1 to 1.7-2.7 for both 0.7 m and 0.9 m diameter cases respectively from a λ value range from 1 to 7. Similarly, the rotor rotational speed being recorded from the first set of simulations was the exact same generator speed value divided by a factor of 10 as stated in equation 4.1. The accuracy of obtaining the expected rotational speed in both motors can be explained due to the implementation of vector oriented control (VOC), that is a standard control from Bosch Rexroth configuration, as explained in chapter 3.

Diameter	Velocity (ms^{-1})	λ	C_p	Rotor Power (W)	Rotor Torque (Nm)	Generator Speed (RPM)
0.7	1	2	0.26	50.78	8.01	-545.67
0.7	1	4	0.48	94.34	8.25	-1091.35
0.7	1	6	0.41	80.80	4.83	-1637.02
0.9	1	2	0.26	83.95	17.02	-424.41
0.9	1	4	0.48	155.95	17.54	-848.83
0.9	1	6	0.41	133.58	10.28	-1273.24

Table 4.1: Theoretical input values for the drive train test rig

On the other hand, it was expected to obtain differences on the generator and rotor torque signals, due to the introduction of a gearbox on the driveshaft and the heating losses variations given the torque-generating current changes as explained in section 3.2.2. However, it was noticed that the torque force feedback value and torque calculated by the use of equation 3.5 had very little variation, enabling to utilise the torque force feedback value signal as expected. Figure 4.4 demonstrates the comparison between the recorded torque force feedback value from the rotor on the test rig for a case scenario of a 0.9 m diameter, with a λ = 4 and a velocity of 1 ms^{-1}, and a torque calculated signal utilising equation 3.5. It shows very little discrepancy on both signals, allowing to utilise the torque force feedback value signal given by the IndraWorks software in the future.

Finally, figure 4.5 shows the torque force feedback value signals obtained from both the rotor and the generator comparing the output given for the two test scenarios of turbine diameters of 0.7 m and 0.9 m at λ =4. Mean values obtained from the rotor torque signals are of 8.25 Nm and 17.53 Nm for turbine diameters of 0.7 m and 0.9 m respectively, that compared to the input theoretical values implemented on the IndraWorks system as established in table 4.1 demonstrates again the effective configuration of the VOC and the satisfactory response of the torque commands on the IndraDrives. However, the generator does not replicate the same torque value as the rotor side. Given

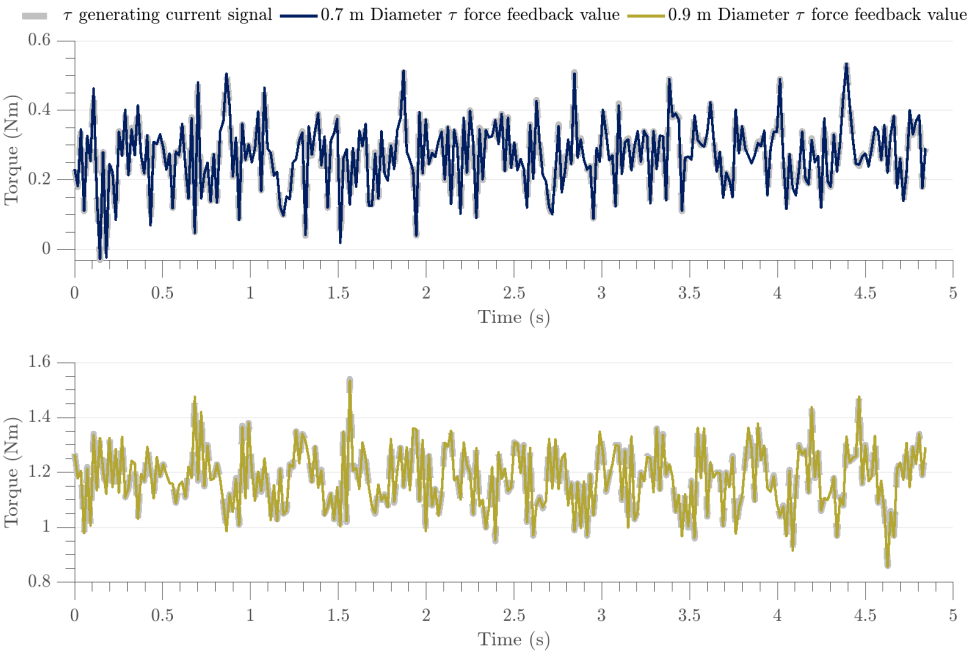

Figure 4.4: Comparison of torque force feedback value and torque calculated utilising equation 3.5 for both turbine diameters of 0.7 m and 0.9 m, with a flow velocity of 1 ms^{-1} at λ = 4 on a period of 5 s.

the 1:10 ratio from the gearbox, the generator recorded torque signal was expected to be the rotor torque signal divided by a factor of 10 as established in equation 4.2. Still, the mean values obtained for both the torque force feedback value recorded signals for turbine diameter of 0.7 m and 0.9 m respectively were of 0.27 Nm and 1.17 Nm. Thus, there are 67% and 31% losses on their obtained signals respectively. The reason of this significant drop could be for different reasons, such as the cogging torque generated by the interaction of the rotor-gearbox-generator, the electromagnetic forces on the generator stator or the increase on the temperature given the time the test rig has been used. Plus, given a gear ratio of 1:10 to reduce the torque and increase the speed on the generator side, heat and rotor shaft vibrations are produced by meshing teeth, therefore energy is lost. As previously mentioned in chapter 3, the installed gearbox has a maximum efficiency η = 94%, that evidently reduces the available torque to be obtained in the generator. Yet, there are significant generator losses as expected in both scenarios, that is particularly higher in the 0.7 m turbine diameter test scenario at optimum λ operation.

The latter could be explained due to the low torque and high rotational speed interaction of both motor drivers, compared to a less proportional interaction when compared to the 0.9 m diameter test scenario.

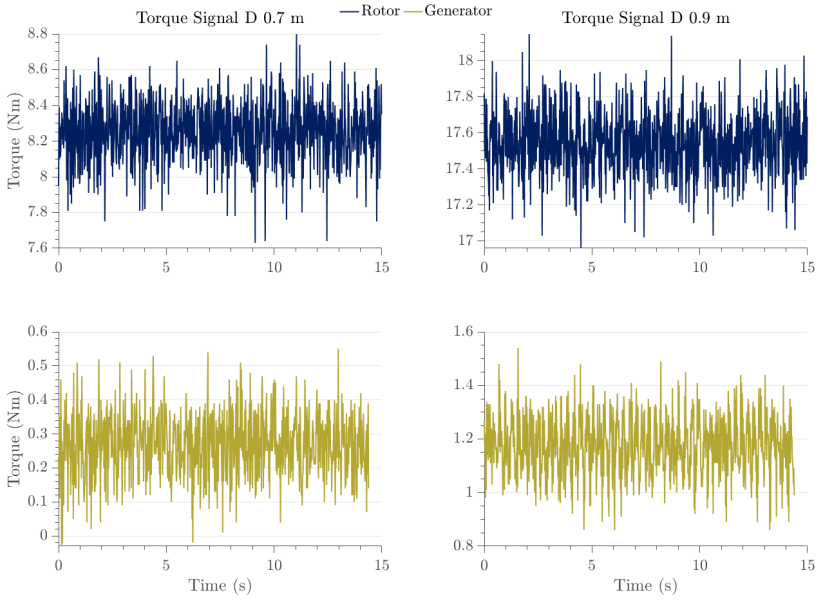

Figure 4.5: Torque signals from IndraWorks system from Rotor and Generator for turbine diameters of 0.7 m and 0.9 m at λ = 4 for a period of 15 *s*.

Histograms of the rotor and the generator signals were elaborated in order to compare the data distribution and determine if they exhibit normal distribution characteristics. As it can be seen in figures 4.6 and 4.7, the three most important operating points (λ = 2,4 and 6) were compared three different times for both turbine diameters of 0.7 m and 0.9 m respectively. Both torque signals were normalised in order to restrict the comparison to the data distribution and avert motor's direction, the gearbox effect and the torque magnitude onto the analysis. Clearly, the rotor histograms display a normally distributed torque signal in both diameter scenarios, whilst the generator torque histograms display a negative skewness in all the test scenarios. Additionally, the rotor histograms display a good repeatibility across λ values in both turbine diameter test scenarios. Meanwhile, the generator signal may also display a good repeatibility across

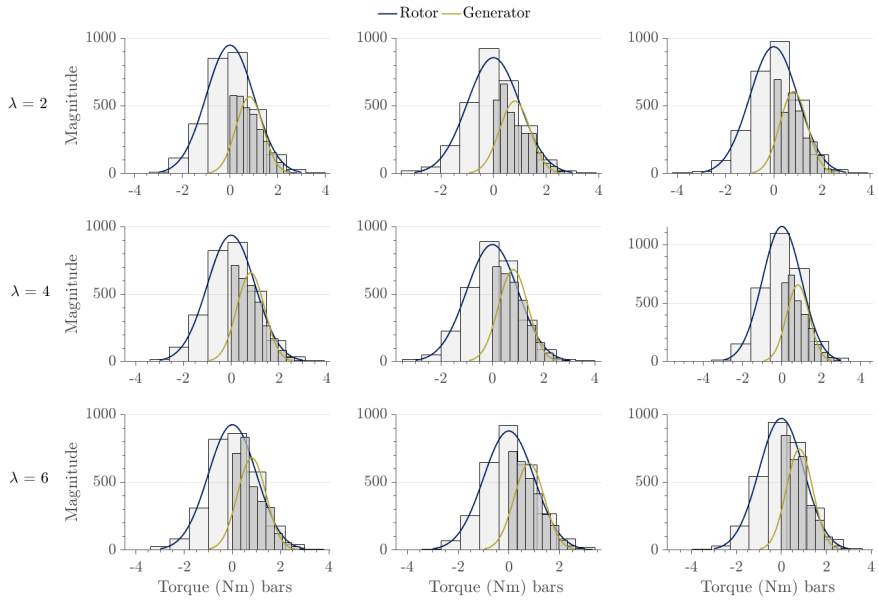

Figure 4.6: Histograms of 0.7 m diameter rotor and generator normalised torque signals for λ = 2,4 and 6.

λ values, despite the fact that data is not normally distributed. Finally, the histograms reproducibility on the rotor side matches again with the VOC configuration on the drive train test rig that demonstrates the effective rotor response to replicate the input theoretical values. A thorough analysis regarding the repeatibility and reproducibility of the simulations performed on the test rig are explained later in section 4.4.

4.3. Steady State Power Curves Results

As previously mentioned, C_p and C_θ curves were elaborated to determine the viability of reproducing scaled-HATT steady state conditions on a drive train test rig. By introducing the theoretical values of torque and rotational speed both recorded for 50 s at the IndraWorks interface from λ values of 1 to 7, both C_p and C_θ values were calculated using equations 3.2 and 3.4. Figures 4.8 and 4.9 display two C_p curves for turbine diameters of 0.7 m and 0.9 m respectively. Notice that the theoretical curve modelled

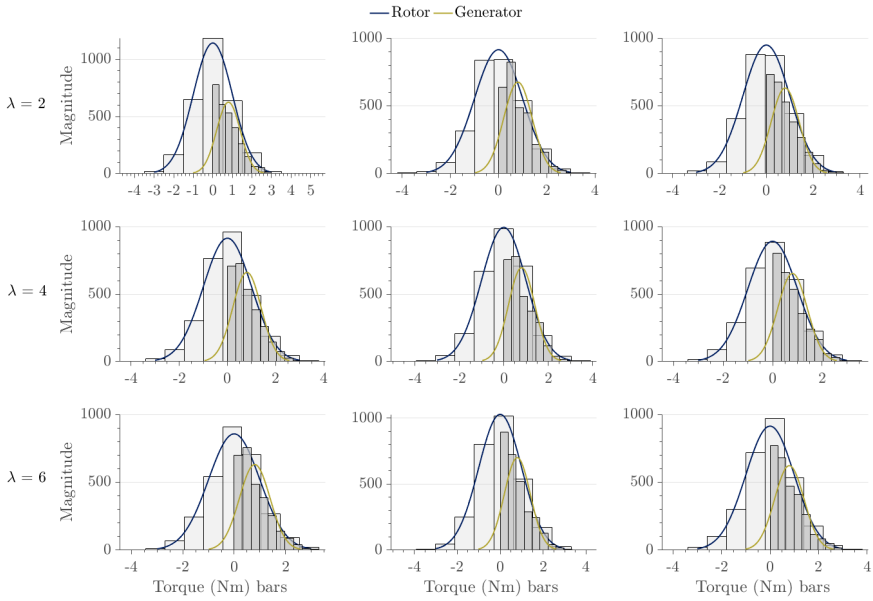

Figure 4.7: Histograms of 0.9 m diameter rotor and generator normalised torque signals for λ = 2,4 and 6.

from the experimental values obtained by Frost et al. [2015] is shown with a blue line, and they represent the C_p values neglecting Reynolds effects, but the torque, speed and power values changes in order to achieve the C_p value given the diameter size of the rotor.

The rotor response on the drive train test rig display a good agreement compared to the theoretical input. Moreover, the error bars on the rotor results illustrate the standard deviation, calculated as a factor of the recorded rotational speed and the torque values from the 50 *s* signals. The standard deviation values are found to be smaller in order of magnitude compared to the generator results. The latter coincides with the small standard deviation previously mentioned for the rotor simulations at λ =4. Notice that both rotor C_p in figures 4.8 and 4.9 represent the same non-dimensional values as expected. C_p = 0.45 and C_p = 0.46 were recorded at λ = 4 in both simulation scenarios of 0.7 m and 0.9 m respectively from the rotor power curves, highlighting the effective reproduction of a C_p curve on the rotor side of the test rig.

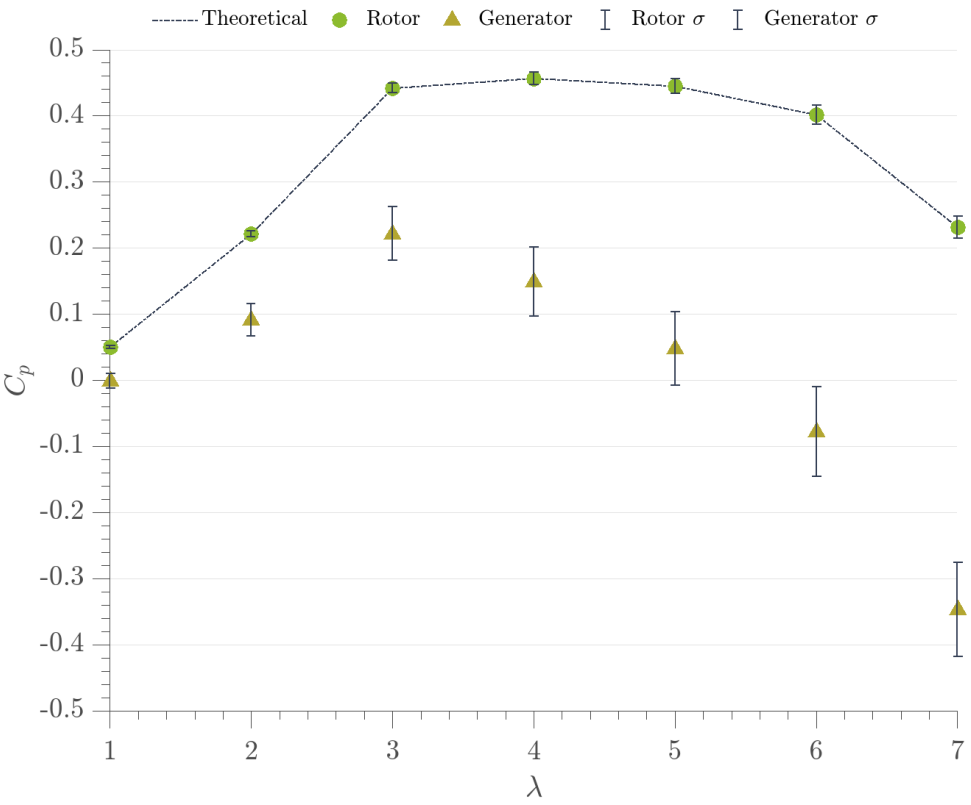

Figure 4.8: Power Curve comparison of theoretical values from CFD validated data, rotor and generator signals from the test rig for diameter 0.7 m.

However, it is evident that the generator output from both test scenarios have significant losses. Generator signal in figure 4.8 demonstrates less power losses from λ values from 1 to 3 compared to the set of λ values from 4 to 7. Additionally, standard deviation increases proportionally along with the λ operating points. Plus, it can be seen that C_p values after $\lambda = 6$ are negative. This was an expected output, as the gearbox decreases the torque magnitude by a factor of 10 as explained before, and torque values in the generator signal for a 0.7 m diameter test scenario is expected to be of values near 0, as detailed in table 4.1. Generally, this represents a power loss through all the λ operating points in the 0.7 m turbine diameter test scenario of 105%. Plus, a recorded C_p of 0.14 was reached on this test scenario for the generator signal at $\lambda = 4$. The latter is attributed to the low torque and high rotational speed interaction of the theoretical in-

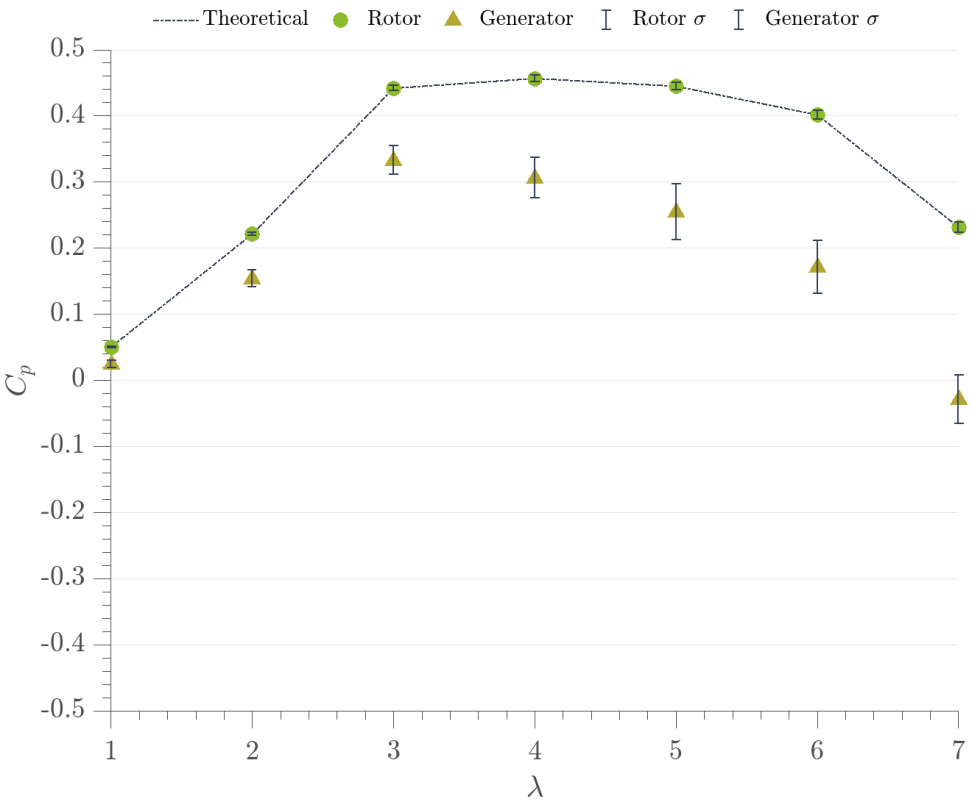

Figure 4.9: Power Curve comparison of theoretical values from CFD validated data, rotor and generator signals from the test rig for diameter 0.9 m.

puts in this scenario, when compared with the 0.9 m one. On the other hand, generator signal in figure 4.9 exhibits less losses when compared to the 0.7 m test scenario. Again, standard deviation and power losses are more evident after $\lambda = 4$ along with higher rotational speed values and smaller torque ones, but only the C_p value at $\lambda = 7$ was recorded as a negative value. Losses through all C_p curve is approximately of 50%. This could be also seen at the maximum C_p value reached on the 0.9 m test scenario at $\lambda = 4$ of 0.30. Still, non-dimensional values in both test scenarios differ from one another, due to the expected losses on the generator side.

The aforementioned can also be compared with the C_θ curves as shown in figures 4.10 and 4.11. C_θ values are higher when angular velocity is lower, and as soon the

angular velocity increases, C_θ values proportionally fall. An exception can be seen after 180 rads^{-1} in figure 4.10, where C_θ values increases again. Hence, it can be inferred that due to the high velocity and low torque interaction, torque values for rotor diameter of 0.7 m or below are less efficient and less accurate to replicate on the test rig. On the other hand, 0.9 m diameter C_θ curve falls onto the desired characteristic C_θ curve from the theoretical values, despite the low C_θ values obtained given the torque losses on the generator side, as seen in figure 4.11.

Clearly, both 0.7 m and 0.9 m turbine diameter test scenarios outline the expected generator losses. Yet, turbine 0.9 m diameter represented significantly less losses when compared to the 0.7 m diameter test scenario. Thus, it was decided to summarise the following simulations by considering only the 0.9 m diameter test scenario, to then rely on the next set of simulations considering other variations on the system. On the other hand, the aim of this first stage of this research was to replicate the HATT-scaled conditions on the test rig. Evidently, both figures 4.10 and 4.11 display the effective reproducibility of C_p curve and the C_θ curve in the 0.9 m diameter test scenario and it has been determined that both follows accurately the expected theoretical shape and data distribution across the λ values. The latter neglects the presence of generator losses, but rather leads to characterise them to be able to determine the repeatibility of power curves to then evince the test rig reliability for future complex simulation conditions.

4.4. Statistical Validation

After validating the test rig effectiveness to reproduce power curves, it is necessary to determine the generator reliability of replicating the theoretical input values. As a matter of practicality, the generator signals were compared each other three different times for the diameter turbine size of 0.9 m and only the three most important operating points through a power curve were considered. From the previous set of simulations, it is expected to obtain variability on the generator repeated signals due to the higher values of standard deviation when compared with the rotor signal. For this set of simu-

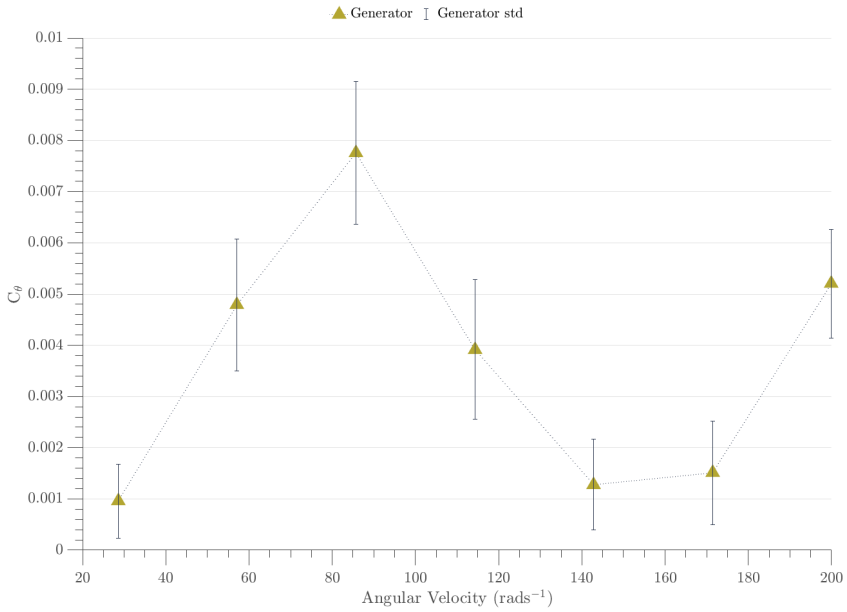

Figure 4.10: C_θ curve of generator signal for diameter 0.7 m.

lations, the λ values of 2, 4 and 6 will be again compared in terms of C_p and C_θ values to graphically represent the natural variability of the motor emulating a generator, to later consider a more thorough statistical analysis to review the reproducibility and repeatability of the process.

Figures 4.12 showcases the comparison within the theoretical C_p input values, the rotor test rig output and three repeated times of the calculated C_p values for λ = 2,4 and 6. Error bars are again utilised to visually define the standard deviation from each recorded simulation. It is observed that λ = 2 recorded the smaller range of standard deviations among the three different recorded times, and that the standard deviation grows proportionally with the λ values. Again, this was previously noticed in the first simulation of the power curve, since increasing the rotational velocity of the turbine drives the variation in the torque signal, that consequently leads to the variation in the non-dimensional values. Nevertheless, it is observed that the mean values of λ 4 and 6 are more consistent and repeatable than λ = 2. Specifically, it appears that λ = 4 is the one

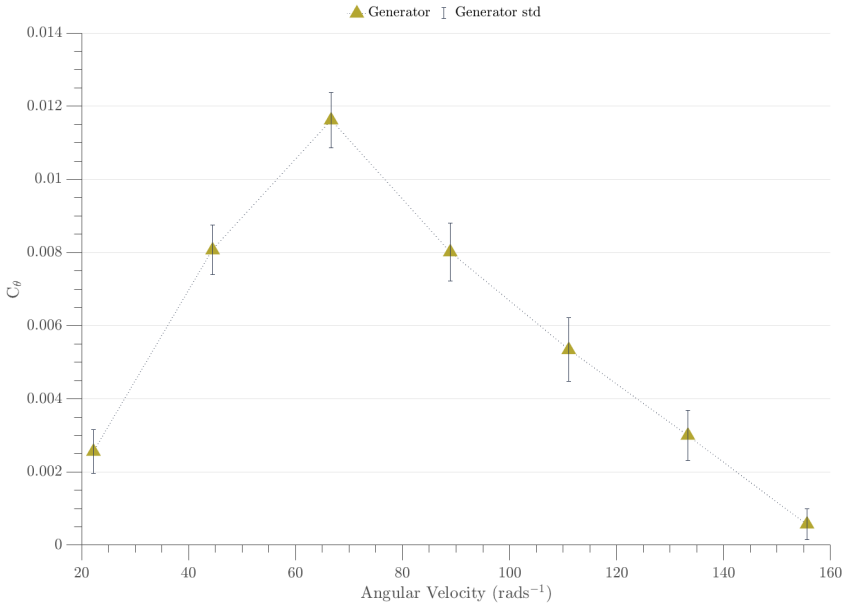

Figure 4.11: C_θ curve of generator signal for diameter 0.9 m.

with less variability compared to other λ values. This is a positive output, as normally the rest of the simulations would be expected to be run at the optimal operational control. Overall, the generator C_p values demonstrates a consistent reproducibility across the three selected λ values.

Different outputs were observed in figure 4.13 for $\lambda = 2$ when compared to the C_p curve. The generator does not clearly reproduce the C_θ value at its highest possible output, where mean values and the standard deviations are not as consistent as the rest of the λ values. However, it shows a better agreement when comparing the three recorded C_θ values in $\lambda = 4$ and 6, despite the increment of the rotational speed. The latter could be explained due to heating losses by forcing the motor emulated as the rotor to be ran at high torque values and repeat the process constantly, leading to a temperature increase in the generator side and consequently difficulties to repeat the input theoretical value. Still, these losses do not represent a drawback to the previously obtained results of these simulations, so it has been decided to conduct an ANOVA one-way test

to statistically determine the reproducibility of the generator signal in the drive train test rig.

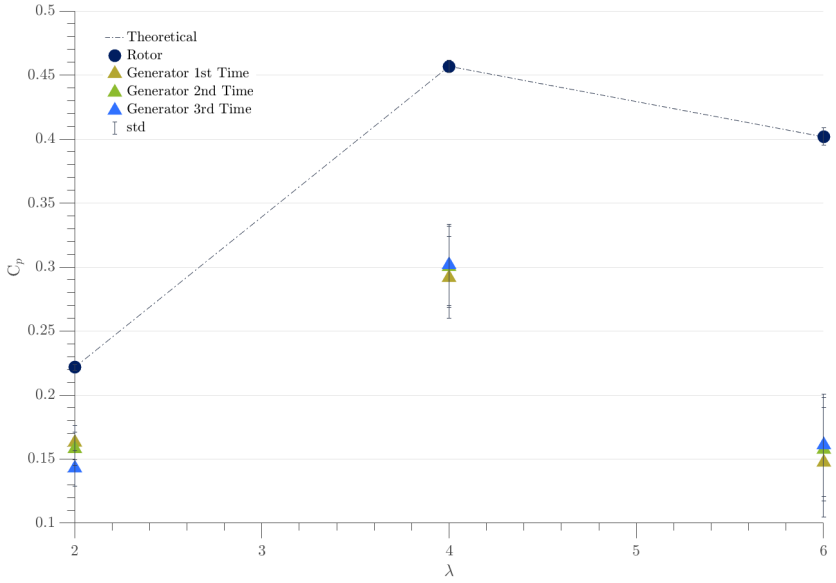

Figure 4.12: Power Curve for a diameter of 0.9 m, generator data repeated three times.

An ANOVA one-way test verifies that an hypothesis of a group means are the same, compared to an alternative hypothesis where it states that at least one group is different from the others [MathWorks, 2020a]. ANOVA is based on the assumption that all sample populations are normally distributed. It assumes that the residuals from the ANOVA model follow a normal distribution. From the previous set of simulations, it is expected to determine that the rotor signal satisfactorily demonstrate the repeatability of the data, whereas the generator may deliver a negative output on this test that need another level of statistical process to determine the type of distribution it follows. This simple statistical tool was decided to be used in order to compare the rotor and the generator outputs three different times, with $\lambda = 2$, 4 and 6 respectively. Hence, two hypothesis are formulated by:

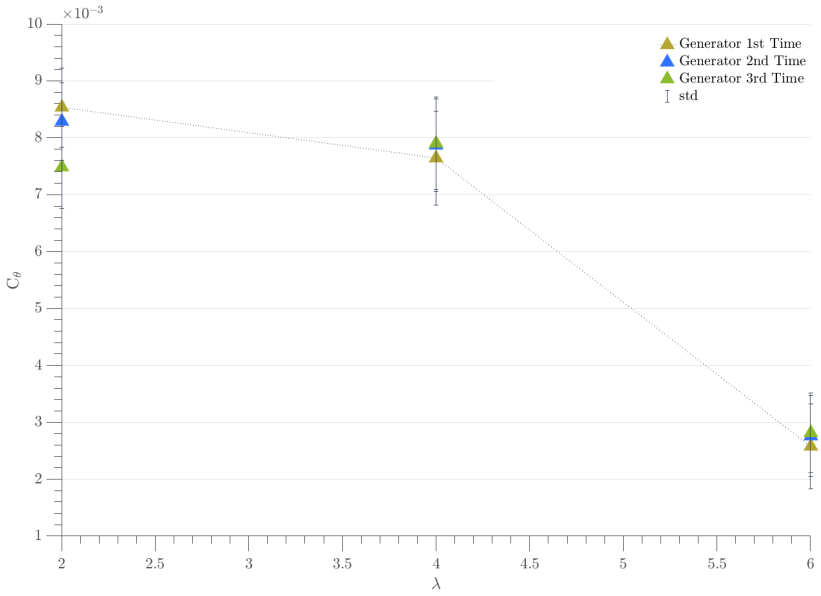

Figure 4.13: C_θ curve for a diameter 0.9 m. generator data repeated three times.

$$H_0 = a_1 = a_2 = a_3 \tag{4.3}$$

$$H_1 = \text{at least one group is different from the rest} \tag{4.4}$$

where a_i could be either the rotor or the generator C_p signals calculated as a factor of the torque and the rotational speed for both motors. If the null hypothesis, or H_0 is true, then the means within the three groups are the same, otherwise the alternative hypothesis (H_1) is accepted, meaning that at least one group mean of the ones being reviewed is different from the rest. In this case both the rotor and generator signals were tested against each other to review the reproducibility of the data. Firstly, it is needed to determine if the data is normally distributed. Relying on the first set of histograms obtained from the rotor and generator signals in figure 4.7, the rotor torque data at a first glance determined that it was following a normal distribution, whilst it is noticeable that the generator data was following a negative skewness in all the compared test scenarios. However, after applying equations 4.3 and 4.4 in MatLAB to the rotor C_p calculated sig-

nal, equation 4.4 was found to be true, hence determining that by applying these equations it is not completely determined whether the rotor and generator datasets follow a normal distribution or not. Therefore, it was decided to run a different test from the MatLAB Statistics and Machine Learning Toolbox, where a set of different techniques may determine again if the signals are following a normal distribution. The difference between running different tests on MatLAB comes from the number of points in a signal or in a sample size.

Among all the different options offered, the Lilliefors test was selected to be performed on these simulations [Lilliefors, 1967]. For this test, a significance level of $\alpha = 0.01$ was chosen. This indicates that there is a 1% risk of concluding that data is different when there is no actual difference. For this test, if the data is following a normal distribution, that means that the H_0 or null hypothesis is accepted. Otherwise, the H_1 is the correct one and data is not normally distributed. The Lilliefors test was conducted in this research three different times for λ = 2,4 and 6, and it was found that in all the different cases, data was following a normal distribution. Figures 4.14 and 4.15 show the normal probability distribution for C_p signals of $\lambda = 4$ for both the rotor and the generator respectively. It can be seen in both cases that the data points are relatively close to the fitted normal distribution line, and that only after approximately a probability of 0.01%, data does not fall onto the distribution line. Finally, given the acceptance of the null hypothesis for each λ value, an ANOVA one-way can be performed on each case to then review the reproducibility of the data.

The ANOVA one-way test was conducted by the author per each λ value as shown in figures 4.16, 4.17 and 4.18. These boxplots display the median values for both signals, and it can be seen that the rotor boxplots for the three λ values are more aligned compared to the ones from the generator signals that varies within three different times this was tested. Moreover, P_{value} indicates the likelihood of accepting H_0 for each case. If $P_{\text{value}} > \alpha = 0.01$, H_0 can be accepted, meaning that C_p signal is reproducible and reliable for future cases. If not, then H_1 is accepted, meaning that at least one of the groups is different from the rest. P_{values} in the rotor side are higher than $\alpha = 0.01$, meaning

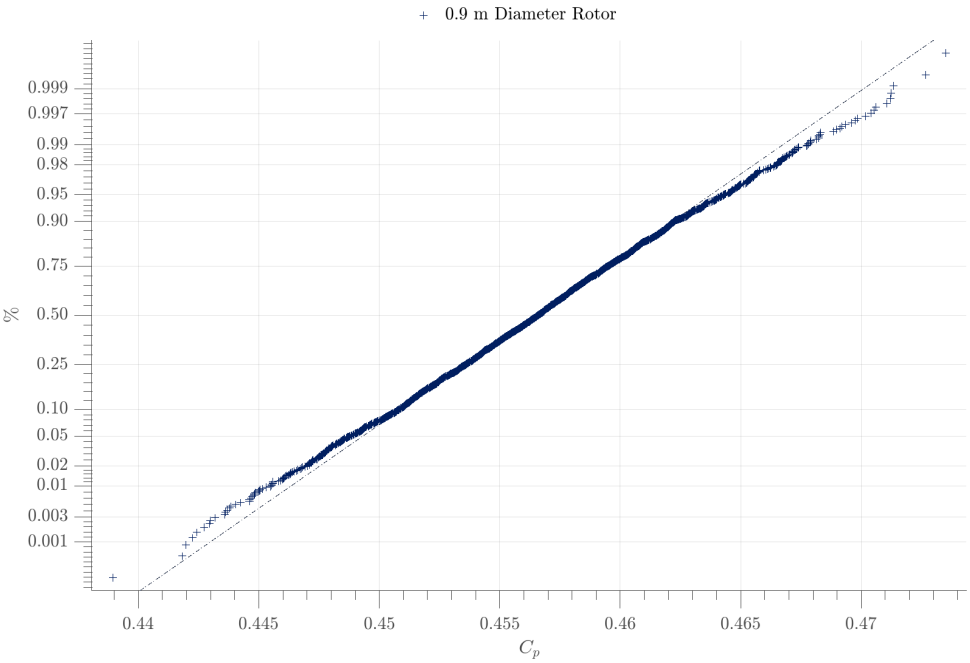

Figure 4.14: Normal Probability Distribution of the Rotor C_p signal for $\lambda = 4$.

that data is reproducible. However, the generator side fails to accept H_0, meaning that data is not reproducible at that significance level. The next step to review whether if the three compared test scenarios are different from one another or if it is just one case that differs from the three recorded signals was performed by the author utilising a MatLAB Statistics and Machine Learning Toolbox function.

In order to make a more in-depth analysis, a multiple comparison test in MatLAB was conducted on the generator C_p signals for $\lambda = 2$, 4 and 6. Multiple comparison tests are useful to review if there is a group that are not significantly similar than the others, hence it might be the cause to reject H_0 beforehand. If one group mean is significantly different from another their intervals are disjoint, otherwise they overlap. Generator signals groups for $\lambda = 2$ and 6 were found to be disjointed from one another, whilst $\lambda = 4$ was the one that found a significant overlap between group 2 and 3, as shown in figure 4.19, meaning that group 1 is the cause of H_0 rejection.

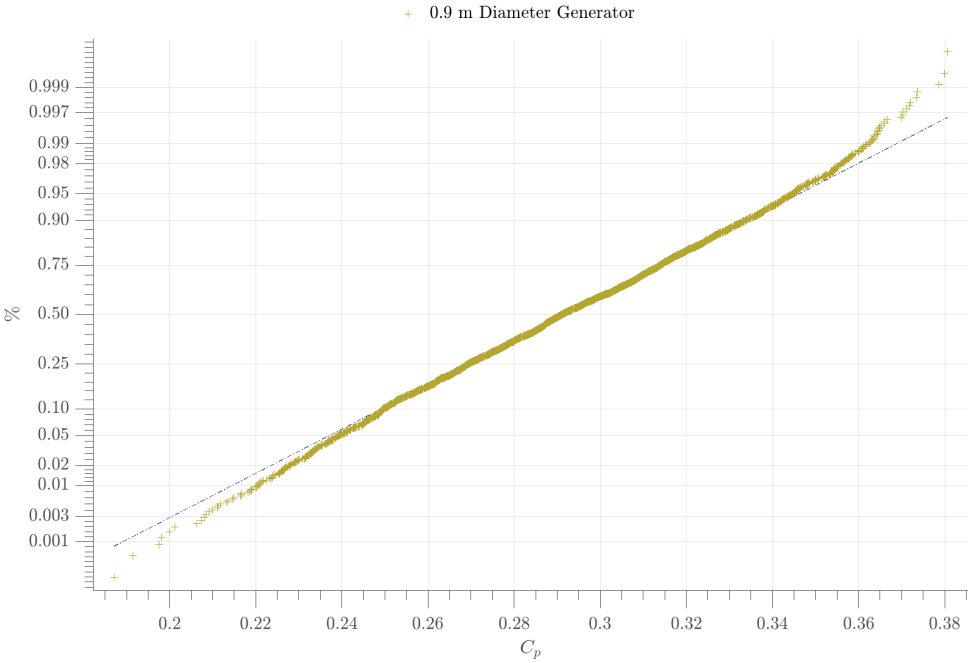

Figure 4.15: Normal Probability Distribution of the Generator C_p signal for $\lambda = 4$.

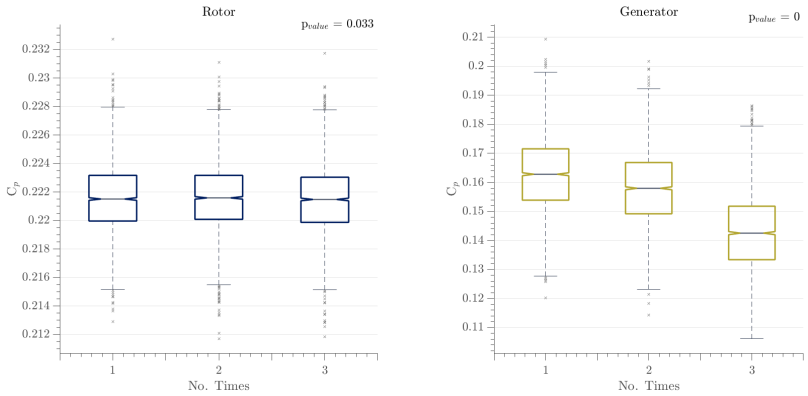

Figure 4.16: ANOVA ran three different times for $\lambda = 2$ in C_p rotor and generator signals.

Finally, the author decided to run a t-test to compare the data from group 2 and 3 of the generator signal of $\lambda = 4$ to review their reproducibility. T-test is similar than the ANOVA one-way test but it is meant to be used for only two group comparisons. Again, t-test was run with a significance level of $\alpha = 0.01$. A P_{value} of 0.09 was obtained, meaning

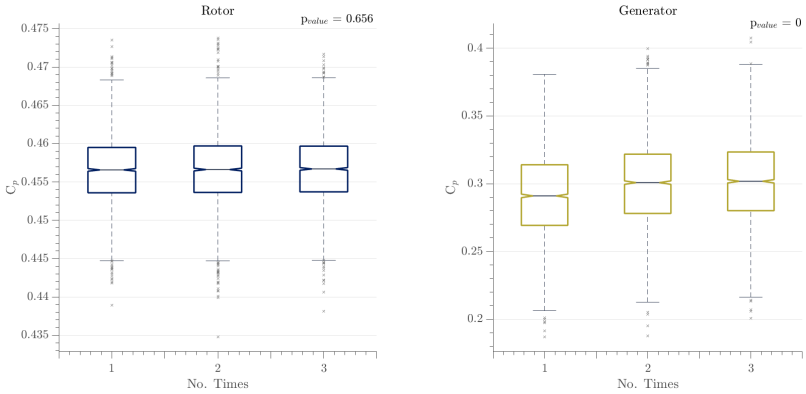

Figure 4.17: ANOVA ran three different times for $\lambda = 4$ in C_p rotor and generator signals.

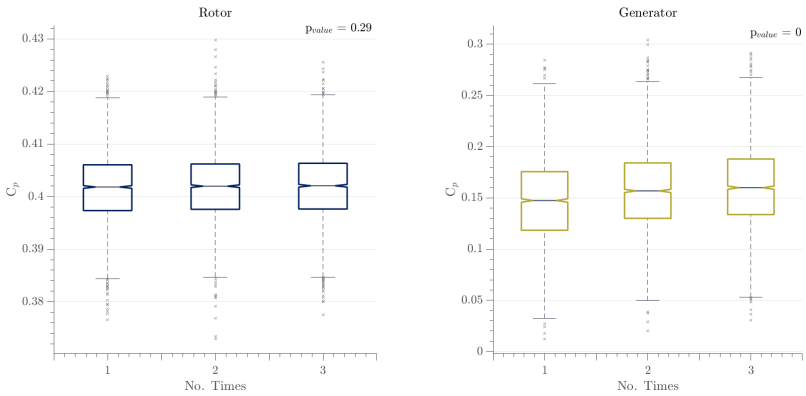

Figure 4.18: ANOVA ran three different times for $\lambda = 6$ in C_p rotor and generator signals.

that H_0 can be accepted and that data within these two groups are reproducible. This can be seen in figure 4.20, where both normal distribution figures overlap within one another. Overall, it can be concluded that the rotor C_p signals for $\lambda = 2$, 4 and 6 are reproducible and reliable to be run in different scenarios, whilst the generator signal in $\lambda = 2$ and 6 may not be statistically reproducible with a significance level of $\alpha = 0.01$, but $\lambda = 4$ can be reproducible and reliable for future scenarios. This is a positive output, as it is expected to utilise the further test rig operations at its maximum operational point and not necessarily at $\lambda = 2$ and 6.

Overall, by the results obtained in the steady state stage of this research, it was

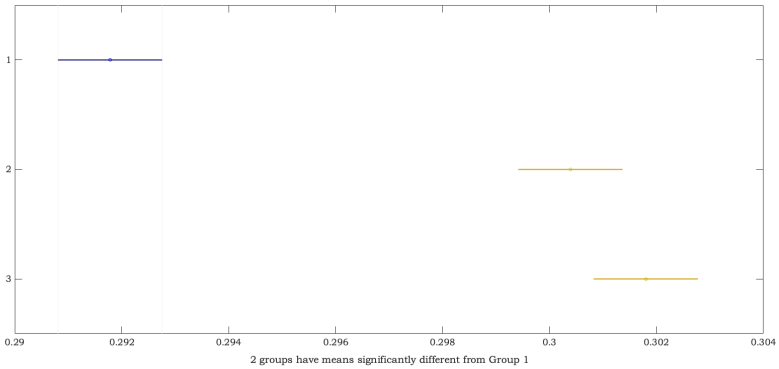

Figure 4.19: Multiple comparison test for Generator C_p signal for $\lambda = 4$.

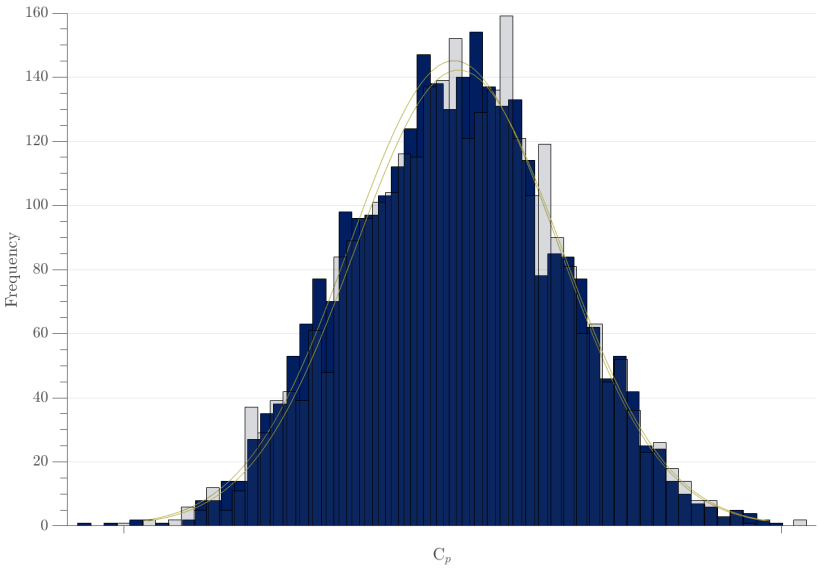

Figure 4.20: Normal distribution data of C_p signal for $\lambda = 4$ overlapped two times.

ascertained the flexibility of utilising the drive train test rig to reproduce HATT-scaled non-dimensional values, obtaining better results emulating a turbine size of 0.9 m than the simulations obtained from 0.7 m, hence the decision of utilising this turbine geometry for the future simulations. Also, it was determined that C_p and C_θ curves were able

to be replicated on the test rig, obtaining up to 50% losses on the generator side through the λ operating points. On the other hand, after a set of statistical methods performed, it was determined that both the rotor and the generator obtained signals when calculating C_p were following a normal distribution at $\lambda = 2$, 4 and 6, yet only $\lambda = 4$ was able to statistically reproduce the generator signals 2 times by performing an ANOVA t-test. This last aspect was crucial for the determination of the generator simulations reliability, to then add more complex variables onto the system and focus on the analysis of those variables only in the future.

5

Rotor Imbalance Fault Condition

This chapter describes the results obtained from a flow tank testing conducted by CMERG in 2019, where three different turbines were evaluated to characterise non-dimensional curves over a range of differing operating points. Then, section 5.2 presents the outputs of analysing the frequency content of the torque and thrust datasets, where an alteration was found in one of the turbines. The CM algorithm building process is outlined in section 5.5, by adapting a technique to extract frequency related data in the given signals and adapt a statistical tool to detect possible rotor based failures. Finally, a validation stage was undertaken to determine the CM algorithm effectiveness in the given experimental data. The results are presented in section 5.5.

5.1. Flow Tank Testing

CMERG has been conducting experimental research to study the effect of torque and speed controls on TSTs and to individually characterise three HATTs. These three devices were built in order to understand the dynamic loading of HATTs singularly as well as in array configurations. These three devices manufacturing were a result of the validation of HATT performance characterisation from the IFREMER testing campaign in 2018. After the 0.9 m diameter turbine was validated, CMERG decided to develop two more turbines that were utilised in this testing campaign. The details of the 0.9 m diameter turbine can be found in chapter 3. Furthermore, these last generation set of turbines were constantly improved, from increasing the turbine diameter from 0.5 m to 0.9 m to enhance the fitted instrumentation. A Wortmann FX 63-137 blade profile has been used by CMERG continuously and has been tested numerically and experimentally [Allmark et al., 2020]. For this set of tests the pitch angle for each blade was set to 6.2° ± 0.5°.

One of their most recent test campaigns was performed on the KHL at Strathclyde University in Glasgow, UK in February 2019 [Allmark et al., 2020]. The experimental data was collected on a 76 m x 4.6 m x 2.5 m tow tank, as shown in figure 5.1. The purpose of this test campaign was to compare the performance of three different turbines in three different facilities under several different control strategies and variations. Data was captured by rotor torque and thrust transducers and the PMSM winding current measurements. Data was captured with a sample rate of 2000 Hz for 50 *s*, but for the purpose of this analysis the turbine acceleration data was omitted, hence giving a total recording signal of 30 *s* per each case. A figure of one of the tested turbines on the flow tank is shown in figure 5.2.

Turbines T1, T2 and T3 were individually set in the test facility to obtain the characteristic non-dimensional curves and to determine two different control strategies. Both torque and speed controls were undertaken during the KHL campaign testing but for the purpose of this analysis, only speed control was taken in consideration. In ad-

Figure 5.1: Tow tank at the KHL at Strathclyde University.

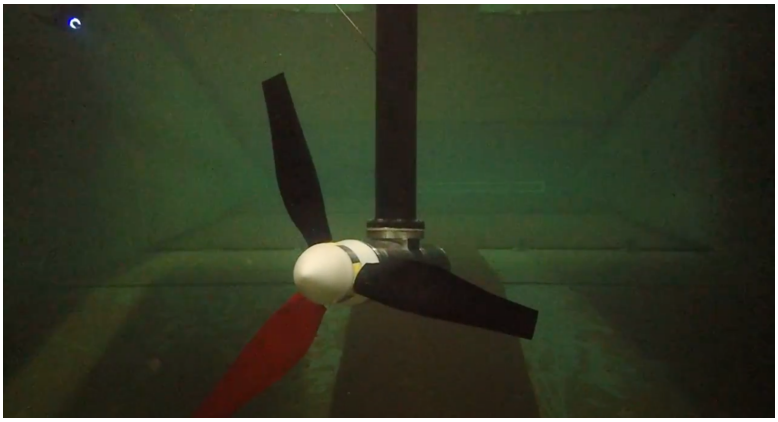

Figure 5.2: One of the CMERG HATTs being tested at KHL.

dition, the author decided to define 0.8 ms^{-1}, 1.0 ms^{-1} and 1.2 ms^{-1} as the three set of steady carriage velocities to compare. Also, λ operating points of 0, 1.5. 2.5, 3, 4, 5 and 6.5 were considered in order to compare the rotor and motor measurements. The author in the undertaken set of experiments clarified that due to time restrictions, the team was unable to test T1 for velocity 1.2 ms^{-1}, therefore this set of experiments was omitted for this analysis. Characteristic power, torque and thrust curves were obtained from the

	T1		T2			T3		
Velocity (ms^{-1})	0.8	1.0	0.8	1.0	1.2	0.8	1.0	1.2
Max C_p	0.46	0.47	0.48	0.48	0.48	0.46	0.47	0.46
Max λ @ C_p	3.97	3.99	3.99	3.99	3.49	3.99	3.5	3.49
Max C_θ	0.15	0.15	0.16	0.16	0.16	0.15	0.16	0.16
Max λ @ C_θ	2.49	2.5	2.49	2.49	2.5	2.49	2.5	2.5
Max C_T	1.04	1.04	1.09	1.09	1.05	1.09	1.08	1.06
Max λ @ C_T	4.99	6.49	6.49	6.49	6.49	6.49	6.49	6.49
Max Power (W)	75.63	150.04	78.63	152.94	265.51	76.22	151.12	255.8
% Power Losses	18.48	13.19	16.02	13.94	12.01	18.54	15.96	14.04
% C_θ Losses	11.51	11.25	16.15	14.31	12.12	17.3	15.11	13.33

Table 5.1: Table providing an overview of peak non-dimensional quantities, power and motor torque and power losses across the 3 different turbines and velocities in analysis.

available data, as shown from figures 5.3 to 5.5 respectively. In addition to the latter, table 5.1 shows the peak non-dimensional values obtained for turbines T1, T2 and T3 under the three different steady carriage velocities.

A comparison was made between the raw and non-dimensional values of the torque, thrust and power developed by three turbines and under three different velocities. The non-dimensional coefficients were calculated using equations 3.2, 3.4, and 3.3. Equally, power and torque, along with the non-dimensional coefficients, were calculated using the measured PMSM winding currents, as explained in chapter 3. As it is described in table 5.1, the peak values of C_p, C_θ and C_t and their respective λ were constantly repeated across different velocities and turbines, with a standard deviation of 0.0093, 0.0052 and 0.022 respectively. The highest power was achieved in T2 under a steady carriage velocity of 1.2 ms^{-1} and with a C_p value of 0.48. As expected, the peak λ value for C_p, C_θ and C_t were 4, 2.5 and 6.5 respectively. There was an exception found in T1 with a velocity of 0.8 ms^{-1} in the C_t coefficient compared to T2 and T3 where the

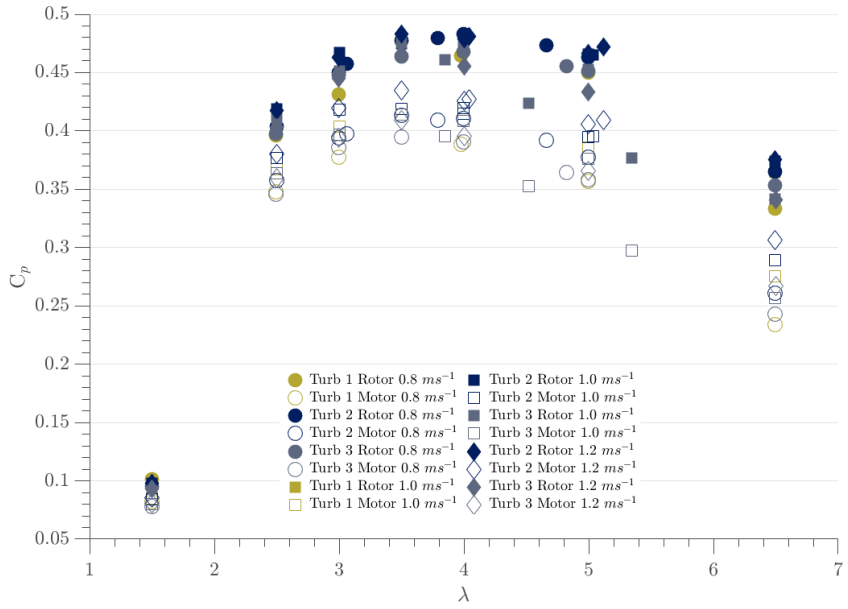

Figure 5.3: Characteristic power curves obtained from the KHL tests for each of the three turbines. The figures show both the power curves obtained considering rotor transducer measurements and motor power measurements.

thrust peak was found at λ of 6.5 and in T1 λ was of 5. This occurred due to the increasing rotational velocity after λ of 4, and the small difference in mean C_t values due to the thrust loading stall.

In addition to the table analysis, figures 5.3 to 5.5 show the power, torque and thrust curves respectively. All curves display a good repeatibility across the three different carriage velocities and the three different turbines. Still, power curve shows a higher dispersion and variability in the motor transducer measurements compared to the rotor data as rotational velocity increases, especially between 2.5<λ<6.5. This is due to the rotor velocity dependency in the power calculation explained in chapter 3. On the other hand, there are losses on the motor power measurements compared to the values from the rotor transducer measurements. Furthermore, it has been found that the higher losses between the rotor and motor transducer measurements were of 20% in

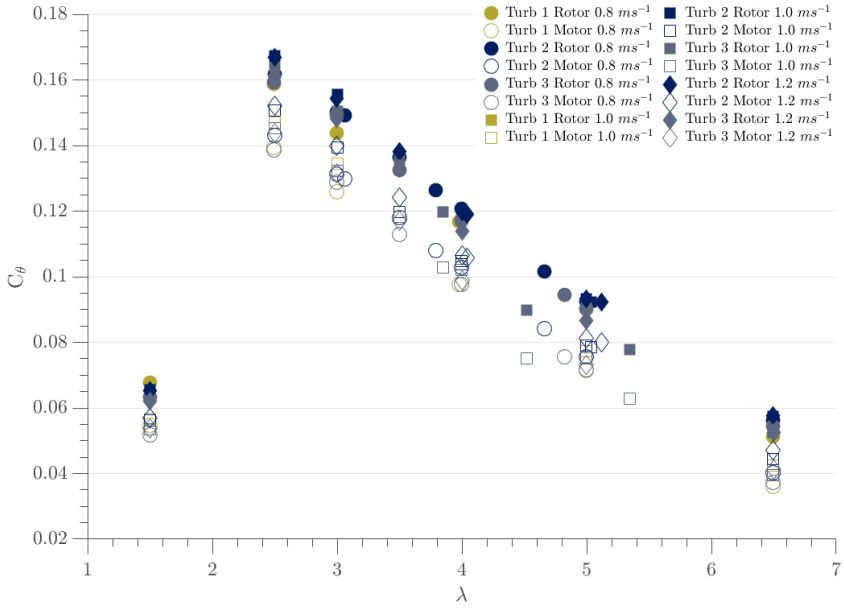

Figure 5.4: Characteristic torque curves obtained from the KHL tests for each of the three turbines. The figures show both the torque curves obtained considering rotor transducer measurements and motor power measurements.

velocity 0.8 ms^{-1}. The latter may be attributed to the fact that the motor current measurements noise in the power production dominates the control functions in no level turbulence set of simulations. Still, the presence of this losses were expected, therefore does not affect the purpose of building a condition monitoring approach.

On the other hand, figure 5.4 demonstrates that there are less losses and variability between the torque rotor and motor data compared to the power measurements figure. This is because of the less variability found in the rotor transducer based values compared to the motor current measurements. The peak C_θ value of 0.16 was repeated across all three velocities and three turbines, and constantly repeated in all simulations with a λ of 2.5. Again, higher losses were found at turbines T2 and T3 with a carriage velocity of 0.8 ms^{-1}. Similarly, figure 5.5 displays good agreement for non-dimensional thrust coefficients with minimal scatter data between the different simulations. A maxi-

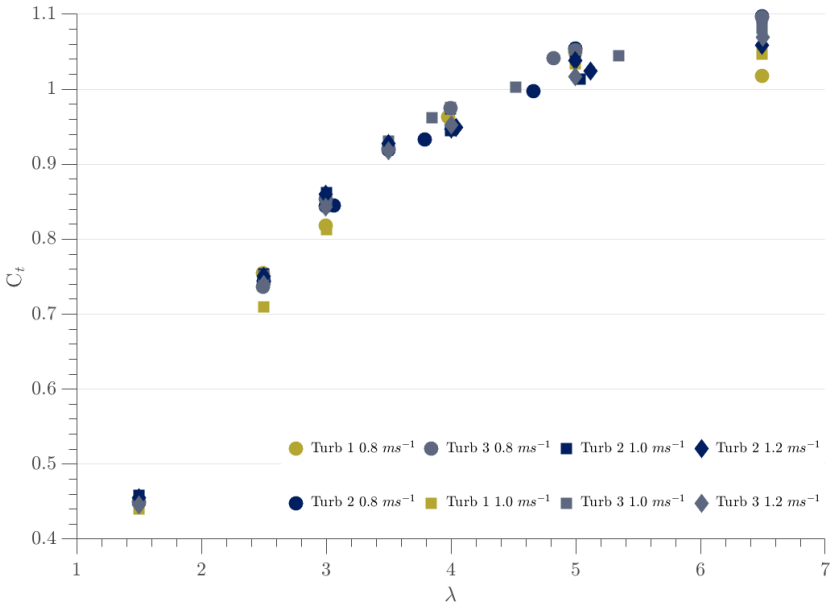

Figure 5.5: Characteristic thrust curves obtained from the KHL tests for each of the three turbines. The figures show both the thrust curves obtained considering rotor transducer measurements and motor power measurements.

mum C_T was observed at λ of 6.5. The author confirms in [Allmark et al., 2020] that the latter proves the high repeatibility in the blade pitch angle setting. The aforementioned analysis conducts to demonstrate the data reliability in terms of turbine performance in order to obtain the mean values that would allow the condition monitoring approach development that has been suggested on this thesis.

5.2. Signal Monitoring

In order to develop a condition monitoring algorithm, the torque, power and thrust signals were monitored. As previously seen in figures 5.3 to 5.5, the mean values per each λ demonstrates a good agreement across the power, torque and thrust characteristic curves. However, by analysing these curves only it will be unfeasible to mon-

itor the turbine conditions through different flow speeds and/or different λ values, and hence to inform of any fault detection. The latter since according to the previous set of simulations that was analysed, there was minimal variance found that could lead to determine there may be a fault within these datasets, plus there is no record of the fault size estimation nor the severity of the fault. Therefore, based upon the research of the author, confirmed by the literature, it has been determined that a more robust condition monitoring technique needs to be developed using other tools, such as analysing the frequency content of a signal or a time series. Hence, it was thought that the signals that should be monitored are the torque, thrust and power transients in a time domain analysis to determine if there are some components that may be useful to build a CM algorithm.

Figures 5.6 and 5.7 compare the rotor thrust and torque time series for T1, T2 and T3 respectively for a λ = 4 and velocities of 0.8 ms^{-1} and 1.0 ms^{-1}, while figure 5.8 showcases the motor torque signal for the aforementioned turbines and velocities. As previously explained, velocity 1.2 ms^{-1} was omitted from this analysis since there is no data from T1. Data in all cases was windowed five times from the total time length and overlapped altogether, giving a total of 30 s time series per each case. This was decided to be presented accordingly in order to find similarities in the time series and identify any possible cyclical pattern that may arise the possibility of finding further irregularities in the signals. The overlapped time series are shown in a gray scale colour. The mean values of the windowed time series are shown with their respective colours. In addition to this, table 5.2 shows the mean values and the standard deviation of the motor and rotor torque and thrust signals for all the cases for a λ = 4.

From table 5.2 it can be deduced that the thrust in T1 is higher in steady carriage velocity of 0.8 ms^{-1} compared to T2 and T3 by a difference of 15 N. Still, thrust in T1, T2 and T3 for velocity 1.0 ms^{-1} is very similar. On the other hand, thrust standard deviation for both velocities in T1 is larger than the ones in T2 and T3. This exhibited thrust variation in T1 may be caused by different factors, including measurement noise or potential rotor imbalance. The latter could also be presented due to a variety of rea-

	T1		T2		T3	
Velocity (ms^{-1})	0.8	1.0	0.8	1.0	0.8	1.0
Rotor τ (Nm) @ λ=4	10.7	16.88	11.06	17.20	10.72	16.99
Rotor τ σ	0.37	0.49	0.35	0.55	0.35	0.44
Motor τ (Nm) @ λ=4	8.9	14.84	9.4	15	8.94	14.6
Motor τ σ	0.37	0.52	0.42	0.57	0.44	0.52
Rotor F (N) @ λ=4	213	310.3	198.3	309.7	198.43	310.08
Rotor F σ	10.88	10.41	4.13	5.66	3.97	4.83

Table 5.2: Table providing an overview of motor and rotor torque and thrust across the three different turbines and velocities in analysis at λ=4.

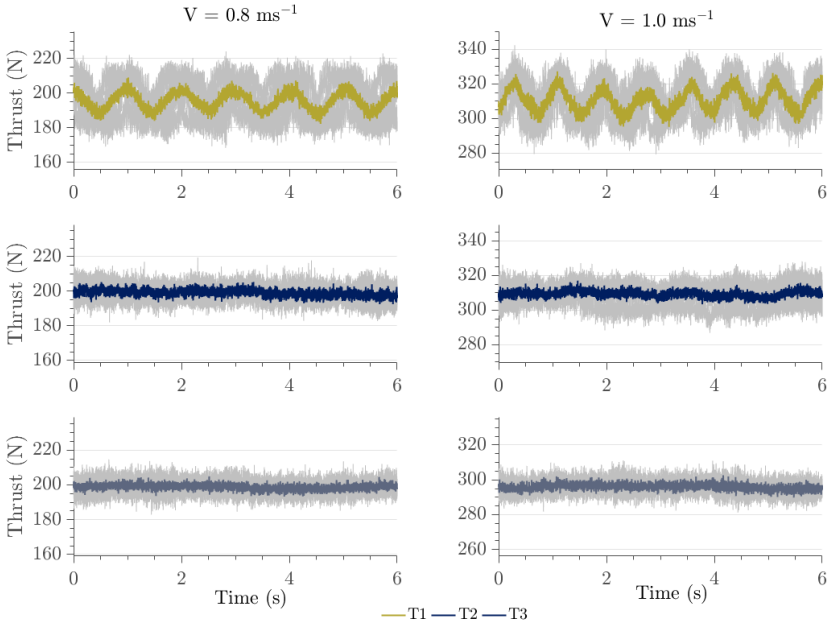

Figure 5.6: Rotor thrust data signals for T1, T2 and T3 at flow velocity of 0.8 ms^{-1} and 1.0 ms^{-1} windowed five times from the total time length and a mean value was calculated from all the iterations.

sons, including pitch misalignment, blade damage, blade offset setting,rotor damage, etc. Along with monitoring the mean and standard deviation values, figure 5.6 demonstrates that the rotor signal from T1 has a clearer cyclical pattern compared to T2 and T3 for both velocities. Particularly for velocity 1.0 ms^{-1}, even though the mean values are

similar in all three turbines, T1 presents the same cyclical and noisier pattern compared to T2 and T3, whereas the rest of the cases the signals are more stable and stationary than the ones presented in T1.

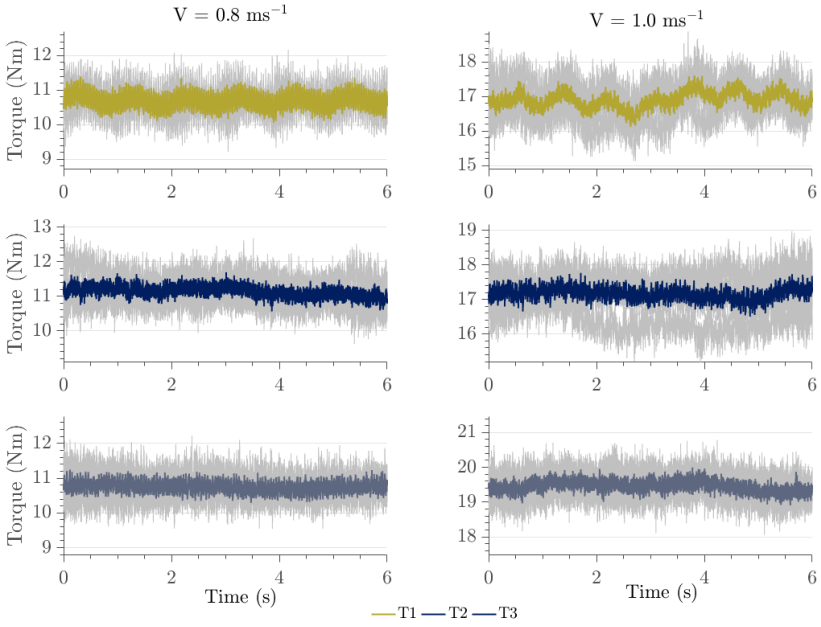

Figure 5.7: Rotor torque data signals for T1, T2 and T3 at flow velocity of 0.8 ms^{-1} and 1.0 ms^{-1} windowed five times from the total time length and a mean value was calculated from all the iterations.

On the other hand, torque values do not differ among the mean nor standard deviation values across the three turbines as shown in the thrust values. Likewise, the same behaviour has been found comparing the motor and rotor torque values, despite the fact that there are losses of about 20% as previously mentioned. However, figure 5.7 demonstrates that again, there is a repeated cyclical pattern as in the thrust figures in T1 compared to T2 and T3. Although this cyclical pattern is more evident in the thrust signal, the rotor torque variation in T1 is evident when compared with T2 and T3 for both velocities. However, this cyclical pattern found in both the thrust and rotor torque signals is not clear in the motor torque signals, as it can be seen in figure 5.8. Therefore, it can be deduced that there is data loss through the turbine driveshaft as the torque signals from the rotor and motor differ from one another, and this could lead to a further

analysis in order to build a CM algorithm that will be useful to utilise in both driveshaft components. The latter is also being replicated in chapter 4, where it is evident that the generator on the test rig had losses due to the gearbox interaction and heating losses.

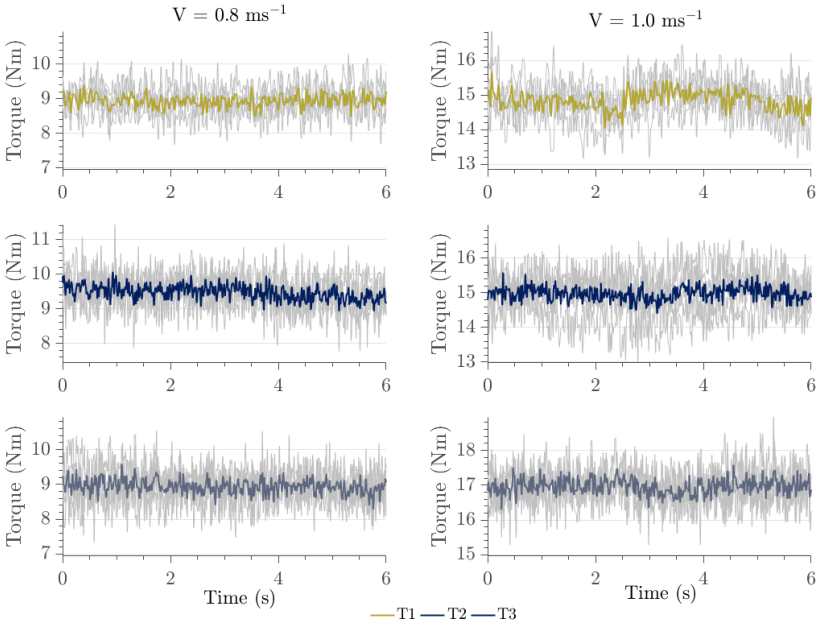

Figure 5.8: Motor torque data signals for T1, T2 and T3 at flow velocity of 0.8 ms^{-1} and 1.0 ms^{-1} windowed five times from the total time length and a mean value was calculated from all the iterations.

As it has been previously determined in [Ordonez-Sanchez et al., 2017, Allmark et al., 2017], major faults can occur to tidal stream turbines due to blade offsets or a pitch misalignment that would lead to unsteady loading in the rotor, that subsequently could cause further turbine damages. So far these potential faults have been defined as rotor imbalance, which is a common fault detected in the wind industry. It could be defined as when all the forces in a rotational machine are not aligned in the centerline, therefore it causes and offset rotation and produces signals such as the ones previously observed in this section[Mobley, 2001]. It must also be noted that the associated rotor imbalance leads to increased stress on the turbine system via the introduction of speed and torsional fluctuations [Hyers et al., 2006]. According to Kusnick et al. [2015], Cacciola et al. [2016], rotor imbalances are due to:

- uneven mass distribution in the rotor blades
- non-uniform accumulation of dirt
- blades damages
- excess material from manufacturing becoming loose and moving toward the blade tip during rotation
- manufacturing defects

The latter matches to the analysis previously made from the KHL testing, confirming that there is an alteration to the data output in both the rotor torque and thrust signals. According to Allmark et al. [2020], the expected results were successfully obtained monitoring the blade root bending moments for each steady carriage velocity. A possible cause to explain the rotor imbalance was not identified. It was possible that the blade pitch angle setting was incorrect, or some variation in surface finish or rotor thrust bearing setup that caused the unsteady signals obtained. It can be stated that similar eccentric loading has caused greater damages to wind turbines [Ma et al., 2018]. The cause of the imbalance was not seen as being important, but the consequences of the imbalance in the rotor are the acceleration of the degradation of the transmission components (bearings, shafts, gear teeth) [Hübner et al., 2021]. These findings would require a further analysis to determine if a rotor imbalance CM algorithm could be potentially built from these and if it could be replicated in a drive train test rig.

5.3. CM algorithm building process

In order to detect a rotor imbalance fault, it has been already determined that by only monitoring the characteristic power, thrust and torque curves, it would be unfeasible to detect an irregularity in tidal stream turbines. Similarly, by only monitoring the mean and standard deviation of the given variables, there were no outcome findings to establish an alteration across the different turbines and steady carriage velocities. Yet, by analysing time series datasets, it has been proven that irregularities have arisen from

the torque and thrust signals in T1 compared to T2 and T3. Therefore, in order to scrutinise the previous performed analysis, by undertaking a time and frequency domain analysis to understand the behaviour of these signals, it could potentially lead to develop a CM algorithm that could be adapted to different conditions. The latter has been severely utilised before in the wind industry, and has been previously used to predict rotor imbalance faults in tidal stream turbines by Tavner [2017], Grosvenor et al. [2014], and Mullings et al. [2017]. Other techniques have been used to detect faults in tidal turbines, such as using BEMT or CFD in order to model the rotor imbalance as it was performed in [Ordonez-Sanchez et al., 2017], or installing sensors that could read the vibration in the rotational frequency of tidal turbines as developed in Grosvenor et al. [2017] and Duhaney et al. [2011].

Developing a CM algorithm to detect a fault condition in the rotor by using a drive train test rig was chosen among all options given the cost-effective and less-time consuming considerations compared to the other techniques. Moreover, test rig simulation and measurement will provide an opportunity to simulate failures and validate the CM algorithm to be able to validate and control it in repeatable conditions, thereby closing the first development loops within the design phase and helping to save cost and reduce risk. As previously mentioned, the utilised drive train test rig was adapted and characterised by Allmark [2016], yet for the purpose of this study rotor imbalance was detected from experimental data during the KHL testing, and the aim will be to continue analysing the data in order to replicate the fault under different loading conditions and determine how to detect it.

The following steps have been defined in order to determine the CM algorithm building process:

- Study the frequency content of the signals
- Formulate a technique to extract the most characteristic feature in a time-domain signal
- Adapt a simple tool to be utilised under different tidal loading conditions

- Conceptualise faulty conditions in a tidal turbine to be implemented on a drive train test rig to check the CM algorithm effectiveness
- Determine the variables and different scenarios to be studied to implement the CM algorithm in the drive train test rig
- Obtain the results from the defined simulations and prove whether the CM algorithm application under faulty conditions was successfully adapted

Following the first step on this process, using conventional techniques, such as the fast Fourier-transform and the power spectral density previously defined in chapter 3, are powerfully capable of analysing non-stationary signals. By using the frequency domain analysis and processing the data spectrum applying the mean turbine rotational velocity for each given dataset, the data harmonics can potentially provide rotor fault indication metrics. The spectral representation of a stationary time series, or its spectral density, is obtained by the Fourier transform of the auto-correlation function of a given signal. The power spectral density of a signal is useful to understand the loading force of a large sinusoidal component with a particular frequency and ensure that is not a resonant frequency of a given signal [Brockwell and Davis, 2002].

As previously mentioned in section 3.4.3, the κ defines the energy per unit frequency and it is utilised to understand the distribution of the energy over a range of frequencies or wave numbers (PSD). Therefore, for the purpose of this analysis, the energy spectral density was calculated using the 'pwelch' function in MatLAB. The aforementioned results of the analysis are shown in figures 5.9, 5.10 and 5.11.

In order to find the dominant amplitudes in the signals and to be able to understand the rotor behaviour, the detection of the harmonics by utilising the Fast-Fourier transform is needed. The frequency domain representation in terms of the energy content of x times the rotational frequency of the turbine in Hz is represented by $f = \frac{V}{60}$, where V is the rotor velocity in RPM. It has been determined that the 1^{st} harmonic or $f/f_0 = 1$ that happens once per revolution represents an imbalance of the turbine setup, whilst the 3^{rd} harmonic or $f/f_0 = 3$ represents the three blades passing the turbine stan-

chion, or an entire turbine revolution. In order to find the latter, the following equation can be implemented:

$$f/f_0 = interp1(fs, fft, f*S, 'nearest') \tag{5.1}$$

where fs is the sampling frequency to obtain the Fast-Fourier transform of fft, and S = 1, 2 or 3 to obtain the 1st, 2nd and 3rd harmonic respectively.

This particular analysis was previously implemented by other researchers, where they have concluded that the spectral energy content and its dominant amplitudes could determine aero/hydrodynamic behaviour. In [Deskos et al., 2020], the authors considered the spectral behaviour of turbulence-driven power fluctuations in a HATT during a experimental campaign at IFREMER, under the influence of different λ values. Herein, it was determined that a potential shift of the peaks away from the f/f_0 = 3 would mean that one of the blades passing the turbine stanchion exhibits a different aero/hydrodynamic behaviour either by design or control. Similarly, Durán Medina et al. [2017] studied the correlation between the flow turbulence and the HATT performance by utilising an Empirical Mode Decomposition to zoom into time-frequency scales where the flow induced some modifications in power production. They determined that there were two significant spikes at f/f_0 = 1 and f/f_0 = 3 in both the torque and thrust PSDs, assigning it again to the blade pass frequency. Finally, Fernandez-Rodriguez et al. [2014] measured the time-varying thrust in a HATT under the influence of turbulent flow and waves in a flume tank. Again, f/f_0 = 1 was denoted as the rotor frequency and f/f_0 = 3 as the natural frequency of the support structure. Finally, an approach designed by Hübner et al. [2021] by utilising the generator currents and voltages to build a Support Vector Machine algorithm to detect rotor imbalance faults was deployed, and it was determined that a peak in the PSDs data was replicated at different levels of imbalances at 1p of the rotational frequency of the simulated wind turbine. Given all these similarities in the literature, this approach was undertaken in order to previously detect any possible high amplitudes at the frequency energy content of both torque and thrust signals, and lastly to formulate a technique to extract rotor behaviour

metrics to possibly determine a condition-based maintenance tool.

5.4. Torque and Thrust frequency content

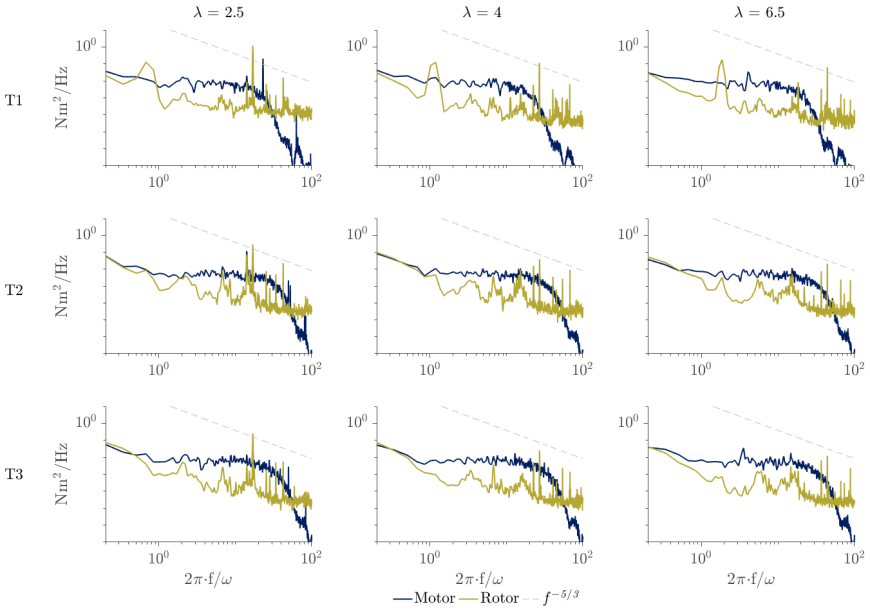

Figure 5.9: PSD of the rotor and motor torque data signals for T1, T2 and T3 at flow velocity of 0.8 ms^{-1} for λ = 2.5, 4 and 6.5.

Figures 5.9 and 5.10 display the PSD of the torque in both the rotor and motor signals for turbines T1, T2 and T3 for λ = 2.5, 5 and 6.5 for velocities 0.8 ms^{-1} and 1.0 ms^{-1} respectively. Also, a $f^{-5/3}$ trace was depicted in each figure with a dashed line, in accordance to Kolmogorov's theory, previously explained in chapter 3. Both the rotor and the generator PSDs exhibit a tendency towards the $f^{-5/3}$ slope, mainly at a portion of the inertial subrange, found at frequencies 1 <$2\pi\cdot$ f/ ω < 10. Still, the generator PSDs show a deviation from the dashed line after $2\pi\cdot$ f/ ω =12. However, it is not the purpose of this research to fit a proper spectral gradient to represent the linear portion of the measured spectrum, but to effectively obtain the torque and thrust energy content from $f / f_0 = 1$.

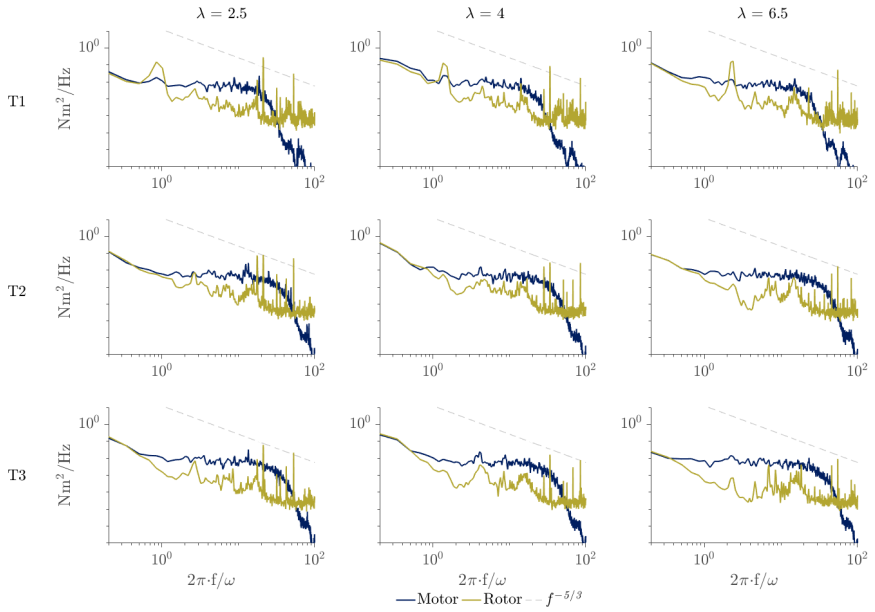

Figure 5.10: PSD of the rotor and motor torque data signals for T1, T2 and T3 at flow velocity of 1.0 ms^{-1} for λ = 2.5, 4 and 6.5.

By delimiting the analysis only to the lower frequencies and yet the higher energy content in both figures, it is very clear that there is a high peak constantly repeated in T1 around 10^0, or $f \cong 1.5\ 2\pi \cdot f/\omega$. In both 0.8 ms^{-1} and 1.0 ms^{-1} scenarios, the rotor signal show higher energy levels compared to the motor ones. Still, 1.0 ms^{-1} scenario yielded the high peak in all λ cases, whereas in the 0.8 ms^{-1} scenario the high amplitude was only repeated by the rotor and motor in the λ optimum value of 4. Now, by analysing the data across turbines, it is clear in both velocity scenarios that the peak at $f/f_0 = 1$ is still visible at T2, yet not in the same magnitude as in T1, but not visible in T3 for neither the rotor nor the motor. This large peak found in T1 in both cases could be related to the cyclical pattern previously shown in figures 5.7 and 5.8 and associated to a rotor imbalance fault. Similarly, it was also found that the peaks at $f/f_0 = 3$ are present in both 0.8 ms^{-1} and 1.0 ms^{-1} scenarios across the three different λ values, but it is particularly higher in the rotor signal compared to the motor one. Looking onto the $f/f_0 = 3$ could be relevant in the future to analyse the turbine behaviour under the presence of tidal

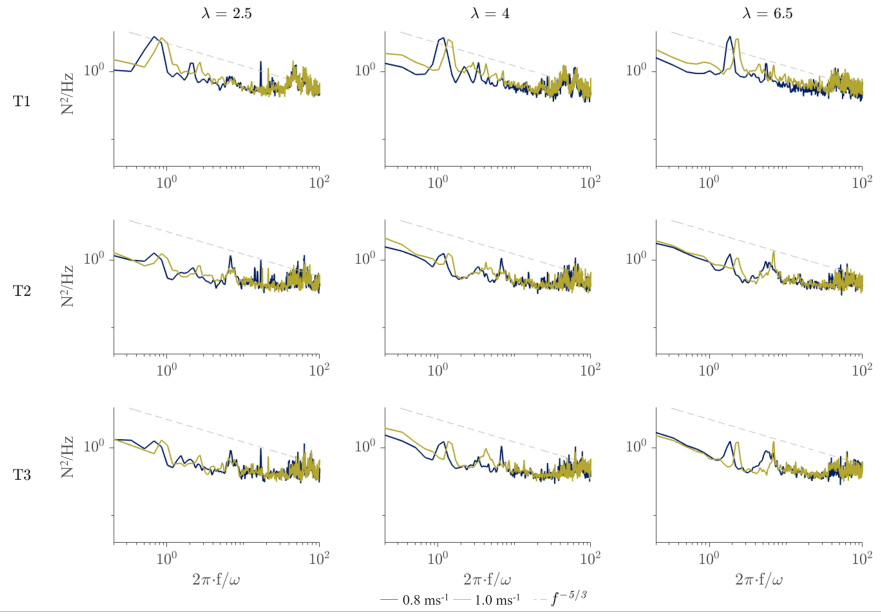

Figure 5.11: PSD of the rotor thrust data signals for T1, T2 and T3 at flow velocity of 0.8 ms^{-1} and 1.0 ms^{-1} for λ = 2.5, 4 and 6.5.

turbulence, as seen in [Allmark et al., 2021a].

Furthermore, it has been also determined that the rotor torque signal has a lower energy content than the motor torque signal of about 0.001 order of magnitude. The main difference is the large peak found at $f/f_0 = 1$, detected in each turbine for λ values of 2.5, 4 and 6.5. Again, these large peaks on the rotor signals are of greater amplitude on T1 compared to T2 and T3. These peaks are replicated on the motor signals but their amplitude sizes are smaller than the ones on the rotor signals, and they are not as visible compared to turbines T2 and T3. This coincides with the aforementioned argument of the potential data losses through the driveshaft, therefore fault on T1 is still undetectable unless a different approach is adapted to the motor signals.

Similarly, the same analysis was deployed to compare the previously found pattern in figure 5.6 to its PSD. Figure 5.11 shows the rotor thrust signals of both 0.8 ms^{-1} and 1.0 ms^{-1} velocities. Again, all the higher amplitudes at $f/f_0 = 1$ in T1 are repeated across

different λ values compared to T2 and T3. Similarly, amplitudes at $f/f_0 = 3$ between the two velocity scenarios and across the three λ values are present. Although, compared to the torque figures, these peaks have been found at lower frequencies of around 10^{-3} and 10^{-4}. This could be explained due to a smaller sampling frequency compared to the rotor torque data when data was captured. Yet, for the purpose of this analysis, only rotor and motor torque data will be used in order to build the CM algorithm due to the the inability of capturing the thrust signals in a drive train test rig. Still, this figure is important to determine the repeated high amplitude found in T1, related to the rotor imbalance fault that has been previously discussed.

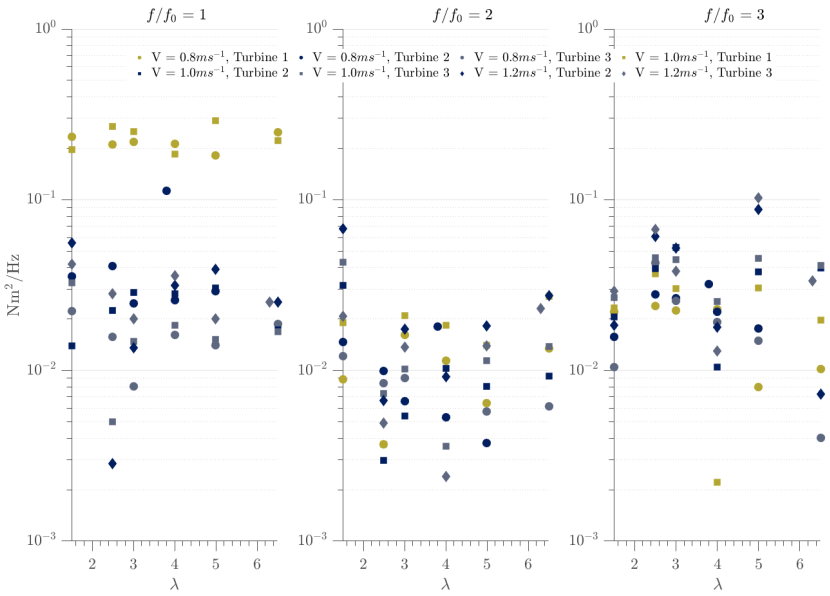

Figure 5.12: Comparison of values $f/f_0 = 1$, $f/f_0 = 2$ and $f/f_0 = 3$ of the rotor torque data signals for turbines T1, T2 and T3, flow velocities of 0.8 ms^{-1}, 1.0 ms^{-1} and 1.2 ms^{-1} for λ values from 1 to 7.

On the other hand, figures 5.12 and 5.13 display a summary of the one, two and three times the rotational frequency of the turbine respectively for the rotor and motor torque data measurements. As it is clearly seen in figure 5.12, data of T1 is significantly higher in magnitude in ($f/f_0 = 1$) compared to T2 and T3 for flow velocities of 0.8 ms^{-1} and 1.0 ms^{-1} across λ values from 1 to 7. Again, as previously detected on the PSD fig-

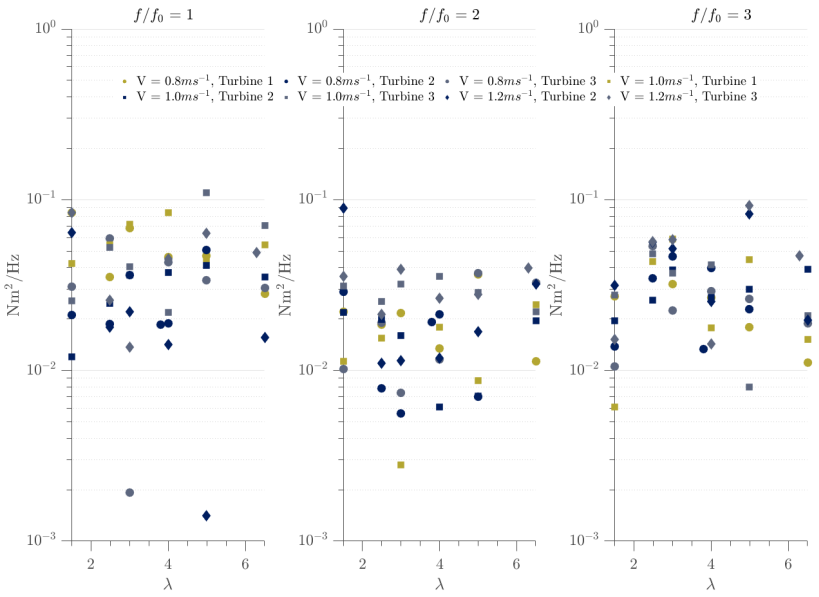

Figure 5.13: Comparison of values $f/f_0 = 1$, $f/f_0 = 2$ and $f/f_0 = 3$ of the motor torque data signals for turbines T1, T2 and T3, flow velocities of 0.8 ms^{-1}, 1.0 ms^{-1} and 1.2 ms^{-1} for λ values from 1 to 7.

ures, the torque data from T2 in both velocities on the rotor signal is particularly higher than the data from T3. Still, in $f/f_0 = 2$ and $f/f_0 = 3$ a similar behaviour as found in $f/f_0 = 1$ with T1 is not visible as data measurements are scattered in both frequencies, meaning that there are not external factors inducing the turbine behaviour in the torque measurements.

However, when comparing the rotor figure with 5.13, data of T1 for both velocities is not showing any particular trend when compared with T2 and T3 data, even when in average most of T1 torque energy content in terms of the $f/f_0 = 1$ for both velocities is higher across the range of λ values when compared with T2 and T3 data. Again, data presented in $f/f_0 = 2$ and $f/f_0 = 3$ represents a normal behaviour in the torque motor measurements for all three turbines. This finding in the motor signal demonstrates that there is still a lack of validation of the rotor imbalance fault detected in T1 compared to the clearly visible frequency content found in the rotor signal; to address this deficiency

other techniques to find the rotor imbalance fault in the motor is explored.

5.5. Feature extraction and Control Charts

Most of the fault detection techniques used in real-time fault detection in power systems are time-domain based. In an attempt to synthesise the frequency domain analysis already explained in the previous section into a more simplistic and traditional but yet effective monitoring technique, the use of control charts have been determined by the author. These are built by using the frequency domain data from the torque measurements of the turbines in order to develop a time series that could be represented on them. The use of time domain analysis as a condition monitoring technique has been utilised in the wind industry several times. For example, vibration sensors are used to detect bearing faults, and algorithms to control a special signal conditioning within the time domain are being developed to identify the signal proportional to the spike energy in a time signal. The algorithm uses the effect that a fault on a bearing element induces spike pulses, that excite the Eigen resonance of the attached vibration sensor. Finally, the signal conditioning unit performs a bandpass filtering of the sensor signal, and the trend analysis of this detects developing bearing damage [Sørensen and Sørensen, 2010]. This combined method of using the frequency domain data to represent a time series graphically has the advantage that no additional sensors or instrumentation are required, and also that could predict any possible failure on turbines, such as the rotor imbalance fault, by the use of control limits.

The control charts produced in this research will display the rotor imbalance feature extracted from the short-time Fourier transform data over time. The latter will be plotted altogether with process-defined control limits, that will allow the user to monitor how many points are above the decided criteria and prevent a possible fault. An approach to scrutinise the analysis made in the previous section has been determined in order to be able to find the rotor imbalance criteria in both the rotor and the motor signal of T1,T2 and T3. This section describes a general algorithm used for the estimation of the

rotor imbalance criteria by extracting the amplitude of $f/f_0 = 1$ from the energy spectra of the torque signal across the different scenarios aforementioned. The implementation can be summarised as follows:

- Normalise the rotor and motor torque signal.
- Apply a high-pass filter with a cutoff frequency of 0.5 Hz to attenuate the low frequencies below this value. Hence by utilising this filter, the high frequencies on the data will be highlighted and the low frequencies are removed from the the time-series data [MathWorks, 2020b]. Plus, the cutoff will allow to highlight the frequencies after the 0.5 Hz, since it has been previously determined that the $f/f_0 = 1$ was found between 1.0-1.5 Hz in most of the tested scenarios.
- Generate a spectrogram with a default "hamming" window type and a number of windows calculated as follows:

$$N_w = \frac{l(\tau)}{N_\omega / f * fs} \tag{5.2}$$

  where N_ω represents the number of rotations of the turbine, $f = \frac{V}{60}$ and it is in RPM and fs the sampling frequency (it has been previously defined that the sampling frequency was of 2000 Hz. The N_ω is suggested to be 5, since there will be a trade off between larger spectral range and less spectras to average over compared to a larger number of windows. Plus, the hamming window was selected over a list of different window type on MatLAB since it is a standard window that will allow the reduction of the spectral leakage of the spectrogram, and to smooth the components of dissimilar frequencies on a time series. Other type of windows are only used when there are similar frequency components on a time series.
- By default, the spectrogram returns the short-time Fourier transform (STFT) of a signal and overlaps the windows to maximise the correlation between frames datasets. Obtain a spectrogram recording the STFT, the overlapped frequencies and the time instants. The mathematical formulation of the spectrogram and the STFT was previously outlined in chapter 3.

- Create a time series given the spectrogram previously calculated limiting their values to be near to 1, in order to extract the amplitude at $f/f_0 = 1$ creating a time series of the amplitude values generated at each window. This time series can be produced by using the following equation:

$$TimeSeries = interp2(t, w, |s|, t, 1, 'nearest') \tag{5.3}$$

  where t, w and s are the time instants, overlapped frequencies and the STFT recorded previously from the spectrogram calculation.

- In order to define control limits to determine a fault detection, a control chart can be developed given two different variables: the mean limit of the data (MCL) and the upper control limit (UCL).

- The mean control limit can be defined by calculating the mean value of the obtained time series for either T2 or T3, as these represent the normal operating conditions and can be defined as healthy turbines. The MCL for this case, was obtained from T3.

- The upper control limit can be defined as:

$$UCL = MCL + 3 * SE \tag{5.4}$$

- where SE is the standard error of the mean. This is calculated by using the following equation:

$$SE = \frac{\sigma}{\sqrt{n}} \tag{5.5}$$

- where σ is the mean of the standard deviation of T3 and n is the number of samples on the time series of T3.

- For this algorithm, 3 SE were selected according to the Western Electric Rules for the statistical process control [MathWorks, 2021] for detecting out-of-control conditions on time series. Typically, control limits on a control chart are at the values MCL-3*SE and MCL+3*SE, but for the purpose of this research, only MCL+3*SE are utilised as the fault will only be shown when the frequency content is above the upper control limit.

- Plot the time series for T1, T2 and T3 along with the mean and upper control limits to visually detect any amplitudes above the upper control limit threshold.

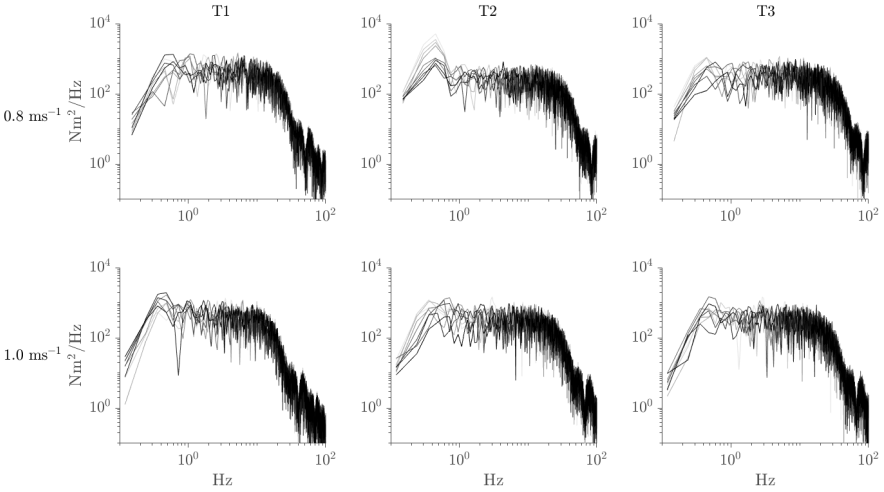

Figure 5.14: Comparison of spectrograms for turbines T1, T2 and T3 respectively for $\lambda = 4$ With a flow velocity of 0.8 ms^{-1} and 1.0 ms^{-1}.

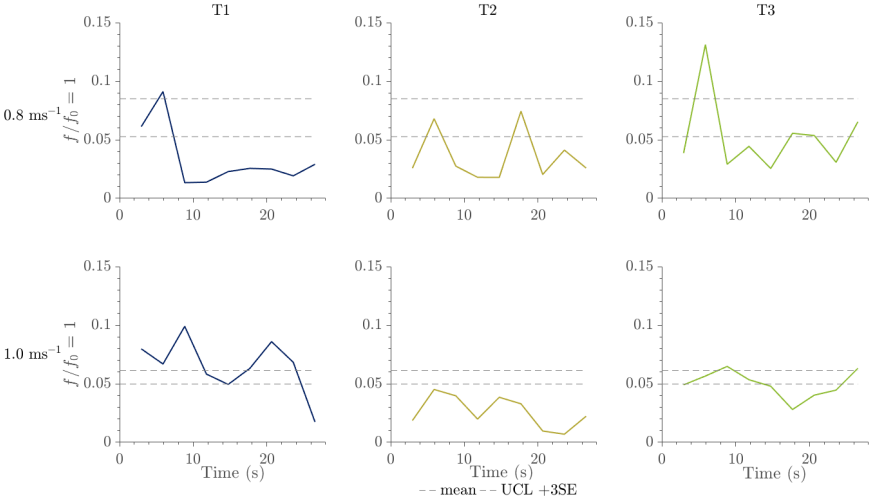

Figure 5.15: Comparison of control charts for T1, T2 and T3 respectively for $\lambda = 2.5$ with a flow velocity of 0.8 ms^{-1} and 1.0 ms^{-1}.

Figure 5.14 display the spectrograms for turbines T1, T2 and T3 for both flow

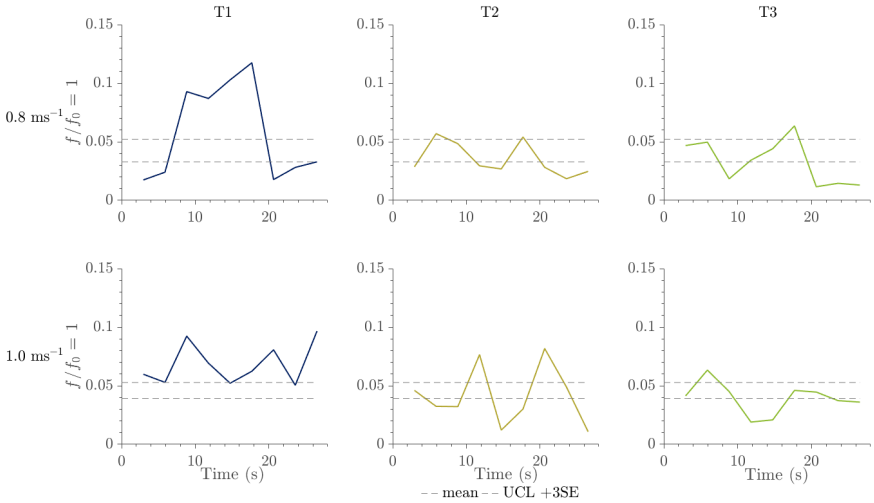

Figure 5.16: Comparison of control charts for T1, T2 and T3 respectively for λ = 4 with a flow velocity of 0.8 ms^{-1} and 1.0 ms^{-1}.

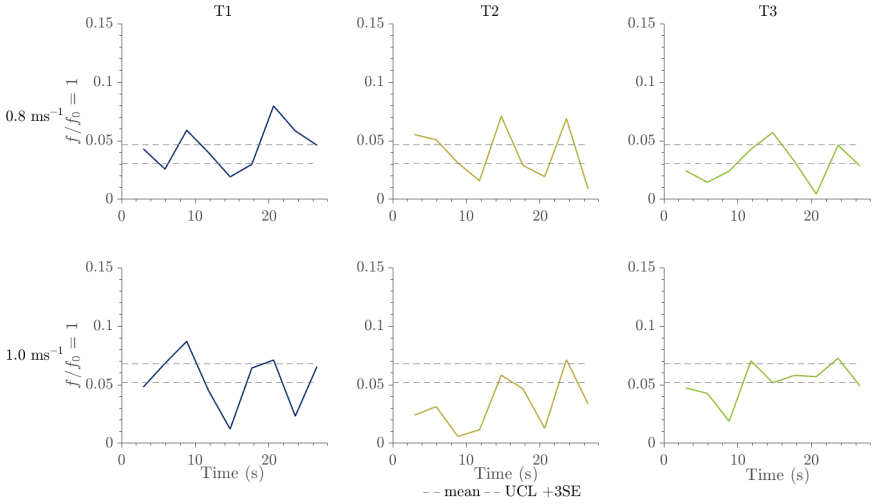

Figure 5.17: Comparison of control charts for T1, T2 and T3 respectively for λ = 6.5 with a flow velocity of 0.8 ms^{-1} and 1.0 ms^{-1}.

velocities 0.8 ms^{-1} and 1.0 ms^{-1} for λ = 4. Each figure overlaps a set of spectrograms based on the number of windows and the time length the torque signal was recorded. It can be seen that the energy content varies from one turbine to another and within flow

velocities. In all the cases, there are high peaks around $f/f_0 = 1$. On the other hand, figures 5.15, 5.16 and 5.17 display the control charts at $f/f_0 = 1$ for T1, T2 and T3 from flow velocities of 0.8 ms^{-1} and 1.0 ms^{-1}, for $\lambda = 2.5$, 4 and 6.5 respectively. In order to demonstrate the ability of the CM algorithm to be performed in the motor data, the control charts demonstrate the time series behaviour of the data obtained near $f/f_0 = 1$. In all cases, the MCL and UCL are shown with 3 SE to compare the data from T1 to T2 and T3 and confirm if the condition monitoring algorithm can then detect the rotor imbalance fault aforementioned. Across different λ values, it can be seen that most of the figures in T1 the time series crosses the UCL threshold in both 0.8 ms^{-1} and 1.0 ms^{-1}, except in 0.8 ms^{-1} in $\lambda = 2.5$. Furthermore, T3 presented less than 2 points above the UCL threshold in all λ values, contrasting the difference of control charts that may be considered under control from the turbine the MCL and UCLs are calculated from, to the control charts obtained in T1. The number of points that crossed their respective UCL dashed lines are presented in table 5.3.

One of the reasons to explain the variability in the results of $\lambda = 2.5$ scenario in both flow velocities is due to the stall region where the turbine operates at such λ value. Since the torque plotted in the control charts are calculated in function of the rotational speed of the turbine and the generator torque remains constant, the fluctuations of the rotational speed are evident to control the torque in that region (see figure 5.4) [Whitby and Ugalde-Loo, 2014]. Controlling the turbine at $\lambda = 2.5$ scenario when the turbine is being controlled at $C_{p_{max}}$ and eventually the flow velocity increases, could be an optimal solution to regulate the C_p and maintain the maximum achievable power, therefore detecting these type of faults may be an attractive solution for turbine developers. On the other hand, the reason that the control chart does not work in a $\lambda = 6.5$ scenario in both flow velocities may be since the torque values that operates at this region are very low, therefore the variability and complexity of again controlling the torque values in a control chart at this λ value. Moreover, in terms of finding solutions that may be useful to turbine developers, operating a turbine at the maximum power coefficient and running it under the appropriate conditions is one of the aims of the current tidal turbine researchers. Hence, the validation of this control algorithm under the $\lambda = 4$ scenario in

Velocity (ms^{-1})	Turbine	λ	Points>UCL (Motor)
		2.5	1
0.8	T1	4	4
		6.5	3
		2.5	0
	T2	4	2
		6.5	4
		2.5	1
	T3	4	1
		6.5	1
		2.5	6
1.0	T1	4	7
		6.5	3
		2.5	0
	T2	4	2
		6.5	1
		2.5	2
	T3	4	1
		6.5	2

Table 5.3: Table providing an overview of the points of the built time series above their respective upper control limits in the motor from control charts of figures 5.15 to 5.17.

both flow velocities achieves the objective of representing a rotor imbalance fault to be replicated in more complex conditions. The implementation of the control charts validates that, considering the number of points from the built time series around f/f_0 = 1 from T1, T2 and T3 at λ = 4, T1 presented a rotor imbalance fault, as a larger number of points surpassed the threshold considered to this process. Both carriage velocities retrieved larger number of points to the respective number of points obtained in T2 and T3, with 4 and 7 points above the UCL for 0.8 ms^{-1} and 1 ms^{-1} respectively. The latter does not appraise that a specific number of points should be obtained for specific HATT operating conditions, but rather provides an insight to prevent a possible failure, based on the selected MCL and UCL previously determined by a CM operator. Plus, the author decided to demonstrate the CM algorithm to be implemented in the motor data, proving that the rotor imbalance faults can be detected in the motor side of T1. Plus, the results obtained from the control charts allows this research to continue with further validation, now through the failure modelling into more stochastic datasets obtained from experi-

mental testing, and CM reliability and applicability through the drive train test rig.

5.6. Unsteady State Methodology Matrix

A methodology matrix was built to test the applicability of the rotor imbalance measure as a condition monitoring metric based on the KHL testing campaign data detailed in the previous section. Specifically the simulations were created to test the application of the proposed CM algorithm by the use of control charts under unsteady state conditions. In this context, the unsteady state conditions were firstly defined to replicate the simulations obtained from IFREMER testing on a flume tank (that will be called experimental data) and data engineered in MatLAB to simulate further scenarios (this test scenario will be called synthetic data). The details of each test scenario are described in 5.18.

Test Scenarios	Synthetic			Experimental		
Velocities	0.8 ms $^{-1}$	1.0 ms $^{-1}$	1.2 ms $^{-1}$	~1.0 ms $^{-1}$		
λ	4			4		
TI%	5%	10%	15%	2%	8%	15.8%
L_x	1 m	5 m	10 m	0.8 - 0.24 m		
Fault Size	No Fault 1 %		5 % 10 % 15 %	No Fault 1 %		5 % 10 % 15 %
Recorded Time Length	30 s	90 s		30 s	90 s	
Test Rig Instrument	Rotor Generator			Rotor Generator		

Figure 5.18: Methodology matrix for unsteady state scenarios defined for this research.

In the experimental test scenario, data was taken from the IFREMER testing performed in 2018, where a scaled HATT was mounted in a flume tank to generated grid

turbulence and wake flow regimes [Allmark et al., 2021a]. In order to schematise the most representative cases on a test rig, three different test scenarios where chosen from the operating points matrix that was built by CMERG utilising speed control at its maximum turbine operating efficiency (λ = 4). For this case, the velocity was around 1.0 ms^{-1}, based on the turbulence intensity registered under different turbine setups undertaken on the flume tank. The three turbulence intensity percentages registered were 2%, 8% and 15.8%. All three cases were chosen accordingly to have a range from low to high turbulence intensity to apply the CM algorithm over a variety of datasets. The detailed information regarding the experimental test scenario will be explained in chapter 6, along with the CM algorithm results applied to the data on the test rig.

In the synthetic test scenario, data was engineered with a MatLAB code to simulate different flow velocities, integral length scales and turbulence intensity percentages. In order to simulate the same velocities that were defined in the KHL testing campaign data, velocities 0.8 ms^{-1}, 1.0 ms^{-1} and 1.2 ms^{-1} were again utilised to assess the CM algorithm effectiveness on the test rig. Since it has been proven that the CM algorithm has positively worked in the λ = 4 scenario across the three different velocities in the preprocessing process of the data, it has been determined to adapt the experiment datasets under this turbine operating condition. Moreover, for this set of experiments, a range from 5% to 15% was chosen with three different integral length scales, from 1 m to 10 m in total. The detailed information regarding the synthetic test scenario will be explained in chapter 7, along with the CM algorithm results applied to the data on the test rig.

Both test scenarios are set to be run in order to obtain both the rotor and the generator signals. In order to assess the CM algorithm effectiveness on the test rig, it has been determined to apply a fault previously defined as rotor imbalance on the rotor torque signal, to be later detected on the generator. The CM algorithm appraisal will come once it is proven that the fault can be detected in both the rotor and generator signals. In order to perform a comparison of different fault magnitudes, a range of fault sizes percentages has been defined in the set of simulations to be performed. It has been decided to run both test scenarios in all the combinations previously defined with no

fault included on the rotor torque signal, 1%, 5%, 10% and 15% of the $f/f_0 = 1$ found on each rotor torque signal. The definition of the fault size will be explained in both chapters 6 and 7.

Finally, it was thought to define a range of time lengths to also assess whether the CM algorithm works based on the limitations of the IndraWorks software and the number of samples per rotation on the test rig. The latter since a question arose as to how long do τ and ω signals must be recorded in the applied software in order to detect the implemented fault on the rotor given a sampling frequency and the inherent limitations both the hardware and software have. Ideally, to build a CM algorithm to be implemented in real turbines, it must be thought to be used over a period of time per day to be a cost-effective alternative. Then, it is crucial to set a scaled recorded time length as part of the variables on the test rig simulations. It has been previously said in chapter 3, the memory depth of the IndraDrives varies: the rotor drivers are set to have a memory depth of 8192 measured values to be recorded for each measurement, whereas the generator drivers have a memory depth of 4096.

The recorded time length has been defined as 90 *s* and 30 *s* for both tested scenarios, in order to compare the flexibility of the CM algorithm in two versions of time lengths. Frequency rates of 50 Hz for a recorded time length of 90 *s* in the rotor side, 25 Hz and 125 Hz for the generator for 90 *s* and 30 *s* respectively were determined, given the fact that the rotor drivers memory depth duplicates the one from the generator. The selected sampling frequencies are in function of the number of rotations that might be needed to detect the fault at $f/f_0 = 1$. For this research 20 and 100 samples per rotation were defined to calculate fs in order to have a range of low to high frequency rates.

This chapter has appraised a condition monitoring tool building process, by analysing the frequency content in the torque and thrust signals obtained at the KHL testing conducted by CMERG. It has detected that at T1, torque and thrust signals at both carriage velocities displayed a cyclical pattern compared to T2 and T3, leading this research into determining a possible rotor imbalance being present. After examining their respective power spectral densities for all the scenarios and extracting the frequency at

its 1^{st} harmonic, a methodology presented herein in order to build a time series bases on each spectrogram was undertaken, to finally compare the results by the use of control charts. These control charts successfully demonstrated that across all cases, T1 presented more points above the upper control limits at $\lambda = 4$, validating that T1 presented a rotor imbalance fault compared to the rest of the turbines. The latter allows this research to conduct further validation of the proposed CM algorithm, by utilising datasets from experimental and synthetic data and model a rotor imbalance fault to be run at the chosen emulator test bed, in order to confirm the CM algorithm applicability across different variables, to be present in the upcoming chapters.

6

Drive Train Simulation Results of Unsteady Experimental Data

This chapter establishes the proposed CM algorithm performance subjected to a series of data taken from an IFREMER flume tank testing campaign. A brief summary of the testing campaign results, followed by the explanation of how the torque obtained from the IFREMER experimental data was characterised to be suited in the test rig, are presented herein. Finally, the results obtained from running the test rig with the experimental datasets and the CM algorithm effectiveness previously presented in chapter 5 are outlined to demonstrate the test rig capability to reproduce unsteady flow conditions and detect rotor imbalance faults in both the rotor and the generator.

6.1. Flume tank testing

To run the first set of unsteady state simulations to test the CM algorithm, the results from a series of simulations undertaken at the IFREMER flume tank were utilised. Testing was carried out at the IFREMER flume tank facility in Boulogne-sur-Mer. The experimental working section is 4 m wide by 2 m deep and 18 m long [Gaurier et al., 2018a]. It has a capacity of 700 m^3 and uses two pumps with a total power of 500 kW to be able to generate fluid velocities within a range from 0.1 ms^{-1} to 2.2 ms^{-1}. Plus, the turbulence intensity % can be regulated by the use of flow straighteners and a grid, and it can be self-sustained throughout the tank due to its own recirculating flume infrastructure. Additionally, there are two travelling cranes that are used to carry heavy loads (i.e. HATTs) and a waver generator composed of 8 independent displacement paddles. It is also equipped with a Laser Doppler Velocimeter (LDV), later explained in this chapter. The schematic of the flume tank can be seen in figure 6.1.

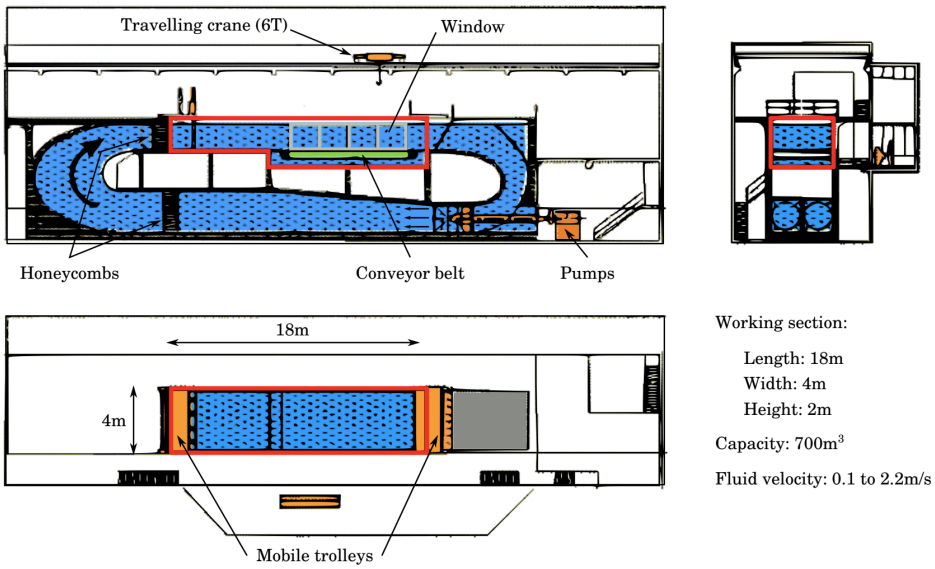

Figure 6.1: IFREMER's Boulogne-sur-Mer flume tank description [Mycek et al., 2014].

The aforementioned lab-scale 0.9 m diameter HATT utilised during the KHL

testing campaign (chapters 3 and 5), was also utilised in this set of simulations, along with the 0.5 m diameter one to test turbine single performance in arrays and wake measurements (also described in chapter 3). The latter was not taken into consideration for the purpose of this research. The main purpose of carrying out this test campaign in 2018 was to characterise the turbine performance of the third generation of HATTs developed by CMERG, that has been the subject of much research, both computationally and experimentally. Still, the obtained results were relevant to this research, since it allowed to acquire turbulence intensity data at different integral length scales, to be later utilised to detect fault conditions.

At this testing campaign carried out in 2018 [Allmark et al., 2021a], five different test cases were developed and tested to study a variety of turbine operating controls, wake and turbulence intensity cases. Initially, the 0.9 m diameter was located 4.0 m from the wall side were the turbulence grid was set to be fixed, except that for Case 1 it was meant to replicate the flow conditions with little turbulence intensity percentage, therefore only the flow straighteners were installed for this Case. Then, for Case 2, the same layout was configured, except that the turbulence grid was fixed to generate flow conditions with high turbulence and the flow straighteners were removed. Finally in Case 3, the turbine was installed 7.5 m from the turbulence grid to generate flow conditions with moderate turbulence. Furthermore, for the first three Cases already mentioned, the turbine was fixed 1 m downstream from the LDV position and 1 m deep from the flow tank surface. The three cases described are pictured in figure 6.2.

6.1.1. Data recording and Instrumentation

Flow was measured using a two-axis LDV system. This well-established technique enables the fluid velocity measurement to be performed at a single point in the flume tank, with a high temporal resolution. In order to measure the flow velocity, the water of the tank is seeded with relative small particles to obtain a good signal ratio (size of 10 μm). The LDV system utilised for this testing campaign was a 2D DANTEC FiberFlow, with a measurement area of 0.12 x 2.51 mm^2, and a mean sampling rate of

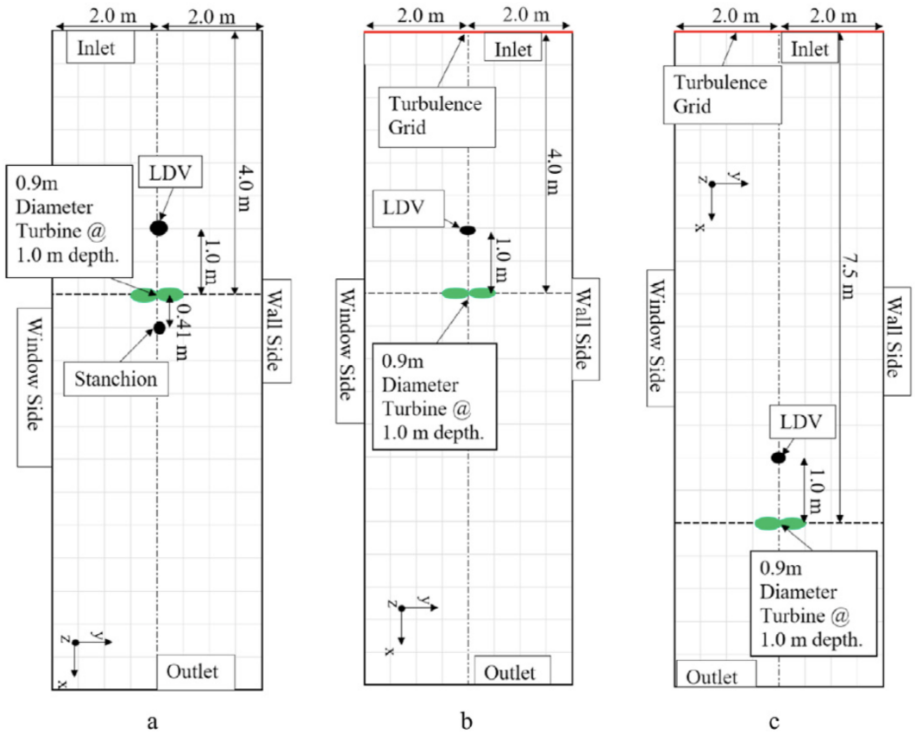

Figure 6.2: Series of test cases setups undertaken at IFREMER test campaign in 2018. (a) Case 1, (b) Case 2, (c) Case 3. Adapted from [Allmark et al., 2021a].

160 Hz for the stream-wise direction. This LDV system widely used at IFREMER is 2 dimensional, therefore it detects a reflecting seeding particle between the intersection of the two laser beams by the use of a beam splitter and subsequently brings them into a probe to modulate the light intensity. Finally, this particle velocity is determined by the frequency of the fluctuation of the scattered light's particle, that is equivalent to the Doppler shift between the incident and scattered light, that consequently is proportional to the component of the particle velocity, or perpendicular to the bisector of the two laser beams [Gaurier et al., 2018a, Dantec Dynamics, 2018]. The LDV was fixed to measure both the stream-wise and cross-stream fluid velocity components, positioning the probe 1 m upstream of the 0.9 m turbine position.

Additionally, the operation of the HATT was controlled via a PMSM integrated

into the nacelle, that was directly coupled to the rotor. The PMSM was also controlled by utilising a servo control and a control loop performing VOC to manage the energy extracted by the PMSM. The device control was operated by utilising speed and torque control, but for the purpose of this research, only the data obtained from the speed control strategy was utilised. Therefore, the main technique to operate the turbine under speed control was to maintain a constant set-point rotational velocity, by a velocity feedback control loop and a proportional integral controller. Speed control cases selected for this test campaign are between a range from 0 to 21.9 $rads^{-1}$ (up to 209.13 RPM), but in order to synthetise the use of the CM algorithm, only the cases ran at its maximum turbine operating efficiency were utilised (λ = 4, or 93.37 RPM). As mentioned in chapter 5, it has been proven that the CM algorithm positively worked in the λ = 4 scenario across the three different velocities in the pre-processing process of the data, and additionally, the objective of representing a rotor imbalance fault at its maximum power coefficient may be useful to turbine developers. Additionally, a sample rate of 200 Hz was used to record the data from the HATT operation.

Finally, turbulence was generated by the use of static grids, an experimental method developed by Blackmore et al. [2016]. Herein, the author describes that velocity shear is generated behind the grid bars producing eddies, that subsequently produce turbulence. The eddies' sizes are proportional to the grid bars' width, which is a simple yet accurate way of controlling integral length scales and turbulence intensities, by respectively changing the grid bars size to produce larger scales of turbulence and moving the turbines further downstream from the grid to decrease the turbulence intensity. A figure of the utilised turbulence grid at this testing campaign can be seen in figure 6.3

6.1.2. Overview of the obtained results

Prior installing the turbine on the flume tank, flow stream was characterised by calculating the flow velocity via a sequence of LDA measurements in the centre of the cross sectional area of the flume. The main results of the flow characteristics observed prior installing the turbine and with the turbine in the flume are shown in table 6.1. It

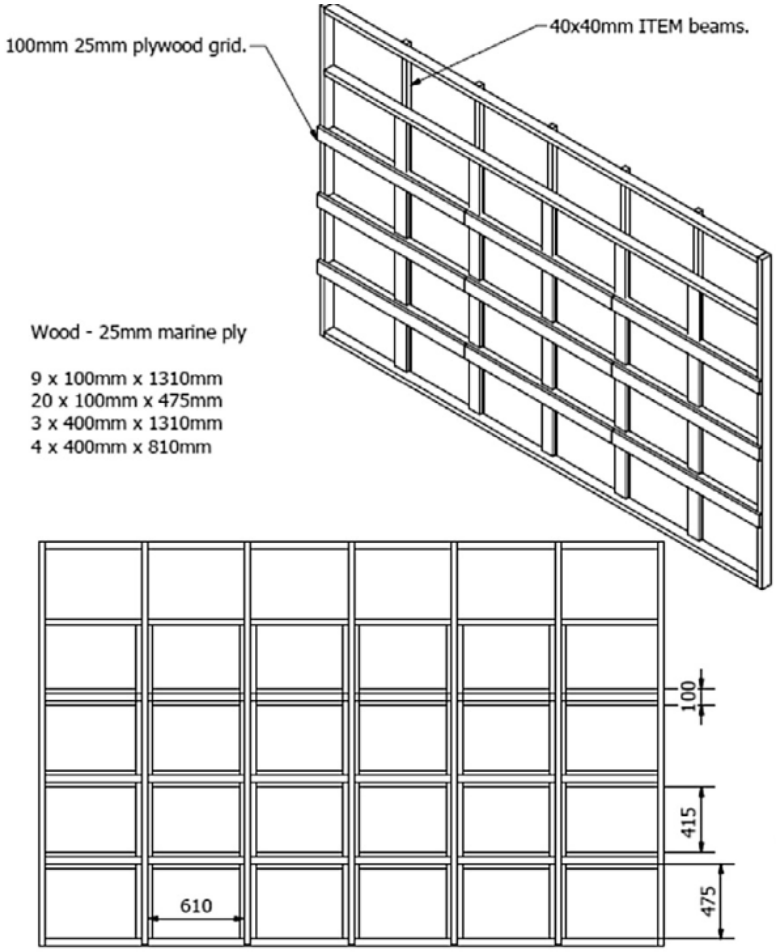

Figure 6.3: Dimensions of the turbulence grid utilised at the IFREMER testing campaign. Adapted from [Blackmore et al., 2016].

was found that the presence of the turbine reduces the flow upstream of the turbine position and alters the mean fluid velocity. However, there were minimal changes on the measured TI values, except for the highest TI case (Case 2), where there was a significant increase in TI when the turbine was installed. It could also be observed that the integral length scale values increased in the low and moderate levels of TI cases (Case 1 and 3), but it decreased in the presence of high turbulent energy. This corresponds to a negative correlation between TI and L_x and it is very clear when comparing Case 1 and Case 3, but

Unit	$\overline{U}_x$ (ms^{-1})	TI_x (%)	L_x (m)	Record length (s)
Case 1: PTI	1.11	1.5	0.48	120
Case 1: TDE	1.06	2	0.80	130
Case 2: PTI	1.02	11.7	0.20	1000
Case 2: TDE	0.94	15.8	0.16	200
Case 3: PTI	1.07	7.10	0.19	1000
Case 3: TDE	1.02	8.0	0.24	200

Table 6.1: LDV measurements obtained at the IFREMER testing campaign of the flow characteristics observed in the pre-turbine installation phase (PTI) vs during experiments (TDE). [Allmark et al., 2021a]

these effects were not yielded similarly when comparing Case 2 and Case 3 as expected, as both cases obtained similar L_x results. Still, the latter alludes the importance of the turbulence grid presence and the reduced distance between this and the turbine position for Case 2. Also, it is important to note that the variation in the profile information for flow velocities measured at 3 m upstream of the turbine plane showed no significant vertical profile, as the flow velocity and the TI varied from 1.50 to 1.53 ms^{-1} and 1.75%–2% respectively, across the diameter of the turbine, indicating a low turbulence and highly uniform flow. The flow profile information of this test campaign is shown in Ebdon [2019]. This result is produced by the use of flow straighteners in the flume tank, allowing this research to rely on the performance of the HATT installed on the flume tank for Cases 1, 2 and 3. Overall, the main characteristics of the flume data obtained when the turbine was installed were adapted to this research in order to reproduce the signals obtained from the turbine under these flow conditions.

Neglecting the fact that power curves generation for this testing campaign is not considered within this research objective, it is important to note that comparing the non-dimensional parameters from the rotor output data showed relatively poor agreement between Case 1 and Cases 2 and 3, since it was expected to obtain homogeneous conditions between TI cases. Particularly in the C_p curve against λ values, a significant drop in generated power with no grid installed is clear when compared with moderate and high TI cases. On the other hand, the σ observed for each of the non-dimensional parameters were found to increase as TI increased. Interestingly, it was also found that that the use of torque or speed control in the turbines had an inconsequential effect in

Unit	C_p	$\overline{\omega}$ (RPM)	τ (Nm)
Case 1	0.45	-933.79	20.04
Case 2	0.47	-757.637	22.86
Case 3	0.47	-865.993	22.13

Table 6.2: Theoretical input values to run the experimental set of data obtained from the IFREMER testing campaign.

the C_p values. The author defined this as a consequence of the similar magnitude found in the torsion developed under the speed control cases, compared with the variation in rotational speed driving the variation of power under the torque control cases [Allmark et al., 2021a]. As previously mentioned in chapter 5, this research was focused in implementing speed control at the DTTR and reproduce the torque signals obtained at this testing campaign with a $\lambda = 4$. This testing campaign yielded for C_p values at $\lambda = 4$ equal to 0.47, 0.47 and 0.45 for Case 3, Case 2 and Case 1 respectively. Also, the mean values of the rotational velocity of the turbine ω were set to run the generator. The mean velocity value was set directly into the IndraWorks software utilising the mean velocity value for each case and multiplied by 10 given the gearbox interaction. On the other hand, the actual obtained torque signal from HATT operation for Cases 1, 2 and 3 were conditioned and set through a LabVIEW interface to operate on the test rig. The main values for the rotational speed obtained from the motor and the mean torque values obtained in the rotor are entitled in 6.2. These values are named onward 'theoretical' values, as they are the basis of this chapter experimental setup to reproduce flume tanks recorded signals at the DTTR.

Comparatively to what it was found in the non-dimensional parameters study, the effect of TI on the variation particularly on the power and torque values is evident. It was found that with speed control, torque and power σ values from Case 1 compared to Case 2 and 3 differs significantly as TI and $\overline{\omega}$ increases. The latter confirms how stochastic conditions on the flow influences the HATT energy production and its variation. Conversely, this effect was not reproduced in the rotational velocity ω σ values, as there was very little variation amongst the three Cases with speed control, but higher variability when torque control was utilised. Additionally, τ PSDs were presented for both torque

and speed controls and it was found that peaks at particular rotational velocities were more noticeable in speed control compared to torque control, and that the amplitude at one of the harmonics were proportional to the TI measured in these three Cases. It is expected for these conditions to be replicated on the DTTR, that only fault sizes will be created in order to recreate possible rotor imbalance conditions and be able to detect them utilising the built CM algorithm early mentioned at chapter 5. The details are defined in section 6.3.

6.2. DTTR torque data characterisation

In order to undertake the CM algorithm implementation outlined above, the mean rotational velocity values recorded at the HATT motor were utilised to be set at the generator, whilst the torque recorded signal from the HATT rotor was conditioned in order to reproduce it directly into the DTTR. The mean ω value was set through the IndraWorks software via a easy startup mode as previously explained in section 3.2.3. Additionally, the generator velocity was multiplied by 10 and set with a negative value. Comparatively from the steady state simulations, at the unsteady state phase of this research the addition of the LabVIEW interface and a PXI Controller was needed in order to simulate the fluctuating components that represent the stochastic behaviour of the torque input signals. The torque signals were handled so different time series lengths could be operated on the test rig. In order to run different time lengths at the DTTR and study the influence of sampling rate and time in the expected CM algorithm output, the selected time lengths were 30 *s* and 90 *s* for the three Cases, with a selected sampling rate of 50 Hz in the rotor side, 125 Hz for the 30 *s* and 25 Hz for the 90 *s* for the generator side. These sampling rates were set at the IndraWorks software, and it is important to note the sampling frequency difference between the motors due to the difference of the available memory depth of the two different drivers connected to each motor, as mentioned in chapter 3. The torque signals were conditioned utilising MatLAB, and data text files were created in 'txt' format in order to be read with the LabVIEW code, explained below.

6.2.1. Software Implementation

The software for this unsteady state phase was developed and integrated using three different platforms. First, the central test control software was developed using NI LabVIEW 2017 and implemented using a PXI running the NI real-time operating system. Then, the master IndraDrive C is connected to the Modbus TCP/IP link to receive the torque and rotational velocity commands. The LabVIEW code was developed in order to read the IFREMER torque recorded signals and run the rotor test rig simultaneously via the implementation of different block diagrams. First, the main block diagram was built so the text file with the main torque data will be read and converted into an array channel. Then, the theoretical torque times series is utilised in order to increase the noise ratio into the signal by 1%, 5%, 10% and 15% and by implementing equations 6.1 and 6.2 as follows:

$$X = x * \overline{\tau} * cos(2 * \pi * \frac{\overline{\omega}}{60}) * T \tag{6.1}$$

$$\sum_{i=1}^{n} \tau_x = \tau + X \tag{6.2}$$

where x is the noise ratio range from 1% to 15%, T is the time vector in seconds and τ is the theoretical torque signal in Nm. After 4 new time series were built, a new block diagram converts the torque time series into volts utilising the voltage range previously explained in section 3.2.4. Subsequently, this new voltage time series is scaled to a DAQ Max instrument, which reads the new time series to send it to the PXI Controller and finally to the IndraWorks software through the connector block NI SCB-68 A. Furthermore, a User Interface was built to run this sequence in order to load the text file and run the test rig. Again, two hosts PCs runs and records simultaneously the set torque time series and the mean rotational velocity inputs for the given time length of all the simulations. Combining the different time lengths, theoretical torque signals, torque with added fault sizes, the rotor and generator obtained signals, different TI percentage, and including repeats, all previously detailed in 5.18, a total of 121 text files were ob-

tained from this set of simulations. The analysis of the latter is explained below. An overview of the LabVIEW code implementation utilised in this chapter is detailed in 6.4.

6.3. DTTR Unsteady Experimental Data Results

The analysis of the results obtained is detailed in this section. Firstly, figure 6.5 displays the mean normalised values from the rotor torque data signals for TI = 2% (navy blue signals), TI = 8% (yellow signals), and TI = 15.8% (green signals), each windowed five times from the total time length of 90 *s*, whilst displaying the actual rotor torque signals overlapped five times (gray signals) for the fault sizes of 0%, 1%, 5%, 10% and 15%. The mean normalised values were taken by returning the actual torque signal to 0 values, disregarding each torque signal's magnitude, and calculating the mean value between the 5 iterations across the time series. Thus, to demonstrate the proportional variability when the TI and fault size increase. Accordingly, the influence of the TI increment is clear when the low TI case is compared with the moderate and high turbulence cases, obtaining more stochastic gray signals and subsequently less pronounced continuous peaks in the mean yellow and green signals compared to the blue navy ones. Additionally, it is shown that when the fault size percentage increases, the higher the magnitude of the obtained mean values from each 5 times windowed iterations are. Particularly, it is seen that when the amplitude of the fault size is increased by 10% and 15% in the TI = 2% case, the normalised torque values reaches up to 1.5 Nm. The latter is likely to happen due to the low variability of the low turbulence case when compared with the moderate and high turbulence ones with a higher variability, and subsequently reproducing clearer torque mean distributions along the recorded time signals.

Similarly to the previous figure, figure 6.6 displays a comparison between the theoretical raw torque dataset, overlapped with the smoothed theoretical torque, rotor torque and generator torque signals for the three aforementioned TI cases. The smooth data was generated via convolution with a simple uniform window function of 20 *s* length. These coloured torque smoothed signals demonstrated a good performance

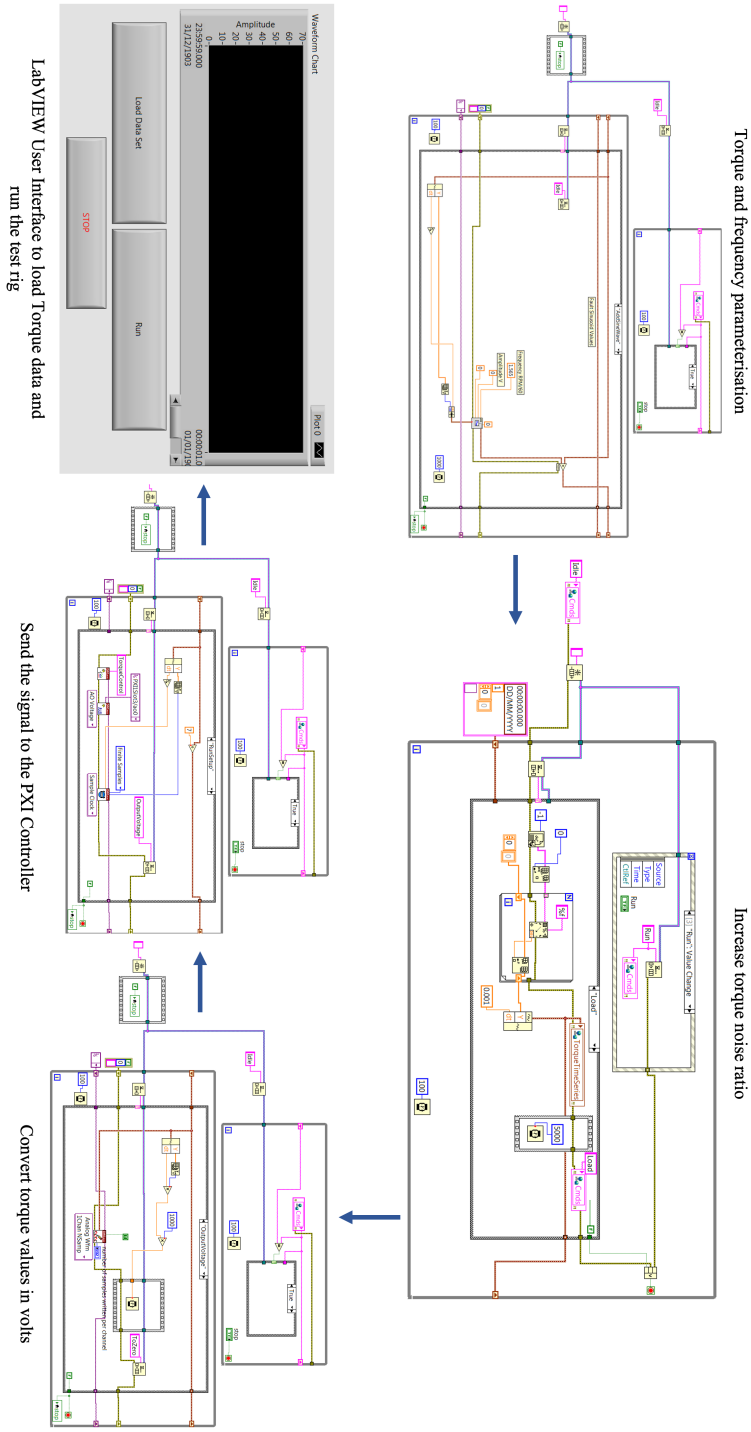

Figure 6.4: An overview of the LabVIEW code implementation.

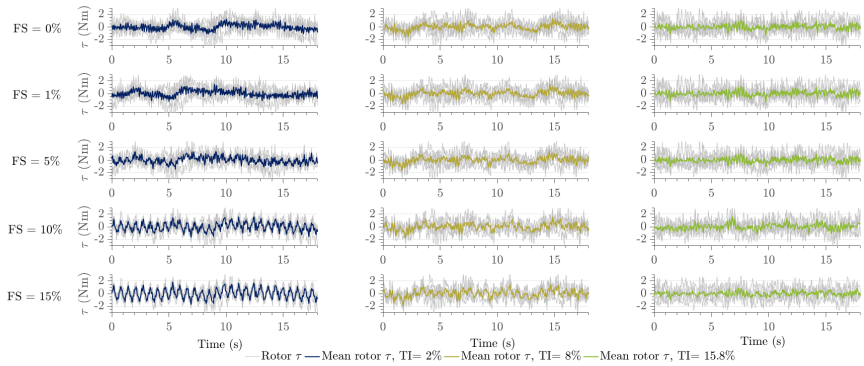

Figure 6.5: Normalised rotor torque data signals for TI = 2%, 8% and 15.8% at λ = 4 and for fault sizes of 0%, 1%, 5%, 10% and 15% windowed five times from the total time length and a mean value was calculated from all the iterations.

in reducing the spread of data whilst representing the torque structure obtained from the raw data (gray line). In the three figures displayed, the blue lines in all cases adequately represent the average transient characteristics of the theoretical raw data obtained from the IFREMER testing, whilst the rotor and generator smoothed data varies between TI cases. Additionally, the transient characteristics of the torque signals under the presence of higher turbulence represents a higher variability, where σ results from TI = 2%, 8% and 15.8% are 0.63, 1.66 and 2.54 respectively. On the other hand, while it is clear that the rotor smoothed data accurately replicates the theoretical data signal in the low turbulence case, it present relatively small differences replicating the theoretical torque signal under the presence of higher turbulence, despite the fact that the mean values are the same ones obtained from the rotor side. As expected, the generator presented losses trying to reach the raw data obtained from the IFREMER testing, of around 30% for all cases, particularly higher losses in the low turbulence case compared to the highest ones (34.84%). The latter is explained due to the drivetrain losses, gearbox interference and the heating losses presented during the simulations undertaken at the DTTR. Still, the rotor and generator developed the same transient characteristics of the theoretical torque values, demonstrating that the DTTR is able to replicate different turbulent conditions utilising the PXI methodology previously mentioned.

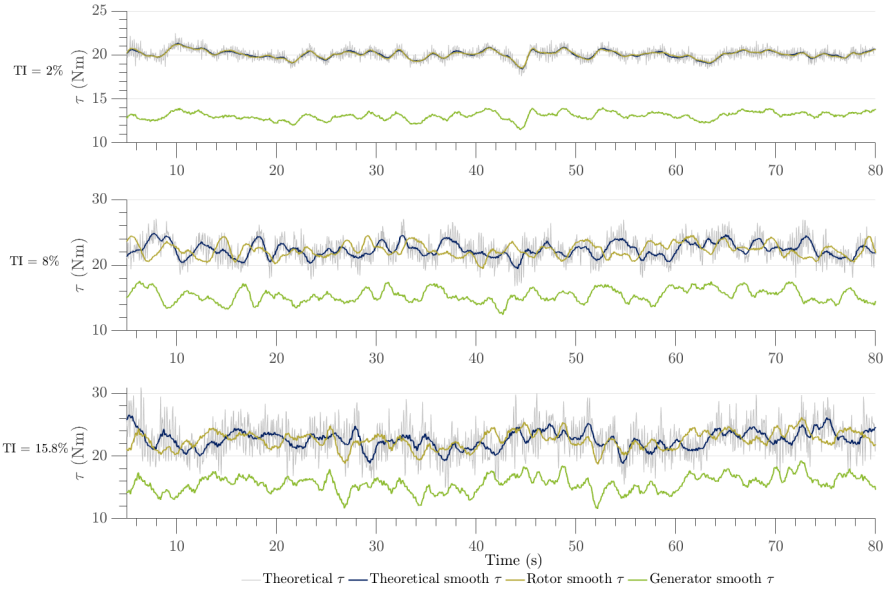

Figure 6.6: Torque loading time series obtained from the rotor and generator on the DTTR, overlapped with the theoretical torque data signals for TI = 2%, 8% and 15.8% at λ = 4 and fault size of 0%

A comparison of boxplots between the torque signals obtained from the rotor and generator given different TI cases, fault signal sizes and repeats are displayed in figure 6.7. The horizontal line within each box indicates the median values of the dataset; the upper and lower bounds of the boxes show the upper and lower quartiles of the dataset (a range of 50% of the data distribution), the whiskers or the two lines outside the box, indicate the maximum and minimum values observed * 1.5 the interquartile range, and the outliers represent the data points that is outside of the minimum and maximum values from the whiskers limits. It is observed that the median values given in all the cases do not vary, yet there are a few cases where the data distribution is larger, such as the TI = 15.8% case compared to the TI = 2% case. On the other hand, the median values on the generator side displays some variability between all different cases and larger data distributions in the moderate and high turbulence cases compared to the low turbulence one. Interesting, the median values variability is higher in the lowest turbulence case, despite the fact that there were more outliers obtained in the TI = 8%

and 15.8% respectively. Overall, the general trends of the obtained boxplots were consistent and symmetrical, demonstrating that the data distribution differences between all cases is relatively small even when TI and fault signal cases increases.

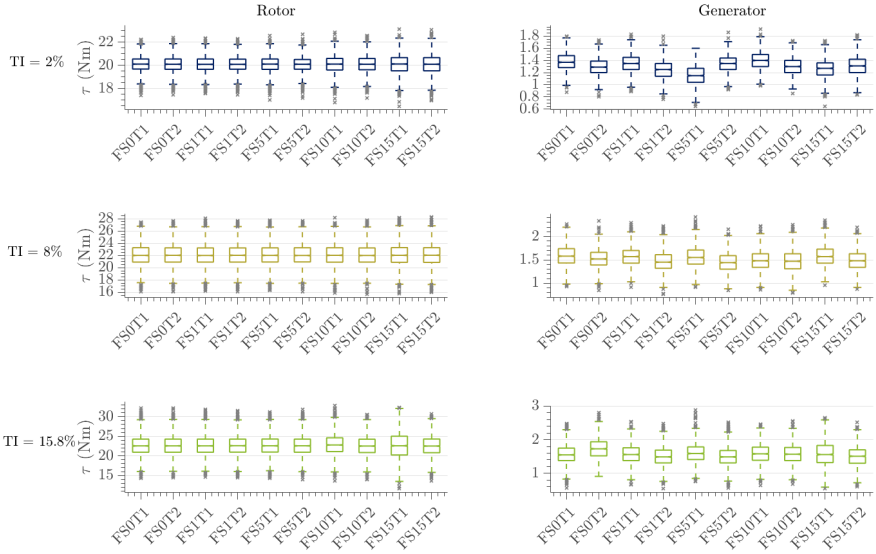

Figure 6.7: Boxplot of torque signals for the three TI cases undertaken and for the five fault sizes cases, including repeats. Left size column are rotor torque signals, right size column are the generator torque signals.

In order to assess the test rig behaviour, the datasets for each of the recorded signals in the generator side were plotted in figure 6.8 for the lowest turbulence case and fault size of 0%, windowing the total time length every 5 s windows (gray line) and obtaining the mean value of all the iterations (navy blue line). Herein, the generator velocity, torque feedback value, torque-generating current, torque-generating voltage, position feedback value, flux-generating current, flux-generating voltage and the generator temperature are shown respectively. As detailed in chapter 3, the torque-generating current and flux-generating current consists in the transformed currents I_q and I_d respectively. As expected, the mean flux-generating currents oscillates around 0, as the PMSM generator side is set to operate at its maximum efficiency and subsequently at its maximum torque value, and the latter is achieved by setting the d-axis current to 0

[Anaya-Lara et al., 2009]. Meanwhile, the torque-generating current represents the same magnitude as the one obtained in the torque feedback value, and utilising equation 3.5, the mean values of the torque-generating current compared to the one obtained in the torque feedback value has a difference of 0.0008. Similarly, the torque and torsional fluctuations are evident in both the torque force feedback value and the velocity plots, obtaining standard deviations of 0.11 Nm and 2.87 RPM respectively. Finally, it is observed that a standard temperature range were adapted for these datasets. The author recognised that in order to eliminate temperature related variations, it was needed to rest the test rig after each case being run.

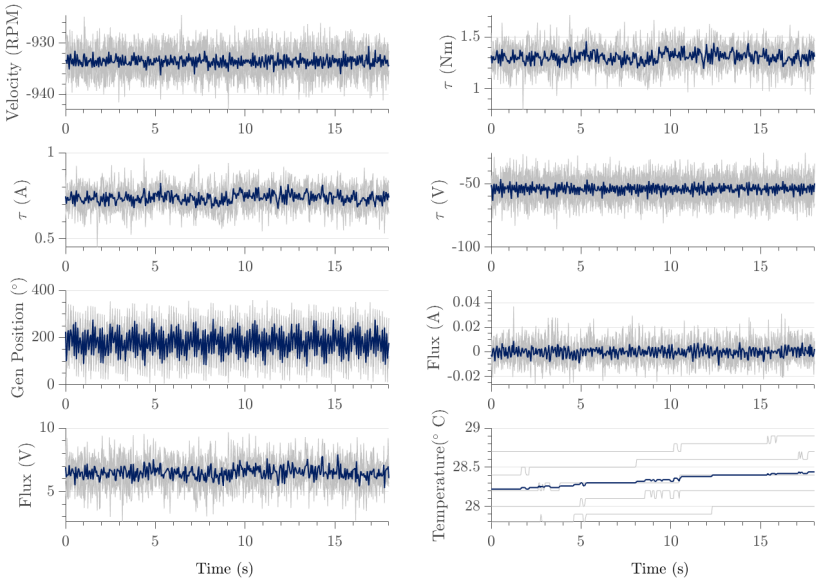

Figure 6.8: Results from all the signals recorded at the generator DTTR for the TI= 2% case, recorded time length ~ 90 *s*, fault size = 0%.

The impact of ambient turbulence intensity during the IFREMER testing and the load fluctuations of different fault conditions implemented onto the rotor torque values, were analysed using the torque obtained from the rotor and generator in the DTTR, along with the comparison of two different recorded time lengths. The latter are presented from figure 6.9 to 6.12, and were built to display the loading forces with respect to

the rotational velocity of the turbine to highlight any harmonics associated with themselves. Specifically, PSDs were calculated utilising the normalised torque generator and rotor signals obtained from the set of simulations of 30 *s* and 90 *s*, comparing the power spectral density for each fault signal size and different TI percentage. The power spectral density was calculated using the 'pwelch' function in MatLAB. The figures were delimited in order to analyse only the lower frequencies and the higher energy content in all of them.

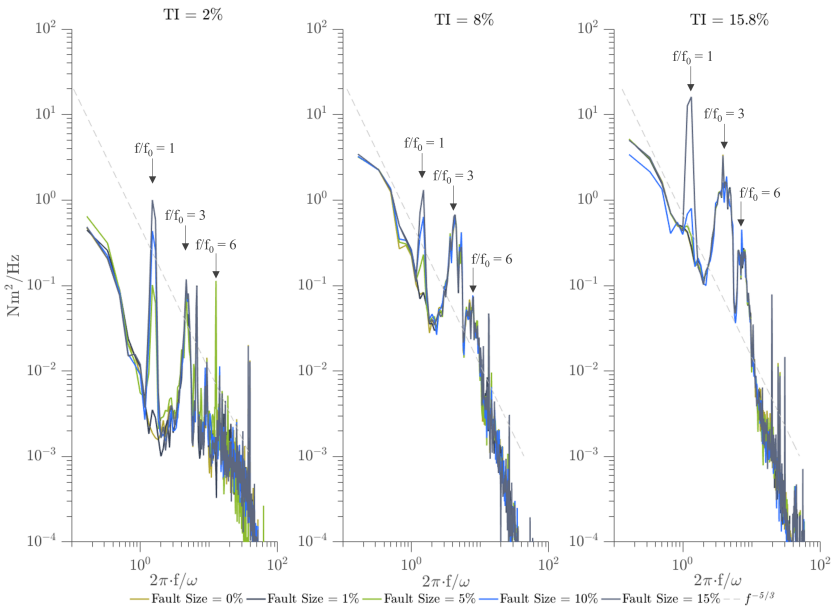

Figure 6.9: PSDs calculated for each of the fault size cases recorded on the DTTR from the Rotor for λ = 4, with a flow velocity of 1.0 ms^{-1} and for three different TI cases. Recorded time length ~ 30 *s*.

The PSDS for the 4 cases being compared, present higher energy content at lower frequencies as expected. Similarly, the torque energy density increase proportionally when TI increases, yielding higher spectral energy values for both the rotor and the generator for TI = 8% and 15.8% with respect to TI = 2%. On the other hand, there is no differences comparing the spectral energy magnitude from the simulations recorded for 30 *s* compared to the ones at 90 *s*, still there may be discrepancies obtaining the same peaks at different harmonics that will be detailed later. However, there are rela-

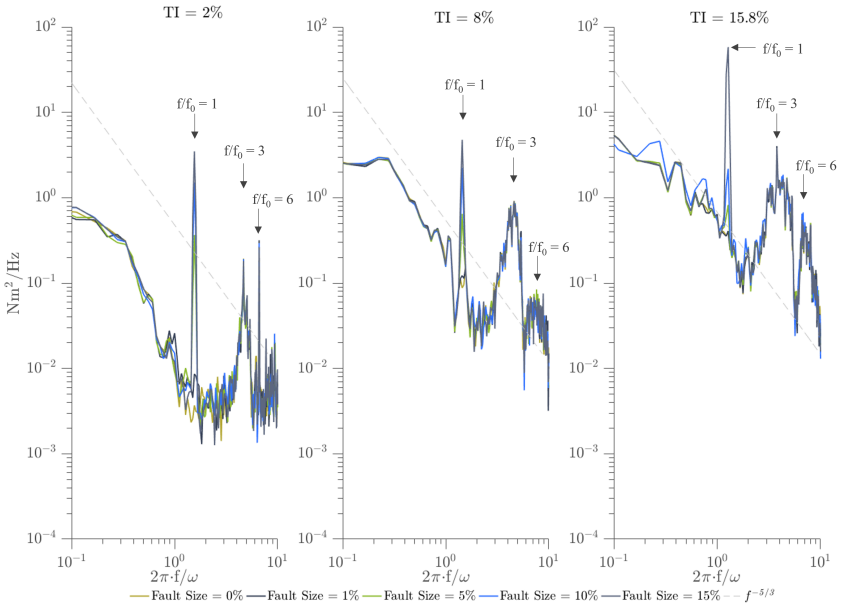

Figure 6.10: PSDs calculated for each of the fault size cases recorded on the DTTR from the Rotor for $\lambda = 4$, with a flow velocity of 1.0 ms^{-1} and for three different TI cases. Recorded time length ~ 90 s.

tively small differences in the PSD structures of both the rotor and the generator when the time length is of 30 s compared to the ones of 90 s between the different fault signal sizes. Specifically, the main differences in the PSD structures between fault signal sizes were found at figure 6.11 at TI = 15.8%, as it is shown that fault sizes from 0% to 10% do not follow the proportional amplitude increment compared with the rest of the cases, but fault size = 15% yields the highest spectral energy of the structure. The latter could be attributed to the low values obtained from the generator PSD and the complexity of obtaining the expected amplitudes when the torque is being recorded in a relatively small time sample. Moreover, there is a significant difference between the spectral energy obtained from the rotor to the generator, of about 100 orders of magnitude. Again, the latter is likely to be a product of the gearbox interference due to the 1:10 gearbox ratio, the influence of inertia and the drivetrain losses, similar to what it was observed in figure 6.6. Still, compared to what it was found in figure 5.9 where the generator PSD obtained in T1 did not show a relatively high amplitude at $f/f_0 = 1$ where there was definitely a rotor

imbalance fault, figures 6.11 and 6.12 display the prominent peaks at this harmonic in all the TI cases and with the different fault signal sizes.

On the other hand, the torque energy spectrum for both the rotor and the generator suggests that there is a reasonable proportionality to the power lay decay of Kolmogorov's theory with a $f^{-5/3}$ slope, illustrating its effect with the dashed line in all figures. Interesting, figures 6.9 and 6.10 exhibit a better agreement compared to the generator figures, where the curve shape present small deviations compared to the rotor figures. The latter could be attributed to the steeper nature of the spectral distribution of the rotor torque energy content, and the large energy content obtained at higher frequencies after $f/f_0 = 6$ in the generator torque energy content. Still, it is not a research purpose to fit a proper spectral gradient to represent the linear portion of the measured spectrum (similarly to what it was done in [Tobin et al., 2015]), but to effectively obtain the torque energy content from the prominent amplitudes in order to define rotor imbalance failures and determine the test rig accessibility to replicate the experimental datasets. Therefore, for the purpose of this research, the $f^{-5/3}$ line up well throughout the inertial subrange of the PSD regime, which will be examined next.

The region of major importance in the PSDs in order to define load transients for the obtained results of the experimental testing were found at $1 < 2\pi \cdot f/\omega < 10$, as it contains the main harmonics to understand the torque loading fluctuations in function of the rotational movement of the DTTR. As previously mentioned in chapter 5, the 1st harmonic that happens once per revolution represents an imbalance of the turbine setup (in this case the DTTR), whilst the 3rd harmonic represents an entire DTTR revolution. This analysis was replicated from [Deskos et al., 2020, Durán Medina et al., 2017]. Overall, there are three harmonics that are of relevance in these results: the ones obtained at $f/f_0 = 1$, $f/f_0 = 3$ and $f/f_0 = 6$. Firstly, comparing the $f/f_0 = 1$ found in both the rotor and the generator for the two recorded lengths aforementioned, the prominent peaks found for each TI case differs from one another, but yet they are consistent as the fault size increases for all the cases. Figure 6.9 displays the dominant amplitude at this frequency, and it clearly reveals the contribution of the fault size added into the rotor sig-

nal, and evidently displays the proportional increase in all the fault size cases across TI cases. The effect of the large fault size was found to be more pronounced in the fault size = 15%, TI = 15.8% rotor results for both recorded time lengths, that is particularly higher compared to the rest of the fault size cases. The latter could be attributed to the higher turbulent flow fluctuations associated with larger turbulent flow structures, leading into less clarity in the prominent peaks found at this rotational speed of the DTTR. Another finding at the first harmonic in figures 6.9 and 6.10 are the large differences in the amplitude size when the time recorded length changes. Again, comparing the fault size = 15%, TI = 15.8% rotor results, the peak of the 90 *s* case is 3 orders of magnitude compared to the 30 *s* one. The latter could suggest that recording these signals in a larger period of time could potentially provide better results onto detecting turbine faults, yet the 30 *s* scenario did not fail into displaying the prominent peaks even when the amplitude was reduced.

Compared to what it was found in figures 6.9 and 6.10, the generator side of the DTTR show two dominant frequencies at $2\pi\cdot$ f/ $\omega \approx 1$ and 1.5, mainly in figures 6.11 and 6.12, both at TI = 2%, where the $2\pi\cdot$ f/ $\omega \approx 1.5$ is higher in amplitude in all TI cases across the generator results compared to $2\pi\cdot$ f/ $\omega \approx 1$. Given the fact that in figure 6.11 at TI = 2%, the amplitudes at these two rotational speeds are likely the same, and that the PSD structure varies compared to the ones shown at figure 6.12, again suggests that the time length has a major impact in the generator side results. Still, this amplitude observed at $2\pi\cdot$ f/ $\omega \approx 1.5$ was consistent in both the rotor and the generator, and mainly in the rotor figures it was shown to be the highest amplitude detected compared to $f/f_0 = 3$ and $f/f_0 = 6$.

Now, the $f/f_0 = 3$ harmonic is displayed with relatively small differences across all cases, yet is also a prominent peak that constantly repeats in each figure. Compared to the $f/f_0 = 1$, the amplitude at this rotational speed neglects the contribution of the fault size, being consistent in size despite the fault size increment. This suggest, as mentioned in chapter 5, that this harmonic reveals the turbine behaviour under the presence of tidal turbulence, and the latter is confirmed by the proportionality of the amplitude size at

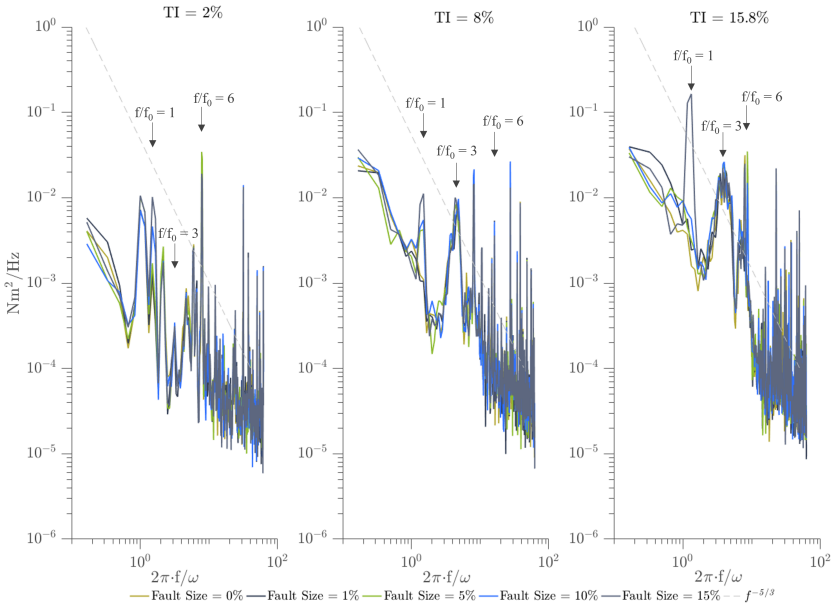

Figure 6.11: PSDs calculated for each of the fault size cases recorded on the DTTR from the Generator for λ = 4, with a flow velocity of 1.0 ms^{-1} and for three different TI cases. Recorded time length ~ 30 s.

this harmonic when TI increases for all the cases. Despite the fact that this peak did not exceed the values at f/f_0 = 1 for all the cases, it is important to note that figures 6.11 and 6.12, mainly at TI = 2% display a f/f_0 = 3 relatively low compared to the rest of the peaks found in this region. This could be attributed to the low values obtained from the generator PSD and the low TI turbulent flow.

Interesting, figures 6.11 and 6.12 presented the most prominent peak at f/f_0 = 6 in TI = 2% and TI = 8%. Relying on Allmark et al. [2021b], this harmonic displays the cogging torque generated by the rotor-gearbox-generator interaction, in order to yield a low synchronous speed in the generator to match the rotor rotational speed to comply with the speed control strategy being used. The fact that this harmonic is higher in the generator side with respect to the rotor side, exhibits the influence of the gearbox in the DTTR.

Generally, various results were generated from the PSDs. Firstly, the variability

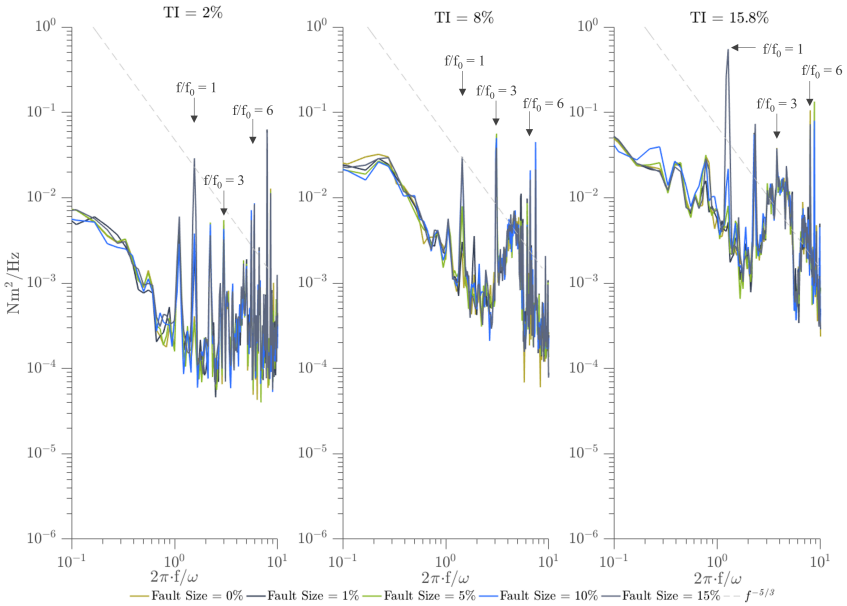

Figure 6.12: PSDs calculated for each of the fault size cases recorded on the DTTR from the Generator for λ = 4, with a flow velocity of 1.0 ms^{-1} and for three different TI cases. Recorded time length ~ 90 s.

in the PSD structures under different TI and fault signal cases provides an insight that could be utilised by turbine developers to understand a HATT behaviour under the presence of tidal turbulent flows and prevent a possible turbine imbalance failure. Overall, PSDs showed a particular consistency in displaying the dominant fault peak at the first rotational speed of the turbine, with some discrepancies observed at the generator given different time lengths. It was also observed that at three rotational speeds of the turbine, the PSD structure for both the rotor and the generator did not vary within the differing fault size cases, yet it had an impact in the highest TI case for all the fault size cases except for fault size = 15% at f/f_0 = 1, as the rest of the fault size cases did not exceed in terms of amplitude to f/f_0 = 3. The latter suggests that under the presence of higher turbulent flows, HATT may struggle to detect smaller fault size cases, and that an additional technique may be implemented (i.e. control charts). Another significant result was the effect of the recorded time length, mainly in the results obtained from the generator side. Yet, utilising a frequency domain analysis in order to replicate the results obtained an exper-

imental campaign and build their respective PSDs accomplish the expectations of this research, by effectively reproducing the technique mentioned in chapter 5 and mimic the HATT behaviour in a flume tank at a DTTR.

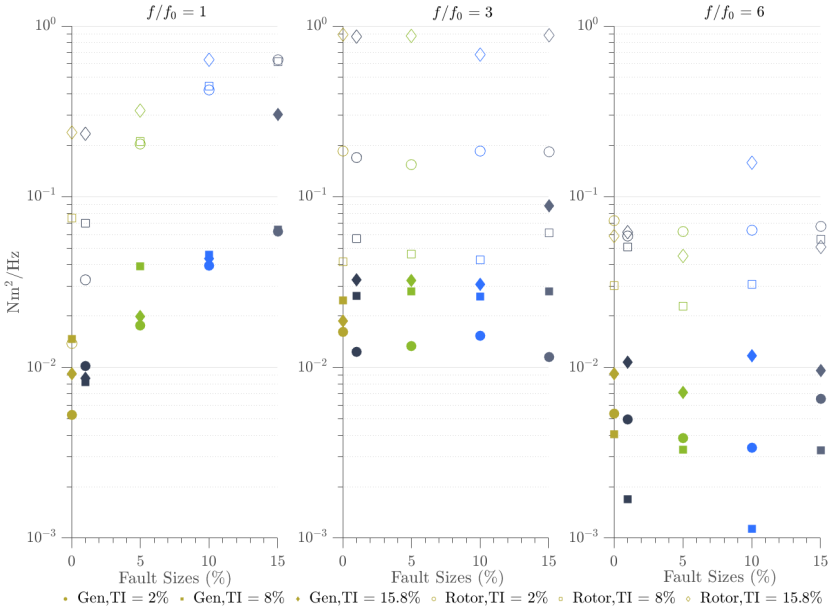

Figure 6.13: Amplitude of each of the fault size cases recorded on the DTTR from the Rotor and the Generator for λ = 4, with a flow velocity of 1.0 ms^{-1}, for f/f_0 = 1, f/f_0 = 3 and f/f_0 = 6 and for three different TI cases. Recorded time length ~ 30 s. Yellow = No Fault Size, Dark blue = 1% Fault Size, Green = 5% Fault Size, Navy blue = 10% Fault Size and Light Blue = 15% Fault Size.

In order to analyse the reciprocal relationship of recorded time length, fault size increase and TI, figures 6.13 and 6.14 show again the highest amplitude values obtained at f/f_0 = 1, f/f_0 = 3 and f/f_0 = 6 for the three TI cases and the rotor and generator signals, against the fault sizes from 0% to 15%, for the two sets of simulations of recorded lengths previously mentioned. The main purpose of plotting these figures is that they visually provide a better result into detecting the highest amplitude in the fault size, TI percentage relationship for both the rotor and the generator. Firstly, for the three rotational speeds chosen in both figures, it is clear that the dominant amplitudes were retrieved by the rotor signals. This was a previous result considered from the PSDs, so

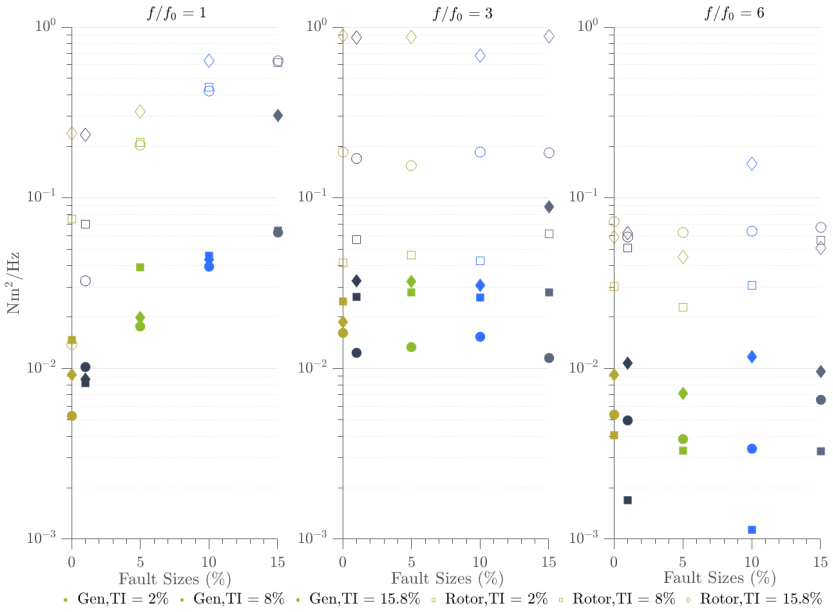

Figure 6.14: Amplitude of each of the fault size cases recorded on the DTTR from the Rotor and the Generator for λ = 4, with a flow velocity of 1.0 ms^{-1}, for f/f_0 = 1, f/f_0 = 3 and f/f_0 = 6 and for three different TI cases. Recorded time length ~ 90 s. Yellow = No Fault Size, Dark blue = 1% Fault Size, Green = 5% Fault Size, Navy blue = 10% Fault Size and Light Blue = 15% Fault Size.

it was evident this would be replicated at these figures. Even though most TI, fault sizes proportional relationships were relatively consistent as the fault size signal and the TI scenario increased, there were some amplitudes that yielded higher amplitude values at TI = 2% than TI = 8%, mainly at the f/f_0 = 3 and f/f_0 = 6 scenarios in both the rotor and the generator. For example, in figure 6.14, amplitude values at f/f_0 = 3 for the generator and rotor TI = 8% are the lowest of the three TI cases compared to TI = 2%, even the rotor values yield the relatively same values of the generator at TI = 2%. The latter suggests that it does not exist a particular trend of the TI high case against the fault size increment, and that the TI is uncorrelated to the rotor imbalance faults, except for the directly proportional relationship between TI = 15% and fault size = 15.8% for both the rotor and the generator.

Lastly, replicating the methodology previously utilised in chapter 5, in order to

configure a more simplistic condition monitoring technique, control charts using the frequency domain data from the torque measurements of the DTTR were built. The results from this set of simulations are shown from figures 6.15 to 6.18. In order to obtain these results, the rotor and generator torque signals were normalised and, as previously done in chapter 5, a high-pass filter with a cutoff frequency of 0.5 Hz was implemented in order to remove the amplitudes yielded prior this frequency, hence the time signals were reduced from 90 s to 71 s and the 30 s to 18 s respectively. By doing so, only the amplitudes reached near $f/f_0 = 1$ are considered. Then, a spectrogram was obtained with this new high-pass filter torque signals, utilising a 'hamming' window and five rotations of the rotor to be considered. Finally, a time series was created by extracting all the values obtained from the spectrogram at $f/f_0 = 1$. A set of MCL and UCL were plotted (gray lines) calculating them by obtaining the mean value of the torque signal at fault size = 0%, and UCL by utilising equation 5.4. Four control charts were obtained for the rotor and generator torque signals, for all the TI cases aforementioned and fault size scenarios, for two different recorded time lengths.

Table 6.3 displays the number of points surpasses the UCL for each fault size case, rotor, generator and differing time recorded lengths. Overall, it is observed that for all four cases when fault size = 0% is plotted, the $f/f_0 = 1$ torque values mostly remain below the UCL, indicating that the time series values extracted from the spectrogram are under control of the selected standard errors. Moreover, it is evident that most of the time series values are above their respective UCL from fault sizes 1% to 15% and that the time series increases in magnitude proportionally as the fault size increases as well. Mainly at the rotor figures 6.15 and 6.16, it is clear that the time series structure replicates itself with a higher magnitude when the fault size is bigger, compared to the time series obtained from the generator side. In fact, it is evident that the rotor control charts provide better results compared to the ones obtained from the generator, specifically at the TI = 2% and 8% scenarios for both recorded time lengths. The latter was expected as it was observed that the standard deviation obtained from the calculated time series was higher across TI cases and fault sizes compared to the ones obtained from the rotor side, leading into discrepancies on the time series structure. On the other hand, it was

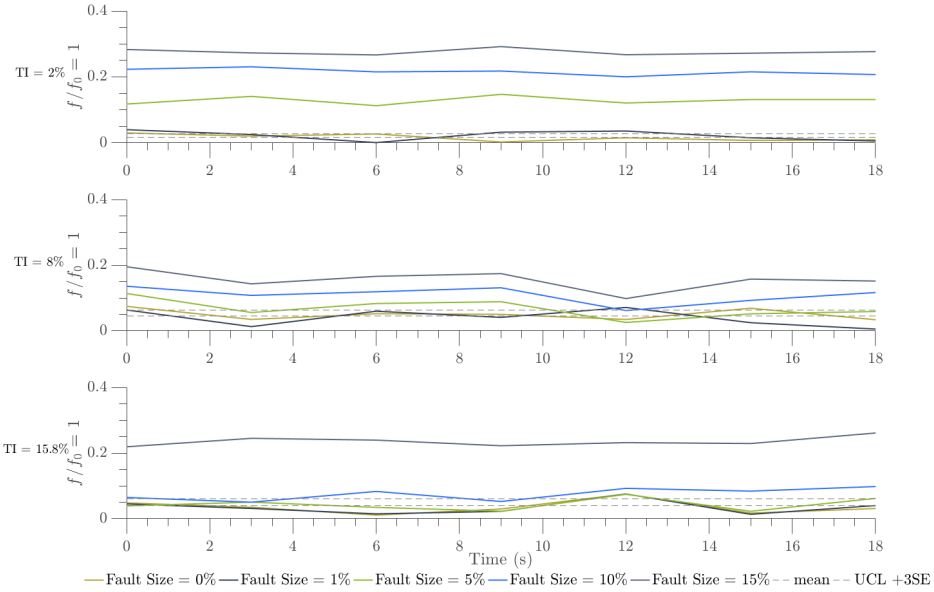

Figure 6.15: Control Charts for each of the fault size cases recorded on the DTTR from the Rotor for $\lambda = 4$, with a flow velocity of 1.0 ms^{-1} and for three different TI cases. Recorded time length ~ 30 s.

observed that at TI = 15.8% fault sizes of 1% and 5% for both recorded time lengths obtained time series points relatively close to the UCL, suggesting that at higher turbulent flows, the control chart algorithm does not clearly detect these faults at these particular sizes. Finally, it is indistinct the effect of the time recorded length from the time series obtained at the rotor side, except for the fact that the 18 s time series obtained less points above the UCL than the ones from the 71 s time series. The latter could be explained again from the smaller amplitudes observed at the PSDs comparing these two scenarios, where the 90 s time series yielded higher amplitude values at $f/f_0 = 1$.

More variability was observed from the results obtained from the generator side for both time length scenarios, where time series did not follow the same structure within fault sizes signals and that most time series varied around the MCL and UCLs. Still, as observed from the results at table 6.3, similar to what happened at the rotor side, as the fault size increased, the more values above UCL were detected. However, it was found

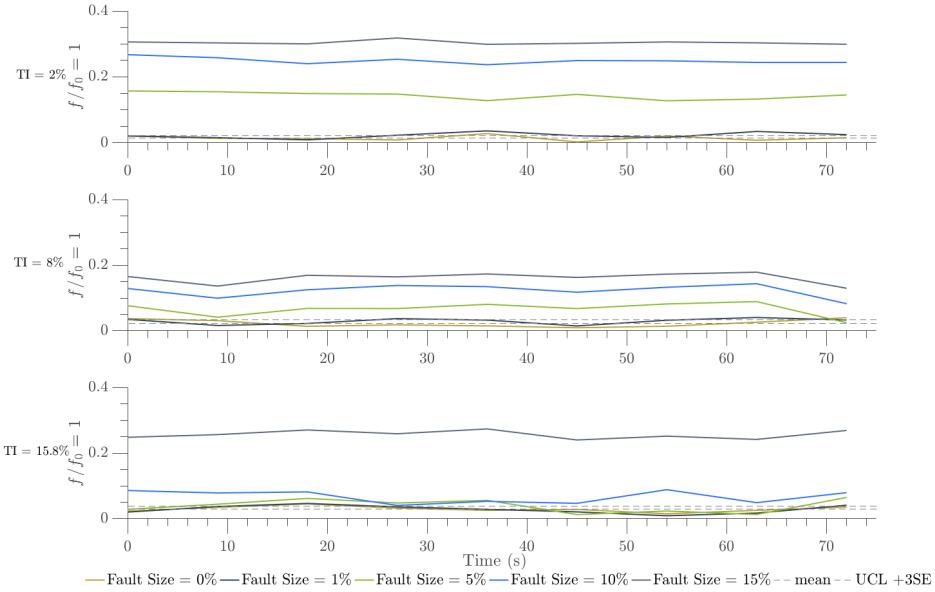

Figure 6.16: Control Charts for each of the fault size cases recorded on the DTTR from the Rotor for λ = 4, with a flow velocity of 1.0 ms^{-1} and for three different TI cases. Recorded time length ~ 90 s.

in figure 6.18 in TI = 2% at fault size of 5% that none of the time series points surpassed its respective UCL, whilst time series for 1%, 10% and 15% are all above the UCL. Interesting, the latter was not replicated at figure 6.17, providing better results for this set of simulations compared to what it was seen at the generator PSDs. It was also observed that the highest time series points were found at TI = 15.8% with a fault size of 15%, and that, as what it was observed from the rotor signals, the control chart does not clearly detect fault sizes of 1% and 5% at higher turbulent flows. Still, the control charts developed for the generator side of the results obtained from the DTTR accomplished to detect most of the fault signals being recorded in this set of simulations, despite the time series variability and other interference such as the gearbox and drivetrain losses.

Finally, considering the results obtained from the control charts generated for both the rotor and the generator, it is noticeable that the DTTR attained to reproduce the experimental set of simulations performed at a flume tank, and that it effectively accom-

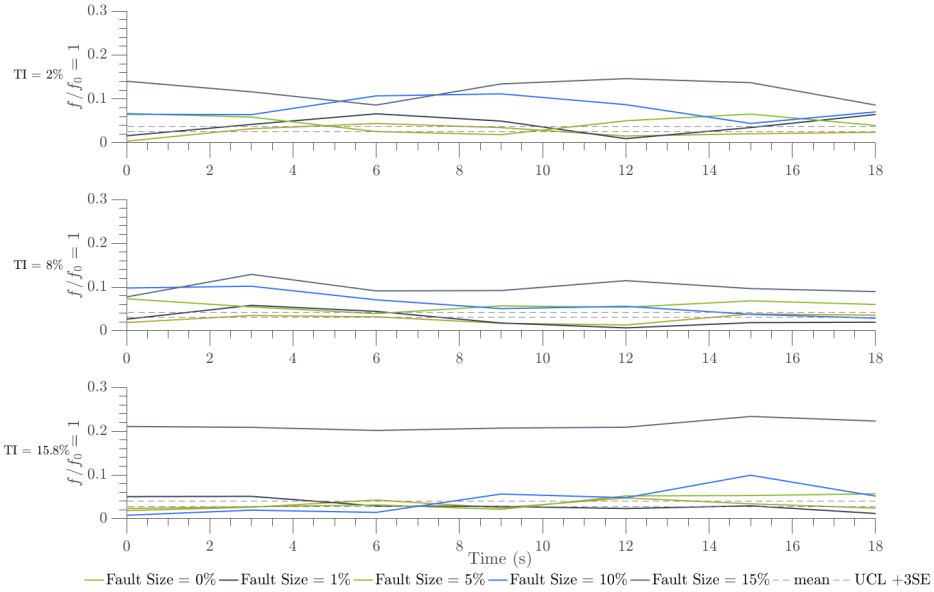

Figure 6.17: Control Charts for each of the fault size cases recorded on the DTTR from the Generator for $\lambda = 4$, with a flow velocity of 1.0 ms^{-1} and for three different TI cases. Recorded time length ~ 30 s.

plished the goal of utilising the proposed CM algorithm to detect possible failures by the use of frequency domain data. Essentially, the use of these control charts at this particular case scenarios demonstrate that in both cases and at different recorded time lengths, they managed to detect rotor imbalance failures with differing fault sizes and under the presence of different tidal turbulent flows. An exception was detected in the generator side, where the CM algorithm failed to detect fault size of 5% at TI = 2%. Even though that it was found that the rotor control charts were more effective into displaying the faults symmetrically, the generator side also managed to reproduce these failures and detect them most of the times. Overall, it can be said that at this particular stage of this research, the DTTR would be able to reproduce and detect fault torque signals if they exceed a magnitude over 5% from its mean harmonic value. It could also be determined that in order to establish a CM tool to prevent a possible failure that may contribute to larger HATT malfunctions, control charts could possibly deliver a trigger if they detect over 4 or 5 points above the UCLs. Therefore, this developed CM tool could possibly support

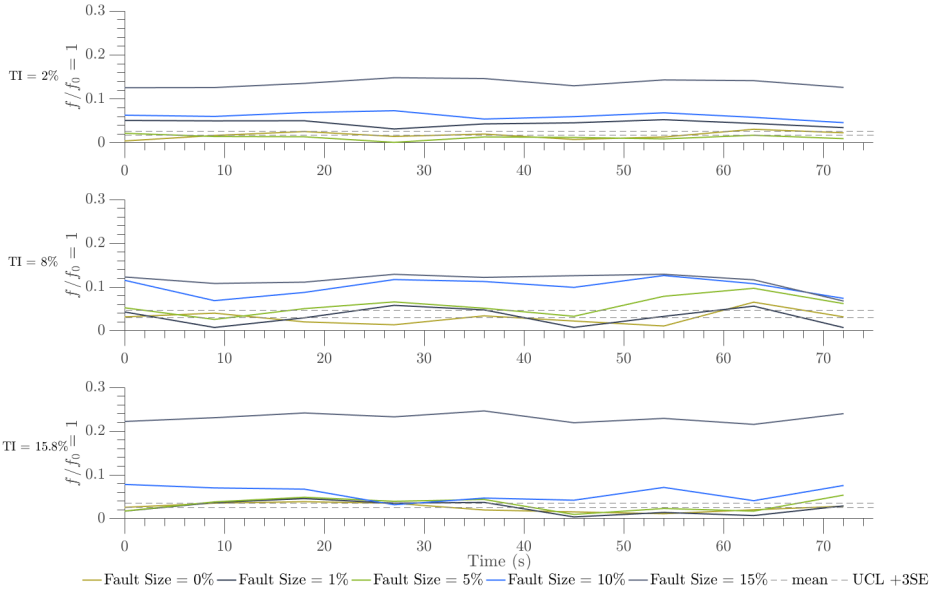

Figure 6.18: Control Charts for each of the fault size cases recorded on the DTTR from the Generator for $\lambda = 4$, with a flow velocity of 1.0 ms^{-1} and for three different TI cases. Recorded time length ~ 90 s.

HATT operators by promising a time-based preventive or corrective maintenance that could lead to cost savings or resource optimisation.

It has been demonstrated that the drive train test rig was able to reproduce the unsteady flow conditions that were obtained from a flume tank set of simulations with different tidal turbulent levels, and that it effectively detected in both the rotor and the generator the different rotor imbalance fault sizes. The latter enables the use of the test rig for further condition monitoring research, where synthetic data was developed to explore differing tidal stream velocities and integral length scales, in addition to the rest of the variables already considered in this chapter. The results of this set of simulations are detailed in chapter 7.

Recorded Time Length	Motor	TI (%)	Fault Sizes 0%	1%	5%	10%	15%
30 *s*	Rotor	2	2	3	9	9	9
		8	2	3	5	8	9
		15.8	1	1	4	7	9
	Generator	2	1	6	5	9	9
		8	1	2	8	7	9
		15.8	2	3	3	6	9
90 *s*	Rotor	2	1	4	9	9	9
		8	2	3	8	9	9
		15.8	1	2	5	9	9
	Generator	2	1	9	0	9	9
		8	1	3	7	9	9
		15.8	2	4	5	8	9

Table 6.3: Table providing an overview of the points of the built time series above their respective upper control limits from control charts of figures 6.15 to 6.18.

7

Drive Train Simulation Results of Unsteady Synthetic Data

This chapter extends the simulation and testing of the CM algorithm under the unsteady 'synthetic' data on the DTTR. This synthetic data was built by the author with a MatLAB code in order to simulate more complex tidal conditions compared to the ones obtained in chapter 6, and therefore to further utilise the CM algorithm under other input flow variables. This follows as in chapter 6 it was demonstrated that the drive train test rig was able to reproduce the unsteady flow conditions that were obtained from an experimental testing campaign in both the rotor and the generator. Details of the developed simulation approach and the results of the CM algorithm implementation are outlined herein, along with the results of the impact of turbulence intensity, velocity and integral length scales in the CM algorithm performance.

7.1. Resource Simulation

The simulation of synthetic data has been previously modelled using MatLAB in the literature. Pawlowicz et al. [2002], utilised the T_TIDE MatLAB program to perform classical harmonic analysis with nodal corrections and tidal predictions using the analysed constituents, effectively calculating the tidal potential, tidal amplitude estimates and confidence intervals using different set of assumptions about the structure of residual noise. Elghali et al. [2007] utilised the French Navy Hydrodynamic and Oceanographic Service current velocities for spring and neap tides from the Raz the Sein, France, in order to model the performance and dynamic load assessment in different operating conditions and further control system development for turbine operation based on pitch and speed control and to compute them in predefined time ranges. Moreover, Elzalabani et al. [2015] modelled the electrical model for tidal current speed profile, turbine, drivetrain and a permanent magnet synchronous generator by the use of the MatLAB/Simulink package. This allowed the author to calculate the maximum electrical power extraction point based on theoretical data utilised from an OpenHydro turbine model and tidal mean values from the Suez Gulf, Egypt. Similar to what it was done in this research, Sousounis et al. [2016] recreated the tidal resource by using mean flow speeds, adding white noise as predicted turbulence and the tide effects by using a first-order Stoke model. Piano et al. [2017] recreated flow profiles from the T_TIDE package in order to inform site selection and turbine installation design criteria by highlighting the spatial assessment of a tidal energy converter farm with optimum orientation to prevent yaw misalignment. All the aforementioned authors defined a simple strategy to model more complex situations in order to contribute to the field and improve the tidal devices performance and operational lifespan. By modelling synthetic data, research can effectively be advanced to simulate possible tidal profile conditions that are either not feasible nor realistic to acquire from experimental testing or are highly computational intensive by the use of numerical models.

The main objective of the work described in this chapter was to create a fluid time series that would consider three different integral length scales and three turbu-

lence intensity percentages, in order to obtain three different fluid velocities with their respective torque values. This was further developed to increase a rotor fault magnitude in the torque into a specific percentage, and finally replicate the rotor torque synthetic signals into the DTTR. First, a range of L_x = 1 m, 5 m and 10 m values were selected to be run in this model as explained later in this chapter. Three sets of turbulence intensity percentages were selected to be as 5%, 10% and 15% to be evaluated on the test rig. These values were selected as they would be very similar to the ones obtained in the experimental test campaign in IFREMER as explained in chapter 6. Finally, three sets of mean tidal flow velocities were chosen to create a set of stochastic fluid velocity time series. These values are 0.8 ms^{-1}, 1.0 ms^{-1} and 1.2 ms^{-1}. There were selected to be the same as the ones obtained in the experimental test campaign in KHL as explained in chapter 5. Finally, the total time length to be chosen to run the MatLAB code to create each time series was of 150 s with a sample rate of 1,000 Hz. However, in order to analyse the results from both chapters 6 and 7 homogeneously, the time series were constrained to 30 s and 90 s respectively when they were implemented to be run on the test rig, given the rotor torque limitations and the influence of high temperatures already described in chapter 3. Overall, a total number of 27 fluid velocity time series were obtained considering the three sets of values of integral length scales, turbulence intensity percentages and mean fluid velocities to later be run on the test rig. It is worth noting that each time series was highly computationally intensive to create, as it took more than 8 hours a day to run a set of 9 time series.

The MatLAB code implemented in this research generates a realisation of a stochastic fluid velocity time series. First, the variance input into the time series is given through the following equation:

$$\sigma = (\frac{TI * \overline{u}}{100})^2 \tag{7.1}$$

where TI % are the three sets already discussed, and $\overline{u}$ is the mean tidal flow velocity. This is utilised once a power spectral density is produced by implementing the equation explained in chapter 3, as follows:

$$\frac{fS(\omega)}{\sigma^2} = \frac{\frac{4fL_x}{\overline{u}}}{[1+70.78(\frac{fL_x}{\overline{u}})^2]^{\frac{5}{6}}} \tag{7.2}$$

where L_x is the integral length scale previously selected and f is a frequency range vector of 1,000 Hz. Finally, in order to create a random fluid velocity time series and adhere to Kolmogorov's theory, a dissipation rate spectrum of the power spectral density was defined from the previous equation, ξ is defined as:

$$\xi = \int_n^{n+1} \frac{fS(\omega)}{\sigma^2} ds \tag{7.3}$$

The latter relates to equations 3.13 and 3.14, since ξ would provide an approximate numerical integration of the energy spectral density dissipation by recreating eddies or a number of waves per unit distance (κ) [Rieutord, 2014]. The MatLAB code was modelled to utilise the trapezoidal numerical integration method, that approximates the integration over an interval by breaking the area under the curve down into trapezoids with more easily computable areas [MathWorks, 2022]. Overall, U was calculated using the following equation:

$$U = U + \sqrt{\xi * Acos(2\pi\frac{\overline{\omega}}{60}) + Bsin(2\pi\frac{\overline{\omega}}{60})} \tag{7.4}$$

where A and B are two vectors with the same time vector length created with random numbers. This process delivers a U time series considering the proposed L_x, the TI % and random velocity changes through a 150 s time vector. Then, the U time series were converted into rotor torque values considering a turbine optimal λ control, by applying the following equation:

$$\tau = \frac{1}{2} C_\theta \rho A r U^2 \tag{7.5}$$

where C_θ is the torque coefficient at $\lambda = 4$, ρ is the water density and is typically

assumed to be 1025 $kg \cdot m^3$ and A the rotor swept area in m^2, that as detailed in chapters 3 and 4, the rotor diameter of the test rig is set to be 0.9 m.

The implementation of the torque time series into the test rig is outlined in section 7.3. As previously mentioned in chapter 3, the test rig was limited to be run up to 70 Nm in order to prevent possible failures and excessive heating. Running the torque time series built for this research needed additional time to ventilate the test rig from one set of simulations to another. The highest torque, obtained from the 27 created torque time series was from L_x = 10 m, TI = 15% and a $\overline{u}$ = 1.2 ms^{-1} was of a τ_{max} = 62.9 Nm. Thus, torque time series were constrained to run two different time lengths at the DTTR and again, study the influence of sampling rate and time in the expected CM algorithm output whilst preventing the test rig being run at a higher torque value than the hardware limitations. The selected time lengths were 30 s and 90 s, similar to what was done in chapter 6.

Before flow characterisation can be completed and considering the hardware limitations, an additional test to effectively determine the accuracy of the results obtained from the built fluid velocity time series was performed. The latter was determined via an autocorrelation function, which was set to verify if TI%, $\overline{u}$ and L_x show a strong relationship against the 150 s the U series were modelled.

7.2. Integral Length Scale and Resource validation

In the wind turbine industry, where the longitudinal scales are typically in the order of hundreds of meters, investigation suggests that they have a secondary role on the blade fatigue loads. In a tidal channel, however, the length scales will be physically constrained by the seabed and surface, and are likely to be of the order of the channel depth and width. Since it is considered that a HATT would occupy a large portion of the water column (i.e. about 30 to 50% of both the depth and width of the water column), the effect of the integral length scale in HATTs would be relevant compared to the impact in the wind industry [Milne et al., 2010]. Observations of integral scales for fast

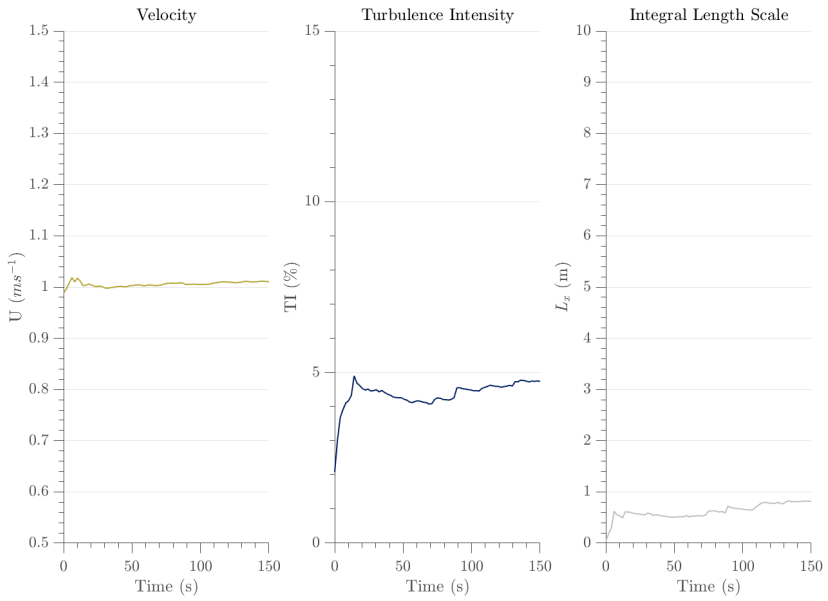

Figure 7.1: Effect of sample time on mean velocity, turbulence intensity and integral length scale with a U= 1 ms^{-1}, TI = 5%, and L_x= 1 m over a time period of 150 s.

7

flowing tidal sites in the literature in order to define a common integral length scale are scarce. To mention a few researchers, Thiébaut et al. [2020] deployed ADCPs near the port of Gaury, in the eastern part of Alderney Race, France. They obtained time series of the integral length scale associated with the streamwise direction calculated at a height matching the hub of a HATT. It was found that L_x ranged between 30 m and 100 m with a mean of 74 m and that it was dependent on the flow speed. Maximum integral length scales were associated with both peak flood and ebb velocity with values of L_x slightly higher during flood tide. On the contrary, Milne et al. [2013] reported that the Sound of Islay the median streamwise length scales at an elevation of z/h = 1 (where h is the channel depth and z is the distance from the seabed) were approximately 10 m and 13 m during the flood and ebb respectively. The author compared this output to what it was previously confirmed by Milne et al. [2010], where theoretically it was expected to obtain a length scale physically constrained by the channel depth and the distance from seabed. This indicates there was a difference of only 7% in the comparison. Similarly to what it

was found in the latter, Perez et al. [2020] developed three different techniques to decomposing wave and turbulence in Bank Strait, Tasmania, quantifying turbulence intensity, turbulent kinetic energy and integral length scales. It was observed that the maximum L_x obtained from a synchrosqueezing wavelet transform (SWT) technique was of 28.82 m in an ebb tide for 22.68 s, with a mean of 8.21 m for a period of 7.09 s. Therefore, inspite of its inherent assumptions associated with an idealised steady flow and a relatively smooth bed, considering the integral length scale component into the streamwise fluid velocity calculation could provide reasonable estimates of the resource.

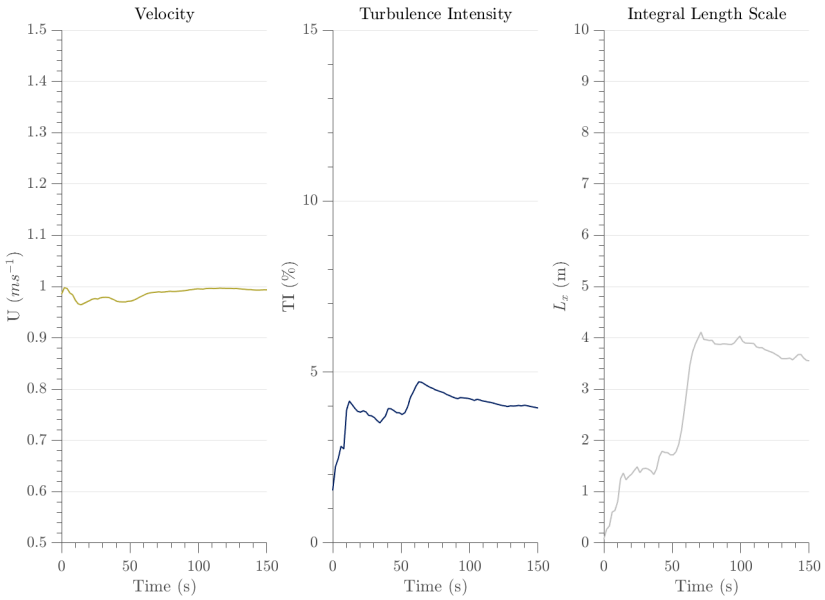

Figure 7.2: Effect of sample time on mean velocity, turbulence intensity and integral length scale with a U= 1 ms^{-1}, TI = 5%, and L_x= 5 m over a time period of 150 s.

Consequently, the range of L_x values for this research were decided by considering, as already mentioned, the test rig limitations. Consideration was also given to the torque values obtained from the integral length scale component of the fluid velocity time series, along with the values obtained from the IFREMER experimental testing utilised for this research and the literature. Therefore, the range was set to be L_x = 1 m,

5 m and 10 m to compare the effect of length scale into the rotor imbalance fault detection through the proposed CM algorithm. The decision of these three values was based on setting a range from the largest L_x value obtained in the IFREMER test campaign as mentioned in table 6.1 (L_x = 1 m, to the largest possible L_x value to be replicated on the test rig given what it was found on the literature (L_x = 10 m). The results of this are presented in section 7.4.

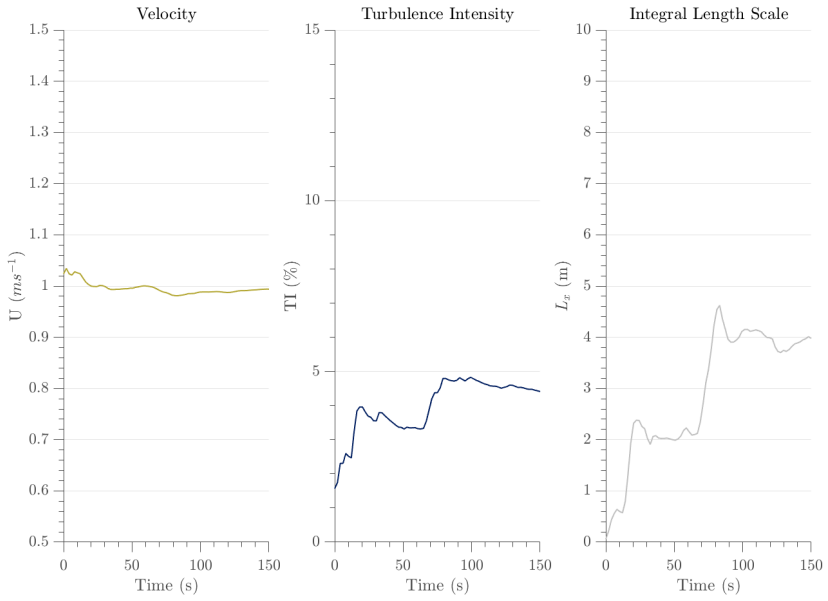

Figure 7.3: Effect of sample time on mean velocity, turbulence intensity and integral length scale with a U= 1 ms^{-1}, TI = 5%, and L_x= 10 m over a time period of 150 s.

Figures 7.1 to 7.3 display the U, TI % and L_x obtained from the U built time series for a time period of 150 s. In terms of practicality, only results of $\overline{u}$ = 1 ms^{-1} and TI = 5% are shown. In figure 7.1 it can be seen that the mean velocity converges after 50 s, but the turbulence intensity stabilises after 100 s. Similar to what is seen in the latter, figure 7.2 demonstrates the same results for both U and TI %, but in figure 7.3, U stabilises after 100 s and TI converges around 150 s. Mean U obtained for the three cases is 0.99 ms^{-1}, although TI in figures 7.2 and 7.3 only reached for a maximum TI of 4.4% when a value of 5% was expected. In terms of validating the integral length scale

component in the built fluid velocity time series, they showed a greater variation and in the three figures needed more than 120 s to stabilise. Particularly, in figure 7.3, which reached a L_x of 4 m. The latter means that in order to be able to accurately model a synthetic U time series with on L_x greater than 5 m, a time series should be built for a longer period of time. However, given the torque limitations of the test rig, it was decided to limit the time series to 90 s and utilise the built U time series as they provides sufficient accuracy for velocity and turbulence intensity for the three cited cases [Blackmore et al., 2016].

7.3. DTTR data characterisation and Software Implementation

Precisely as was done in chapter 6, the rotor torque time series obtained from the U time series were conditioned in order to shorten the time period from 150 s to 30 s and 90 s for the 27 cases performed at the DTTR. The sampling rates to record both the rotor and generator outputs were set at the IndraWorks software and they were 50 Hz in the rotor side, 125 Hz for the 30 s and 25 Hz for the 90 s for the generator side. As mentioned in both chapters 3 and 6, these sampling rates were set this way as the available memory depths for each driver that enables both the rotor and generator to operate are different. Likewise, the mean rotational velocity was set to be 674.74 RPM, 848.7 RPM and 1018.6 RPM for each case where the $\overline{u}$ are 0.8 ms^{-1}, 1.0 ms^{-1} and 1.2 ms^{-1} respectively. As explained in chapter 3, only speed control was considered during this research development, so the effect of turbulence and integral length scale in the rotational velocity of the test rig were considered negligible for this purpose. The rotational velocity was set through the IndraWorks software via the easy startup mode as previously explained in section 3.2.3. Additionally, the generator rotational speed was multiplied by 10 and set with a negative value, due to the gearbox interaction.

Similar to what was done in chapter 6, the rotor torque values were obtained from the built U time series utilising the equation 7.5, and were converted into a 'txt' for-

mat, for both scenarios of 30 s or 90 s to be recorded at the DTTR. The rest of the process is as outlined previously in section 6.2.1. An overview of the LabVIEW code implementation in order to obtain a stochastic torque input into the rotor based in the fluid velocity components for this chapter, is displayed in figure 6.4. Finally, a total of 718 text files were obtained for this research, including all the combinations of variables, the different fault sizes and repeats.The data obtained from both the test rig rotor and generator were analysed and processed in order to obtain the results, explained in the following section.

7.4. DTTR Unsteady Synthetic Data Results

The analysis of the results obtained are detailed in this section. Figures 7.4, 7.5 and 7.6 display the mean normalised values from the rotor torque data signals obtained from the DTTR for $\overline{u}$= 1 ms^{-1} and a range of turbulence intensities of TI = 5% (navy blue signals), TI = 10% (yellow signals), and TI = 15% (green signals). Each signals windowed five times from the total time length of 90 s, whilst displaying the actual rotor torque signals overlapped five times (gray signals) for the fault sizes of 0%, 1%, 5%, 10% and 15%. Each figure shows the normalised torque values for L_x = 1 m, 5 m and 10 m respectively. Compared to what it was seen in figure 6.5, when the fault sizes increased in all three L_x cases, they are visually imperceptible in these graphs. In the experimental data the cyclical patterns in the mean torque values as the fault size increased were evident across the TI cases. Herein, the added fault size in the torque values is indistinct across the L_x and TI cases, yet it is expected to be detected under the CM algorithm implementation. The stochastic nature of the turbulence is evident when TI increases, as the gray signals show higher peaks and standard deviations, reaching values above 7 Nm under TI = 15%. Furthermore, comparing the three different figures obtained for each L_x and the obtained standard deviations, the presence of the L_x is negligible to the obtained torque values when recorded on the DTTR. Still, it is important to verify if there is an influence of the selected length scales in this research when the torque values are examined under the frequency analysis, that will be explained later in this chapter.

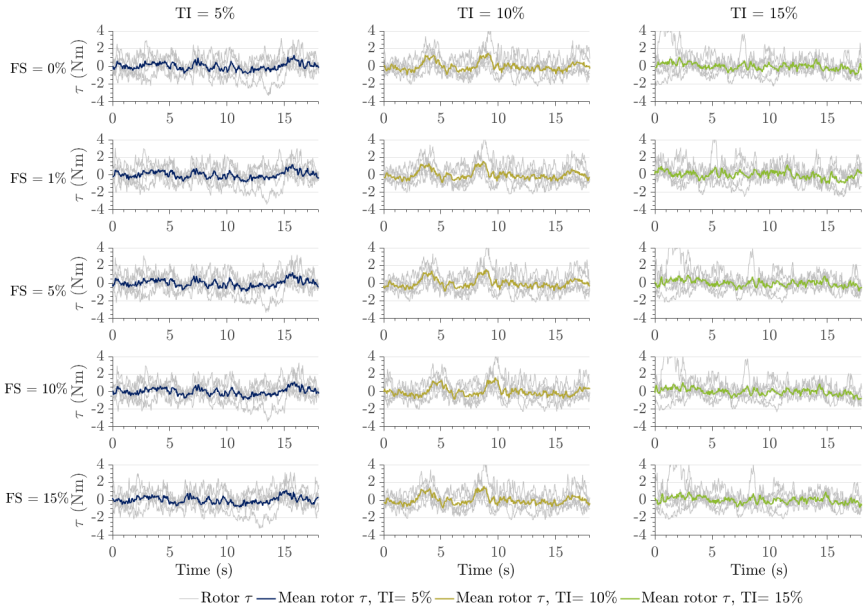

Figure 7.4: Normalised rotor torque data signals for TI = 2%, 5% and 15% at $\overline{u}$ = 1 ms^{-1}, L_x = 1 m, and for fault sizes of 0%, 1%, 5%, 10% and 15% windowed five times from the total time length and a mean value was calculated from all the iterations.

7

Now, in order to compare the outcome obtained from the rotor and the generator signals, figure 7.7 exhibits the torque signal over a period of 80 s from the synthetic data, and the obtained results from the DTTR from both the rotor and the generator. Again, the results are compared in terms of the three L_x and TI cases aforementioned, for a $\overline{u}$ = 1 ms^{-1} and a fault size = 0%. The smooth data was generated via convolution function in MatLAB with a simple uniform window function of 20 s length. Similar to what it was shown in figures 7.4, 7.5 and 7.6, the three smoothed signals display a higher variability when TI increases, and represent an unsteady torque loading that may significantly affect the gearbox and subsequently, the generator output [Sørensen and Sørensen, 2010]. Interesting, higher torque values were found at L_x = 1 m when compared to L_x = 5 m and L_x = 10 m, where there is a difference of 10 Nm comparing the L_x = 1 m to L_x = 10 m, with TI = 15%. However, mean values across L_x = 10 m are larger compared to the ones obtained in L_x = 1 m, and standard deviations do not differ sig-

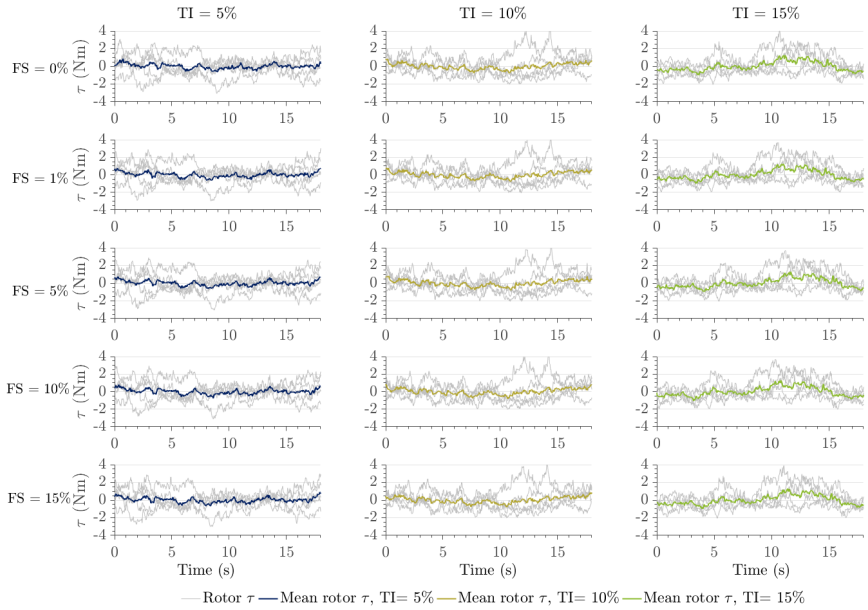

Figure 7.5: Normalised rotor torque data signals for TI = 2%, 5% and 15% at $\overline{u}$ = 1 ms^{-1}, L_x = 5 m, and for fault sizes of 0%, 1%, 5%, 10% and 15% windowed five times from the total time length and a mean value was calculated from all the iterations.

7

nificantly from each simulation. It can be seen that there is a high variability when TI increases in each L_x scenario, where the standard deviation increases three times in order of magnitude when TI = 5% is compared to TI = 15%. The latter was replicated in previous research [Ebdon, 2019], where the impact of turbulence intensity and integral length scale were analysed over a range of different C_p, C_T and C_θ values. Herein, it was established that there was a tendency to produce the highest fluctuations at C_θ performance metrics at the highest turbulence intensity values. Furthermore, the author described a dependence on length scale values, with a larger length scale also leading to greater fluctuations in turbine performance, with this dependence becoming more pronounced at higher values of turbulence intensities. Therefore, the fact that the maximum values being obtained at L_x = 1 m compared to L_x = 10 m, both found at TI = 15% may be considered inconsistent to what it was determined in the literature. However, given the randomness nature of turbulence it may be expected that this will not be a consistent or

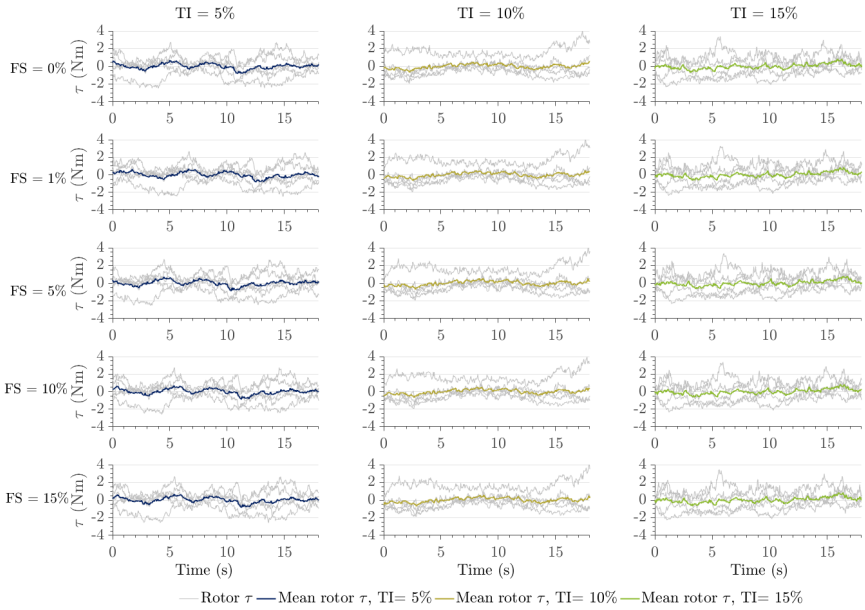

Figure 7.6: Normalised rotor torque data signals for TI = 2%, 5% and 15% at $\overline{u}$ = 1 ms^{-1}, L_x = 10 m, and for fault sizes of 0%, 1%, 5%, 10% and 15% windowed five times from the total time length and a mean value was calculated from all the iterations.

coherent determination for every given simulation. Still, these figure demonstrate that if the turbulence in a flow consists of many large-scale features, it may be expected that any given rotor performance metric, in this case torque values, will result in greater fluctuations and therefore a larger torque to be delivered. The latter may suggest that at all cases of L_x = 10 m and TI = 15%, a greater variation in torque would be observed.

In contrast to this, it was observed in figure 7.7, that the DTTR presented further discrepancies in replicating the theoretical data in both the rotor and the generator obtained signals, and exhibited a proportional increment in fluctuations as TI increases. As expected, the rotor accomplished the mean values obtained in the theoretical data across smaller TI and integral length scale values, but presented a negative phase shift as these values increased. On the other hand, the generator signals presented losses of around 30% in all cases, similar to what it was found in the experimental set of simulations, again obtaining the highest % loss in the L_x = 1 m and TI = 5% with a value of 36.81

%. Plus, the generator signals also presented phase shift across all cases, with the highest value obtained in the L_x = 10 m and TI = 15% scenario. Still, the DTTR was shown to replicate multiple torque signals and represent the stochastic nature of turbulence with its most characteristic features. Therefore, for the purpose of this research, the developed synthetic data and the outputs obtained from the rotor and generator are able to be utilised in order to analyse the frequency content and review the CM algorithm effectiveness, which will be discussed in detail below.

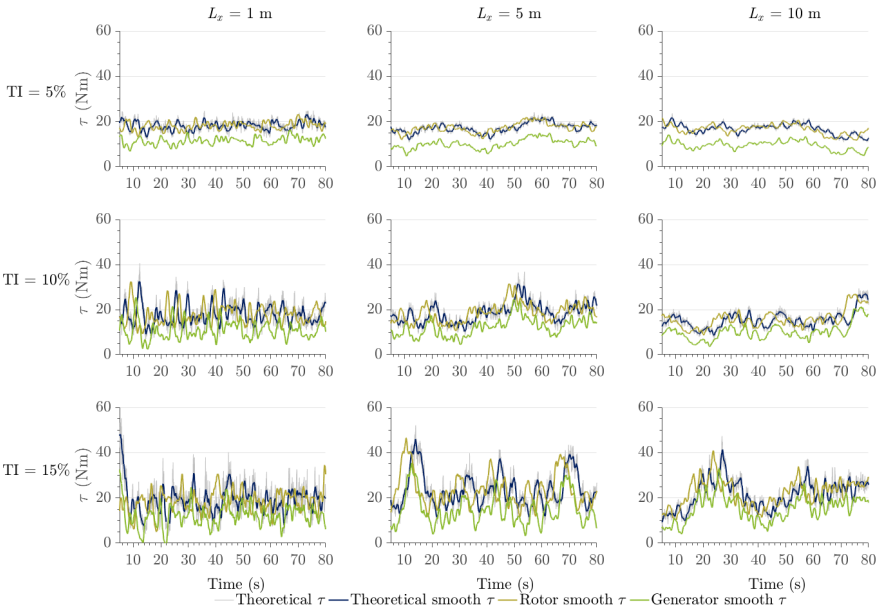

Figure 7.7: Torque loading time series obtained from the rotor and generator on the DTTR, overlapped with the theoretical torque data signals for TI = 2%, 8% and 15.8% at $\overline{u}$ = 1 ms^{-1}, L_x = 1 m, L_x = 5 m, L_x = 10 m, and fault size of 0%.

Again, a comparison of boxplots to showcase the rotor and generator torque signals, are displayed in figure 7.8. For this case, only the boxplot of $\overline{u}$ = 1 ms^{-1}, L_x = 5 m and the three previously mentioned TI cases, including the five fault sizes and repeats are shown. First, it is clear than in TI = 5% and TI = 15%, most of the whiskers limits are in each of the maximum values for its respective boxplot. The latter means that most of the values obtained from the rotor and the generator are above the median values and

upper quartiles. Evidently, this is correlated with figure 7.7, where it was mentioned that the standard deviation's magnitudes were directly proportional to the TI increment. Still, the rotor signals display a consistent tendency across all cases and repeats, as it has been previously observed in both the steady state and unsteady state simulations. Contrarily, the generator torque signals show variation between repeats of each simulation, particularly in the TI = 15%, fault size = 5%, where the upper quartile is larger in the second dataset compared to the first one, with a difference of 0.3 Nm. Except for this case, median values difference between repeats across all cases is around 0.10 to 0.20 Nm, and the data distribution differences are relatively small. It can therefore be stated that these boxplots demonstrate the test rig reliability to replicate rotor and generator torque signals.

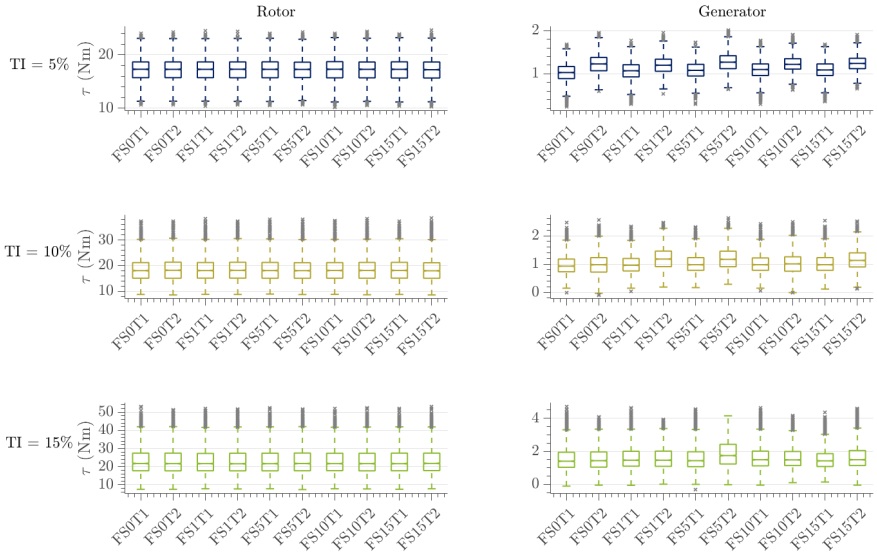

Figure 7.8: Boxplot of torque signals for the three TI cases undertaken, $\overline{u} = 1\ ms^{-1}$, $L_x = 5$ m and for the five fault sizes cases, including repeats. Left size column are rotor torque signals, right size column are the generator torque signals.

The generation of the PSDs were replicated for this analysis in order to review the influence of integral length scale, turbulence intensity, and time. This in turn was in

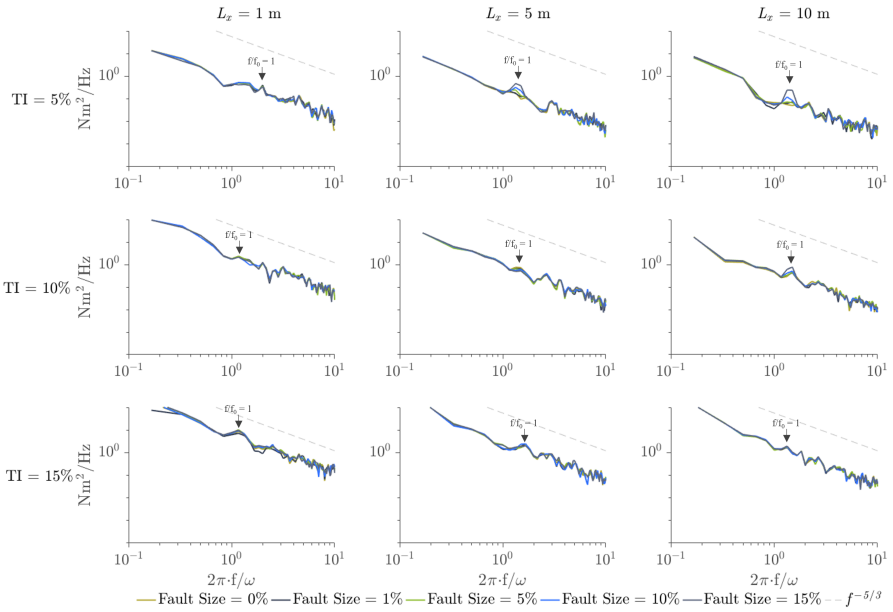

Figure 7.9: PSDs calculated for each of the fault size cases recorded on the DTTR from the Rotor for the $\overline{u}$ = 1.0 ms^{-1}, all three L_x cases and for three different TI cases. Recorded time length ~ 30 s.

7

order to be able to implement the CM algorithm to detect torque imbalance faults. For terms of practicality, only results obtained from $\overline{u} = 1\ ms^{-1}$ are displayed at the moment. PSDs were calculated with the 'pwelch' function utilising the normalised rotor and generator for recorded time lengths of 30 s and 90 s for each motor, and are displayed from figures 7.9 to 7.12. Herein, the normalised torque signals are plotted against the rotor or generator rotational velocity in order to highlight any harmonics associated in their torque loading fluctuations. The figures were delimited in order to analyse only the lower frequencies and the higher energy content in all of them. Replicating the methodology performed in chapter 6, the analysis of the harmonics in the inertial subrange area is undertaken to examine possible peaks that may appear at $f/f_0 = 1$, $f/f_0 = 3$ and $f/f_0 = 6$. It is also important to note that the 1st harmonic amplitudes are found to be phased about 0.5 $2\pi \cdot f/\omega$ for all cases.

The synthetic data frequency content yields lower energy content than the one

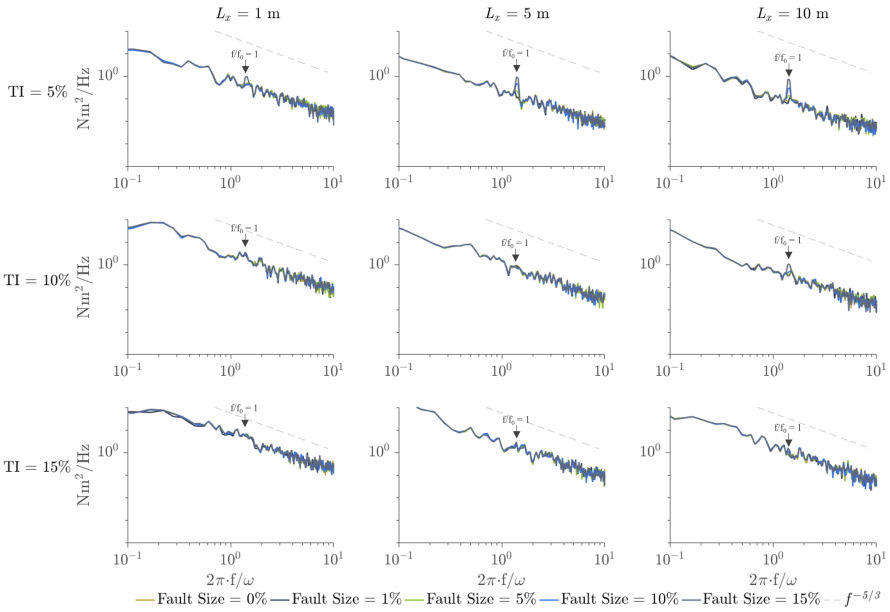

Figure 7.10: PSDs calculated for each of the fault size cases recorded on the DTTR from the Rotor for the $\overline{u}$ = 1.0 ms^{-1}, all three L_x cases and for three different TI cases. Recorded time length ~ 90 s.

shown from the experimental data detailed in chapter 6. First, across all figures it is noticeable that the PSDs lack of prominent peaks as compared to the previous figures displayed in chapters 5 and 6, yet $f/f_0 = 1$ are still revealed in most of the cases. Again as expected, higher energy content is shown to be present at lower frequencies. Also, it is important to observe that the energy content for each case presented varies, demonstrating a proportional increase as TI increases. This is approximately 10 times order of magnitude in the rotor compared to the generator output. The $f^{-5/3}$ trace was represented again with the dashed line, and similarly to what it was observed in chapter 6, it displays a better agreement in the rotor figures compared to the generator ones, where there is a high energy content at higher frequencies. Still, the $f^{-5/3}$ line up well throughout the inertial subrange of the PSD regime, which is of this research interest to analyse mainly the data obtained at $f/f_0 = 1$ in both DTTR motors.

For example in figure 7.9, the PSDs show a proportional increment in the fault

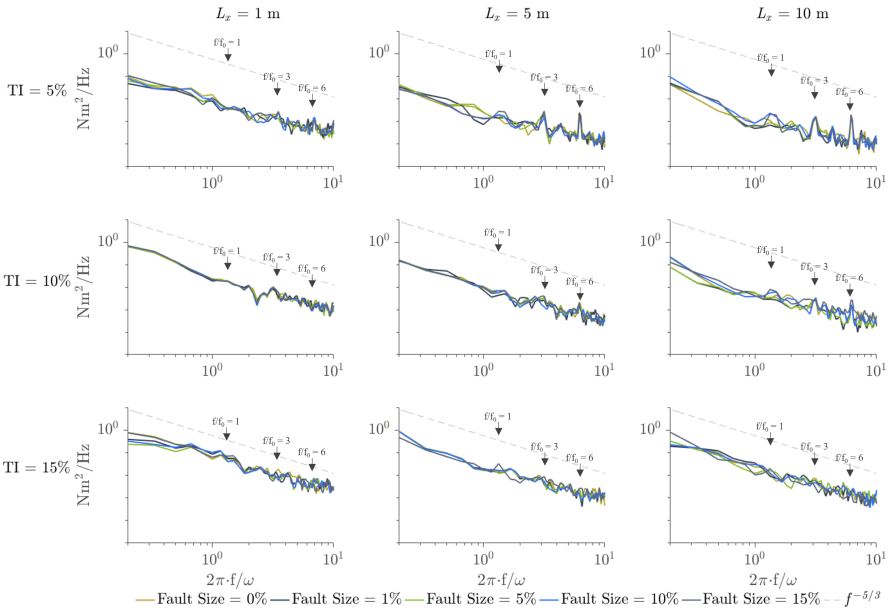

Figure 7.11: PSDs calculated for each of the fault size cases recorded on the DTTR from the Generator for the $\overline{u}$ = 1.0 ms^{-1}, all three L_x cases and for three different TI cases. Recorded time length ~ 30 s.

size at f/f_0 = 1, exposing the contribution of the fault size added into the rotor signal, with the fault size of 15% being the dominant amplitude. However, these peaks are only found in some of the cases, mainly when the TI % is of 5%. The 1st harmonic is also evident in cases L_x = 10 m, TI = 10%, and L_x = 1 m, TI = 15%. On the other hand, looking into figure 7.10, the 1st harmonic amplitudes are again found at lower turbulence intensities values across all selected integral length scales, but this is not clearly replicated in higher turbulent energy %. The imbalance of the rotor setup is also found in L_x = 10 m, TI = 10%. On the other hand, f/f_0 = 3 which represents an entire DTTR revolution, is again only detected in all TI = 5% cases across length scale values, but they are not obvious after TI increases for the rotor side, at both recorded time lengths.

Looking into figures 7.11 and 7.12, it is evident that within a larger period of time, the generator PSDs provide more consistent and significant harmonic peaks than when the generator was run for 30 s only. Although there are relatively prominent peaks

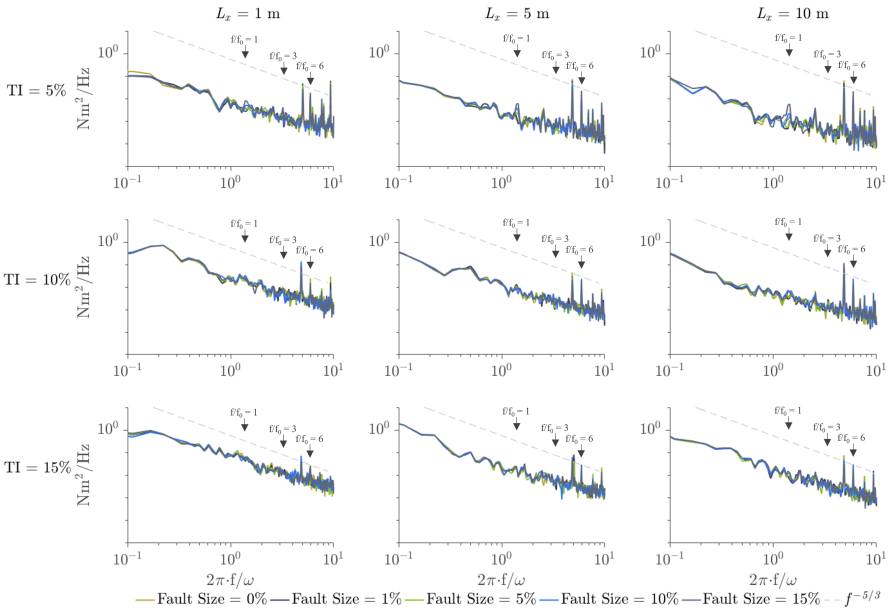

Figure 7.12: PSDs calculated for each of the fault size cases recorded on the DTTR from the Generator for the $\overline{u}$ = 1.0 ms^{-1}, all three L_x cases and for three different TI cases. Recorded time length ~ 90 s.

7

found at f/f_0 = 1 and f/f_0 = 3 in the TI = 5% cases across integral length scales in figure 7.11, it is also noticed that there is a higher variation in the obtained PSDs for all the different fault sizes, and that the expected peaks at these aforementioned frequencies are not consistent nor noticeable in the TI = 10% and TI = 15% cases. Contrastingly, figure 7.12 exhibits higher amplitudes in some of the relevant peaks being analysed. First, similar to what it was observed in the rotor figures, the 1st harmonic amplitude is only evident in the TI = 5% cases across integral length scales, displaying a proportional increment in each fault size case. Interesting, f/f_0 = 1 appears again in TI = 10%, L_x = 10 m. The latter agrees with the fact that in the rotor figures, this peak is also evident. Contrarily to what it was observed in the rotor figures, f/f_0 = 3 and f/f_0 = 6 are more repeated across all cases, where the f/f_0 = 3 was consistent being repeated at lower turbulence intensity cases and in the TI = 10%, L_x = 10 m case, and f/f_0 = 6 is seen in all cases. The three times rotational velocity of the generator neglects the contribution of the fault size to the process, yet it reveals the contribution of the tidal turbulence in the synthetic

flow. However, it was expected that a proportional increment at $f/f_0 = 3$ would be evident when TI increased, but this torque amplitude is not visible. The latter does not mean there are no discernible differences between cases, since it was seen in figure 7.4 the stochastic nature of turbulence in the obtained torque signals. On the other hand, $f/f_0 = 6$ is consistent across all cases, neglecting the influence of turbulence intensity nor the integral length scale values at the obtained cogging torque generated from the gearbox interaction. Interestingly, there was a prominent peak found at $f/f_0 = 5$ for all the cases. The latter is a topic that may be developed for future research, as it has not being referred to previously in the literature.

Overall, the PSDs development showcased contrasting results from the ones developed in the experimental data. First, the observed peaks at selected frequencies were perceptible mostly at TI = 5%, and in the TI = 10% across all the integral length scales values, particularly more certainly in the $L_x = 1$ m cases. This suggest that rotor imbalance faults are more perceptible under the influence of lower integral length scale values, for both the rotor and the generator. However the latter could be compared with the results obtained from the control charts, later explained in this chapter. It is also the case that time played a significant role in the results obtained in the inertial subrange area, particularly in the generator figures. Here there is a proportional relation with the prominent peaks obtained when the generator was run for 90 *s* compared to the 30 *s* set of simulations. Therefore, only the results obtained from the 90 *s* scenarios are displayed from here on. Finally, the fact that the 1^{st} and 3^{rd} harmonic amplitudes are not discernible in the synthetic data could be attributed to the lack of computational time in order to effectively generate a fluid velocity for higher turbulence intensity values and integral length scales respectively, as shown in figures 7.1 to 7.3, and the DTTR rotor limitations in reproducing values above 65 Nm. This may suggest that the influence of the integral length scale represents a significant factor in being able to recreate even more random, stochastic load transients in order to recognise a rotor imbalance fault under these conditions. The latter could provide an insight to determine the analysis of frequency content limitations in order to prevent a fault in a HATT operation.

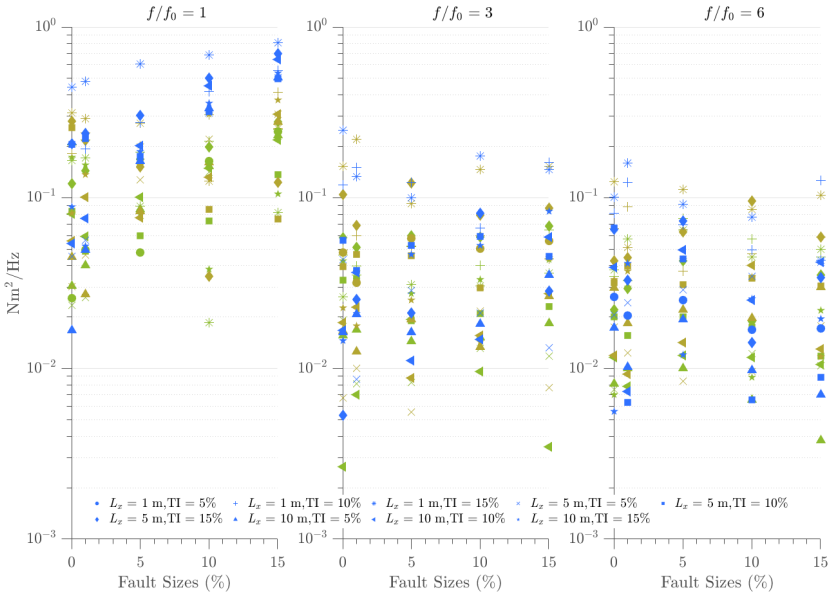

Figure 7.13: Amplitude of each of the fault size cases recorded on the DTTR from the Rotor for flow velocities of 0.8 ms^{-1}, 1.0 ms^{-1} and 1.2 ms^{-1}, for f/f_0 = 1, f/f_0 = 3 and f/f_0 = 6 and for three different TI cases and L_x cases. Recorded time length ~ 90 s.Green = $\overline{u}$ = 0.8 ms^{-1}, Yellow = $\overline{u}$ = 1.0 ms^{-1} and Light Blue = $\overline{u}$ = 1.2 ms^{-1}.

Now, figures 7.13 and 7.14 show the amplitude values obtained at f/f_0 = 1, f/f_0 = 3 and f/f_0 = 6 respectively, for both the rotor and the generator outputs. In order to compare the output obtained from the other $\overline{u}$ values (0.8 ms^{-1} and 1.2 ms^{-1}), their respective results are plotted in these figures utilising the methodology explained in chapter 5. The amplitudes are plotted against the range of fault sizes selected to represent the torque imbalance fault and determine a possible relationship in the selected harmonics. As expected, there is a proportional relationship with the obtained torque values from each synthetic flow velocity for both the rotor and the generator in f/f_0 = 1, with some exceptions found at L_x = 10 m. As previously mentioned, the trend differences between figures 7.13 and 7.14 are about 10 times order of magnitude, and it is likely to be a product of the gearbox interference due to the 1:10 gearbox ratio, the influence of inertia and the drivetrain losses.

From figure 7.13, it can be observed that in f/f_0 = 1, there is a proportional

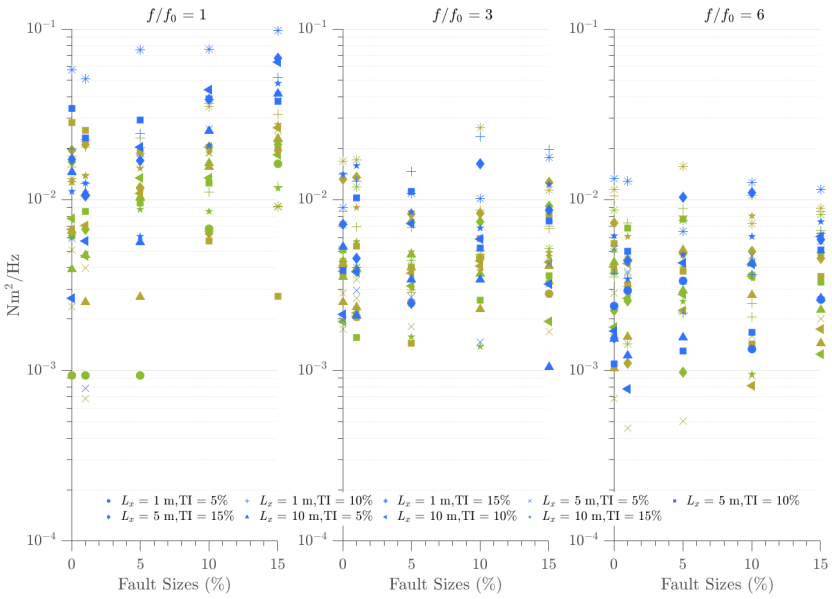

Figure 7.14: Amplitude of each of the fault size cases recorded on the DTTR from the Generator for flow velocities of 0.8 ms^{-1}, 1.0 ms^{-1} and 1.2 ms^{-1}, for f/f_0 = 1, f/f_0 = 3 and f/f_0 = 6 and for three different TI cases and L_x cases. Recorded time length ~ 90 s.Green = $\overline{u}$ = 0.8 ms^{-1}, Yellow = $\overline{u}$ = 1.0 ms^{-1} and Light Blue = $\overline{u}$ = 1.2 ms^{-1}.

increment in the rotor torque amplitudes as fault size increases, with the highest amplitudes detected to be the ones obtained from the $\overline{u}$ = 1.2 ms^{-1}, L_x = 1 m, TI = 15%. Similar to what it was observed in chapter 6, fault sizes between 0% and 1% display discrepancies in the correlation between the simulations obtained from different TI, integral length scales and fluid velocities. Also, the TI = 15% across L_x and $\overline{u}$ values achieved a good agreement with the torque imbalance fault sizes. This indicates that a rotor under the presence of high turbulent energy content would produce the largest amplitudes. Still, the latter needs to be further considered using each respective mean values obtained from a no-torque fault being added. This is analysed later in this chapter. Plus, it is observed that there are higher amplitudes from smaller integral length scale values compared to L_x = 10 m, as it was expected across different TI and $\overline{u}$ cases. This could be attributed again to the lack of computational time in order to reach and effectively

emulate larger integral lengths scales into the test rig due to the torque limitations previously defined. As a result, it generated a more chaotic turbulence profile in the fluid velocity, that consequently lead to a poor agreement with the torque imbalance faults. On the other hand, $f/f_0 = 3$ displays a different output to that observed in $f/f_0 = 1$. Here there is not a particular trend between $\overline{u}$ and fault sizes, but it does display the influence of turbulence intensity over the signal, where the TI = 15% cases are the ones with the highest amplitudes across length scales and velocities.

In figure 7.14, there is a deviation from the previous correlation observed in the rotor side at $f/f_0 = 1$. Although it appears to have a proportional relation when TI increases and it does replicate the highest amplitude to be found at the $\overline{u} = 1.2\ ms^{-1}$, $L_x =$ 1 m, TI = 15% case. There are some harmonic amplitudes that are not consistent when fault size is increased, mainly the data obtained from $\overline{u} = 0.8\ ms^{-1}$ and $L_x = 10$ m. On the other hand, $f/f_0 = 3$ manifests the effect of turbulence intensity in the generator, providing a strong cohesion with the highest turbulence intensity cases presented, mainly at velocities of $1.2\ ms^{-1}$ and $1.0\ ms^{-1}$. The latter demonstrate the generator's ability to represent differing torque signals under the presence of high turbulent profiles in a synthetic fluid velocity. Finally, $f/f_0 = 6$ shows a dependency between TI and the generated cogging torque from the rotor-gearbox-generator interaction. This could be attributed to the addition of torque needed to overcome the opposing torque created by the rotor. This is correlated to the created torque signals yielding higher torque values as TI increases. Even though the 3rd and 6th harmonics displayed better results to determine the DTTR behaviour, the $f/f_0 = 1$ would be observed clearly with the developed CM algorithm, to establish the CM algorithm limitations when is being used with more complex variables.

It can be stated that figures 7.13 and 7.14 provide good insight in order to compare the harmonics amplitude size for all the cases. However, they neglect the effect of the probability distribution of the reached amplitudes in respect to a threshold or a limit that could be considered unusual if the rotor or generator are operating under the presence of a torque imbalance in the rotor, for a given $\overline{u} = 1\ ms^{-1}$. Figures 7.15 and 7.16,

Recorded Time Length	Motor	L_x (m)	TI (%)	Fault Sizes 0%	1%	5%	10%	15%
30 *s*	Rotor	1	5	2	2	1	2	0
			10	3	3	3	1	2
			15	1	1	2	1	0
		5	5	2	2	3	3	5
			10	2	1	1	1	1
			15	2	2	2	2	2
		10	5	3	4	2	4	8
			10	2	2	2	4	4
			15	2	2	1	1	2
	Generator	1	5	2	1	3	2	2
			10	2	2	1	0	1
			15	2	1	0	0	3
		5	5	1	1	3	3	5
			10	1	0	2	2	1
			15	2	2	2	3	6
		10	5	2	0	2	4	4
			10	1	1	3	3	3
			15	2	1	4	3	4
90 *s*	Rotor	1	5	1	1	1	2	5
			10	1	1	1	1	2
			15	1	3	1	1	1
		5	5	1	2	3	7	9
			10	2	1	1	1	2
			15	2	2	2	1	2
		10	5	1	1	5	6	9
			10	2	2	2	2	6
			15	1	1	1	2	3
	Generator	1	5	1	1	1	2	4
			10	2	3	1	2	4
			15	2	2	2	3	3
		5	5	2	4	4	8	9
			10	1	2	2	0	2
			15	1	2	1	1	1
		10	5	2	0	0	4	9
			10	2	0	1	2	2
			15	1	1	1	2	3

Table 7.1: Table providing an overview of the points of the built time series above their respective upper control limits from control charts of figures 7.15 to 7.16.

display the results of the implemented CM algorithm previously explained in chapters 5 and 6. Additionally, table 7.1 displays the number of points that surpasses their respective UCLs, for each fault size case, rotor, generator and both time recorded lengths. This time, only the results for a recorded time length of 90 *s* are being shown for both the rotor and the generator outputs in the figures. By implementing a high-pass filter to remove the torque data that is found before the 0.5 Hz and calculating a spectrogram from each torque time series, new time series were created extracting the values obtained from the spectrogram near $f/f_0 = 1$. Each set of simulations of different integral length scales and turbulence intensities are plotted in each figure, with the five different time series obtained from each of the fault sizes being examined. Then, the MCLs are set given the mean value when each torque time signal has no fault being added, and the UCLs are obtained by utilising equation 5.4. Since the original torque signal was cut-off with the high-pass filter where time series were reduced in time to 72 *s* each.

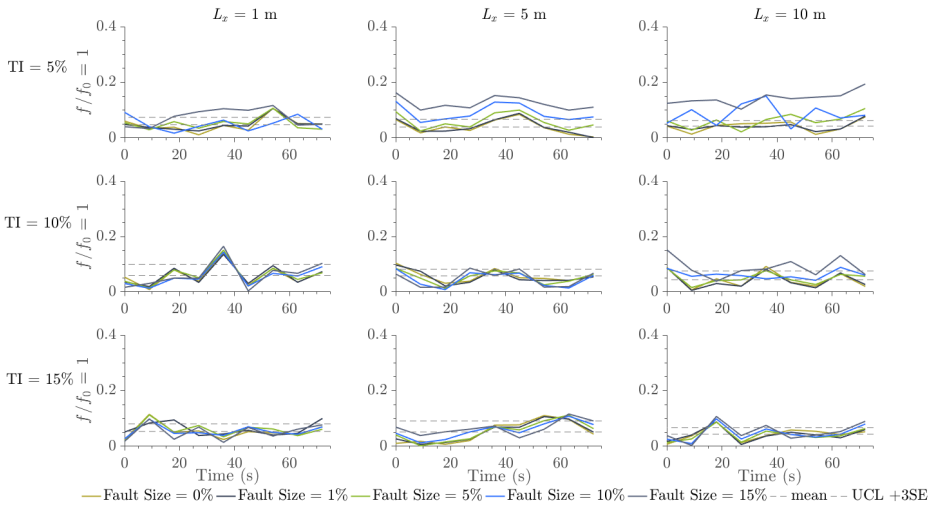

Figure 7.15: Control Charts for each of the fault size cases recorded on the DTTR from the Rotor, with a flow velocity of 1.0 ms^{-1} and for three different TI cases and L_x cases. Recorded time length ~ 90 *s*.

Comparing both figures, it is evident that the rotor control charts provide better results than the generator ones. Firstly, the original torque signal with no fault added are below the UCL for each case, whereas with L_x = 5 m, TI = 10% and TI = 15% and L_x = 10

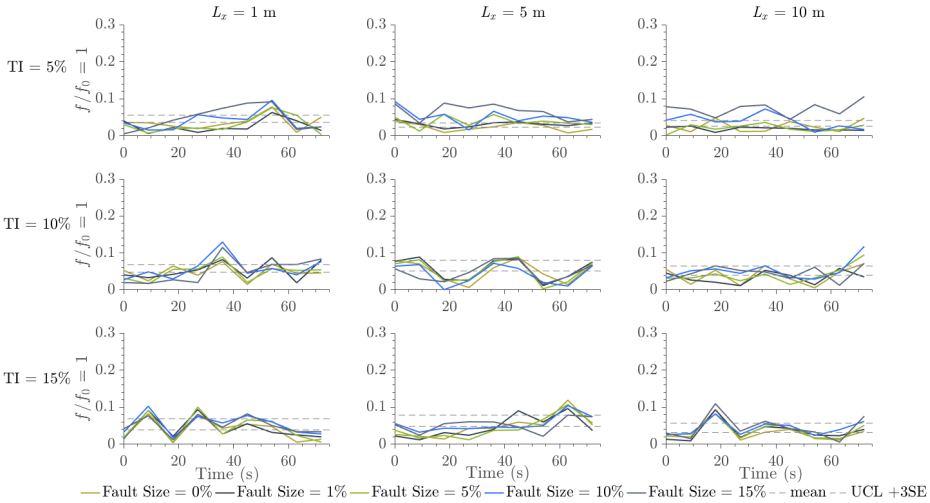

Figure 7.16: Control Charts for each of the fault size cases recorded on the DTTR from the Generator, with a flow velocity of 1.0 ms^{-1} and for three different TI cases and L_x cases. Recorded time length ~ 90 s.

m, TI = 10% only two points are found above this limit. Similar to what it was observed in figure 7.13, the discrepancies between the results obtained from the torque time series with no fault at 1% size are replicated in the control charts for both the rotor and the generator. There is not a proportional increment being repeated across length scales and turbulence intensities cases. The latter could be attributed to the relative small magnitude difference between the two torque signals being compared. This demonstrates that the CM algorithm would struggle to detect torque imbalance irregularities under the presence of higher turbulent energy and length scales. Yet, the proportional increment between torque time series when the fault size increases is noticeable, mainly in fault sizes of 10% and 15%.

Certainly, examining both rotor and generator outputs, TI = 5% represents the turbulence case that produces the most accuracy in finding rotor imbalance faults, across different fault sizes and length scales. Then, TI = 10% also delivers a good agreement in the expected proportional increment of torque time series, yet it presented inconsistencies between fault size = 0% and 1%, as previously explained. However, TI = 15% cases generally yielded lower number of points to surpass its respective UCL, mainly at L_x =

5 m and L_x = 10 m. Then, similar to what was observed in figure 7.7, it may be determined that higher turbulence intensities and length scales represent large contributions into generating greater fluctuations into the fluid velocity. This has the effect of delivering more stochastic structure characteristics that would translate into more challenges for a CM algorithm application to detect faults. Contrarily to what it was determined by Blackmore et al. [2016], where the authors have claimed that integral length scale has a much greater effect than turbulence intensity, by analysing the control charts in this research it is shown that turbulence had greater impact into the CM algorithm effectiveness compared to length scales. Here, TI = 15% did not result in time series points above the implemented UCLs across all length scales. However, it has been also acknowledged that a correlation between high turbulence and large length scale values would lead to larger fluctuations [Ebdon, 2019], since the control charts performance at these particular cases were less accurate compared to the rest of the cases. This does not diminish the fact that control charts at smaller integral length scale values and lower turbulence intensity cases successfully detected the faults added in the torque signals, for both the rotor and the generator.

7.5. Impact of tidal conditions on CM algorithm

Lastly, an assessment of the CM algorithm effectiveness is undertaken to visualise the impact of velocity, turbulence intensity and integral length scale. Figure 7.17 show the results of the effectiveness of detecting a rotor imbalance fault at a fault size = 15% in the generator. This effectiveness was determined by calculating a ratio of how many points surpassed the UCL (obtained from table 7.1), and considering that all time series points should be found above the control limits. The colorbar denotes the effectiveness percentage, where 1 means that all time series points surpassed the UCLs for each respective case. It is clear that the CM algorithm successfully detected the fault = 15% under the presence of their respective variables being compared. For this case, only the generator results were plotted, as this research's purpose is to define a CM based in implementing a cost-effective mechanism to be utilised in real tidal turbines. Although

deploying a CM mechanism to detect faults in the rotor would be optimal, defining rotor imbalance faults through the generator is considered a simpler and more effective option. However, it is important to note that the torque values could be reduced due to different reasons, such as the cogging torque generated by the interaction of the rotor-gearbox-generator, the electromagnetic forces on the generator stator or the inherent losses that would be produced due to the heat and rotor shaft vibrations on the meshing teeth.

Finally, the lowest or more representative values were considered to be displayed for each figure, in order to effectively compare the two variables for each figure without the effect of other tidal condition.

The impact of velocity and turbulence intensity in the generator is presented in figure 7.17a. For this case, the L_x = 1 m was considered. As shown here does not represent a significant tendency to determine a strong relationship between theses two variables, but it demonstrates that a time series where all points are above the UCL are more likely to be found at lower turbulence intensities (<7 %) and higher velocities on a range between 1.1 ms^{-1} and 1.2 ms^{-1}. Still, it appears to be a 50 % effectiveness of detecting a 15% rotor imbalance fault when $\overline{u}$ = 1 ms^{-1} between turbulence intensities of 5% to approximately 12%. When comparing velocity and integral length scales at a low TI % (TI = 5%) to determine the CM effectiveness, contrasting results appear in figure 7.17b. At length scales > 5 m and a range of velocities from 0.8 ms^{-1} to 1.2 ms^{-1}, the effectiveness metrics demonstrates that it has a better performance, compared to when it operates under the presence of lower integral length scales and fluid velocities. These two last approaches effectively prove that TI has a higher impact in determining a fault condition compared to the integral length scale. This is because the CM algorithm was able to find the 15% fault across the range of velocities at higher integral length scales (figure 7.17b), but only found the fault when it was subjected to a higher velocity and a lower turbulence intensity (figure 7.17a). Finally, figure 7.17c demonstrates the relationship between TI and L_x under the presence of $\overline{u}$ = 1 ms^{-1}. This shows that the CM algorithm will be more likely to detect the 15% rotor fault when TI is between 8%- 15% and L_x <

6 m and would be less accurate to detect the faults at TI> 10% and L_x > 6 m. Note that in previous sections, it was determined that the control charts' performance were less accurate when a high TI, high L_x were present in the synthetic flow condition for general fault sizes. However, this result demonstrates that at a fault size of 15% in the generator, the CM algorithm has a better performance when is subjected to the aforementioned conditions. Therefore, it can be determined that the impact that turbulence intensity has in the CM algorithm is also attributed to a slight dependence on length scale, as the CM effectiveness is reduced at high integral length scales and high TI values. Overall, these three presented figures allows this research to determine the operating tidal conditions that the proposed CM algorithm may be subjected to, and effectively demonstrates that the generator would be able to detect a major rotor fault when operating in a range of fluid velocities.

This chapter presents the results of the developed CM algorithm being applied through a resource simulation and the use of a drive train test rig, subjected to the presence of a range of turbulence intensities, fluid velocities and integral length scales.The simulation of synthetic data was presented herein, demonstrating an option to create a stochastic fluid time series with more realistic conditions. Built fluid time series achieved more accurate results for the L_x =1 m and L_x = 5 m compared to the largest L_x case, establishing the need to run larger time series in the test rig in order to achieve a fluid time series with L_x = 10 m. However, a larger rotor diameter size would be needed in order to be able to run torque values higher than 65 Nm, that is the torque limitations given by the hardware. The torque imbalance fault was indiscernible when the torque time series obtained from the test rig are being compared, but it was noticed that τ maximum values are higher in L_x = 1 m case, yet mean values are higher in L_x = 10 m. It was also detected that PSDs did not accomplish to deliver the prominent peaks previously observed in chapters 5 and 6, only in the TI = 5% cases across length scales, for both the rotor and the generator. It was also validated the need to run the test rig for a larger period of time in order to obtain better PSDs, mainly to be able to extract the $f/f_0 = 1$ feature. Finally, control charts implementation demonstrated that TI = 5% cases accomplished to find the rotor imbalance faults, across different fault sizes and length scales. It

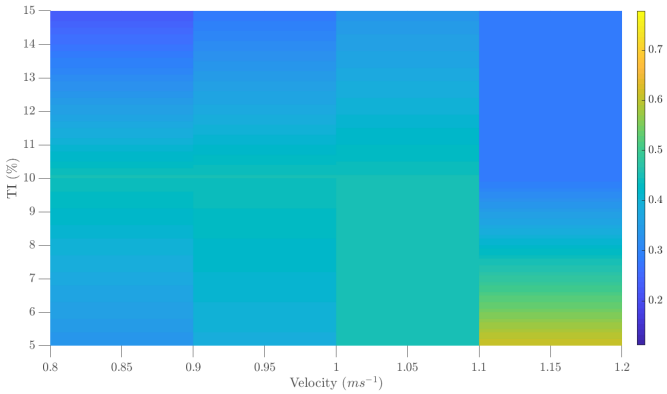

(a) Impact of Velocity and turbulence intensity on the effectiveness of detecting a rotor imbalance fault of 15% in the generator, at L_x = 1 m.

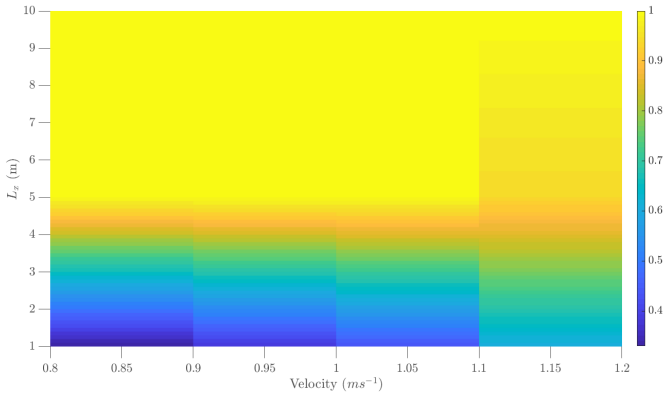

(b) Impact of Velocity and integral length scale on the effectiveness of detecting a rotor imbalance fault of 15% in the generator, at TI = 5%.

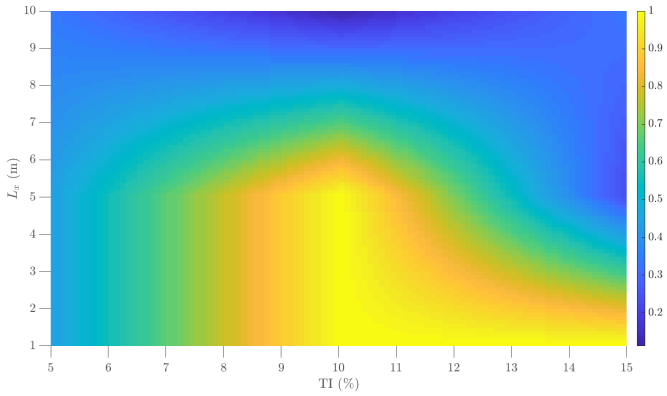

(c) Impact of turbulence intensity and integral length scale on the effectiveness of detecting a rotor imbalance fault of 15% in the generator, at $\overline{u}$ = 1 ms^{-1}.

Figure 7.17: Impact of Tidal Conditions in CM algorithm

was determined that under the operating conditions of these datasets, the CM algorithm struggled to detect failures of 1% of rotor imbalance fault, but most cases of 10% and 15% sizes represented higher points surpassing their respective UCLs. For this chapter, it was determined that turbulence intensity had greater impact into the CM algorithm effectiveness compared to length scales, and that the CM algorithm demonstrated little reliability in the presence of high turbulence and large length scale values. The latter was attributed for two reasons: the lack of computational time in order to effectively generate a fluid velocity for higher turbulence intensity values and integral length scales respectively, and the influence of the integral length scale, which represents a significant factor to recreate even more random, stochastic load transients with greater fluctuations, in order to recognise a rotor imbalance fault under these conditions.

Overall, it has been discussed that tidal energy large-scaled projects are still under development, due to the lack of long-term reliability due to the harsh environments that the turbines will be subjected to. Any advancement to move to a higher TRL is constrained by the lack of funding and an associated high LCoE. The results obtained in this research have successfully represent a rotor imbalance fault under complex conditions to be presented in real-life turbine operations, with a range of different recorded time lengths and fault magnitudes. This CM algorithm represents a positive impact that could be directly implemented to large-scaled projects, due to the fact that TST above 10 m (such as the ones that exist in the market) would operate at higher torque and lower rotational speed. Given the fact that this CM algorithm is sensible to low torque values, this approach is well aligned for scaling up to real torque values. The higher the torque signals that would be obtained in larger TSTs, the higher the probability of finding fault conditions in the control charts. It can be concluded that this research provides an insight that could be utilised by turbine developers to understand a HATT behaviour under the presence of tidal turbulent flows and prevent a possible turbine imbalance failure. Therefore, utilising this CM algorithm in the tidal turbine industry, could potentially support the industry to move up the TRL from 6 to 8, that consequently would lead to reduce the associated LCoE.

8

Conclusions and Contributions to Research

A summary of the key findings related to the aims and objectives outlined in chapter1.

8.1. Steady State HATT Characterisation in a DTTR

The capability to simulate a particular HATT theoretical model in steady flow conditions was demonstrated by utilising a drive train test rig. CFD validated values obtained from the CMERG Turbine 3.0 model were used under a wide range of steady state operating values. A drive train test rig was engineered and used to test different HATT diameters, λ values and mean fluid velocities. The rotor signals for all cases exhibited normal distribution characteristics, whilst the generator side displayed a negative skew-

ness in all scenarios. It was determined that the 0.9 m diameter scenario, at λ = 2,4 and 6 values were normally distributed for the generator signals, yet only for λ = 4 was it able to statistically reproduce the generator signals.

8.2. Rotor Imbalance Fault Parameterisation

Applying the signal monitoring process indicated that torque and thrust signals displayed significant cyclical patterns in a specific turbine (T1) that was not replicated in the others (T2 and T3). A frequency signal analysis was conducted to show that at the 1st harmonic a dominant amplitude was being replicated in T1 and it was not predominant in T2 and T3. It was determined that this higher amplitude will be associated to a rotor imbalance fault condition. A condition monitoring algorithm was engineered in order to effectively detect this fault condition by the use of control charts. The different case scenarios were used to build a time series. The mean and upper control limits were set for each case to determine the classical statistical process controls to detect out-of-control conditions.

It was found that the CM algorithm identified a rotor imbalance fault. It is possible to state that this approach could be scaled up to larger turbines.

8.3. CM algorithm effectiveness in experimental data

The CM algorithm was applied to HATT operating under the presence of turbulence intensity case scenarios. The torque signals obtained from the test campaign were utilised in order to define the case scenarios. The torque signals obtained from the testing campaign were manipulated in order to increment the torque noise ratio.This range of no fault and torque fault time series were built to compare the DTTR obtained outputs for both the rotor and the generator and implement the proposed CM algorithm.

It was found that the implementation of control charts in an attempt to detect

the torque-fault time series was accomplished. It was also found that the rotor data obtained from the control charts delivered better agreement with most cases being detected, even under the presence of higher turbulent flows. Under these conditions, the generator control charts delivered a high degree of reliability in the data obtained. At higher turbulent flows, the CM algorithm may be less successful in determining a rotor imbalance fault. When the CM algorithm was implemented in the rotor side, it developed better agreement and reliability when simulated through a longer period of time. The latter confirms the need to further analyse the impact of time in large-scaled turbine operating conditions, to determine the CM algorithm effectiveness for turbine developers.

8.4. CM algorithm effectiveness in synthetic data

The simulation of unsteady data to build further tidal profiles under the presence of more complex conditions was performed. The validation via a correlation function to determine the effective applicability of these tidal stream features into the built fluid time series was undertaken. This showed that, in order to be able to accurately model a time series, a longer period of time was required. Currently, length scales conditions > 5 m would be unfeasible, indicating the need to increase the rotor test rig diameter for future work to maximise the potential to simulate these conditions.

It was found that the presence of high turbulent flows and large length scales have a great impact on detecting rotor imbalance faults by the use of the proposed CM algorithm. It was also determined that time played an important role in the capability of the CM algorithm to detect faults. Higher turbulence intensities and length scales represent large contributions into generating greater fluctuations into the fluid velocity. This produces more stochastic structure characteristics that would translate into more challenges for a CM algorithm application to detect faults. For this research, the turbulence intensity had greater impact into the CM algorithm effectiveness compared to length scales. However, the rotor side control charts demonstrated the successful application

of the CM algorithm to detect rotor imbalance faults, for both recorded time lengths. The generator side was not able to detect rotor imbalance faults of 1% and 5%, yet it successfully detected larger fault sizes. The latter confirms that a condition monitoring signal processing technique could be implemented under the presence of a range of tidal profile conditions, to be detected in the generator when a fault has been present in the rotor side. The implementation of the proposed CM algorithm would allow turbine developers to prevent major HATTs faults to occur.

8.5. Recommendations for further work

- The implementation of a larger rotor diameter size should be explored, to be able to accurately simulate larger length scale values.

- The proposed CM algorithm could be implemented in different test rigs, and the implementation of more complex CM techniques could be explored.

- Further type of HATT faults could be implemented by utilising the proposed control charts monitoring process. This research focused in the frequency analysis given data, yet it may be utilised for the given statistical or electrical signals to detect other possible faults, such as cracks, delaminations or fatigue.

- Site-specific of real-time tidal current conditions, should be acquired or simulated in order to further analyse the detection of rotor imbalance faults with the proposed CM algorithm.

- The use of a variable speed, variable torque control strategy could be extended to provide more realistic CM outcomes and assess the reliability of the proposed CM algorithm for this control set.

- More realistic tidal conditions could be investigated, including the effect of waves and a wider range of integral length scales and turbulence intensities.

8.6. Contributions to research

- The characterisation of a drive train test rig was successfully achieved, in order to obtain cost-effective turbine simulations, and the reproducibility of both rotor and generator results.
- The parameterisation of a CM algorithm to be utilised under optimal operation control conditions was explored. This can be tested under the presence of more complex conditions.
- The application of control charts in this context showed potential for wider application in real-life applications.
- The CM algorithm was successfully deployed to identify faults on both the rotor and the generator under a range of tidal profile conditions.
- Overall the effectiveness of the test rig was demonstrated. It can become a valuable resource in the cost-effective identification of turbine faults in future CM deployments.

References

I. Afgan, J. McNaughton, S. Rolfo, D. D. Apsley, T. Stallard, and P. Stansby. Turbulent flow and loading on a tidal stream turbine by les and rans. *International Journal of Heat and Fluid Flow*, 43:96–108, 2013. ISSN 0142-727X. doi: https://doi.org/10.1016/j.ijheatfluidflow.2013.03.010. URL https://www.sciencedirect.com/science/article/pii/S0142727X13000672.

J. C. Alcérreca-Huerta, J.B. Encarnacion, S. Ordoñez-Sánchez, M. Callejas-Jiménez, G. Gallegos Diez Barroso, M. Allmark, I. Mariño-Tapia, R. Silva Casarín, T. O'Doherty, C. Johnstone, and L. Carrillo. Energy yield assessment from ocean currents in the insular shelf of cozumel island. *Journal of Marine Science and Engineering*, 7(5):147, 2019. ISSN 2077-1312. URL https://www.mdpi.com/2077-1312/7/5/147.

M. Allmark. *CM and Fault Diagnosis of Tidal Stream Turbines Subjected to Rotor Imbalance Faults*. Phd thesis, School of Engineering, Cardiff University, 2016.

M. Allmark, R. Grosvenor, and P. Prickett. An approach to the characterisation of the performance of a tidal stream turbine. *Renewable Energy*, 111:849–860, 2017. doi: 10.1016/j.renene.2017.05.010.

M. Allmark, R. Ellis, C. Lloyd, S. Ordonez-Sanchez, K. Johannesen, C. Byrne, C. Johnstone, T. O'Doherty, and A. Mason-Jones. The development, design and characterisation of a scale model horizontal axis tidal turbine for dynamic load quantification. *Renewable Energy*, 156:913–930, 2020. ISSN 0960-1481. doi: https://doi.org/10.1016/j.renene.2020.04.060. URL http://www.sciencedirect.com/science/article/pii/S0960148120305929.

M. Allmark, R. Ellis, T. Ebdon, C. Lloyd, S. Ordonez-Sanchez, R. Martinez, A. Mason-Jones, C. Johnstone, and T. O'Doherty. A detailed study of tidal turbine power production and dynamic loading under grid generated turbulence and turbine wake operation. *Renewable Energy*, 169:1422–1439, 2021a. ISSN 0960-1481. doi: https://doi.org/10.1016/j.renene.2020.12.052. URL https://www.sciencedirect.com/science/article/pii/S0960148120319789.

M. Allmark, R. Martinez, S. Ordonez-Sanchez, C. Lloyd, T. O'Doherty, G. Germain, B. Gaurier, and C. Johnstone. A phenomenological study of lab-scale tidal turbine loading under combined irregular wave and shear flow conditions. *Journal of Marine Science and Engineering*, 9(6):593, 2021b. ISSN 2077-1312. URL https://www.mdpi.com/2077-1312/9/6/593.

O. Anaya-Lara, N. Jenkins, and J. Ekanayake. *Wind energy generation modelling and control*. Wind energy generation : modelling and control. Wiley, Oxford, 2009. ISBN 9780470748237.

Andritz. Tidal current turbines, 2022. URL https://www.andritz.com/products-en/hydro/products/tidal-current-turbines. [Online; accessed 23 October 2022].

Andritz Hydro Hammerfest. Renewable energy from tidal currents, 2022. URL https://www.andritz.com/resource/blob/31444/cf15d27bc23fd59db125229506ec87c7/hy-hammerfest-data.pdf. [Online; accessed 23 October 2022].

R. Ansari and L. Valbonesi. 1 - signals and systems. In WAI-KAI CHEN, editor, *The Electrical Engineering Handbook*, pages 813–837. Academic Press, Burlington, 2005. ISBN 978-0-12-170960-0. doi: https://doi.org/10.1016/B978-012170960-0/50061-X.

Aqua-RET Project. Tidal stream technologies, 2012. URL https://www.aquaret.com/indexea3d.html?option=com_content&view=article&id=203&Itemid=344&lang=en#Animations. [Online; accessed 15 October 2022].

E. Artigao, A. Honrubia-Escribano, S. Martin-Martinez, and E. Gomez-Lazaro. The use of electrical measurements of wind turbine generators for drive train condition mon-

itoring. *Design Optimization of Wind Energy Conversion Systems with Applications*, pages 69–90, 2020. doi: 10.5772/intechopen.90127.

Atlantis Resources Ltd. Ar1500 tidal turbine, 2016. URL https://simecatlantis.com/wp-content/uploads/2016/08/AR1500-Brochure-Final-1.pdf. [Online; accessed 5 November 2020].

A. S. Bahaj. Generating electricity from the oceans. *Renewable and Sustainable Energy Reviews*, 15(7):3399–3416, 2011. ISSN 1364-0321. doi: https://doi.org/10.1016/j.rser.2011.04.032. URL http://www.sciencedirect.com/science/article/pii/S1364032111001900.

C. S. K. Belloni. *Hydrodynamics of ducted and open-centre tidal turbines*. Thesis, Oxford University, UK, 2013.

M. E. H. Benbouzid, H. Titah-Benbouzid, and Z. Zhou. Ocean energy technologies. In *Encyclopedia of Sustainable Technologies*, pages 73–85. Elsevier, Oxford, 2017. ISBN 978-0-12-804792-7. doi: https://doi.org/10.1016/B978-0-12-409548-9.10097-1.

Black and Veatch. Lessons learnt from meygen phase 1a final summary report. Report, Black & Veatch, 2020.

T. Blackmore, L. E. Myers, and A. S. Bahaj. Effects of turbulence on tidal turbines: Implications to performance, blade loads, and condition monitoring. *International Journal of Marine Energy*, 14:1–26, 2016. ISSN 2214-1669. doi: https://doi.org/10.1016/j.ijome.2016.04.017. URL http://www.sciencedirect.com/science/article/pii/S2214166916300297.

P. Bloomfield. The fast-fourier transform. In *Fourier analysis of time series : an introduction*, pages 57–61. Wiley, New York, 2nd ed. edition, 2000. ISBN 0471889482.

B. Boashash. Chapter 2 - heuristic formulation of time-frequency distributions. In Boualem Boashash, editor, *Time-Frequency Signal Analysis and Processing (Second Edition)*, pages 65–102. Academic Press, Oxford, second edition edition, 2016. ISBN 978-0-12-398499-9. doi: https://doi.org/10.1016/B978-0-12-398499-9.00002-9.

G. Boyle. *Renewable energy : power for a sustainable future*. Oxford : Oxford University Press in association with the Open University, Oxford, 3rd ed. edition, 2012.

Peter J Brockwell and Richard A Davis. *Introduction to time series and forecasting*. Springer, 2002.

L. Burke, Y. Kura, K. Kassem, C. Revenga, M. Spalding, and D. McAllister. Pilot analysis of global ecosystems: Coastal ecosystems. Report, World Resources Institute, 2001. URL https://www.wri.org/sites/default/files/pdf/page_coastal.pdf.

T. Burton, N. Jenkins, D. Sharpe, E. Bossanyi, and M. Graham. *Wind energy handbook*. John Wiley and Sons, Inc., Hoboken, NJ, third edition. edition, 2021. ISBN 9781119451143.

S. Butler. *Prognostic algorithms for condition monitoring and remaining useful life estimation*. Phd thesis, Faculty of Science and Engineering, National University of Ireland, Maynooth, 2012.

J. F. Bárcenas Graniel, J. V. H. Fontes, Hector F. G. Garcia, and R. Silva. Assessing hydrokinetic energy in the mexican caribbean: A case study in the cozumel channel. *Energies*, 14(15):4411, 2021. ISSN 1996-1073. URL https://www.mdpi.com/1996-1073/14/15/4411.

S. Cacciola, I. M. Agud, and C. L. Bottasso. Detection of rotor imbalance, including root cause, severity and location. *Journal of Physics: Conference Series*, 753(7):072003, 2016. ISSN 1742-6596 1742-6588. doi: 10.1088/1742-6596/753/7/072003. URL https://dx.doi.org/10.1088/1742-6596/753/7/072003.

M. Calaf, C. Meneveau, and J. Meyers. Large eddy simulations of fully developed wind-turbine array boundary layers. *Physics of Fluids*, 22, 2010. doi: 10.1063/1.3291077.

J. Candela, J. Sheinbaum, J. Ochoa, A. Badan, and R. Leben. The potential vorticity flux through the yucatan channel and the loop current in the gulf of mexico. *Geophysical Research Letters*, 29(22):16–1–16–4, 2002. doi: doi:10.1029/2002GL015587. URL https://agupubs.onlinelibrary.wiley.com/doi/abs/10.1029/2002GL015587.

Carbon Trust. Technology innovation needs assessment marine energy: Summary report. Report, Carbon Trust, 2012. URL www.carbontrust.com/media/168547/tina-marine-energy-summary-report.pdf.

J. Carroll, A. McDonald, and D. McMillan. Failure rate, repair time and unscheduled o and m cost analysis of offshore wind turbines. *Wind Energy*, 19(6):1107–1119, 2016. ISSN 1099-1824. doi: 10.1002/we.1887. URL http://dx.doi.org/10.1002/we.1887.

R. H. Charlier. Forty candles for the rance river tpp tides provide renewable and sustainable power generation. *Renewable and Sustainable Energy Reviews*, 11(9):2032–2057, 2007. ISSN 1364-0321. doi: https://doi.org/10.1016/j.rser.2006.03.015. URL https://www.sciencedirect.com/science/article/pii/S1364032106000621.

M. Cheah-Mane, J. Liang, and N. Jenkins. Permanent magnet synchronous generator for wind turbines: Modelling, control and inertial frequency response. In *2014 49th International Universities Power Engineering Conference (UPEC)*, pages 1–6, 2014. doi: 10.1109/UPEC.2014.6934799.

L. Chen and W. H. Lam. A review of survivability and remedial actions of tidal current turbines. *Renewable and Sustainable Energy Reviews*, 43:891–900, 2015. ISSN 1364-0321. doi: https://doi.org/10.1016/j.rser.2014.11.071. URL http://www.sciencedirect.com/science/article/pii/S1364032114010107.

A. Cherian. Where is the "energy" in global climate change negotiations outcomes? In *Energy and Global Climate Change*, pages 55–119. John Wiley and Sons, Ltd, 2015. ISBN 9781118846070. doi: 10.1002/9781118846070.ch2.

M. J. Churchfield, Y. Li, and P. J. Moriarty. A large-eddy simulation study of wake propagation and power production in an array of tidal-current turbines. *Philosophical Transactions of the Royal Society A: Mathematical, Physical and Engineering Sciences*, 371(1985):20120421, 2013. doi: doi:10.1098/rsta.2012.0421. URL https://royalsocietypublishing.org/doi/abs/10.1098/rsta.2012.0421.

D. Coles, C. Greenwood, A. Vogler, T. Walsh, and D. Taaffe. Assessment of the turbulent flow upstream of the meygen phase 1a tidal stream turbines. In *Proceedings of the Asian Wave and Tidal Energy Conference (AWTEC), Taipei, Taiwan*, pages 9–13, 2018.

D. Coles, A. Angeloudis, D. Greaves, G. Hastie, M. Lewis, L. Mackie, J. McNaughton, J. Miles, S. Neill, and M. Piggott. A review of the uk and british channel islands practical tidal stream energy resource. *Proceedings of the Royal Society A*, 477(2255):20210469, 2021. ISSN 1364-5021.

CONABIO. Política nacional de mareas y costas de méxico: Gestión integral de las regiones más dinámicas del territorio nacional. Report, CONABIO, 2015. URL http://www.biodiversidad.gob.mx/pais/mares/pdf/A4_PNMC_actualizada_dic2015.pdf.

C. Crabtree. *Condition monitoring techniques for wind turbines*. Phd thesis, School of Engineering, Durham University, 2011.

Dantec Dynamics. Measurement principles of lda, 2018. URL https://www.dantecdynamics.com/solutions-applications/solutions/fluid-mechanics/laser-doppler-anemometry-lda/measurement-principles-of-lda/. [Online; accessed 5 August 2021].

A. Davies. *Handbook of condition monitoring : techniques and methodology*. London : Chapman and Hall, London, 1997.

W.S. De Oliveira and A.J. Fernandes. Optimization model for economic evaluation of wind farms-how to optimize a wind energy project economically and technically. *International Journal of Energy Economics and Policy*, 2(1):10–20, 2012.

T. Delorm. *Tidal stream devices: reliability prediction models during their conceptual and development phases*. Phd thesis, School of Engineering and Computing Sciences Durham University, 2014.

E. Denny. The economics of tidal energy. *Energy Policy*, 37(5):1914–1924, 2009. ISSN 0301-4215. doi: http://dx.doi.org/10.1016/j.enpol.2009.01.009. URL http://www.sciencedirect.com/science/article/pii/S0301421509000408.

G. Deskos, G. S. Payne, B. Gaurier, and M. Graham. On the spectral behaviour of the turbulence-driven power fluctuations of horizontal-axis turbines. *Journal of Fluid Mechanics*, 904:A13, 2020. ISSN 0022-1120. doi: 10.1017/jfm.2020.681.

S. Dey. Turbulence in open-channel flows. In *Fluvial Hydrodynamics: Hydrodynamic and Sediment Transport Phenomena*, pages 95–187. Springer Berlin Heidelberg, Berlin, Heidelberg, 2014. ISBN 978-3-642-19062-9. doi: 10.1007/978-3-642-19062-9_3.

S. Djebarri, J.F. Charpentier, F. Scuiller, and M. Benbouzid. Influence of fixed-pitch tidal turbine hydrodynamic characteristic on the generator design. In *11th European Wave and Tidal Energy Conference (EWTEC),Nantes, France*, pages 8A2–2. EWTEC, 2015.

Darrel A Doman, Robynne E Murray, Michael J Pegg, Katie Gracie, Cameron M Johnstone, and Thomas Nevalainen. Tow-tank testing of a 1/20th scale horizontal axis tidal turbine with uncertainty analysis. *International Journal of Marine Energy*, 11:105–119, 2015.

D. E. Dombroski and J. P. Crimaldi. The accuracy of acoustic doppler velocimetry measurements in turbulent boundary layer flows over a smooth bed. *Limnology and Oceanography: Methods*, 5(1):23–33, 2007. ISSN 1541-5856. doi: https://doi.org/10.4319/lom.2007.5.23. URL https://aslopubs.onlinelibrary.wiley.com/doi/abs/10.4319/lom.2007.5.23.

J. F. Douglas. *Fluid mechanics*. Harlow New York : Pearson Prentice Hall, Harlow New York, 6th ed. edition, 2011.

J. Duhaney, T. M. Khoshgoftaar, and J. C. Sloan. Feature level sensor fusion for improved fault detection in mcm systems for ocean turbines. In *Twenty-Fourth International FLAIRS Conference*, 2011.

O. Durán Medina, F. G. Schmitt, R. Calif, G. Germain, and B. Gaurier. Turbulence analysis and multiscale correlations between synchronized flow velocity and marine turbine power production. *Renewable Energy*, 112:314–327, 2017. ISSN 0960-1481. doi:

https://doi.org/10.1016/j.renene.2017.05.024. URL https://www.sciencedirect.com/science/article/pii/S0960148117304093.

T. Ebdon. *The impact of turbulence and turbine operating condition on the wakes of tidal turbines*. Phd thesis, School of Engineering, Cardiff University, 2019.

F. Elasha, D. Mba, and J. A. Teixeira. Condition monitoring philosophy for tidal turbines. *International Journal of Performability Engineering*, 10(5):521–534, 2014a. URL https://www.scopus.com/inward/record.uri?eid=2-s2.0-84906849176&partnerID=40&md5=05b9823f6ac6645ed3615c89e252ae0a.

F. Elasha, D. Mba, J. A. Teixeira, and B. Cranfield. Failure prediction of tidal turbines gearboxes. *eMaintenance*, page 49, 2014b.

S. E. B. Elghali, R. Balme, K. L. Saux, M. E. H. Benbouzid, J. F. Charpentier, and F. Hauville. A simulation model for the evaluation of the electrical power potential harnessed by a marine current turbine. *IEEE Journal of Oceanic Engineering*, 32(4):786–797, 2007. ISSN 1558-1691. doi: 10.1109/JOE.2007.906381.

O. Ellabban, H. Abu-Rub, and F. Blaabjerg. Renewable energy resources: Current status, future prospects and their enabling technology. *Renewable and Sustainable Energy Reviews*, 39:748–764, 2014. ISSN 13640321. doi: 10.1016/j.rser.2014.07.113.

R. Ellis. *The Influence of Inter-device Spacing on the Performance of a Tidal Stream Turbine*. Phd thesis, School of Engineering, Cardiff University, 2016.

M. Elzalabani, F. H. Fahmy, A. E.S. A Nafeh, and G. Allam. Modelling and simulation of tidal current turbine with permanent magnet synchronous generator. *TELKOMNIKA Indonesian Journal of Electrical Engineering*, 13(1):57–64, 2015. ISSN 2460-7673.

EMEC. Open hydro, 2022. URL https://www.emec.org.uk/about-us/our-tidal-clients/open-hydro/. [Online; accessed 24 July 2023].

ENCORE Project. Eel energy pilot, 2020. URL https://www.energisingcoasts.eu/eelenergy. [Online; accessed 20 February 2021].

European Comission. Set plan – declaration of intent on strategic targets in the context of an initiative for global leadership in ocean energy. Report, European Comission, 2016. URL https://setis.ec.europa.eu/system/files/integrated_set-plan/declaration_of_intent_ocean_0.pdf.

E. Fernandez-Rodriguez, T. J. Stallard, and P. K. Stansby. Experimental study of extreme thrust on a tidal stream rotor due to turbulent flow and with opposing waves. *Journal of Fluids and Structures*, 51:354–361, 2014. ISSN 0889-9746. doi: https://doi.org/10.1016/j.jfluidstructs.2014.09.012. URL https://www.sciencedirect.com/science/article/pii/S0889974614002151.

P. L. Fraenkel. Power from marine currents. *Proceedings of the Institution of Mechanical Engineers, Part A: Journal of Power and Energy*, 216(1):1–14, 2002. doi: doi:10.1243/095765002760024782. URL http://journals.sagepub.com/doi/abs/10.1243/095765002760024782.

P. L. Fraenkel. Tidal current energy technologies. *International Journal of Avian Science*, 148(s1):145–151, 2006. doi: doi:10.1111/j.1474-919X.2006.00518.x. URL https://onlinelibrary.wiley.com/doi/abs/10.1111/j.1474-919X.2006.00518.x.

C. Frost, C. E. Morris, A. Mason-Jones, D. M. O'Doherty, and T. O'Doherty. The effect of tidal flow directionality on tidal turbine performance characteristics. *Renewable Energy*, 78:609–620, 2015. ISSN 0960-1481. doi: http://dx.doi.org/10.1016/j.renene.2015.01.053. URL http://www.sciencedirect.com/science/article/pii/S0960148115000713.

A. Garanovic. Openhydro tidal turbine at emec up for removal, 2021. URL https://www.offshore-energy.biz/openhydro-tidal-turbine-at-emec-up-for-removal/. [Online; accessed 24 July 2023].

F. P. García Márquez, A. M. Tobias, J. M/ Pinar Pérez, and M. Papaelias. Condition monitoring of wind turbines: Techniques and methods. *Renewable Energy*, 46:169–

178, 2012. ISSN 0960-1481. doi: https://doi.org/10.1016/j.renene.2012.03.003. URL http://www.sciencedirect.com/science/article/pii/S0960148112001899.

B. Gaurier, G. Germain, J.V. Facq, and T. Bacchetti. Wave and current flume tank of ifremer at boulogne-sur-mer. description of the facility and its equipment. Report 19CSMBL18, IFREMER, 2018a. URL https://archimer.ifremer.fr/doc/00470/58163/.

B. Gaurier, G. Germain, and G. Pinon. How to correctly measure turbulent upstream flow for marine current turbine performances evaluation? In *Advances in Renewable Energies Offshore: Proceedings of the 3rd International Conference on Renewable Energies Offshore, Lisbon*, pages 23–30, 2018b.

R. I. Grosvenor, P. W. Prickett, and H. Jianhao. An assessment of structure-based sensors in the condition monitoring of tidal stream turbines. In *2017 Twelfth International Conference on Ecological Vehicles and Renewable Energies (EVER)*, pages 1–11, 2017. doi: 10.1109/EVER.2017.7935942.

R.I. Grosvenor, P.W. Prickett, C. Frost, and M. Allmark. Performance and condition monitoring of tidal stream turbines. In *PHM Society European Conference*, volume 2, 2014.

M. Guerra and J. Thomson. Turbulence measurements from five-beam acoustic doppler current profilers. *Journal of Atmospheric and Oceanic Technology*, 34(6):1267–1284, 2017. ISSN 0739-0572. doi: 10.1175/jtech-d-16-0148.1. URL https://journals.ametsoc.org/view/journals/atot/34/6/jtech-d-16-0148.1.xml.

C. Hachmann, T. Stallard, B. Lin, and P. Stansby. Characterising the effect of turbine operating point on momentum extraction of tidal turbine arrays. In *Asian Wave and Tidal Energy Conference (AWTEC),Taipei, Taiwan*, 2018.

G. Hagerman, B. Polagye, R. Bedard, and M. Previsic. Methodology for estimating tidal current energy resources and power production by tidal in-stream energy conversion (tisec) devices. *EPRI North American tidal in stream power feasibility demonstration project*, 1, 2006.

Z. Hameed, Y. S. Hong, Y. M. Cho, S. H. Ahn, and C. K. Song. Condition monitoring and fault detection of wind turbines and related algorithms: A review. *Renewable and Sustainable Energy Reviews*, 13(1):1–39, 2009. ISSN 13640321. doi: 10.1016/j.rser.2007.05.008.

J. Hardisty. *The Analysis of Tidal Stream Power*. John Wiley and Sons, 2009. doi: 10.1002/9780470743119.

M. Harrold. *School of Engineering, Experimental and Numerical Assessment of a Tidal Turbine Control Strategy*. Phd thesis, University of Stratchclyde, 2016.

M. Harrold and P. Ouro. Rotor loading characteristics of a full-scale tidal turbine. *Energies*, 12(6):1035, 2019. ISSN 1996-1073. URL https://www.mdpi.com/1996-1073/12/6/1035.

M. Harrold, P. Ouro, and T. O'Doherty. Performance assessment of a tidal turbine using two flow references. *Renewable Energy*, 153:624–633, 2020. ISSN 0960-1481. doi: https://doi.org/10.1016/j.renene.2019.12.052.

E. Hau. *Wind turbines : fundamentals, technologies, application, economics*. Springer, Heidelberg, 3rd translated ed. edition, 2013. ISBN 9783642271502.

J. Helsen, F. Vanhollebeke, F. De Coninck, D. Vandepitte, and W. Desmet. Insights in wind turbine drive train dynamics gathered by validating advanced models on a newly developed 13.2mw dynamically controlled test-rig. *Mechatronics*, 21(4):737–752, 2011. ISSN 0957-4158. doi: https://doi.org/10.1016/j.mechatronics.2010.11.005. URL https://www.sciencedirect.com/science/article/pii/S0957415810002059.

T. Hernandez. *Technical and economic feasibility analysis of a horizontal axis tidal turbine when operating in low velocity conditions*. Phd thesis, School of Engineering, Cardiff University, 2020.

R. Hyers, J. McGowan, K. Sullivan, J. Manwell, and B. Syrett. Condition monitoring and prognosis of utility scale wind turbines. *Energy Materials: Materials Science and Engineering for Energy Systems*, 1:187–203, 2006. doi: 10.1179/174892406X163397.

G. R. Hübner, H. Pinheiro, C. E. de Souza, C. M. Franchi, L. D. da Rosa, and J. P. Dias. Detection of mass imbalance in the rotor of wind turbines using support vector machine. *Renewable Energy*, 170:49–59, 2021. ISSN 0960-1481. doi: https://doi.org/10.1016/j.renene.2021.01.080. URL https://www.sciencedirect.com/science/article/pii/S0960148121000872.

IEA. Iea: Governments not on track for paris goals: Key actions to peak emissions around 2020. Report, International Energy Agency, 2016. URL http://newsroom.unfccc.int/unfccc-newsroom/iea-governments-not-on-track-to-achieve-paris-agreement-goals/.

IEA. Global energy review: Co2 emissions in 2021. Report, IEA, 2022. URL https://www.iea.org/reports/global-energy-review-co2-emissions-in-2021-2.

IPCC. Climate change 2022 mitigation of climate change. Report, IPCC, 2022. URL https://www.ipcc.ch/report/ar6/wg3/.

IRENA. Tidal energy: Technology brief. Report, International Renewable Energy Agency, 2014. URL https://www.irena.org/publications/2014/Jun/Tidal-Energy.

IRENA. Innovation outlook: Ocean energy technologies. Report, International Renewable Energy Agency, 2020. URL https://www.irena.org/Publications/2020/Dec/Innovation-Outlook-Ocean-Energy-Technologies.

IRENA. Tracking sdg 7: The energy progress report. Report, International Renewable Energy Agency, 2022. URL https://www.irena.org/Publications/2022/Jun/Tracking-SDG-7-2022.

IRENA. Scaling up investments in ocean energy technologies. Report, International Renewable Energy Agency, 2023. URL https://www.irena.org/Publications/2023/Mar/Scaling-up-investments-in-ocean-energy-technologies.

P. Jamieson and G. Hassan. *Innovation in Wind Turbine Design*. John Wiley and Sons Ltd, Chichester, 2011.

P. Jeffcoate, T. Whittaker, C. Boake, and B. Elsaesser. Field tests of multiple 1/10 scale tidal turbines in steady flows. *Renewable Energy*, 87:240–252, 2016. ISSN 0960-1481. doi: https://doi.org/10.1016/j.renene.2015.10.004. URL https://www.sciencedirect.com/science/article/pii/S0960148115303578.

W.Q. Jeffries, J. A. Chambers, and D. G. Infield. Experience with bicoherence of electrical power for condition monitoring of wind turbine blades. *IEE Proceedings-vision, image and signal processing*, 145(3):141–148, 1998. ISSN 1359-7108.

M. S. Kan, A. C. C. Tan, and J. Mathew. A review on prognostic techniques for non-stationary and non-linear rotating systems. *Mechanical Systems and Signal Processing*, 62:1–20, 2015. ISSN 0888-3270. doi: http://dx.doi.org/10.1016/j.ymssp.2015.02.016. URL http://www.sciencedirect.com/science/article/pii/S0888327015000898.

J. Kusnick, D. E. Adams, and D. T. Griffith. Wind turbine rotor imbalance detection using nacelle and blade measurements. *Wind Energy*, 18(2):267–276, 2015. ISSN 1095-4244. doi: https://doi.org/10.1002/we.1696. URL https://onlinelibrary.wiley.com/doi/abs/10.1002/we.1696.

M. Lewis, S. P. Neill, P. E. Robins, and M. R. Hashemi. Resource assessment for future generations of tidal-stream energy arrays. *Energy*, 83:403–415, 2015. ISSN 0360-5442. doi: http://dx.doi.org/10.1016/j.energy.2015.02.038. URL http://www.sciencedirect.com/science/article/pii/S0360544215001930.

J. Liang and B. Whitby. Field oriented control of a permanent magnet synchronous generator for use in a variable speed tidal stream turbine. In *2011 46th International Universities' Power Engineering Conference (UPEC)*, pages 1–6, 2011.

H. W. Lilliefors. On the kolmogorov-smirnov test for normality with mean and variance unknown. *Journal of the American Statistical Association*, 62(318):399–402, 1967. ISSN 0162-1459. doi: 10.1080/01621459.1967.10482916. URL https://www.tandfonline.com/doi/abs/10.1080/01621459.1967.10482916.

D. Llano, M. Tatlow, and R. McMahon. Control algorithms for permanent magnet generators evaluated on a wind turbine emulator test-rig. In *7th IET International Conference on Power Electronics, Machines and Drives (PEMD 2014)*, pages 1–7, 2014. doi: 10.1049/cp.2014.0304.

T. P. Lloyd, S. R. Turnock, and V. F. Humphrey. Assessing the influence of inflow turbulence on noise and performance of a tidal turbine using large eddy simulations. *Renewable Energy*, 71:742–754, 2014. ISSN 0960-1481. doi: https://doi.org/10.1016/j.renene.2014.06.011. URL https://www.sciencedirect.com/science/article/pii/S0960148114003516.

Y. Ma, P. Martinez-Vazquez, and C. Baniotopoulos. Wind turbine tower collapse cases: A historical overview. *ICE Proceedings Structures and Buildings*, 172:547–555, 2018. doi: 10.1680/jstbu.17.00167.

D. Magagna and A. Uihlein. Ocean energy development in europe: Current status and future perspectives. *International Journal of Marine Energy*, 11:84–104, 2015. ISSN 2214-1669. doi: https://doi.org/10.1016/j.ijome.2015.05.001. URL http://www.sciencedirect.com/science/article/pii/S2214166915000181.

V. Magar. Línea estratégica: Corrientes y mareas. [Online; accessed 25 November 2017], 2018.

V. Magar, L. González-García, and M. S. Gross. Evaluación técnico-económica del potencial de desarrollo de parques eólicos en el mar: el caso de golfo de california. *2017*, 19:6, 2017. ISSN 1665-1456. doi: 10.18633/biotecnia.v19i0.358. URL https://biotecnia.unison.mx/index.php/biotecnia/article/view/358.

A. Mason-Jones. *Performance assessment of a Horizontal Axis Tidal Turbine in a high velocity shear environment*. Phd thesis, School of Engineering, Cardiff University, 2009.

A. Mason-Jones, D. M. O'Doherty, C. E. Morris, T. O'Doherty, C. B. Byrne, P. W. Prickett, R. I. Grosvenor, I. Owen, S. Tedds, and R. J. Poole. Non-dimensional scaling of tidal stream turbines. *Energy*, 44(1):820–829, 2012. ISSN 0360-5442. doi:

https://doi.org/10.1016/j.energy.2012.05.010. URL http://www.sciencedirect.com/science/article/pii/S0360544212003891.

I. Masters, A. Williams, T. N. Croft, M. Togneri, M. Edmunds, E. Zangiabadi, I. Fairley, and H. Karunarathna. A comparison of numerical modelling techniques for tidal stream turbine analysis. *Energies*, 8(8), 2015. ISSN 1996-1073. doi: 10.3390/en8087833.

MathWorks. One-way anova (r2020a), 2020a. URL https://www.mathworks.com/help/stats/one-way-anova.html. [Online; accessed 25 May 2020].

MathWorks. Highpass (r2021b), 2020b. URL https://uk.mathworks.com/help/signal/ref/highpass.html. [Online; accessed 15 June 2021].

MathWorks. Control rules (r2021b), 2021. URL https://uk.mathworks.com/help/stats/controlrules.html. [Online; accessed 30 June 2021].

MathWorks. Trapezoidal numerical integration (r2022b), 2022. URL https://uk.mathworks.com/help/matlab/ref/trapz.html. [Online; accessed 13 August 2022.

A. McCrea. *Renewable energy : a user's guide*. Ramsbury, Marlborough : Crowood Press, Ramsbury, Marlborough, 2008.

C. J. Mejia-Olivares, I. D. Haigh, M. J. Lewis, and S. P. Neill. Sensitivity assessment of bathymetry and choice of tidal constituents on tidal-stream energy resource characterisation in the gulf of california, mexico. *Applied Ocean Research*, 102:102281, 2020. ISSN 0141-1187. doi: https://doi.org/10.1016/j.apor.2020.102281. URL https://www.sciencedirect.com/science/article/pii/S0141118719304870.

I. A. Milne, R. N. Sharma, R.G.J. Flay, and S. Bickerton. The role of onset turbulence on tidal turbine blade loads. In *Proc. 17th Australasian Fluid Mechanics Conference, Auckland, NZ*, 2010.

I. A. Milne, R. N. Sharma, R. G. J. Flay, and S. Bickerton. Characteristics of the turbulence in the flow at a tidal stream power site. *Philosophical Transactions of the Royal Society A: Mathematical, Physical and Engineering Sciences*, 371(1985):20120196, 2013.

doi: 10.1098/rsta.2012.0196. URL http://rsta.royalsocietypublishing.org/content/roypta/371/1985/20120196.full.pdf.

I. A. Milne, A. H. Day, R. N. Sharma, and R. G. J. Flay. The characterisation of the hydrodynamic loads on tidal turbines due to turbulence. *Renewable and Sustainable Energy Reviews*, 56:851–864, 2016. ISSN 1364-0321. doi: https://doi.org/10.1016/j.rser.2015.11.095. URL https://www.sciencedirect.com/science/article/pii/S1364032115013623.

Minesto, 2021. URL https://minesto.com/. [Online; accessed 23 October 2022].

M. Mjit, P.P.J. Beaujean, and D.J. Vendittis. Comparison of fault detection techniques for an ocean turbine. In *Annual Conference of the PHM Society*, volume 3, 2011. ISBN 2325-0178.

R.K. Mobley. 43 - vibration fundamentals. In *Plant Engineer's Handbook*, pages 721–755. Butterworth-Heinemann, Woburn, 2001. ISBN 978-0-7506-7328-0. doi: https://doi.org/10.1016/B978-075067328-0/50045-8.

P. Moin. Revisiting taylor's hypothesis. *Journal of Fluid Mechanics*, 640:1 – 4, 2009.

M. Mueller and R. Wallace. Enabling science and technology for marine renewable energy. *Energy Policy*, 36(12):4376–4382, 2008. ISSN 03014215. doi: 10.1016/j.enpol.2008.09.035.

H. R. Mullings, T. J. Stallard, and G. S. Payne. Operational loads on a tidal turbine due to environmental conditions. In *The 27th International Ocean and Polar Engineering Conference*. OnePetro, 2017.

H. Murakami and T. Matsuki. A non-parametric control chart based on the mood statistic for dispersion: Control chart based on the mood statistic. *International Journal of Advanced Manufacturing Technology*, 49(5-8):757–763, 2009. ISSN 0268-3768.

D. B. Murray, P. Gallagher, B. Duffy, and V. McCormack. Energy storage solutions for offshore wave and tidal energy prototypes. In *2017 Twelfth International Conference*

on Ecological Vehicles and Renewable Energies (EVER), pages 1–8, 2017. doi: 10.1109/EVER.2017.7935944.

P. Mycek, B. Gaurier, G. Germain, G. Pinon, and E. Rivoalen. Experimental study of the turbulence intensity effects on marine current turbines behaviour. part i: One single turbine. *Renewable Energy*, 66:729–746, 2014. ISSN 0960-1481. doi: https://doi.org/10.1016/j.renene.2013.12.036. URL https://www.sciencedirect.com/science/article/pii/S096014811400007X.

A. Mérigaud and J. V. Ringwood. Condition-based maintenance methods for marine renewable energy. *Renewable and Sustainable Energy Reviews*, 66:53–78, 2016. ISSN 13640321. doi: 10.1016/j.rser.2016.07.071.

S. P. Neill and M. R. Hashemi. Chapter 8 - ocean modelling for resource characterization. In *Fundamentals of Ocean Renewable Energy*, pages 193–235. Academic Press, London, 1 edition, 2018. ISBN 978-0-12-810448-4. doi: https://doi.org/10.1016/B978-0-12-810448-4.00008-2.

OES. Ocean energy in islands and remote coastal areas: Opportunities and challenges. Report, IEA Technology Collaboration Programme for Ocean Energy Systems, 2020. URL www.ocean-energy-systems.org.

Offshore Energy. Estimate of global potential tidal resources, 2015. URL http://www.energybc.ca/cache/tidal3/tidalreserves_files/estimate-of-global-tidal-resources.jpg. [Online; accessed 8 October 2022].

S. Ordonez-Sanchez, K. Porter, C. Johnstone, M. Allmark, T. O'Doherty, R. Ellis, C. Frost, and T. Nevalainen. Numerical modelling techniques to predict rotor imbalance problems in tidal stream turbines. In *12th European Wave and Tidal Energy Conference (EWTEC), Cork, Ireland*, pages 752–1 – 752–9, 2017.

S. Ordonez-Sanchez, R. Ellis, K. E. Porter, M. Allmark, T. O'Doherty, A. Mason-Jones, and C. Johnstone. Numerical models to predict the performance of tidal stream turbines working under off-design conditions. *Ocean Engineering*, 181:198–211, 2019. ISSN

0029-8018. doi: https://doi.org/10.1016/j.oceaneng.2019.04.027. URL https://www.sciencedirect.com/science/article/pii/S0029801818312848.

P. Ouro and T. Stoesser. An immersed boundary-based large-eddy simulation approach to predict the performance of vertical axis tidal turbines. *Computers and Fluids*, 152:74–87, 2017. ISSN 0045-7930. doi: https://doi.org/10.1016/j.compfluid.2017.04.003. URL https://www.sciencedirect.com/science/article/pii/S0045793017301202.

R. Pawlowicz, B. Beardsley, and S. Lentz. Classical tidal harmonic analysis including error estimates in matlab using t tide. *Computers and Geosciences*, 28(8):929–937, 2002. ISSN 0098-3004. doi: https://doi.org/10.1016/S0098-3004(02)00013-4. URL https://www.sciencedirect.com/science/article/pii/S0098300402000134.

L. Perez, R. Cossu, C. Couzi, and I. Penesis. Wave-turbulence decomposition methods applied to tidal energy site assessment. *Energies*, 13(5):1245, 2020. ISSN 1996-1073. URL https://www.mdpi.com/1996-1073/13/5/1245.

M. Piano, S. P. Neill, M. J. Lewis, P. E. Robins, M. R. Hashemi, A. G. Davies, S. L. Ward, and M. J. Roberts. Tidal stream resource assessment uncertainty due to flow asymmetry and turbine yaw misalignment. *Renewable Energy*, 114:1363–1375, 2017. ISSN 0960-1481. doi: https://doi.org/10.1016/j.renene.2017.05.023. URL https://www.sciencedirect.com/science/article/pii/S0960148117304081.

H. Polinder, F. F. A. van der Pijl, G. J. de Vilder, and P. J. Tavner. Comparison of direct-drive and geared generator concepts for wind turbines. *IEEE Transactions on Energy Conversion*, 21(3):725–733, 2006. ISSN 1558-0059. doi: 10.1109/TEC.2006.875476.

W. Qiao and D. Lu. A survey on wind turbine condition monitoring and fault diagnosis—part ii: Signals and signal processing methods. *IEEE Transactions on Industrial Electronics*, 62(10):6546–6557, 2015. ISSN 1557-9948. doi: 10.1109/TIE.2015.2422394.

H. Rashid, M. Benbouzid, H. Titah-Benbouzid, Y. Amirat, and A. Mamoune. Tidal stream turbine biofouling detection and estimation: A review-based roadmap. *Journal of*

Marine Science and Engineering, 11, 2023. ISSN 5. doi: https://doi.org/10.3390/jmse11050908.

RenewableUK. Policy actions for wind, wave and tidal energy in the uk. Report, RenewableUK, 2013. URL http://www.renewableuk.com/en/publications/index.cfm/Manifesto-2010.

Michel Rieutord. *Fluid dynamics: an introduction*. Springer, 2014.

G. Rinaldi, L. Johanning, P.R. Thies, and R.T. Walker. A novel reliability-based simulation tool for offshore renewable technologies. In *Progress in Renewable Energies Offshore: Proceedings of the 2nd International Conference on Renewable Energies*, pages 775–784. Taylor & Francis Books Ltd, 2016.

H. Ritchie, M. Roser, and P. Rosado. Energy, 2020. URL https://ourworldindata.org/energy. [Online; accessed 30 August 2021].

A. Roberts, B. Thomas, P. Sewell, Z. Khan, S. Balmain, and J. Gillman. Current tidal power technologies and their suitability for applications in coastal and marine areas. *Journal of Ocean Engineering and Marine Energy*, 2(2):227–245, 2016. ISSN 2198-6452. doi: 10.1007/s40722-016-0044-8. URL https://doi.org/10.1007/s40722-016-0044-8.

C. Rorres. The turn of the screw: Optimal design of an archimedes screw. *Journal of Hydraulic Engineering*, 126(1):72–80, 2000. doi: doi:10.1061/(ASCE)0733-9429(2000)126:1(72). URL https://ascelibrary.org/doi/abs/10.1061/%28ASCE%290733-9429%282000%29126%3A1%2872%29.

J. B. Russell. 10 - longitudinal response. In *Performance and Stability of Aircraft*, pages 195–221. Butterworth-Heinemann, Oxford, 1996. ISBN 978-0-340-63170-6. doi: https://doi.org/10.1016/B978-034063170-6/50012-8.

S. Sai, L. A. Kumar, and S. Paneerselvam. *Solar PV and Wind Energy Conversion Systems*. Springer, 2015. ISBN 978-3-319-14940-0. doi: 10.1007/978-3-319-14941-7.

T. Schechtl, S. Hötzl, P. Rutschmann, and W. Knapp. Development of a low head tidal turbine. part 2: Test rig and model turbine design. In *Proceedings of the 12th European Wave and Tidal Energy Conference (EWTEC), Cork, Ireland*, pages 687–1, 2017.

M.J. Schulz and M.J. Sundaresan. Smart sensor system for structural condition monitoring of wind turbines: 30 may 2002–30 april 2006. Report, National Renewable Energy Lab.(NREL), Golden, CO (United States), 2006. URL https://www.nrel.gov/docs/fy06osti/40089.pdf.

S. Sheng. Wind turbine gearbox reliability database, condition monitoring, and operation and maintenance research update. Report NREL/PR-5000-66028, NREL, 2016. URL https://www.nrel.gov/docs/fy16osti/66028.pdf.

SIMEC Atlantis Energy Ltd, 2022. URL https://simecatlantis.com/. [Online; accessed 5 November 2022].

M. C. Sousounis, J. K.H. Shek, and M. A. Mueller. Modelling, control and frequency domain analysis of a tidal current conversion system with onshore converters. *IET Renewable Power Generation*, 10(2):158–165, 2016. ISSN 1752-1416.

R. Starzmann, I. Goebel, and P. Jeffcoate. Field performance testing of a floating tidal energy platform-part 1: Power performance. *Proceedings of the Asian Wave and Tidal Energy Conference, Taipei, Taiwan*, 2018.

Sustainable Development Comission. Uk tidal stream energy resource assessment. Report, Metoc PLC, 2007. URL https://www.sd-commission.org.uk/data/files/publications/TidalPowerUK1-Tidal_resource_assessment.pdf.

D. R. J. Sutherland, D. R. Noble, J. Steynor, T. Davey, and T. Bruce. Characterisation of current and turbulence in the flowave ocean energy research facility. *Ocean Engineering*, 139:103–115, 2017. ISSN 0029-8018. doi: https://doi.org/10.1016/j.oceaneng.2017.02.028. URL https://www.sciencedirect.com/science/article/pii/S0029801817300951.

J. D. Sørensen and J. N. Sørensen. *Wind energy systems: Optimising design and construction for safe and reliable operation*. Elsevier, 2010.

N. Tandon and A. Choudhury. A review of vibration and acoustic measurement methods for the detection of defects in rolling element bearings. *Tribology international*, 32(8): 469–480, 1999. ISSN 0301-679X.

P. J. Tavner. *Wave and Tidal Generation Devices: Reliability and availability*. IET, 2017. ISBN 9781849197342. doi: 10.1049/PBRN018E.

P.J. Tavner. Review of condition monitoring of rotating electrical machines. *IET Electric Power Applications*, 2(4):215–247, 2008. ISSN 1751-8679.

G. I. Taylor. Statistical theory of turbulence. *Proceedings of the Royal Society of London. Series A, Mathematical and Physical Sciences*, 151(873):421–444, 1935. ISSN 00804630. URL http://www.jstor.org/stable/96557.

P. R. Thies, L. Johanning, and G.H. Smith. Towards component reliability testing for marine energy converters. *Ocean Engineering*, 38(2-3):360–370, 2011. ISSN 0029-8018.

P. R. Thies, L. Johanning, K. A. Karikari-Boateng, C. Ng, and P. McKeever. Component reliability test approaches for marine renewable energy. *Proceedings of the Institution of Mechanical Engineers, Part O: Journal of Risk and Reliability*, 229(5):403–416, 2015. ISSN 1748-006X.

M. Thiébaut, J.F. Filipot, C. Maisondieu, G. Damblans, C. Jochum, L.F. Kilcher, and S. Guillou. Characterization of the vertical evolution of the three-dimensional turbulence for fatigue design of tidal turbines. *Philosophical Transactions of the Royal Society A*, 378(2178):20190495, 2020. ISSN 1364-503X.

J. Thomson, B. Polagye, M. Richmond, and V. Durgesh. Quantifying turbulence for tidal power applications. In *OCEANS 2010 MTS/IEEE SEATTLE*, pages 1–8, 2010. ISBN 0197-7385. doi: 10.1109/OCEANS.2010.5664600.

J. Thomson, B. Polagye, V. Durgesh, and M. Richmond. Measurements of turbulence at two tidal energy sites in puget sound, wa. *IEEE Journal of Oceanic Engineering - IEEE J OCEANIC ENG*, 37:363–374, 2012. doi: 10.1109/JOE.2012.2191656.

T.W. Thorpe. A brief review of wave energy. Report ETSU-R120, AEA Technology, 1999. URL http://www.homepages.ed.ac.uk/shs/Wave%20Energy/Tom%20Thorpe%20report.pdf.

W. Tian, Z. Mao, and H. Ding. Design, test and numerical simulation of a low-speed horizontal axis hydrokinetic turbine. *International Journal of Naval Architecture and Ocean Engineering*, 10(6):782–793, 2018. ISSN 2092-6782. doi: https://doi.org/10.1016/j.ijnaoe.2017.10.006. URL https://www.sciencedirect.com/science/article/pii/S2092678217301978.

Tidal Lagoon Power. Harnessing the power of our tides, 2012. URL http://www.tidallagoonpower.com/projects/swansea-bay/. [Online; accessed 25 November 2017].

N. Tobin, H. Zhu, and L. Chamorro. Spectral behaviour of the turbulence-driven power fluctuations of wind turbines. *Journal of Turbulence*, 16:832–846, 2015. doi: 10.1080/14685248.2015.1031242.

K. Touimi, M. Benbouzid, and P. Tavner. Tidal stream turbines: With or without a gearbox? *Ocean Engineering*, 170:74–88, 2018. ISSN 0029-8018. doi: https://doi.org/10.1016/j.oceaneng.2018.10.013. URL http://www.sciencedirect.com/science/article/pii/S0029801818313155.

K. Touimi, M. Benbouzid, and Z. Chen. Optimal design of a multibrid permanent magnet generator for a tidal stream turbine. *Energies*, 13(2), 2020. ISSN 1996-1073. doi: 10.3390/en13020487.

UNFCCC. United nations framework convention on climate change. Report, UNFCCC, 2014. URL https://unfccc.int/files/essential_background/background_publications_htmlpdf/application/pdf/conveng.pdf.

D. V. Val, L. Chernin, and D. V. Yurchenko. Reliability analysis of rotor blades of tidal stream turbines. *Reliability Engineering and System Safety*, 121:26–33, 2014. ISSN 0951-8320. doi: https://doi.org/10.1016/j.ress.2013.07.011. URL http://www.sciencedirect.com/science/article/pii/S0951832013002214.

A. Vazquez and G. Iglesias. Lcoe (levelised cost of energy) mapping: A new geospatial tool for tidal stream energy. *Energy*, 91:192–201, 2015. ISSN 0360-5442. doi: https://doi.org/10.1016/j.energy.2015.08.012. URL https://www.sciencedirect.com/science/article/pii/S0360544215010828.

Verdant Power Inc. The rite project, 2022. URL https://www.verdantpower.com/copy-of-project-development. [Online; accessed 5 November 2022].

H.K. Versteeg and W. Malalasekera. *An Introduction to Computational Fluid Dynamics: The Finite Volume Method*. Pearson Education Limited, 2007. ISBN 9780131274983.

C. Veth. Turbulence measurements in the tidally mixed southern bight of the north sea. *Netherlands Journal of Sea Research*, 25(3):301–330, 1990. ISSN 0077-7579. doi: https://doi.org/10.1016/0077-7579(90)90041-E. URL https://www.sciencedirect.com/science/article/pii/007775799090041E.

W. Wang, D. Z. Li, and J. Vrbanek. An evolving neuro-fuzzy technique for system state forecasting. *Neurocomputing*, 87:111–119, 2012. ISSN 0925-2312. doi: https://doi.org/10.1016/j.neucom.2012.02.006. URL https://www.sciencedirect.com/science/article/pii/S0925231212000732.

W. Q. Wang, M. F. Golnaraghi, and F. Ismail. Prognosis of machine health condition using neuro-fuzzy systems. *Mechanical Systems and Signal Processing*, 18(4):813–831, 2004. ISSN 0888-3270. doi: https://doi.org/10.1016/S0888-3270(03)00079-7. URL https://www.sciencedirect.com/science/article/pii/S0888327003000797.

S. Waters and G. Aggidis. Tidal range technologies and state of the art in review. *Renewable and Sustainable Energy Reviews*, 59:514–529, 2016. ISSN 1364-0321. doi: https://doi.org/10.1016/j.rser.2015.12.347. URL https://www.sciencedirect.com/science/article/pii/S136403211501730X.

S. R. Waters. *Analysing the performance of the Archimedes Screw Turbine within tidal range technologies*. Phd thesis, Department of Engineering, Lancaster University, 2015.

Y. Wenxian, P. J. Tavner, C. J. Crabtree, and M. Wilkinson. Cost-effective condition monitoring for wind turbines. *IEEE Transactions on Industrial Electronics*, 57(1):263–271, 2010. ISSN 0278-0046. doi: 10.1109/tie.2009.2032202.

B. Whitby. *Control of an Axial Flow Tidal Stream Turbine*. Phd thesis, School of Engineering, Cardiff University, 2013.

B. Whitby and C. E. Ugalde-Loo. Performance of pitch and stall regulated tidal stream turbines. *IEEE Transactions on Sustainable Energy*, 5(1):64–72, 2014. ISSN 1949-3037. doi: 10.1109/TSTE.2013.2272653.

J.D. Winchester and S.D. Quayle. Torque ripple and variable blade force: A comparison of darrieus and gorlov-type turbines for tidal stream energy conversion. In *Proceeding of the 8th European Wave and Tidal Energy Conference (EWTEC), Uppsala, Sweden*, 2009.

R. J. K. Wood, A. S. Bahaj, S. R. Turnock, L. Wang, and M. Evans. Tribological design constraints of marine renewable energy systems. *Philosophical Transactions of the Royal Society A: Mathematical, Physical and Engineering Sciences*, 368(1929):4807–4827, 2010. doi: 10.1098/rsta.2010.0192.

W. Yang, P. J. Tavner, and M. R. Wilkinson. Condition monitoring and fault diagnosis of a wind turbine synchronous generator drive train. *IET Renewable Power Generation*, 3 (1):1–11, 2009. ISSN 1752-1416. doi: 10.1049/iet-rpg:20080006.

Y. Zhang, M. Li, Z. Y. Dong, and K. Meng. Probabilistic anomaly detection approach for data-driven wind turbine condition monitoring. *CSEE Journal of Power and Energy Systems*, 5(2):149–158, 2019. ISSN 2096-0042. doi: 10.17775/CSEEJPES.2019.00010.